FLOW OBSTRUCTION EFFECTS ON HEAT TRANSFER IN CHANNELS AT SUPERCRITICAL AND HIGH SUBCRITICAL PRESSURES

by

Ahmad Eter

Thesis submitted to the
Faculty of Graduate and Postdoctoral Studies
in partial fulfillment of the requirements
for the Doctorate in Philosophy degree in Mechanical Engineering

Ottawa-Carleton Institute for Mechanical and Aerospace Engineering
Faculty of Engineering
University of Ottawa

Abstract

The objective of this thesis research is to improve our understanding of the flow obstacle effect on heat transfer at supercritical and high subcritical pressures by experimentally studying the effect of different obstacles on heat transfer in two vertical upward-flow test sections: a 3-rod bundle and an 8 mm ID tube. The heat transfer measurements cover the region of interest of the Canadian Super-critical Water Cooled Reactor (SCWR). A thorough analysis of the obstacle effect on supercritical heat transfer (SCHT) was performed. In the 3-rod bundle, two types of obstacles were employed: wire wraps and low-impact grid spacers. Wire wraps were found to be more effective than grid spacers to enhance the SCHT. In the tubular test section, obstacles appeared to suppress the heat transfer deterioration (HTD) or decrease its severity; obstacles also generally enhanced the SCHT both in the liquid-like and the gas- like region. The experiment in the tubular test section revealed that, at certain flow conditions (low mass flux, low inlet subcooling), flow obstacles can have an adverse impact on the SCHT. A criterion to predict the onset of this adverse effect was developed. At high subcritical pressures, obstacles increased the CHF and reduced the maximum post-CHF temperature. A comparison of the experimental data with prediction methods for the SCHT, single phase heat transfer, CHF and post-dryout heat transfer was performed. Lastly, a new correlation to predict the enhancement in SCHT due to obstacles was developed for heat transfer in the liquid-like and gas-like regions.

Acknowledgements

My most sincere thanks go to my supervisors, Dr. Dé Groeneveld and Dr. Stavros Tavoularis. I would also like to thank the staff of the University of Ottawa Mechanical Engineering Machine Shop, especially Leo Denner, for all their support throughout my studies.

I also gratefully acknowledge the financial support of the Natural Resources Canada through the Office of Energy Research and Development, Atomic Energy of Canada Limited, and Natural Sciences and Engineering Research Council of Canada.

Finally, this journey would not have been possible without the support of my family and friends. Thank you for encouraging me in all of my pursuits and inspiring me to follow my dreams.

Contents

List of Tables

List of Figures

Nomenclature

C_A	acceleration coefficient
C_B	buoyancy coefficient
c_p	specific heat, kJ kg^{-1} K^{-1}
$\bar{c_p}$	average specific heat, kJ kg^{-1} K^{-1}
D	diameter, m
d	minimum diameter, mm
f	friction factor
G	mass flux, kg m^{-2} s^{-1}
G^*	dimensionless mass flux
H	heat transfer coefficient, kW m^{-2} K^{-1}
h	specific enthalpy, kJ kg^{-1}
h_{fg}	latent heat, kJ kg^{-1}
k	thermal conductivity, kW m^{-1} K^{-1}
K	obstacle shape factor
$\mathrm{K_{ob}}$	local single-phase pressure-loss coefficient
L_h	heated length, mm
L_{sp}	distance to the nearest upstream obstacle, mm
$\dot{m}$	mass flow rate, kg s^{-1}
Od	obstacle's outer diameter, mm
P	pressure, MPa
P_c	critical pressure, MPa
Q_e	nominal electrical power supplied to the test section, kW
q	heat flux, kW m^{-2}
q_{loss}	heat flux to surroundings (heat losses), kW m^{-2}
q^v	volumetric heat generation, kW m^{-3}
$\mathrm{R_{SCHT}}$	ratio of heat transfer coefficient of the obstructed tube to that of the bare tube
r	test section radius, mm
S	rib pitch, mm

T	temperature, K or °C
t	spacer length, mm
V	bulk velocity, m s^{-1}
X	thermodynamic quality
v	specific volume, m^3 kg^{-1}
v_{fg}	change in specific volume, m^3 kg^{-1}
z	axial distance from the unheated test section inlet, mm
z_h	axial distance from the heated test section inlet, mm

Dimensionless Numbers:

Ac_b^*	Acceleration parameter $\left(=\dfrac{Q_b^*}{\mathrm{Re}_b^{1.625}\,\mathrm{Pr}_b}\right)$
Bo_b^*	Buoyancy parameter $\left(=\dfrac{Gr_b^*}{\mathrm{Re}_b^{3.425}\,\mathrm{Pr}_b^{0.8}}\right)$
Gz	Graetz number $\left(=\dfrac{D}{L}\mathrm{Re}\,\mathrm{Pr}\right)$
Gr_b^*	Modified Grashof number $\left(=\dfrac{g\beta_b q D^4}{k_b v_b^2}\right)$
Nu	Nusselt number $\left(=\dfrac{HL}{k}\right)$
Pr	Prandtl number $\left(=\dfrac{\mu Cp}{k}\right)$
Q_b^*	Thermal loading $\left(=\dfrac{\beta_b q D}{k_b}\right)$
Re	Reynolds number $\left(=\dfrac{GD}{\mu}\right)$

Greek Letters:

β	thermal expansion, K^{-1}
ΔP	pressure drop, kPa
ΔQ_e	power imbalance, kW
Δz	distance to the nearest upstream obstacle, mm

ε	blockage ratio, %
ζ	coefficient of local resistance or friction factor
θ	angle of thermocouple location relative to the obstacles, °
μ	dynamic viscosity, kg m^{-1} s^{-1}
ν	kinematic viscosity, m^2 s^{-1}
ξ	friction factor
ρ	fluid density, kg m^{-3}

Subscripts:

b	bulk
c	critical
e	equivalent
fd	fully developed
g	gas
h	hydraulic diameter
LO	single phase
l	liquid
Lsat	liquid/saturated case
nb	nucleate boiling
o	bare/without spacer or flow obstruction
obs	obstructed
out	outlet of the test section
PC	pseudo-critical
smooth	without flow obstruction
TP	two phase
th	thermodynamic
w	internal wall
w,o	outer wall

Abbreviations and Acronyms:

CHF	Critical Heat Flux
CSC	Central Sub-channel
DPT	Differential Pressure Transducer
HTC	Heat Transfer Coefficient
HTD	Heat Transfer Deterioration
DHT	Deteriorated Heat Transfer
ID	Inner Diameter
LUT	Lookup Table
OD	Outer Diameter
OSC	Outer Sub-channel
PDO	Post Dryout
PS	Power Supply
PT	Pressure Transducer
SC	Super Critical
SCHT	Super Critical Heat Transfer
SCUOL	Super Critical University Of Ottawa Loop
SCWR	Super Critical Water Reactor
SP	Spacer
UO	University Of Ottawa

Chapter 1

Introduction

1.1 Background

The Super-Critical Water-Cooled Reactor (SCWR) is one of the candidate designs considered by the Generation IV International Forum as an innovative nuclear energy system. A SCWR would have several advantages over existing systems. It would be safer and more compact and would have lower cost of energy production and reduced volume of nuclear waste. This research is in support of the Canadian National Program to develop the water-cooled Canadian SCWR. The water critical pressure and temperature are 22.1 MPa and 374 °C, respectively. In the development stage of the SCWR design, the idea of using CO_2 as a surrogate fluid for water has been adopted based on many investigations: researchers such as Jackson (2008), Zwolinski *et al.* (2011), Cheng *et al.* (2011) and Zahlan *et al.* (2015) have all developed fluid to fluid scaling laws based on the similarity of these fluids at supercritical pressures. Using supercritical CO_2 in the laboratory is more practical and safer than water, because of its lower critical pressure and temperature, 7.4 MPa and 31 °C, respectively.

There are other applications of supercritical heat transfer to CO_2. For example, the Brayton cycle using supercritical CO_2 has been identified as a promising approach for a Generation IV reactor. The CO_2 would either be used in a direct cycle as the primary coolant of nuclear fuel bundles, or in an indirect cycle in which the primary coolant could be liquid sodium, which would heat up the SC CO_2 in a heat exchanger. In both cases the CO_2 would be heated to a temperature of about 500 °C and expanded to a much lower pressure and temperature in a series of gas turbines. The high density of CO_2 at supercritical pressures, results in a high power density and very compact turbo-machinery compared to conventional gas turbines having the same nominal generated power but operating at much lower thermal efficiencies. Sandia National Laboratories began studying these turbines more than five years ago as part of their investigation of Generation IV advanced nuclear reactors.

From a heat transfer point of view, heat transfer in a fluid at near-critical and supercritical pressures has distinct characteristics, which are not present at subcritical pressures. When the fluid pressure and temperature are near their critical values, or when the pressure is supercritical and the temperature is near its pseudo-critical value, small changes in temperature cause large changes in the thermo-physical properties (e.g. see Figure 1.1) and the heat transfer may undergo enhancement or deterioration. Of particular importance for the safety of SCWR is the phenomenon of heat transfer deterioration (HTD). The supercritical heat transfer coefficient (HTC) falls below that expected during normal forced convective heat transfer (NHT), and therefore the heated walls might encounter high temperatures. Heat transfer deterioration is thought to be associated with the suppression of turbulence near the wall. This reduction in turbulence is due to buoyancy forces that are significant at this instant. Hence, the flow accelerates near the walls, which leads to a dramatic reduction in Reynolds stresses. Afterwards, turbulence recovery could happen when M shape velocity profile starts developing near the wall, see Figure 1.2. As will be shown in the next chapter, turbulence generators such as flow obstructions and rod bundle spacers generally suppress the occurrence of HTD and result in an improvement in supercritical heat transfer (SCHT).

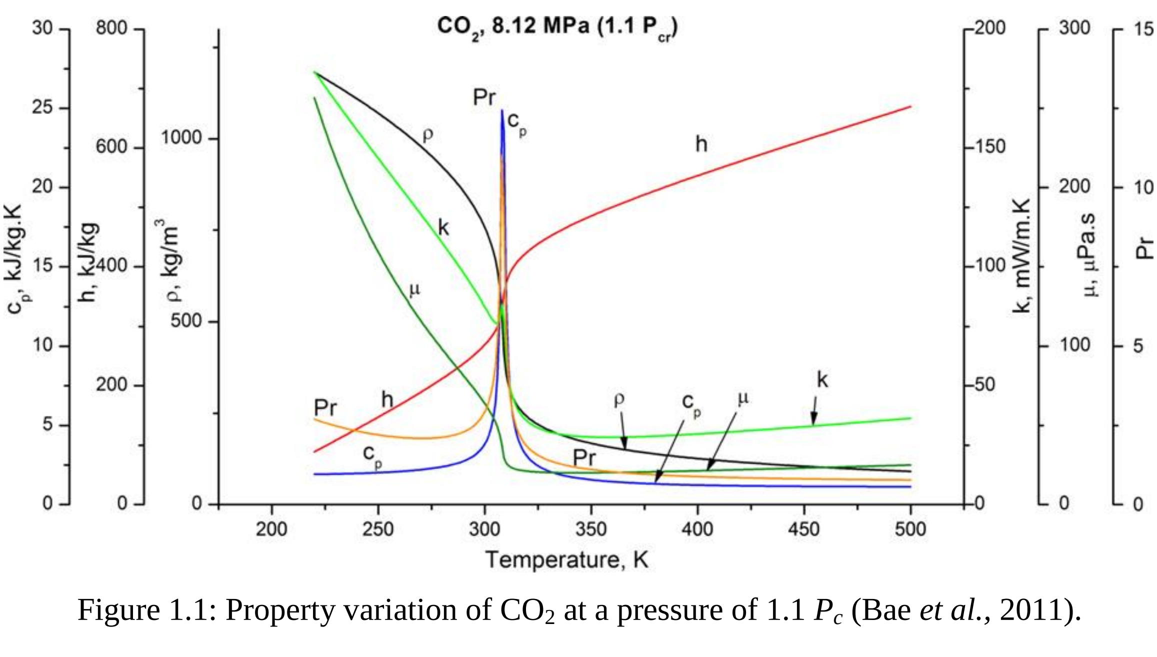

Figure 1.1: Property variation of CO_2 at a pressure of 1.1 P_c (Bae *et al.*, 2011).

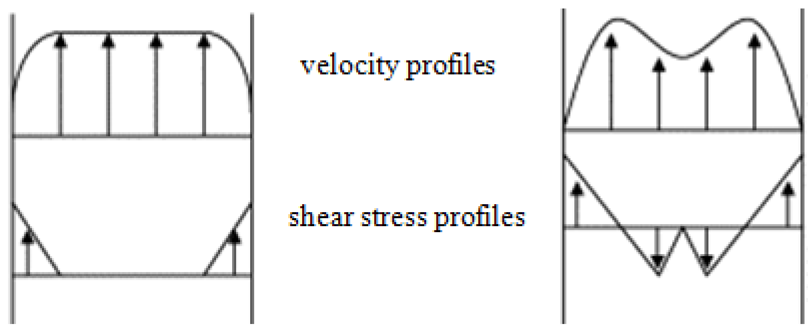

Figure 1.2: Schematic drawing of buoyancy effect, in upward pipe flow, leading to either a flattened velocity profile and decreased shear stress or to an M-shaped velocity profile and increased shear stress (Kraan *et al.*, 2005).

Heat transfer data at high subcritical pressures can be classified into four groups, based on the encountered heat transfer mode: (i) single-phase heat transfer to liquid CO_2, (ii) nucleate boiling heat transfer, (iii) film boiling heat transfer and (iv) single-phase heat transfer to CO_2 gas. Depending on the flow conditions and heat flux, not all of the above heat transfer regions will be encountered.

At supercritical pressures, the CO_2 heat transfer data can be classified into three types based on the bulk temperature (T_b) and heated wall temperature (T_w) along the heated section: (i) liquid-like ($T_b<T_w<T_{pc}$), (ii) gas-like ($T_w>T_b>T_{pc}$) and (iii) near-critical region ($T_b<T_{pc}<T_w$) where T_{pc} is the pseudo-critical temperature. As discussed earlier, in the near-critical region the properties vary drastically and the conventional single-phase heat transfer correlations do not perform well. However, for pressures well above the critical pressure and/or temperatures well away from the critical temperature, the property variation becomes minor and the single-phase heat transfer correlations again apply. The supercritical heat transfer data can be further divided into normal heat transfer and deteriorated heat transfer cases.

1.2 Motivation

The motivation for this investigation comes from the current lack of a relevant SCHT heat transfer database for spacers-equipped fuel bundles to be used in the Canadian SCWR design. An additional motivation is the recently identified use of supercritical CO_2 in reactors using the Brayton cycle; either for direct cooling of spacer-equipped fuel bundles, or in an indirect cycle where fluids such as liquid sodium are used in the primary cooling system.

1.3 Objectives

The general objective is to study experimentally heat transfer characteristics in channels of different shapes for high subcritical and supercritical pressures. The specific objectives are as follows.

- Study the impact of wire wrap and grid spacers on the SCHT of CO_2 in a three-rod bundle.
- Obtain SCHT data of CO_2 in a bare 8 mm ID tube at low mass fluxes.
- Perform a parametric study of the impact of isolated obstacles on heat transfer at supercritical pressures; the parameters considered are the operating conditions and the obstacle shape, pitch, and blockage ratio.
- Study the impact of obstacles on the heat transfer coefficient for single-phase heat transfer, nucleate boiling and film boiling, as well as on the critical heat flux (CHF).

1.4 Organization of the thesis

This thesis is prepared in the form of a manuscript-based thesis. A literature review is provided in Chapter 2. Chapter 3 contains a description of the experimental facility. The main results are presented in Chapters 4-7, each of which explores a different facet of flow obstruction effects on heat transfer. Chapter 4 addresses the obstacles (wire wraps and grid spacers) effects on supercritical heat transfer in a 3-rod bundle as presented in the following manuscript:

> Eter, A., Groeneveld, D., Tavoularis, S., 2016a. An experimental investigation of supercritical heat transfer in a three-rod bundle equipped with wire-wrap and grid spacers and cooled by carbon dioxide. Nucl. Eng. Des. 303, 173-191.

Chapter 5 addresses the obstacles effects on supercritical heat transfer in an 8 mm ID tube at supercritical pressures as presented in the following manuscript:

Eter, A., Groeneveld, D., Tavoularis, S., 2016b. Convective heat transfer in supercritical flows of CO_2 in tubes with and without flow Obstacles. Under review by Nucl. Eng. Des.

Chapter 6 addresses the obstacles effects on heat transfer at high subcritical pressures in an 8 mm ID tube as presented in the following manuscript:

Eter, A., Groeneveld, D., Tavoularis, S., 2016c. Convective heat transfer to CO_2 - cooled tubes with and without Flow obstacles at high sub-critical pressures. To be submitted to Nucl. Eng. Des.

Chapter 7 provides an assessment of the promising heat transfer correlations during normal and deteriorated heat transfer based on the 8 mm database of University of Ottawa, and discusses a new finding (adverse obstacle effect on the SCHT) and provides a criteria to avoid it.

Finally, a summary of the main results of this thesis is presented in Chapter 8 with a list of the main contributions of this thesis and recommendations for future work.

Chapter 2

Literature Review

The objective of this literature review is to assess and analyze the effects of flow obstacles on heat transfer at super-critical (SC) pressures. The review is based on SC heat transfer data obtained in different flow geometries such as tubes, annuli, and rod bundles cooled by water, refrigerants, or other fluids. To better understand the analytical work conducted in this field, a review of the evolution of prediction methods for supercritical heat transfer to upward bare tube flows for normal heat transfer (section 2.1.1), and for deteriorated heat transfer (section 2.1.2) is carried out intensively. The emphasis in this section is on describing SCHT prediction methods that may be of use in the thermal and safety analysis of either SC fossil-fueled power plants or nuclear power plants. To better understand the obstacle effect on heat transfer in general, the obstacle effect on subcritical heat transfer has also been reviewed. The basic concept of enhancement of single phase heat transfer is by increasing the turbulence level using obstacles, such as ribs, helical wires inside tubes and spacers in rod bundles, also applies at supercritical pressures. Heat transfer enhancement due to turbulence promotion devices is accompanied with an increase in frictional pressure drop. Therefore, frictional pressure drop due to flow obstacles will be considered in this literature review as well. This literature review includes heat transfer enhancement in single phase flow at subcritical pressures (Section 2.2), heat transfer enhancement during flow boiling (Section 2.3), and heat transfer enhancement at supercritical pressures (Section 2.4).

2.1 Evolution of prediction methods for supercritical heat transfer

2.1.1 Normal heat transfer

This section discusses the evolution of SCHT prediction methods for normal heat transfer that has taken place during the past 60 years, covering all known SCHT equations up to 2016. Previous reviews by Ghajar and Asadi (1986), Bazargan (2001), Pioro and Duffey (2007), Zahlan (2011), Chen and Fang (2013) and Churkin (2015) were more limited in scope, reviewing fewer prediction methods, and did not provide sufficient details to comprehend the SCHT correlation evolution. Most of the SCHT prediction methods use the **Dittus-Boelter (1930)** heat transfer correlation,

$$Nu_b = 0.023 Re_b^{0.8} Pr_b^{0.4}, \tag{2.1}$$

as a basis for the correlation's development. This correlation was found to predict many of the observed trends surprisingly well at conditions where the temperature variations across the flow are modest ("normal" SCHT) but cannot predict the changes in HTC caused by steep radial temperature gradients and those due to DHT at high heat fluxes and low flows.

Empirical correlations for supercritical heat transfer data were first proposed in 1957. Based on extensive experimentation of water at near-critical and SC conditions, **Miropol'skiy and Shitsman (1957**) noted that the Pr could vary widely from very high values at low inlet temperatures (due to the high viscosity) to smaller values at temperatures of 100-300 °C to again very high values near T_{pc}. They were able to fit their water data reasonably well using a modified form of the Dittus-Boelter (1930) correlation, by considering the minimum Prandtl number evaluated either at the heated wall or the bulk temperature instead of Prandtl number evaluated at the bulk temperature:

$$Nu_b = 0.023 Re_b^{0.8} Pr_{min}^{0.8} \, . \tag{2.2}$$

This correlation is applicable to both subcritical and supercritical pressures.

Bringer and Smith (1957) measured SCHT in water (P/P_c = 1.6) and CO_2 (P/P_c = 1.1) and analyzed the impact of a theoretically-derived dimensionless heat flux on Nu. They attempted to convert their analytical solution into a more practical prediction method by modifying the Dittus-Boelter (1930) correlation. They were able to approximately fit their data by (i) adjusting the factor 0.023 to C = 0.0266 for water and C = 0.0375 for CO_2 flows and (ii) evaluating the Nu and Re at T_b if E<0, $E = (T_{Pc}-T_b)/(T_w-T_b)$, T_{Pc} if 0<E<1, and T_w if E>1, where Their recommended correlation is:

$$Nu_x = C Re_x{}^{0.77} Pr_w{}^{0.55}, \tag{2.3}$$

for SC conditions except those close to the critical point where good agreement was more difficult to obtain. Note that the large difference in *C* values between water and CO_2 was probably due to the large differences in the reduced pressure between his SC water and CO_2 data, since at low subcritical pressures the Dittus-Boelter (1930) equation was able to predict the CO_2 data with good accuracy.

The **Petukhov *et al.* (1958)** correlation,

$$Nu_o = \frac{Re_b Pr_b \, {}^{\xi}/_{8}}{1.07 + 12.7\left({}^{\xi}/_{8}\right)^{0.5}\left(Pr_b{}^{2/3} - 1\right)} \tag{2.4}$$

$$\xi = (1.82 \log_{10} Re_b - 1.64)^{-2},$$

is the first widely used heat transfer correlation based on water data obtained in tubes at subcritical pressures that depends on the friction factor. It was tested with other fluids by different researchers as described later. This correlation was used as a basis for development of several SC correlations.

Petukhov *et al.* (1961) modified the Petukhov *et al.* (1958) equation for subcritical pressures by considering the variations of dynamic viscosity, thermal conductivity and specific heat across the tube diameter as follows:

$$Nu_b = Nu_o \left(\frac{\mu_b}{\mu_w}\right)^{0.11} \left(\frac{k_b}{k_w}\right)^{-0.33} \left(\frac{\overline{C_p}}{C_{pb}}\right)^{0.35}, \tag{2.5}$$

where Nu_o is given by Petukhov *et al.* (1958) and $\overline{C_p} = \frac{H_w - H_b}{T_w - T_b}$.

This correlation was based on their CO_2 data at supercritical pressures obtained in a horizontal tube with no buoyancy effect. In addition, they validated their correlation with water and CO_2 data obtained in vertical tubes by other investigators.

Bishop *et al.* (1965) performed SCHT measurements in water over a wide range of conditions (*P*, *G*, *q* and T_{in} were all varied significantly). A large reduction in HTC with a small increase in heat flux was observed that was attributed to changes in fluid properties. The Dittus-Boelter and Sieder-Tate Equations predicted their data reasonably well for wall temperatures less than T_{pc}. — the best agreement with all data was obtained with the **Petukhov *et al.* (1961)** equation although large deviations were observed in the near-critical region. They followed the approach of Petukhov in using an integrated average specific heat in the Prandtl number equation. They also introduced an entrance effect factor, $\left(1 + 2.4\frac{D}{x}\right)$ where x is the distance from the start of the heated length to account for the improved HTC observed near the inlet. Their modified form of the Dittus-Boelter (1930) correlation is based on optimized exponents for Re and Pr, and a density ratio factor $\left(\frac{\rho_w}{\rho_b}\right)^{0.43}$ to account for differences between wall and core fluid density:

$$Nu_b = 0.0069 Re_b^{0.9} \overline{Pr}_b^{0.66} \left(\frac{\rho_w}{\rho_b}\right)^{0.43} \left(1 + 2.4\frac{D}{x}\right), \text{where } \overline{Pr}_b = \left(\frac{\overline{C_P}\mu_b}{k_b}\right). \tag{2.6}$$

This equation was able to predict Bishop's data as well as the SCHT data of Dickerson and Welch, and of McAdams with an agreement of ±15%. A very limited comparison against SCHT data for CO_2, Oxygen and Freon showed an agreement of ±25%.

Swenson *et al*. (1965) employed the wall temperature as a reference temperature to evaluate Nusselt, Reynolds, and averaged Prandtl number in the following equation; the following correlation has a relative error of ±10%.

$$Nu_w = 0.00459 Re_w^{0.923} \overline{Pr}_w^{0.613} \left(\frac{\rho_w}{\rho_b}\right)^{0.231} \text{ where } \overline{Pr}_w = \left(\frac{\overline{C_P}\mu_w}{k_w}\right). \tag{2.7}$$

Note that the general form of Swenson *et al*.'s equation is similar to the correlation of Bishop *et al.* (1965). They found the density ratio factor is more effective in correlating their data than factors based on thermal conductivity or dynamic viscosity. The integrated specific heat between wall and bulk temperature is included in $\overline{Pr}_w$. Their correlation fitted the water data with ± 15% and CO_2 data with an acceptable accuracy (accuracy for CO_2 data fit was not specified).

Krasnoshchekov *et al.* (1967) conducted SCHT experiments to CO_2 covering a wide range of bulk temperatures. They found the heat transfer for $T_b > T_{pc}$ to be similar to single phase heat transfer while Nu was always overestimated in the near-pseudo-critical region by a single phase correlation that does not consider the property variation across the cross-section. They assumed that the dependence of Nu on Re and Pr remains the same as under conditions with no property variation (i.e. based only on bulk temperature), while the effect of the variable physical properties was accounted by introducing correction factors for the density and specific heat variations across the tube diameter, i.e. , $\left(\frac{\rho_w}{\rho_b}\right)^{0.3}$, $\left(\frac{\overline{C_p}}{C_{pb}}\right)^{n}$. The exponent n has different values depending on whether T_b is lower or higher than T_{Pc}, as shown:

$$Nu_b = Nu_o \left(\frac{\rho_w}{\rho_b}\right)^{0.3} \left(\frac{\overline{C_p}}{C_{pb}}\right)^{n} \tag{2.8}$$

where Nu_o is given by Petukhov et al. (1958) and n is defined as

$n = 0.4$ for $T_b<T_w<T_{pc}$ (liquid-like region)

$n = 0.4$ for $1.2T_{pc}<T_b<T_w$ (gas-like region)

$n = 0.4+0.2[(T_w/T_{pc})-1]$ for $T_b < T_{pc} <T_w$

$n = 0.4+0.2[(T_w/T_{pc})-1]\{1-5[(T_b/T_{pc})-1]\}$ for $T_{pc} < T_b <1.2T_{pc}$ and $T_b < T_w$

Yamagata *et al.* (1972) suggested a correlation based on their SCHT water data obtained in horizontal and vertical tubes; the correlation was a combination of the Dittus-Boelter (1930) and Krasnoshchekov *et al.* (1967) correlation. They optimized the constant factor and the exponents of Re and Pr as well as they included Pr number at the pseudo critical pressure in the equation of the exponent 'n' of $\left(\frac{\overline{C_p}}{C_{pb}}\right)^{n}$ as the following:

$$Nu_b = 0.0135 Re_b^{0.85} Pr_b^{0.8} F_c \tag{2.9}$$

$F_c = 1.0$ when $E > 1$

$Fc = 0.67 Pr_{pc}^{-0.05} \left(\frac{\overline{C_p}}{C_{pb}}\right)^{n1}$ when $0 \leq E \leq 1$, and $Fc = \left(\frac{\overline{C_p}}{C_{pb}}\right)^{n2}$ when $E < 0$.

$$n1 = -0.77\left(1 + \frac{1}{Pr_{pc}}\right) + 1.49,\ n2 = 1.44\left(1 + \frac{1}{Pr_{pc}}\right) - 0.53$$

$$E = (T_{pc} - T_b)/(T_w - T_b).$$

The authors examined the impact of using correction factors based on density, thermal conductivity, dynamic viscosity, and specific heat; they found that the correction factor based on the specific heat ratio was the only successful one in correlating their data. Yamagata's correlation fitted their water data (ranges: P = 22.6-29.4 MPa, G = 310-1830 kg m^{-2} s^{-1}, q = 116-930 kW m^{-2}, T_b = 230-540 °C) with an accuracy of ±20% in the normal heat transfer region. The authors suggested $q = 0.2G^{1.2}$ as a limiting heat flux criteria beyond which HTD will occur.

Jackson and Fewster (1975) (as reported by Pioro and Duffey, 2007) also suggested a modified form of the Krasnoshchekov *et al.* (1967) equation,

$$Nu_b = 0.0183 Re_b^{0.82} Pr_b^{0.5} \left(\frac{\rho_w}{\rho_b}\right)^{0.3}, \qquad (2.10)$$

in which density variations across the tube diameter was accounted by $\left(\frac{\rho_w}{\rho_b}\right)^{0.3}$. No further details were reported by Pioro & Duffey.

Ghajar and Asadi (1986) assessed the several equations, as specified in Table 2.1, by comparing their predictions against a compilation of experimental data obtained for CO_2 and water in the near-critical region. Prior to this comparison they first needed to select the most reliable equations for the thermodynamic and transport properties for water and CO_2 in the near critical region. They found that the correlation of Jackson and Fewster (1975) provided the best fit compared to the experimental data of carbon dioxide and water with a maximum deviation of 31 %. They subsequently modified the correlation of Jackson and Fewster (1975) based on water and carbon dioxide data. The proposed correlation has an average absolute error of 15% and 20% for carbon dioxide and water data, respectively. The following correlations are for carbon dioxide and water, respectively:

$$Nu_b = 0.025 Re_b^{0.8} Pr_b^{0.417} \left(\frac{\rho_w}{\rho_b}\right)^{0.32} \left(\frac{\overline{C_p}}{C_{pb}}\right)^{n}, \qquad (2.11)$$

$$Nu_b = 0.0064 Re_b^{0.91} Pr_b^{0.48} \left(\frac{\rho_w}{\rho_b}\right)^{0.6} \left(\frac{\overline{C_p}}{C_{pb}}\right)^{n}. \tag{2.12}$$

Kirillov *et al.* (1990) (as reported by Pioro and Duffey) accounted for the free convection within forced convection heat transfer using a buoyancy parameter, k*.

$$Nu_b / Nu_o = \left(\frac{\overline{C_p}}{C_{pb}}\right)^{n} \left(\frac{\rho_w}{\rho_b}\right)^{m} \text{ when } k^* < 0.01 \tag{2.13}$$

$$Nu_b / Nu_o = \left(\frac{\overline{C_p}}{C_{pb}}\right)^{n} \left(\frac{\rho_w}{\rho_b}\right)^{m} f(k^*) \text{ when } k^* > 0.01 \tag{2.14}$$

The buoyancy parameter $k^* = \left(1 - {}^{\rho_w}/_{\rho_b}\right)\left({}^{Gr_b}/_{Re_b^2}\right)$ accounts for free convection, m depends on the flow direction, n depends on $\left(\frac{\overline{C_p}}{C_{pb}}\right)$, T_b and T_w. Nu_o is defined as the Dittus-Boelter (1930) correlation and the Grashof number is defined as:

$$\mathrm{Gr_b} = \frac{\rho_b(\rho_b - \bar{\rho})gd^3}{\mu_b^2}. \tag{2.15}$$

Griem (1996) suggested a Dittus-Boelter (1930) type correlation with different constant factor and exponents for Re and Pr. He also introduced a factor, which is a function of the bulk enthalpy as shown:

$$Nu_{sel} = 0.0169 {Re_b}^{0.8356} {Pr_{sel}}^{0.432} \omega, \tag{2.16}$$

$$Pr_{sel} = Cp_{sel}\, \mu_b / \bar{k}\ , \ \bar{k} = 0.5(k_b + k_w)$$

$\omega = min\left(1.0, max\left(0.82; 0.82 + 9.7 \times 10^{-7}(H_b - 1.54 \times 10^6)\right)\right)$, H_b in kJ kg^{-1}.

He determined Cp at five reference temperatures between T_b and T_w; the selected specific heat Cp_{sel} was based on the average of the least 3 values among the five Cp values;

$$Cp_{sel} = \left(\sum_{j=1}^{j=5} Cp,_j - Cp,_{1^{st}\ \max} - C_p,_{2^{nd}\ \max}\right)/3 .$$

This procedure is more or less similar to the previous one suggested by Petukhov *et al.* (1961).

Pioro and Duffey (2007) devoted Chapter 11 of their book to review subcritical and supercritical heat transfer correlations proposed between 1957 to 2002. **Jackson (2002)** (as reported by Pioro and Duffey (2007)) used the following correlation to account for the bare tube heat transfer coefficient:

$$Nu_b = 0.0183 Re_b^{0.82} \overline{Pr}_b^{0.5} \left(\frac{\rho_w}{\rho_b}\right)^{0.3} \left(\frac{\overline{C_p}}{C_{pb}}\right)^{n} \tag{2.17}$$

where *n* is defined as in Krasnoshchekov *et al.* (1967) .

His correlation as well as the correlations of Bishop *et al.* (1964), Swenson *et al.* (1965), Krasnoshchekov *et al.* (1967), Yamagata *et al.* (1972), Jackson and Fewster (1975), were tested against SCHT water data (~1500 points) and carbon dioxide data (~500 data points). Results showed that Krasnoshchekov *et al.* (1967) and its modified version of Jackson (2002) correlation provided the best results; 79% of the data were correlated with an accuracy of ±25%.

The correlation of Jackson (2002) was tested against normal CO_2 heat transfer data obtained in a 3-rod bundle and an 8 mm ID tube at the University of Ottawa (Eter *et al.*, 2016a). The results showed a maximum deviation of 30 % in the bundle case and 25 % in the bare tube case.

Yang and Khartabil (2005) suggested two correlations to predict the normal and the deteriorated heat transfer CO_2 data reported by Pioro and Khartabil (2005) at supercritical pressures. They multiplied the Petukhov *et al.* (1958) correlation by correction factors that account for variations in dynamic viscosity, thermal conductivity and specific heat across the tube diameter. The following equation was recommended for normal heat transfer:

$$Nu_b = 3.4445 \left(\frac{P}{P_c}\right)^{-0.4493} \left(\frac{T_b}{T_{pc}}\right)^{1.9737} \left(10000\frac{q}{GH_b}\right)^{0.2533}$$
$$(Nu_0)^{1.0649} \left(\frac{\mu_b}{\mu_w}\right)^{-1.4362} \left(\frac{k_b}{k_w}\right)^{0.3879} \left(\frac{\overline{C_p}}{C_{pb}}\right)^{0.9771} \tag{2.18}$$

where Nu_o is defined as in Petukhov *et al.* (1958).

For the deteriorated heat transfer they recommended an equation with different coefficients and exponents:

$$Nu_b = 9.3886\left(\frac{P}{P_c}\right)^{-0.5196}\left(\frac{T_b}{T_{pc}}\right)^{2.5939}\left(10000\frac{q}{GH_b}\right)^{-0.2858}$$

$$(Nu_0)^{0.9467}\left(\frac{\mu_b}{\mu_w}\right)^{0.2244}\left(\frac{k_b}{k_w}\right)^{-0.4083}\left(\frac{\overline{C_p}}{C_{pb}}\right)^{0.764}. \quad (2.19)$$

The correlations have a reported RMS error of 11.7% and 6.65% for normal and deteriorated heat transfer, respectively. The correlations were also able to predict selected water data sets reasonably well, although the accuracy for the water data was not specified. Note that the reported RMS errors for the CO_2 data do not seem credible since the RMS error of normal heat transfer is expected to be lower than that of HTD.

Kuang *et al.* (2008) compiled a SCHT water database from different sources and used this data base to assess several correlations (specified in Table 2.1). They found all correlations to be inapplicable; therefore, they developed a new correlation which accounts for property variations across the tube diameter, buoyancy, and thermal acceleration as follows:

$$Nu_b = 0.0239\, Re_b^{0.959}\overline{Pr}_b^{0.833}\left(\frac{k_w}{k_b}\right)^{0.0863}\left(\frac{\mu_w}{\mu_b}\right)^{0.832}\left(\frac{\rho_w}{\rho_b}\right)^{0.31}(Gr^*)^{0.014}(q^+)^{-0.021} \quad (2.20)$$

where

$$Gr^* = Gr.Nu = \frac{G\beta D^4 q}{k v^2}$$

$$q^+ = \frac{q.\beta}{G.Cp_b}$$

The correlation predicted 92 % of the data within ±30%.

Jackson (2009) used the following correlation to account for the bare tube heat transfer coefficient:

$$Nu_b = 0.021\, Re_b^{0.8}\overline{Pr}_b^{0.4}\left(\frac{\rho_w}{\rho_b}\right)^{0.3}\left(\frac{\overline{C_p}}{C_{pb}}\right)^{n}. \quad (2.21)$$

This correlation is similar to the correlation of Jackson (2002) but with different constants. Jackson didn't recommend this correlation at very high heat fluxes because his assessment to this correlation showed a very small heat transfer enhancement near the pseudo critical enthalpy; *q/G* is not specified by the original paper. As indicated by the author, this is attributed to the scarcity of data at high heat fluxes used to derive the correlation.

Mokry et al. (2009) recommended a modified version of Swenson et al. (1965) by adjusting the constant factor and the exponents:

$$\mathrm{Nu_b} = 0.0061 Re_b^{0.904} \overline{\mathrm{Pr}}_\mathrm{b}^{0.684} \left(\frac{\rho_w}{\rho_b}\right)^{0.564}. \qquad (2.22)$$

The authors noted that using only a correction of density was sufficient to fit their water data. This agrees with the previous study of Swenson *et al.* (1965) and the specific heat is corrected through $\overline{Pr}$.

Zhu *et al.* (2009) used supercritical water data obtained in a tube at Xi'an Jiaotong University to develop their correlation,

$$\mathrm{Nu_b} = 0.0068 Re_b^{0.9} \overline{\mathrm{Pr}}_\mathrm{b}^{0.63} \left(\frac{\rho_w}{\rho_b}\right)^{0.17} \left(\frac{k_w}{k_b}\right)^{0.29}. \qquad (2.23)$$

The correlation is derived from normal heat transfer data and accounts for density and thermal conductivity variations across the radial direction.
The correlation predicted 88 % of the data within ±10%.

Gupta *et al.* (2010) used the SCHT water data obtained by Kirillov *et al.* (2005) at the Institute for Physics and Power Engineering (Obninsk, Russia) to develop their correlation. They found that the physical properties based on the wall temperature provided better results than the properties based on the bulk temperature, which was proposed by Bishop *et al.* (1965) and followed by Mokry *et al.* (2009). Gupta *et al.* (2010) proposed a modified form of the Swenson *et al.* (1965) correlation, which evaluates the properties for Nu, Re and average Pr at wall temperature. An additional correction factor for the dynamic viscosity was added by the authors, to account for viscosity variations between wall and bulk fluid. As well as, a correction factor accounting for the developing boundary layer effects at the entry region was developed, similar to that of Bishop *et al.* (1965); it is a function decaying exponentially along the axial distance from the beginning of the heated section (*L/D*). The proposed correlation has a relative error of ±25% and it is given as follows:

$$\mathrm{Nu_w} = 0.004\,\mathrm{Re_w^{0.923}}\,\overline{\mathrm{Pr_w}}^{0.773}\left(\frac{\mu_w}{\mu_b}\right)^{0.366}\left(\frac{\rho_w}{\rho_b}\right)^{0.186}$$

$$\mathrm{Nu_{w\_entrance}} = \mathrm{Nu_w}\left(1+\exp\left(\frac{x}{1.5\,D}\right)\right)^{0.648} \quad (2.24)$$

Wang *et al.* (2010) assessed the following correlations: Dittus-Boelter (1930), Krasnoshchekov *et al.* (1967), Jackson (2002), and Yang and Khartabil (2005). The assessment was based on SCHT water database compiled from different works. They found the correlation of Jackson provided the highest accuracy (standard deviation of 32% and RMS error of 39.7%) among the tested correlations. However, testing this correlation for upward and downward flows showed a higher error of predicting the upward heat transfer coefficient than that of the downward flow. Therefore, the authors modified the correlation of Jackson to be applicable for both downward and upward flows as follows:

$$Nu_b = 0.01503\,Re_b^{0.82}\overline{Pr}_b^{0.5}\left(\frac{\rho_w}{\rho_b}\right)^{0.3}\left(\frac{\overline{C_p}}{C_{pb}}\right)^{n}, \text{ for upward flows and}$$

$$Nu_b = 0.01763\,Re_b^{0.82}\overline{Pr}_b^{0.5}\left(\frac{\rho_w}{\rho_b}\right)^{0.3}\left(\frac{\overline{C_p}}{C_{pb}}\right)^{n}, \text{ for downward flows.} \quad (2.25)$$

where the exponent ‘n’ can be calculated by the following equations:

$n = 0.5$ for $T_b<T_w<T_{pc}$ (liquid-like region)

$n = 0.5$ for $1.2T_{pc}<T_b<T_w$ (gas-like region)

$n = 0.5+0.2[(T_w/T_{pc})-1]$ for $T_b < T_{pc} <T_w$

$n = 0.5+0.2[(T_w/T_{pc})-1]\{1-5[(T_b/T_{pc})-1]\}$ for $T_{pc} < T_b <1.2T_{pc}$ and $T_b < T_w$

The (modified) correlations predicted 86.9% and 91.3 % upward and downward flows data, respectively, compared to 67.4% and 86.5% predicted by Jackson (2002) within ±30%.

Zahlan *et al.* (2011) assessed eleven SCHT correlations that were reported in the literature between ***1965 and 2010*** (they are specified in Table 2.1). They also compiled a very large SC and near critical HTC database for water-cooled tubes consisting of over 24,000 data points. They found that the correlation of Mokry *et al.* (2009) provided the best predictions compared to the experimental water data (database) with a maximum rms error of 26% in the three supercritical sub-regions, liquid-like, gas-like, and near the critical point.

Gupta *et al.* (2013) used CO_2 SCHT data obtained in a 8 mm ID tube at AECL laboratories to develop their correlations. They proposed 3 correlations for the same database. The three correlations used different reference temperature to evaluate the physical properties as follows:

(I) bulk fluid temperature as a reference point,

$$\mathrm{Nu_b} = 0.01 Re_b^{0.89} \overline{\mathrm{Pr}}_\mathrm{b}^{-0.14} \left(\frac{\rho_w}{\rho_b}\right)^{0.93} \left(\frac{k_w}{k_b}\right)^{0.22} \left(\frac{\mu_w}{\mu_b}\right)^{-1.13} \quad (2.26)$$

(II) film temperature, $T_f = (T_w + T_b)/2$), as a reference point

$$\mathrm{Nu_f} = 0.0043 Re_f^{0.94} \left(\frac{\rho_w}{\rho_b}\right)^{0.57} \left(\frac{k_w}{k_b}\right)^{-0.52} \quad (2.27)$$

(III) wall temperature as a reference point

$$\mathrm{Nu_w} = 0.0038 Re_w^{0.96} \overline{\mathrm{Pr}}_\mathrm{w}^{-0.14} \left(\frac{\rho_w}{\rho_b}\right)^{0.84} \left(\frac{k_w}{k_b}\right)^{-0.75} \left(\frac{\mu_w}{\mu_b}\right)^{-0.22}. \quad (2.28)$$

The correlations predicted their CO_2 SCHT within relative errors of ± 20 to +30%.

Kurganov *et al.* (2013) used the Reynolds analogy between the heat transfer and friction to find a solution of the normal heat transfer at supercritical pressures. They proposed a new correlation to predict the normal heat transfer at supercritical pressures in terms of Stanton number ($St = \frac{q}{G(h_w - h_b)}$ or $St = \frac{Nu}{RePr}$).

$$St = \frac{\xi_n/8}{1 + \left(\frac{900}{Re_b}\right) + 12.7\sqrt{\xi_n/8}\,\{[\overline{Pr}_{b-w}(\overline{Cp}/Cp_b)^{nc}]^{2/3} - 1\}}$$

$$\overline{Pr}_{b-w} = \overline{Cp}/(\overline{k/\mu}) = \Delta h/\iint_{T_b}^{T_w}(\overline{k/\mu})dT$$

$$\xi_n/\xi_{ob} = (\rho_w/\rho_b)^{n_\rho}(\mu_w/\mu_b)^{n_\mu}$$

where $\xi_{ob} = 8\tau_w/(\rho_b u_b^2)$, $n_\rho = 0.35$ and $n_\mu = 0.2 + 70/Re_b^{2/3}$. (2.29)

The authors claimed that the proposed correlation, based on the extended Reynolds analogy using the integral relationship for the Prandtl number and the friction coefficient correlation, properly describes the normal heat transfer.

Yang (2013) used the same database that was used earlier by Yang and Khartabil (2005) to develop a new correlation of SCHT applicable for normal and deteriorated heat transfer. The correlations are modified forms of those presented earlier by Yang and Khartabil (2005) as follows:

(i) for normal heat transfer:

$$Nu_b = 0.41179\left(\frac{P}{P_c}\right)^{-0.43274}\left(\frac{T_b}{T_{pc}}\right)^{1.84087}\left(10000\frac{q}{GH_b}\right)^{0.13205}$$
$$\left(Nu_0\right)^{1.10223}\left(\frac{\mu_b}{\mu_w}\right)^{-0.92839}\left(\frac{k_b}{k_w}\right)^{0.16801}\left(\frac{\overline{C}_p}{C_{pb}}\right)^{0.72487} \quad (2.30)$$

where Nu_o is defined as in Petukhov *et al.* (1958).

(ii) for deteriorated heat transfer:

$$Nu_b = 1.7065\left(\frac{P}{P_c}\right)^{-0.53838}\left(\frac{T_b}{T_{pc}}\right)^{2.46823}\left(10000\frac{q}{GH_b}\right)^{-0.32562}$$

$$\left(Nu_0\right)^{0.94871}\left(\frac{\mu_b}{\mu_w}\right)^{0.50388}\left(\frac{k_b}{k_w}\right)^{-0.54941}\left(\frac{\overline{C_p}}{C_{pb}}\right)^{0.57156}. \quad (2.31)$$

The correlations have an RMS error of 10.3% and 6.91% for normal and deteriorated heat transfer, respectively. These errors are very similar to those reported earlier by Yang and Khartabil (2005).

Wang and Li (2014) used the normal SCHT water data of Yamagata *et al.* (1972) and normal SCHT water data obtained at IPPE (Institute for Physics and Power Engineering, the State Scientific Center of Russian Federation) to asses different correlations, see Table 2.1. The correlation of Swenson *et al.* (1965) provided the best prediction with a standard deviation of 17.4 %.

Subsequently Wang & Li developed a new correlation,

$$\mathrm{Nu_b} = 0.00684 Re_b^{0.89765}\overline{\mathrm{Pr}}_\mathrm{b}^{0.68625}\left(\frac{\rho_w}{\rho_b}\right)^{0.31142}\left(\frac{k_w}{k_b}\right)^{0.26185}. \quad (2.32)$$

The proposed correlation predicted the water SCHT within ± 20 %; the authors didn’t report the standard deviation of the predicted data using their correlation.

Chen and Fang (2014) assessed SCHT correlations for supercritical pressures as specified in Table 2.1. The experimental data was collected from different resources (13 papers). They found that the correlation of Mokry *et al.* (2009) had the least mean absolute error of 13.6% for the total data of normal, improved, and deteriorated heat transfer. Chen and Fang (2014) developed a correlation having a better accuracy (average absolute error of 5.4 %) than the accuracy of the Mokry *et al.* (2009) correlation. The correlation is valid for both normal and deteriorated heat transfer and accounts for the variations of Prandtl number, specific heat, and Grashof number,

$$Nu_b = 0.46 Re_b^{0.16}\left(\frac{Pr_w}{Pr_b}\right)^{0.1}\left(\frac{v_w}{v_b}\right)^{-0.55}\left(\frac{\overline{C_p}}{C_{pb}}\right)^{0.88}\left(\frac{Gr_b^*}{Gr_b}\right)^{0.81}. \quad (2.33)$$

Churkin *et al.* (2015) proposed a correlation based on water data, which is similar to the correlation of Jackson (2002) but with different values of the exponent 'n' as shown later. They assessed Dittus-Boelter (1930) and recent correlations: Mokry *et al.* (2009), Cheng *et al.* (2009), Kurganov *et al.* (2013), and Churkin *et al.* (2015) against water experimental data. The experimental data was collected from different resources (12 papers) and was limited to normal heat transfer data. The results showed that the correlation of Churkin *et al.* (2015) had the least rms error (25%) among the tested correlations.

$$Nu_b = 0.023 Re_b^{0.8} Pr_b^{0.4} \left(\frac{\rho_w}{\rho_b}\right)^{0.25} \left(\frac{\overline{C_p}}{C_{pb}}\right)^n$$

where n = 0.4 at $\left(\frac{\overline{C_p}}{C_{pb}}\right) \geq 1$ and n = 0.6 at $\left(\frac{\overline{C_p}}{C_{pb}}\right) < 1$. (2.34)

In conclusion, all correlations were modified forms of the Dittus-Boelter (1930) or the Petukhov (1958) correlation. Many investigators found an improved prediction of Nu by considering variation of fluid properties across the radial direction such as $\left(\frac{\rho_w}{\rho_b}\right)$, $\left(\frac{\mu_w}{\mu_b}\right)$, and $\left(\frac{C_{p_w}}{C_{p_b}}\right)$. Table 2.1 lists correlations to predict Nusselt number during normal / deteriorated heat transfer regime along with the main comments about each single correlation. Finally, the correlations based on the Dittus-Boelter (1930) or Petukhov *et al.* (1958) form correlations with a correction factor for specific heat and density are capable to predict the normal heat transfer. However, at HTD conditions, these empirical correlations were deemed to have a questionable accuracy.

Look-up Table Methods: A practical way of these correlations was applied, which is called lookup table. A look-up table is a dimensional table aims to predict a certain property at certain parameters. The data included in a Look up table is either pure experimental data or data predicted by the best correlations at certain conditions. **Loewenberg *et al.* (2008)** constructed the first look-up table to predict wall temperature of the normal heat transfer at supercritical pressures for water as a function of mass flux, pressure, heat flux, diameter, and bulk enthalpy. The reported standard deviation is

10.2 %. This look-up table is not applicable for HTD as all HTD data were removed by the authors at the beginning of their work. **Kuang *et al.* (2011)** constructed a lookup table to predict wall temperature of different tube diameters 7, 10, and 20 mm and water used as a coolant. This lookup table required (P, G, q, h_b) to predict T_w. The authors claimed that HTD data were included in the look up tables. However, the applicability of their lookup table is limited due to the narrow range of pressure, mass and heat flux; the accuracy is not provided. A recent lookup table to predict the heat transfer at near critical pressures was constructed by **Zahlan *et al.* (2015)**. Zahlan's *et al.* look-up table has a wide range of flow conditions (P, G, q, h_b) including HTD data. The accuracy of Zahlan's *et al.* look-up table varied between ±10 – 50 % depending on the heat transfer region. A comparison of the predicted data by the look-up table and other correlations against the experimental data showed that the look up table is more reliable than a single correlation when used over a wide range of flow conditions.

2.1.2 Deteriorated heat transfer (DHT)

A number of investigators have proposed different criteria for the onset of DHT. Many of the published studies were based on a criteria based on (q/G) values which represented a lower limit for DHT. This ratio has different values depending on the experimenter and fluid type. Table 2.2 summarizes all reported DHT criteria. These criteria are generally purely empirical, and do not reflect the physics behind the DHT; its applicability is limited to a single fluid. More recently, experimenters have attempted to develop HTD models that are discussed below and are summarized in Table 2.3.

Watts and Chou (1982) modified the correlation of Jackson and Fewster (1975) by using a function that depends on the buoyancy parameter as follows:

$$Nu_b = 0.021 Re^{0.8} \overline{Pr}_b^{0.55} \left(\frac{\rho_w}{\rho_b}\right)^{0.35} . f(K) \qquad (2.35)$$

$$K = \frac{\overline{\mathrm{Gr}}_b}{\mathrm{Re}_b^{2.7} \overline{\mathrm{Pr}}_b^{0.5}}$$

$f(K) = (1 - 3000K)^{0.295}$ when $K \leq 1.0*10^{-4}$ (standard deviation of 7.7%)

$f(K) = (7000K)^{0.295}$ when $K > 1.0*10^{-4}$ (standard deviation of 5.4%).

The buoyancy factor (K) is a modified factor of the buoyancy parameter proposed by Jackson and Hall (1979) ($K = \frac{\overline{Gr_b}}{Re_b^{2.7}}$) and includes the Prandtl number. A discussion of Jackson and Hall (1979) is given in the next section as part of the study of Jackson *et al.* (2011). These $f(K)$ correction functions were derived from SCHT data with no wall temperature peaks (wall temperature peaks occurred at the first 40 % of the heated section; the data used to derive $f(K)$ were obtained downstream from the peaks). The following correction functions were derived from SCHT data having wall temperature peaks (i.e. from the deteriorated database):

$f(K) = (1.27 - 19500K)^{0.7}$ when $K \leq 4.5*10^{-5}$ (standard deviation of 13%)

$f(K) = (2600K)^{0.305}$ when $K > 4.5*10^{-5}$ (standard deviation of 6.4%).

Although the authors stated that wall temperature peaks were not significant in the down-flow as they were in the up-flow but they used the buoyancy factor (K) to fit the down-flow data. The authors felt that using the buoyancy factor with some algebraic manipulation or modification to the exponent could fit even normal heat transfer data. Whether the data obtained downstream from the peaks is also representative of normal heat transfer is unclear.

Bae and Kim (2009) developed a set of correlations based on CO_2 data. Their correlation takes into consideration the effect of buoyancy and thermal acceleration; which is embedded in the exponent n.

$$Nu = Nu_f f(Bu) \tag{2.36}$$

$f(Bu) = (1 + 1 \times 10^8 Bu)^{-0.032}$ for $5*10^{-8}<Bu<7*10^{-7}$

$f(Bu) = 0.00185 \times (Bu)^{-0.43465}$ for $7*10^{-7}<Bu<1*10^{-6}$

$f(Bu) = 0.75$ for $1*10^{-6}<Bu<1*10^{-5}$

$f(Bu) = 0.0119 \times (Bu)^{-0.36}$ for $1*10^{-5}<Bu<3*10^{-5}$

$f(Bu) = 32.4 \times (Bu)^{0.40}$ for $3*10^{-5}<Bu<1*10^{-4}$

$$Nu_f = 0.0183 Re_b^{0.82} Pr_b^{0.5} \left(\frac{\rho_w}{\rho_b}\right)^{0.3} \left(\frac{\overline{C_P}}{C_{Pb}}\right)^n$$

where $Bu = \frac{\overline{Gr_b}}{\left(Re_b^{2.7}\overline{Pr_b}^{0.5}\right)}$, $\overline{Gr_b} = \frac{\rho_b(\rho_b - \bar{\rho})gd^3}{\mu_b^2}$ and n is defined by Krasnoshchekov *et al.* (1967).

Cheng *et al.* (2009) derived a simple heat transfer correlation based on SCHT water data of Herkenrath *et al.* (1967),

$$Nu = 0.023Re^{0.8}Pr^{1/3}F \tag{2.37}$$

$$F = min(F_1, F_2)$$

$$F_1 = 0.85 + 0.776(\pi_A \times 10^3)^{2.4},\ F_2 = \frac{0.48}{\left(\pi_{A,PC} \times 10^3\right)^{1.55}} + 1.21\left(1 - \frac{\pi_A}{\pi_{A,PC}}\right)$$

$$\pi_A = \frac{\beta_b q_w}{GC_{P,b}}.$$

which is a function of the bulk temperature only. Thus, the solution is free of any numerical instability. An acceleration dimensionless number, $\pi_A = \frac{\beta_b q_w}{GC_{P,b}}$, was introduced to correct the deviation of heat transfer from its conventional behavior.

Bae *et al.* (2011) constructed a correlation based on their CO_2 data. The buoyancy function was generated as the best fit of the normalized Nusselt number (Nu_{exp}/Nu_f) vs. the buoyancy number ($Bu = \frac{Gr_b}{Re_b^{2.7}}$) as follows:

$$Nu = Nu_f F \tag{2.38}$$

$F = (1 - 7000Bu)^{0.7}$, for $Bu<2*10^{-5}$,

$F = 0.00386(Bu)^{-0.504}$, for $2*10^{-5}<Bu<1*10^{-4}$

$F = 44.4(Bu)^{0.51}$, for $Bu>1*10^{-4}$

$$Nu_f = 0.021Re_b^{0.8}\overline{Pr_b^{0.55}}\left(\frac{\rho_b}{\rho_w}\right)^{0.35}$$

where $Bu = \frac{Gr_b}{Re_b^{2.7}}$, $\overline{Gr_b} = \frac{\rho_b(\rho_b - \rho_w)gd^3}{\mu_b^2}$.

Jackson *et al.* (2011) suggested that there are two major causes of HTD. These are discussed in the following paragraphs:

<u>1. Buoyancy Induces DHT</u>: DHT due to buoyancy forces was initially discussed by Jackson and Hall (1979). In a heated vertical tube flow, buoyancy minimizes the shear stress across the wall layer region, where the near wall layer accelerates faster than the

core, and consequently laminarizes the flow (reduce turbulent stresses) that lead to a HTD. The following model accounts for the buoyancy effect on heat transfer to a fully developed tube flow as given by Jackson *et al.* (2011).

Under conditions of variable property mixed convection:

$$\frac{Nu_b}{Nu_o} = \left[1 \mp C_B Bo_b^* \frac{F_{VP1}F_{VP3}F_{VP4}}{F_{TD}F_{VP2}} \left(\frac{Nu_b}{Nu_o}\right)^{-2.1}\right]^{0.46} \quad (2.39)$$

in wich

$$F_{VP1} = \left(\frac{\bar{\mu}}{\mu_b}\right)\left(\frac{\bar{\rho}}{\rho_b}\right)^{-1/2},\ F_{VP3} = \left(\frac{\overline{Pr}}{Pr_b}\right)^{-0.4}, \text{ and } F_{VP4} = \left(\frac{\overline{\rho\beta}}{\rho_b\beta_b}\right)$$

The negative sign refers to the upward flow and the positive sign refers to the downward flow.

According to Krasnoshchekov *et al.* (1967), the variable property factor F_{VP2} can take the form

$$F_{VP2} = \left(\frac{\rho_w}{\rho_b}\right)^{0.3}\left(\frac{\overline{C_P}}{C_{Pb}}\right)^{0.4}$$

in which *Cp* is an integrated mean value of specific heat over the temperature range from T_b to T_w.

The coefficient C_B was estimated as 10^5 based on a universal turbulent buffer layer thickness δ^+ of 30. However, the estimated value of C_B might need to be adjusted to enhance the prediction method.
Using the buoyancy parameter

$$Bo_b^* = \left(\frac{Gr_b^*}{Re_b^{3.425} Pr_b^{0.8}}\right) \quad (2.40)$$

for ‘partial laminarization’, a criterion of a buoyancy-aided flow can be found as the following

$$Bo_b^* \approx 4 \times 10^{-6}.$$

The influence of buoyancy forces on the convective heat transfer becomes dominant when

$$Bo_b^* \geq 10^{-3}.$$

If this is the case, then Nu_b will be independent of flow rate:

$Nu_b = CGr_b^{*0.23}Pr_b^{0.23}F_{VP}$ where $Gr_b^* = \frac{g\beta_b q_w d^4}{k_b v_b^2}$, β_b is the bulk volumetric thermal expansion (K^{-1}) and Fvp = Fvp_2 as defined above by Krasnoshchekov *et al.* (1967).

For conditions of mixed convection with negligible non-uniformity of fluid properties across the radial direction, the model is the following

$$\frac{Nu_b}{Nu_o} = \left[1 \mp C_B Bo_b^* \left(\frac{Nu_b}{Nu_o}\right)^{-2.1}\right]^{0.46}. \tag{2.41}$$

<u>2. *Acceleration-induced DHT:*</u> The acceleration effect on the SCHT was explained by Jackson *et al.* (2011) as follows:

"*When fluid flows through a heated tube, its enthalpy increases, its bulk temperature rises and its density falls. Because the mass flow rate doesn't change with axial distance, the bulk velocity must increase. An extra pressure difference (other than that to come over friction) has to be applied to cause this acceleration. Near-wall layers have velocities lower than the bulk velocity; hence the extra pressure gradient applied near the wall is higher than that needed to accelerate the fluid. Therefore, the shear stress gradient across the flow near the walls has to be adjusted to balance the excess pressure gradient. Consequently, the shear stress would vanish quickly with distance from the tube wall than what would have occurred in the absence of flow acceleration. In conclusion, the viscous sub-layer/buffer-layer region has a lower shear stress than that of a steady fully developed flow at the same flow rate and the turbulence production is degraded, and then the effectiveness of heat transfer is reduced".*

A semi-empirical model of the heat transfer with thermally-induced flow acceleration was given by Jackson *et al.* (2011) as the following:

$$\frac{Nu_b}{Nu_{bo}} = \left[1 \mp C_A \frac{Q_b^*}{Re_b^{1.625} Pr_b} \left(\frac{\bar{\mu}}{\mu_b}\right) \left(\frac{\bar{\rho}}{\rho_b}\right)^{-1/2} \left(\frac{Nu_b}{Nu_{bo}}\right)^{-1.1}\right]^{0.46} \tag{2.42}$$

$$Q_b^* = \frac{\beta_b q_w d}{k_b}$$

Substituting:

$$F_{VP1} = \left(\frac{\bar{\mu}}{\mu_b}\right) \left(\frac{\bar{\rho}}{\rho_b}\right)^{-1/2}$$

$$Ac_b^* = \frac{Q_b^*}{Re_b^{1.625} Pr_b}$$

Then the model becomes

$$\frac{Nu_b}{Nu_{bo}} = \left[1 - C_A Ac_b^* F_{VP1} \left(\frac{Nu_b}{Nu_{bo}}\right)^{-1.1}\right]^{0.46}. \tag{2.43}$$

The coefficient C_A was estimated as 10^4 for an assumed universal turbulent buffer layer thickness δ+ of 30. However, the estimated value of C_A might need to be adjusted to enhance the prediction method.

Since the Fvp_1 is of order unity, Jackson *et al.* (2011) suggested the criterion for impairment of heat transfer due to thermally-induced bulk flow acceleration to be less 1 % obtained from the equation is $C_A Ac_b^* < 0.02$, in which $Ac_b^* = \frac{Q_b^*}{Re_b^{1.625} Pr_b}$. Using the estimated value for the coefficient C_A of 10^4 this gives $Ac_b^* < 2 \times 10^{-6}$.

As Ac_b^* increases, parameter $C_A F_{VP1} Ac_b^*$ will increase, and the ratio of $\frac{Nu_b}{Nu_{bo}}$ is predicted to decrease systematically due to bulk flow acceleration. As Jackson *et al.* (2011) noted that $\frac{Nu_b}{Nu_{bo}}$ falls to a value of 0.6 when $C_A F_{VP1} Ac_b^*$ reaches 0.385; the following criterion for strong impairment of heat transfer due to flow acceleration can be obtained from the equation noting that F_{VP1} is of the order of unity

$$Ac_b^* \approx 2 \times 10^{-5}$$

This condition has been described as a partial laminarization.

Table 2.1: List of available Nu correlations for forced flows based in bare tubes data.

Author(s)	**Correlations**	**Comments**
Dittus-Boelter (1930)†(2,3,5,6)	$Nu_b = 0.023Re_b^{0.8}Pr_b^{0.4}$	First widely used heat transfer correlation based on water data at subcritical pressures obtained in radiator tubes. It was tested with other fluids over the past decades.
Sieder and Tate (1936)†(3)	$Nu_b = 0.027Re_b^{0.8}Pr_b^{0.33}\left(\frac{\mu_b}{\mu_w}\right)^{0.14}$	Widely used heat transfer correlation based on water data at subcritical pressures obtained in long tubes. It is more accurate than Dittus-Boelter correlation because it accounts for dynamic viscosity variations across the tube diameter.
Miropol'skiy and Shitsman (1957) (1,5)	$Nu_b = 0.023Re_b^{0.8}Pr_{min}^{0.8}$	First SCHT correlation based on water data obtained in a tube.
Bringer and Smith (1957) (1,5)	$Nu_x = CRe_x{}^{0.77}Pr_w{}^{0.55}$ Nu_x and Re_x are evaluated at T_b if E <0.0 , $T\,pc$ if 0.0 ≤E ≤1.0 , and $T\,w$ if E >1.0 C = 0.0266 for water and 0.0375 for CO_2. $E = (T_{pc} - T_b)/(T_w - T_b)$	First SCHT correlation that considers property variations along the bulk enthalpy. It is based on water and carbon dioxide data obtained in tubes with an accuracy of ±16%.
Petukhov *et al.* (1958) †	$Nu_o = \frac{Re_b Pr_b \, {}^{\xi}/_{8}}{1.07 + 12.7\left({}^{\xi}/_{8}\right)^{0.5}\left(Pr_b^{\,2/3} - 1\right)}$ $\xi = (1.82\log_{10} Re_b - 1.64)^{-2}$	First widely used heat transfer correlation based on water data at subcritical pressures that accounts for pressure drop along the heated section obtained in tubes. It was used by many researchers to develop the SCHT correlations.
Petukhov *et al.* (1961) (1,5)	$Nu_b = Nu_o\left(\frac{\mu_b}{\mu_w}\right)^{0.11}\left(\frac{k_b}{k_w}\right)^{-0.33}\left(\frac{\overline{C_p}}{C_{pb}}\right)^{0.35}$ Nu_o is given by Petukhov (1958).	First SCHT correlation based on CO_2 and water data obtained in tubes and accounts for dynamic viscosity, thermal conductivity and specific heat across the tube diameter.
Bishop *et al.* (1965) (2,5)	$Nu_b = 0.0069Re_b^{0.9}\overline{Pr}_b^{0.66}\left(\frac{\rho_w}{\rho_b}\right)^{0.43}\left(1 + 2.4\frac{D}{x}\right)$	First SCHT correlation based on water data that accounts for the entrance effects with an accuracy of ±15%.
Swenson *et al.* (1965) (1,2,3,4,5)	$Nu_w = 0.00459Re_w^{0.923}\overline{Pr}_w^{0.613}\left(\frac{\rho_w}{\rho_b}\right)^{0.231}$	Similar to Bishop *et al.* (1965) correlation, based on water data obtained in a tube with an accuracy of ±15%.

Krasnoshchekov *et al.* (1967) (1,2,3,5)	$Nu_b = Nu_o \left(\frac{\rho_w}{\rho_b}\right)^{0.3} \left(\frac{\overline{C_p}}{C_{pb}}\right)^{n}$ where n is defined as n= 0.4, for $T_b<T_w<T_{pc}$ or for $1.2T_{pc}<T_b<T_w$ n= 0.4+0.2[(T_w/T_{pc})-1], for $T_b < T_{pc} < T_w$ n= 0.4+0.2[(T_w/T_{pc})-1]{1-5[(T_b/T_{pc})-1]}, for $T_{pc} < T_b < 1.2T_{pc}$ and $T_b < T_w$ Nu_o is given by Petukhov et al. (1958).	First reliable SCHT correlation that accounts for property variation along the bulk enthalpy based on water and carbon dioxide data obtained in tubes.
Yamagata *et al.* (1972) (3,5)	$Nu_b = 0.0135 Re_b^{0.85} Pr_b^{0.8} F_c$ F_c= 1.0 when E >1 $0.67 Pr_{pc}^{-0.05} \left(\frac{\overline{C_p}}{C_{pb}}\right)^{n1}$ when 0 ≤E ≤1, and $\left(\frac{\overline{C_p}}{C_{pb}}\right)^{n2}$ when E <0 . $n1 = -0.77\left(1+\frac{1}{Pr_{pc}}\right)+1.49,\ n2 = 1.44\left(1+\frac{1}{Pr_{pc}}\right)-0.53$ $E = (T_{pc}-T_b)/(T_w-T_b)$	SCHT correlation based on water data obtained in a tube and similar to Krasnoshchekov *et al.* (1967) with an accuracy of ±20%.
Jackson and Fewster (1975) (1)	$Nu_b = 0.0183 Re_b^{0.82} Pr_b^{0.5} \left(\frac{\rho_w}{\rho_b}\right)^{0.3}$, where n is given by Krasnoshchekov *et al.* (1967)	SCHT correlation based on water data obtained in a tube and similar to Dittus-Boelter correlation.
Ghajar and Asadi (1986)	For carbon dioxide: $Nu_b = 0.025 Re_b^{0.8} Pr_b^{0.417} \left(\frac{\rho_w}{\rho_b}\right)^{0.32} \left(\frac{\overline{C_p}}{C_{pb}}\right)^{n}$, For water: $Nu_b = 0.0064 Re_b^{0.91} Pr_b^{0.48} \left(\frac{\rho_w}{\rho_b}\right)^{0.6} \left(\frac{\overline{C_p}}{C_{pb}}\right)^{n}$, where n is given by Krasnoshchekov *et al.* (1967)	Modified form of the correlation of Jackson and Fewster (1975) based on water and carbon dioxide data with an average absolute error of 15 % and 20 % for carbon dioxide and water, respectively.
Kirillov et al. (1990)	${Nu_b}/{Nu_o} = \left(\frac{\overline{C_p}}{C_{pb}}\right)^{n} \left(\frac{\rho_w}{\rho_b}\right)^{m}$ when k^* <0.01 ${Nu_b}/{Nu_o} = \left(\frac{\overline{C_p}}{C_{pb}}\right)^{n} \left(\frac{\rho_w}{\rho_b}\right)^{m} f(k^*)$ whenk^* >0.01 $k^* = \left(1-{\rho_w}/{\rho_b}\right)\left({Gr_b}/{Re_b^2}\right)$ accounts for free convection. m depends on	SCHT correlation based on water data obtained in a tube and accounts for HTD.

	the flow direction. n depends on $\left(\frac{\overline{C_p}}{C_{pb}}\right)$, T_b, and T_w	
Griem (1996) [3]	$Nu_b = 0.0169 {Re_b}^{0.8356} {Pr_{sel}}^{0.432} \omega,$ $Pr_{sel} = Cp_{sel}\, \mu_b/\bar{k}$, $\bar{k} = 0.5(k_b + k_w)$ $\omega = min\left(1.0, max\left(0.82; 0.82 + 9.7 \times 10^{-7}(H_b - 1.54 \times 10^6)\right)\right),$ H_b in kJ kg^{-1}	SCHT correlation based on water data obtained in a tube and similar to the Dittus-Boelter correlation.
Jackson (2002) [2,3,5,7]	$Nu_b = 0.0183 Re_b^{0.82} \overline{Pr}_b^{0.5} \left(\frac{\rho_w}{\rho_b}\right)^{0.3} \left(\frac{\overline{C_p}}{C_{pb}}\right)^{n}$ where n is defined as n= 0.4, for $T_b<T_w<T_{pc}$ or for $1.2T_{pc}<T_b<T_w$ n= 0.4+0.2[(T_w/T_{pc})-1], for $T_b < T_{pc} < T_w$ n= 0.4+0.2[(T_w/T_{pc})-1]{1-5[(T_b/T_{pc})-1]}, for $T_{pc} < T_b < 1.2T_{pc}$ and $T_b < T_w$	SCHT correlation based on water and carbon dioxide data obtained in tubes and similar to Krasnoshchekov *et al.* (1967).
Yang and Khartabil (2005)	$Nu_b = 3.4445 \left(\frac{P}{P_c}\right)^{-0.4493} \left(\frac{T_b}{T_{pc}}\right)^{1.9737} \left(10000\frac{q}{GH_b}\right)^{0.2533}$ $(Nu_0)^{1.0649} \left(\frac{\mu_b}{\mu_w}\right)^{-1.4362} \left(\frac{k_b}{k_w}\right)^{0.3879} \left(\frac{\overline{C_p}}{C_{pb}}\right)^{0.9771}$ Nu_o is defined as in Petukhov *et al.* (1958).	Modified form of Dittus- Boelter correlation based on CO_2 data at supercritical pressures obtained in a tube with many correction factors and with an RMS error of 11.7 %.
	$Nu_b = 9.3886 \left(\frac{P}{P_c}\right)^{-0.5196} \left(\frac{T_b}{T_{pc}}\right)^{2.5939} \left(10000\frac{q}{GH_b}\right)^{-0.2858}$ $(Nu_0)^{0.9467} \left(\frac{\mu_b}{\mu_w}\right)^{0.2244} \left(\frac{k_b}{k_w}\right)^{-0.4083} \left(\frac{\overline{C_p}}{C_{pb}}\right)^{0.764}$	Modified form of Dittus- Boelter correlation based on CO_2 data at supercritical pressures obtained in a tube with many correction factors and with an RMS error of 6.65 %; it is applicable for HTD conditions.
Kuang *et al.* (2008)[5]	Nu_b $= 0.0239\, Re_b^{0.959} \overline{Pr}_b^{0.833} \left(\frac{k_w}{k_b}\right)^{0.0863} \left(\frac{\mu_w}{\mu_b}\right)^{0.832} \left(\frac{\rho_w}{\rho_b}\right)^{0.31} (Gr^*)^{0.014} (q^+)^{-0.021}$ $Gr^* = Gr.Nu = \frac{G\beta D^4 q}{k v^2}$ $q^+ = \frac{q.\beta}{G.Cp_b}$	Modified form of Dittus- Boelter correlation based on water data at supercritical pressures obtained in tubes accounts for property variations radially, buoyancy, and thermal acceleration with a maximum relative error of 30%.

Jackson (2009)	$Nu_b = 0.021\, Re_b^{0.8} \overline{Pr}_b^{0.4} \left(\frac{\rho_w}{\rho_b}\right)^{0.3} \left(\frac{\overline{C_p}}{C_{pb}}\right)^{n}$	Similar to the coorelation of Jackson (2002) and not recommended at high heat fluxes, *q/G* is not specified by the original paper.
Mokry *et al.* (2009) [3,4,6]	$Nu_b = 0.0061 Re_b^{0.904} \overline{Pr}_b^{0.684} \left(\frac{\rho_w}{\rho_b}\right)^{0.564}$	Modified form of the Dittus- Boelter correlation based on water data at supercritical pressures obtained in a tube with a relative error of ±25 %.
Zhu *et al.* (2009)	$\mathrm{Nu_b} = 0.0068 Re_b^{0.9} \overline{\mathrm{Pr}}_\mathrm{b}^{0.63} \left(\frac{\rho_w}{\rho_b}\right)^{0.17} \left(\frac{k_w}{k_b}\right)^{0.29}$	Modified form of the Dittus- Boelter correlation based on water data at supercritical pressures obtained in a tube with a maximum relative error of 10 %.
Gupta *et al.* (2010) [3,6]	$\mathrm{Nu_w} = 0.004\, \mathrm{Re_w^{0.923}}\, \overline{\mathrm{Pr_w}}^{0.773} \left(\frac{\mu_w}{\mu_b}\right)^{0.366} \left(\frac{\rho_w}{\rho_b}\right)^{0.186}$ $\mathrm{Nu_{w\_entrance}} = \mathrm{Nu_w} \left(1 + \exp\left(\frac{x}{1.5\, D}\right)\right)^{0.648}$	Modified form of the Swenson *et al.* (1965) correlation which considers properties for Nu, Re and average Pr at wall temperature with an extra correction factor for the dynamic viscosity; it has an accuracy of ±25 %.
Wang *et al.* (2010)	$Nu_b = 0.01503\, Re_b^{0.82} \overline{Pr}_b^{0.5} \left(\frac{\rho_w}{\rho_b}\right)^{0.3} \left(\frac{\overline{C_p}}{C_{pb}}\right)^{n}$, for upward flows and $Nu_b = 0.01763\, Re_b^{0.82} \overline{Pr}_b^{0.5} \left(\frac{\rho_w}{\rho_b}\right)^{0.3} \left(\frac{\overline{C_p}}{C_{pb}}\right)^{n}$, for downward flows. where the exponent 'n' can be calculated by the following equations: n = 0.5 for $T_b<T_w<T_{pc}$ (liquid-like region) n = 0.5 for $1.2T_{pc}<T_b<T_w$ (gas-like region) $n = 0.5+0.2[(T_w/T_{pc})-1]$ for $T_b < T_{pc} < T_w$ $n = 0.5+0.2[(T_w/T_{pc})-1]\{1-5[(T_b/T_{pc})-1]\}$ for $T_{pc} < T_b < 1.2T_{pc}$ and $T_b < T_w$	Modified form of the Jackson (2002) correlation with a maximum relative error of 30 %.
Gupta *et al.* (2013)	$\mathrm{Nu_b} = 0.01 Re_b^{0.89} \overline{\mathrm{Pr}}_\mathrm{b}^{-0.14} \left(\frac{\rho_w}{\rho_b}\right)^{0.93} \left(\frac{k_w}{k_b}\right)^{0.22} \left(\frac{\mu_w}{\mu_b}\right)^{-1.13}$ $\mathrm{Nu_f} = 0.0043 Re_f^{0.94} \left(\frac{\rho_w}{\rho_b}\right)^{0.57} \left(\frac{k_w}{k_b}\right)^{-0.52}$ $\mathrm{Nu_w} = 0.0038 Re_w^{0.96} \overline{\mathrm{Pr}}_\mathrm{w}^{-0.14} \left(\frac{\rho_w}{\rho_b}\right)^{0.84} \left(\frac{k_w}{k_b}\right)^{-0.75} \left(\frac{\mu_w}{\mu_b}\right)^{-0.22}$	3 different correlations for the same SCHT CO_2 database based on different reference temperatures to evaluate the thermo-physical properties with a relative error range of ± 20 - 30 %.
Kurganov *et al.* (2013) [6]	$St = \frac{\xi_n/8}{1 + \left(\frac{900}{Re_b}\right) + 12.7\sqrt{\xi_n/8}\,\{[\overline{Pr}_{b-w}(\overline{Cp}/Cp_b)^{nc}]^{2/3} - 1\}}$	SCHT correlation based on Reynolds analogy between heat transfer and friction.

	$$\overline{Pr}_{b-w} = \overline{Cp}/(\overline{k/\mu}) = \Delta h / \iint_{T_b}^{T_w} (\overline{k/\mu}) dT$$ $$\xi_n / \xi_{ob} = (\rho_w/\rho_b)^{n_\rho} (\mu_w/\mu_b)^{n_\mu}$$ where $\xi_{ob} = 8\tau_w/(\rho_b u_b^2)$, $n_\rho = 0.35$ and $n_\mu = 0.2 + 70/Re_b^{2/3}$.	
Yang (2013)	$$Nu_b = 0.41179\left(\frac{P}{P_c}\right)^{-0.43274}\left(\frac{T_b}{T_{pc}}\right)^{1.84087}\left(10000\frac{q}{GH_b}\right)^{0.13205}$$ $$(Nu_0)^{1.10223}\left(\frac{\mu_b}{\mu_w}\right)^{-0.92839}\left(\frac{k_b}{k_w}\right)^{0.16801}\left(\frac{\overline{C}_p}{C_{pb}}\right)^{0.72487}$$ where Nu_o is defined as in Petukhov *et al.* (1958).	Similar to the normal SCHT correlation derived by Yang and Khartabil (2005) with an RMS error of 10.3%.
	$$Nu_b = 1.7065\left(\frac{P}{P_c}\right)^{-0.53838}\left(\frac{T_b}{T_{pc}}\right)^{2.46823}\left(10000\frac{q}{GH_b}\right)^{-0.32562}$$ $$(Nu_0)^{0.94871}\left(\frac{\mu_b}{\mu_w}\right)^{0.50388}\left(\frac{k_b}{k_w}\right)^{-0.54941}\left(\frac{\overline{C}_p}{C_{pb}}\right)^{0.57156}.$$	Similar to the deteriorated SCHT correlation derived by Yang and Khartabil (2005) with an RMS error of 6.91%.
Wang and Li (2014)	$$\mathrm{Nu_b} = 0.00684 Re_b^{0.89765}\overline{\mathrm{Pr}}_\mathrm{b}^{0.68625}\left(\frac{\rho_w}{\rho_b}\right)^{0.31142}\left(\frac{k_w}{k_b}\right)^{0.26185}$$	Modified form of the Dittus-Boelter correlation based on water data at supercritical pressures obtained in tubes with a maximum relative error of 20 %.
Chen and Fang (2014)	$$Nu_b = 0.46 Re_b^{0.16}\left(\frac{Pr_w}{Pr_b}\right)^{0.1}\left(\frac{v_w}{v_b}\right)^{-0.55}\left(\frac{\overline{C_p}}{C_{pb}}\right)^{0.88}\left(\frac{Gr_b^*}{Gr_b}\right)^{0.81}$$	Modified form of the Dittus-Boelter correlation based on water data at supercritical pressures obtained in a tube with mean absolute error of 5.4 % and accounts for HTD.
Churkin *et al.* (2015)	$$Nu_b = 0.023 Re_b^{0.8} Pr_b^{0.4}\left(\frac{\rho_w}{\rho_b}\right)^{0.25}\left(\frac{\overline{C_p}}{C_{pb}}\right)^{n}$$ Where n = 0.4 at $\left(\frac{\overline{C_p}}{C_{pb}}\right) \geq 1$ and n = 0.6 at $\left(\frac{\overline{C_p}}{C_{pb}}\right) < 1$	Modified form of the Krasnoshchekov *et al.* (1967) correlation based on water data obtained in a tube with an rms error of 25 %.
Loewenberg *et al.* (2008)	SCHT Lookup Table	First look-up table to predict wall temperature at supercritical pressures constructed based on normal heat transfer data of water obtained in tubes, and with

		a standard deviation of 10.2%.
Liu *et al.* (2011)	SCHT Lookup Table	Look-up table to predict wall temperature of tubes having water flows at supercritical pressures, accounts for both normal heat transfer and HTD. Its applicability is limited due to the narrow ranges of the operating conditions.
Zahlan *et al.* (2015)	SCHT Lookup Table	Most recent look-up table to predict water SCHT of tubes and accounts for both normal heat transfer and HTD, based on wide ranges of the operating conditions. The relative error varied from ±10 - 50% depending on the heat transfer regime.

[†] For turbulent flows at subcritical pressures.

Table 2.2: List of available HTD criteria

Author(s)	Criterion	Coolant
Vikhrev et al. (1967)	$q/G \geq 0.4$ kJ kg^{-1}	Water
Ornatsky et al. (1970)	$q/G \geq 0.95$-1.05 kJ kg^{-1} (stable flow) $q/G \geq 0.68$-0.9 kJ kg^{-1} (oscillatory flow)	Water
Kondrat'ev (1971)	$q \geq 5.515 \times 10^{-17} Re_b^{1.7} \left(\frac{P}{0.101325}\right)^{4.5}$	Water
Yamagata et al. (1972)	$q = 0.2G^{1.2}$	Water
Protopopov and Silin (1973)	$\frac{q}{G} \geq \frac{1.3}{(t_{pc} - t_b) C_{pb} \left(\frac{\xi}{8}\right) \left(\frac{\nu_w}{\nu_{pc}}\right)^{1.3}}$	Water
Alekseev et al. (1976)	$q/G \geq 0.8$ kJ kg^{-1}	Water
Kirillov et al. (1990)	$k^* < 0.4$ or $\frac{Gr}{Re^2} < 0.6$ Where $Gr = \frac{g\left(1 - \frac{\rho_w}{\rho_b}\right) D^3}{\nu_b^2}$ $k^* = \left(1 - \frac{\rho_w}{\rho_b}\right) \frac{Gr}{Re^2}$	Water
Mikielewicz et al. (2002)	$Bo^* = \frac{Gr^*}{Re^{3.425} Pr^{0.8}} \geq 6 \times 10^{-7}$ where $Gr^* = \frac{g\beta q D^4}{k\nu^2}$	Gas: helium
Yang and Khartabil (2005)	$q = 0.27G^{0.94}$	CO_2
Gabaraev et al. (2007)	$q = 7.9 \times 10^{-4} G \left(\frac{P}{P_c}\right)^{1.5}$	Water
Farah et al. (2010)	$q = -58.97 + 0.745G$	Water

Table 2.3: List of available Nu models for forced flows in bare tubes valid for both normal and deteriorated heat transfer.

Author(s)	Correlations	Comments
Watts and Chou (1982)[(2,3)]	$Nu_b = 0.021Re^{0.8}\overline{Pr}_b^{0.55}\left(\frac{\rho_w}{\rho_b}\right)^{0.35} . f(K)$ For downstream wall temperature peaks data: $f(K) = (1-3000K)^{0.295}$ when $K \leq 1.0*10^{-4}$ (standard deviation of 7.7%) $f(K) = (7000K)^{0.295}$ when $K > 1.0*10^{-4}$ (standard deviation of 5.4%). $k = \frac{\overline{\mathrm{Gr}}_{\mathrm{b}}}{\mathrm{Re}_{\mathrm{b}}^{2.7}\,\overline{\mathrm{Pr}}_{\mathrm{b}}^{0.5}}$ For data including wall temperature peaks: $f(K) = (1.27-19500K)^{0.7}$ when $K \leq 4.5*10^{-5}$ (standard deviation of 13%) $f(K) = (2600K)^{0.305}$ when $K > 4.5*10^{-5}$ (standard deviation of 6.4%).	First SCHT correlation that accounts for both wall temperature peaks and downstream wall temperature peaks data by considering buoyancy forces based on water data obtained in a tube.
Bae and Kim (2009): slightly modified by Bae *et al.* (2011)	$Nu = Nu_f f(Bu)$ $f(Bu) = (1 + 1\times 10^8 Bu)^{-0.032}$ for $5*10^{-8}<Bu<7*10^{-7}$ $f(Bu) = 0.00185 \times (Bu)^{-0.43465}$ for $7*10^{-7}<Bu<1*10^{-6}$ $f(Bu) = 0.75$ for $1*10^{-6}<Bu<1*10^{-5}$ $f(Bu) = 0.0119 \times (Bu)^{-0.36}$ for $1*10^{-5}<Bu<3*10^{-5}$ $f(Bu) = 32.4 \times (Bu)^{0.40}$ for $3*10^{-5}<Bu<1*10^{-4}$ $Nu_f = 0.0183Re_b^{0.82}Pr_b^{0.5}\left(\frac{\rho_w}{\rho_b}\right)^{0.3}\left(\frac{\overline{C_P}}{C_{Pb}}\right)^{n}$ $Bu = \frac{\overline{Gr_b}}{\left(Re_b^{2.7}\overline{Pr_b}^{0.5}\right)}$ $\overline{Gr_b} = \frac{\rho_b(\rho_b - \bar{\rho})gd^3}{\mu_b^2}$ where *n* is defined by Krasnoshchekov *et al.* (1967).	Derived based on CO_2 SCHT data obtained in tubes, has different buoyancy functions for different buoyancy ranges.
Cheng et al. (2009)	$Nu = 0.023Re^{0.8}Pr^{1/3}F$ $F = min(F_1, F_2)$ $F_1 = 0.85 + 0.776(\pi_A \times 10^3)^{2.4}$ $F_2 = \frac{0.48}{(\pi_{A,PC}\times 10^3)^{1.55}} + 1.21\left(1 - \frac{\pi_A}{\pi_{A,PC}}\right)$ $\pi_A = \frac{\beta_b q_w}{GC_{P,b}}$	Simple correlation based on bulk temperature only, its accuracy is questionable based on the assessment of Bae *et al*. (2011) and the present estimation.
Bae *et al.* (2011)	$Nu = Nu_f F$ $F = (1-7000Bu)^{0.7}$, for $Bu<2*10^{-5}$, $F = 0.00386(Bu)^{-0.504}$, for $2*10^{-5}<Bu<1*10^{-4}$ $F = 44.4(Bu)^{0.51}$, for $Bu>1*10^{-4}$ $Nu_f = 0.021Re_b^{0.8}\overline{Pr_b^{0.55}}\left(\frac{\rho_b}{\rho_w}\right)^{0.35}$ $Bu = \frac{Gr_b}{Re_b^{2.7}}$ $\overline{Gr_b} = \frac{\rho_b(\rho_b - \rho_w)gd^3}{\mu_b^2}$	Similar to Bae and Kim (2009) with coarse buoyancy ranges and different Nu_f.

Jackson (2010)	$$\frac{Nu_b}{Nu_o} = \left[1 \mp 1875 Bo_b F_{V1} \left(\frac{Nu_b}{Nu_o}\right)^{-1.1}\right]^{0.46}$$ $$Nu_o = 0.023 Re^{0.8} Pr^{1/3}$$ $$F_{V1} = \left(\frac{\bar{\mu}}{\mu_b}\right)\left(\frac{\bar{\rho}}{\rho_b}\right)^{-1/2}$$ $$Bo_b = \left(\frac{Gr_b}{Re_b^{2.625} Pr_b^{1/3}}\right)$$ $$Gr_b = \frac{\rho_b(\rho_b - \rho_w) g d^3}{\mu_b^2}$$	Semi-analytical solutions of buoyancy effect on SCHT.
Jackson *et al.* (2011)	$$\frac{Nu_b}{Nu_o} = \left[1 \mp C_B Bo_b^* \frac{F_{VP1} F_{VP3} F_{VP4}}{F_{TD} F_{VP2}} \left(\frac{Nu_b}{Nu_o}\right)^{-2.1}\right]^{0.46}$$	
Jackson *et al.* (2011)	$$\frac{Nu_b}{Nu_{bo}} = \left[1 \mp C_A \frac{Q_b^*}{Re_b^{1.625} Pr_b} \left(\frac{\bar{\mu}}{\mu_b}\right)\left(\frac{\bar{\rho}}{\rho_b}\right)^{-1/2} \left(\frac{Nu_b}{Nu_{bo}}\right)^{-1.1}\right]^{0.46}$$	Semi-analytical solutions of acceleration effect on SCHT.

2.2 Heat transfer enhancement for single-phase flow at subcritical pressures

Many investigators have examined various options to enhance single-phase heat transfer at subcritical pressures. Their results showed that the augmentation of HTC depends primarily on specific geometric factors, i.e. obstacle shape, obstacle ratio and pitch.

Yao *et al.* (1982) observed that the Nusselt number of an obstructed single-phase flow in bundles reaches a maximum at, or slightly downstream of the flow obstacle. The obstacle induced heat transfer enhancement was found to decay exponentially downstream of an obstacle.

The authors recommended Eq. (2.44) for Reynolds number higher than 10^4.

$$\left(\frac{Nu_{obs}}{Nu_o}\right) = 1 + 5.55\varepsilon^2 e^{-0.13(z/D)} \tag{2.44}$$

where Nu_o is Nusselt number of the bare bundle and Nu_{obs} refers the bundle equipped with flow obstacles, ε is the blockage ratio and z is the distance downstream of the obstacle.

Yoder (1985) discussed the effect of a grid spacer on single-phase heat transfer using a wide range of experimental data obtained from different rod bundles as shown in Table 2.4.

His results indicate that the heat transfer augmentation downstream of a grid spacer depends on three factors, i.e. grid blockage ratio, Reynolds number and the distance downstream of the grid spacer. The peak Nusselt number ratio increases as the spacer blockage ratio increases, but decreases with increasing Reynolds number. The maximum enhanced heat transfer distance downstream the spacer is nearly 30 hydraulic diameters.

Tanase and Groeneveld (2015) identified the following three primary mechanisms that may enhance single-phase heat transfer at subcritical pressures.

1) Disruption of boundary layer, **Yao *et al.* (1982)** suggested that the redevelopment of the boundary layer is similar to the entrance effect in a heated channel. This similarity is based on the assumption that in both cases the viscous boundary layer develops and it needs a certain distance to reach its fully developed profile.

2) Increase of turbulent mixing, **Yao *et al.* (1995), Doerffer *et al.* (1996), Becker *et al.* (2002) and Soussa (2002)** show that around and downstream of a flow obstacle, steady and unsteady structures (eddies) are formed. These eddies obey the energy cascade theorem. Based on this theorem, large eddies will collide with small eddies and this collision is accompanied with mass and energy transfer from large to small eddies. This process continues until the smallest eddies are dissipated by viscous forces. The flow downstream of an obstacle splits into two paths, i.e. (i) forward flow and (ii) backward flow or reverse flow; the time to reattach to each other depends on flow and geometric factors such as Reynolds number, obstacle shape and pitch. This reattachment region represents a local maximum in heat transfer coefficient as indicated by **Terekhov *et al.* (2002)**; the reattachment lengths varies from 16.5 to 18.5 obstacle heights for obstacle height 20 and 10, respectively.

3) Fin effect, this mechanism can be used when relatively large obstacles with high thermal conductivity and good thermal contact with the heated wall are present. The affected region of the fin effect will be limited to the region very close to the obstacle where thermal conduction effects are significant.

Various degrees of augmentation of single phase HT at subcritical pressures have been observed. **Doerffer *et al.* (1996)** found that the maximum HT enhancement was 1.14 times the smooth channel value when a single obstacle at high Re numbers ($2\cdot10^5$) is used, while

Hong and Hsieh (1991) found that the enhancement is 4.6 times the smooth channel value at low Re numbers (~ 10^4) and a short obstacle pitch (5.4 times the obstacle height). Moreover, the axial distance downstream of an obstacle, where the enhancement was observed, varies significantly between the studies. For example, **Doerffer *et al.* (1996)** reported that the effect of flow obstruction extended between 5 and 15 tube diameters, depending on Re number but **Yao *et al.* (1982)** and **Holloway *et al.* (2004)** reported that enhancement effects were noted up to 35 channel diameters, while **Yoder (1985)** reported that the augmentation region extended up to 30 hydraulic diameters downstream of the flow obstacle. This variation appears to depend mainly on the turbulence level which is related to the flow blockage ratio. **Miller *et al.* (2013)** studied heat transfer to superheated steam in a typical 7 × 7 pressurized water reactor (PWR) bundle; heat transfer data obtained from the Penn State/NRC Rod Bundle Heat Transfer (RBHT) facility. An improved heat transfer correlation accounted for the effect of obstructed area, axial distance downstream from the grid and flow Reynolds number was derived. The correlation was recommended for $15.6 < \varepsilon < 36.2$ and Re numbers between 8000 and 30,000. **Tanase and Groeneveld (2015)** performed heat transfer experiments on a single-phase heat transfer in a heated tube equipped with flow obstructions using R-134a as a coolant over a wide range of Re number (14,000 to 97,000). Three types of flow obstruction were tested: eccentric cylinders with either blunt or rounded edges, and annular obstacles, each having a flow blockage of either 0.15 or 0.30. The heat transfer measurements were between 3D to 70D downstream the trailing edge of the obstruction. Their experimental data showed that heat transfer augmentation downstream from the flow obstructions depends strongly on the obstructed area, flow Reynolds number, and distance from the flow blockage. A weak dependence of the heat transfer augmentation on the shape or circumferential location of the obstruction was found. They derived an improved prediction method that correlates the obstructed flow area, Re number and the distance from the trailing edge of the obstacle. Table 2.5 and Table 2.6 show the correlations that predict the effects of flow obstacles on single phase heat transfer and pressure drop, respectively.

Table 2.4: Experiments investigating the obstacle effect on single-phase heat transfer as reported by Yoder (1985) and additional studies.

Reference	Test section/ No.rods	Fluid	Rod dia.(mm)	Pitch to diameter ratio	Spacer/obstacle details	Mass flux kg m^{-2} s^{-1} (Re)
Marek and Rehme (1979)	3	Air	21.2	1.45	ε = 0.253-0.348 Honeycomb type grid, 30 mm long.	1.27 $*10^4$ (Re)
Hassan and Rehme (1981)	3	Air	21.2	1.45	ε = 0.302-0.348 Honeycomb type grid, 30 mm long.	(0.006-2.0) * 10^5 (Re)
Krett and Majer (1971)	7	Air	7.6	-	ε = 0.303	(0.4-1.5) $*10^5$ (Re)
Vlcek and Weber (1970)	1	Air	8.0	-	ε = 0.24	(1.3-2.1) $*10^5$ (Re)
Hoffman *et al.* (1970)	7	Air	19.1	1.33	ε = 0.23	1-80
Anklam *et al.* (1982)	64	Steam	9.5	1.34	ε = 0.30	5-30
Wong *et al.* (1981)	161	Steam	9.5	1.3	ε = 0.35	3-23
Holloway *et al.* (2004)	5*5	Water	9.5	-	Different grid designs with and without mixing vanes.	28000 and 42000 (Re)
Karoutas *et al.* (1995)	5*5	Water	-	-	Two grid designs were investigated.	average velocity = 6.79 $m.s^{-1}$
Miller et al. (2013)	7*7	Steam	-	-	0.156 < ε < 0.362	(8000-30,000)
Tanase and Groeneveld (2015)	tube	R134A	5.59	-	Blunt, rounded, and annular obstacles	14,000 to 97,000(Re)

Table 2.5: Prediction methods for spacer effect on single-phase heat transfer.

Reference	Prediction method	Flow regime	Comments
Marek and Rehme (1979)	$\frac{Nu_{Max}}{Nu_o} = 1 + 5.55\varepsilon^2$, maximum enhancement at spacer plane.	Single-phase Gas	Predicts only maximum enhancement
Hassan and Rehme (1981)	At spacer leading edge: $\frac{Nu_{Max}}{Nu_o} = 1 + K\varepsilon^2$ Downstream from spacer: $\frac{Nu}{Nu_o} = KGz^m$ Gz is Graetz number, $m = -30.34\,\mathrm{Re}^{-0.253}\,\varepsilon^2$, for smooth surface $m = -(1 + 4.9\times10^4\,\mathrm{Re}^{-1.2})\varepsilon^2$, for rough surface $K = 0.426 + 0.113C - 2.25\varepsilon$, for smooth surface $K = \min\begin{bmatrix} 0.344 + 0.35C - 2.25\varepsilon \\ -0.1298C^2 + 1.2466C - 1.8478 - 2.25\varepsilon \end{bmatrix}$, for rough surface, and $C = \log \mathrm{Re}$	Single-phase gas	Smooth and rough surfaces
Yao *et al.* (1982)	Downstream from spacer: $\left(\frac{Nu}{Nu_o}\right)sp = 1 + 5.55\varepsilon^2 e^{-0.13(L/D)}$	Single-phase and PDO	$\mathrm{Re} > 10^4$ For bundles equipped with straight egg crate spacer
Holloway *et al.* (2004)	Downstream from spacers: $\frac{Nu}{Nu_o} = 1 + C_1\varepsilon^2 e^{-\alpha L/D_{hy}}$, where C_1 = 6.5, α = 0.8	Single-phase water	Re: 28000 and 42000 *L/D* = 1.4 to 33, Bundle equipped with support grid (standard without flow enhancing features like swirling vanes)
Miller et al. (2013)	$\frac{Nu}{Nu_0} = 1 + 465.4\,\mathrm{Re}^{-0.5}\,\varepsilon^2 \exp\left(-7.31\times10^{-6}\,\mathrm{Re}^{1.15}\,\frac{x}{D_h}\right)$	Single-phase steam	Grid spacers/rod bundle
Tanase and Groeneveld (2015)	$\frac{Nu}{Nu_0} = 1 + A\varepsilon^B e^{-0.13(L/D)}$ $A = 3.58\times10^{-5}\,\mathrm{Re}$ $B = 0.47\ln(\mathrm{Re}) - 3.32$	Single-phase R134A	Obstructed tube by blunt obstacles

Table 2.6: Spacers (obstacles) pressure drop correlations for single phase flow.

Reference	Prediction method	Flow regime	Spacer	Comments
Groeneveld and Yousef (1980)	$\Delta P_{sp} = K_{ob}\frac{\rho V_o^2}{2} + f_{sp}\frac{t}{De_{sp}}\frac{\rho V_{sp}^2}{2} - f_o\frac{t}{De}\frac{\rho V_o^{sp}}{2}$ f_{sp}, f_0 are the friction factors for spacer and for tube wall without spacer over the spacer length, respectively, *t* is the spacer length, V_0 is the bulk velocity without the influence of the spacer, *De* is the equivalent diameter	Single-phase	Rod bundles	First term on RHS of equation represents ΔP due to spacer, second term, skin friction ΔP of spacer and third term, skin friction ΔP of bare bundle over spacer length
Rehme and Trippe (1979)	$K_{ob} = C_v \varepsilon^2$	Single-phase	Rod bundles/ four different shapes and flow blockage ratios	The modified drag coefficient, *Cv* =6−7, for Re > 5×10^4, round leading edges, short spacers and 0.20 > ε >0.45
Leung and Hotte (1997)	$K_{ob} = 9.3797\left(\tan(\frac{\pi}{2}(\varepsilon)^2)\right)^{1.088}$	Single-phase	Central-segment flow obstacle	-
Yao et al. (1982)	$\left(\frac{\Delta p}{\Delta P_o}\right)sp = \frac{f + K_{ob}\frac{D}{L}}{f} = 1 + (\frac{D}{fL})K_{ob}$	Single-phase	Grid spacers	-

2.3 Heat transfer and CHF enhancement during flow boiling

Heat transfer during flow boiling becomes inefficient when the film boiling heat transfer is present after the occurrence of a critical heat flux (CHF). Here a vapor layer blankets the heated wall and works as an insulator by reducing heat transfer from the heated wall to the coolant ─ this region is referred to as the post dry-out region (PDO), post-CHF region or film boiling region. **Shin *et al.* (2003)** carried out an experimental work aimed to enhance the CHF (and thus suppress film boiling) inside a 2x2 rod bundle by varying the location of the grid spacers. Their results indicate that the grid spacers enhanced the CHF by 10% at 180 mm and 20% at 90 mm downstream of the grid spacers. They also noted that (i) CHF occurs preferentially just before the grid spacer and (ii) the spacer enhancement effect on

CHF decays with distance downstream of the grid spacer. Similar results have been observed by several other investigators, e.g. **Groeneveld and Yousef (1980), Doerffer *et al.* (1996)**. **Groeneveld and Yousef (1980)** concluded that the spacing devices in a bundle enhance the post-dryout heat-transfer rate due to improvement of the sub-channel mixing and the increased flow turbulence level in the downstream regions. The accompanying increase in hydraulic resistance due to rod spacing devices can be reduced by 50%, by streamlining the leading and trailing edge of the spacing device. However, streamlining decreases the post-dryout heat transfer enhancement.

Many researchers have performed experiments on heat transfer enhancement in the PDO region using flow obstacles, see Table 2.7. Investigation of the spacer effects on PDO heat transfer in rod bundles have been carried out by **Yoder (1985)** and **Stosic (1995)**. Results obtained by **Yoder (1985)** indicate similar effects of spacers as found in single phase heat transfer. He assumed that grid spacers decrease droplet sizes which increase the surface area, and then drive the flow closer to equilibrium state. **Stosic (1995)** found that spacers increased the heat-transfer coefficient by about 20 to 25% at the spacer plane, and the spacer enhancement effects was up to L/D = 20 to 30 downstream of a spacer. **Uchida *et al.* (1999)** and **Anglart *et al.* (2005)** performed experiments on post CHF heat transfer near obstacles in rod bundles, annuli, and tubes. **Zahlan (2008)**, investigated effect of different obstacles types on film boiling heat transfer over a wide range of flow conditions. His experiments showed that film boiling heat transfer coefficients along the test section are enhanced significantly by decreasing the obstacle pitch, by increasing the obstacle size and by using a blunt instead of a streamline-shaped obstacle. Table 2.8 and Table 2.9 show the prediction methods of obstacles effects on PDO heat transfer and pressure drop, respectively.

Table 2.7: Experiments investigating the obstacle effect on PDO heat transfer as reported by Yoder (1985) and additional studies.

Reference	Test section/ No.rods	Fluid	Rod dia. mm	Pitch to diameter ratio	Spacer/obstacle details	Mass flux kg m^{-2} s^{-1} (Re)
Cluss (1978)	Tube	steam/water	9.5	-	ε = 0.367	25.4
Era *et al.* (1966)	1	steam/water	15 and 17	-	ε = 0.30	22-38
Yoder *et al.* (1982)	64	steam/water	9.5	1.34	ε = 0.30	200-800
Yoder *et al.* (1983)	64	steam/water	9.5	1.34	ε = 0.30	40-260
Morris *et al.* (1982)	64	steam/water	9.5	1.34	ε = 0.30	145-1100
Lee *et al.* (1982)	161	steam/water	9.5	1.3	ε = 0.35	1-140
Gonin and Sergeev	Tube	steam/water	1.0	-	ε = 0.154 and 0.326 Pitch = 100 and 500 mm	500-1500
Sergeev *et al.* (1990)	Tube	steam/water	1.4	-	ε = 0.154 and 0.326 Pitch = 100 and 500 mm	500-1500
Kim and Korol'kov (1991)	Annulus	steam/water	-	-	ε = 0.10 3 spacers, box-shape Pitch = 500 mm	420, 847, and 1200
Peng *et al.* (2003)	Tube	HFC-134a	6.92	-	ε = 0.12, long cylinder, OD = 2.4 mm, length = 10 mm	1000, 2000, and 3000
Leung *et al.* (2005)	Tube	HFC-134a	4.1	-	ε = 0.37 Ring, cube, and hexagon-shape	2000, and 3000
Anglart *et al.* (2005)	Annulus	Water	22.1*10	-	-	500-2000
Uchida *et al.* (1999)	3*3	HFC-123	9.5	1.26	Standard, non-mixing, and grid with mixing vanes, pitch = 460 mm	560-3060
Zahlan (2008)	Tube	HFC-134a	5.46	-	ε = 0.12 and 0.24, Obstacle pitches (150and 300 mm) for blunt and round.	1395-3575

Table 2.8: Prediction methods for the spacer effect on PDO heat transfer.

Reference	Prediction method	Flow regime	Comments
Sergeev *et al*. (1990)	Complex calculation procedure	PDO Water	Tube, bundle, and annulus
Gonin and Sergeev	Complex calculation procedure	PDO Water	Tube, bundle, and annulus
Kim and Korol'kov (1991)	$\frac{Nu}{Nu_o} = 1 + K_e \varepsilon^2 e^{\left(-0.13 \frac{L}{D_{hy}}\right)}$, where $K_e = A(x - X_{thr})(1 - X)$, A is a numerical factor defined experimentally, x_{thr} is the dryout quality	PDO Water	Annulus, A needs to be derived from obstacle data.
Leung *et al.* (2005)	$Nu^* = \frac{Ni}{Nu_o} =$ $1 + (0.47 + 0.481 X_e (1 - X_e)^{0.105}) \times K_{ob} \exp(-0.13 \frac{L}{D_{hy}})$ $\frac{Nu_{dev}}{Nu_{fd}} =$ $1 + \left(\frac{Nu_{nb}}{Nu_{fd}} \frac{k_f}{k_g} - 1\right) \exp\left[-10.83 \left(\frac{q}{CHF_{ob}} - 1\right)^{0.37}\right]$ $* \psi_{tp}^{-0.18} \left(\frac{\rho_f}{\rho_g}\right)^{0.28}$	PDO HFC-134a	K_{ob} takes into account obstacle Shape and location.
Sergeev (2005)	Calculation procedure similar to Sergeev (1990)	PDO Water	Considers AFD; different flow geometries: tube, bundle, and annulus
Zahlan (2008)	$\frac{Nu}{Nu_o} = 1 + A_2 \left(\mathrm{Re}_g\right)^{B_2} K_{ob} e^{\left(-C_2 \frac{L}{D}\right)}$ where A_2 = 25, B_2 = -0.08, C2 = 0.035, K_{ob} is the single-phase pressure-loss coefficient $K_{ob} = E_1 \varepsilon \mathrm{Re}^{-E_2}$ where E_1 = 2.835, E_2 = 0.07.	PDO HFC-134a	Stream-lined obstacles

Table 2.9: Spacers (obstacles) pressure drop correlations at PDO conditions.

Reference	Prediction method	Flow regime	Spacer	Comments
Groeneveld and Yousef (1980)	$\frac{\Delta P_{TP}}{\Delta P_{LO}} = 1 + x \frac{v_{fg}}{v_{L,Sat}}$	PDO	Rod bundles	The homogeneous two-phase multiplier is recommended by the authors
Stosic (1995)	$\Delta P_{sp} = K_{ob} \frac{G^2}{2\rho_{l,Sat}} \left(1 + \frac{v_{fg}}{v_{l,Sat}}(x)\right)$ where, $K_{ob} = C_v \varepsilon^2$	PDO	Rod bundles, different types of grid spacers	The homogeneous multiplier is used: $1 + \frac{v_{fg}}{v_{l,Sat}}$
Yao et al. (1982)	$\left(\frac{\Delta p}{\Delta P_o}\right) sp = \frac{f + K_{ob} \frac{D}{L}}{f} = 1 + (\frac{D}{fL}) K_{ob}$	PDO	Grid spacers	-

2.4 Heat transfer enhancement experiments at supercritical pressures

The main objective of this literature review is to get a better understanding of the flow obstacle effect on heat transfer and pressure drop at supercritical pressures. Most experiments have been carried out in tubes rather than rod bundles.

Pioro and Duffey (2007) devoted Chapter 9 of their book to SCHT enhancement; they reviewed various investigations reported between 1968 and 2005. These and additional studies are discussed in more detail below.

2.4.1 Experimental studies of supercritical heat transfer in simple geometries

Shiralkar and Griffith (1970) observed that the swirl generated by a twisted tape inside a tube of 6.35 mm ID has a significant effect on heat transfer to upwardly flowing CO_2 in a tube having a 1.524 m heated length at a pressure of 7.58 MPa. The twisted tape was one turn of 360° in four diameters. However, the deterioration in heat transfer was not completely eliminated. It occurred to some extent at higher heat fluxes in both upflow and downflow. Figure 2.1 shows wall temperature profiles at a heat flux of 147 kW m^{-2}. As the mass flux reduced, some heat transfer deterioration occurred at a mass flux of 1139 kg m^{-2} s^{-1} and below.

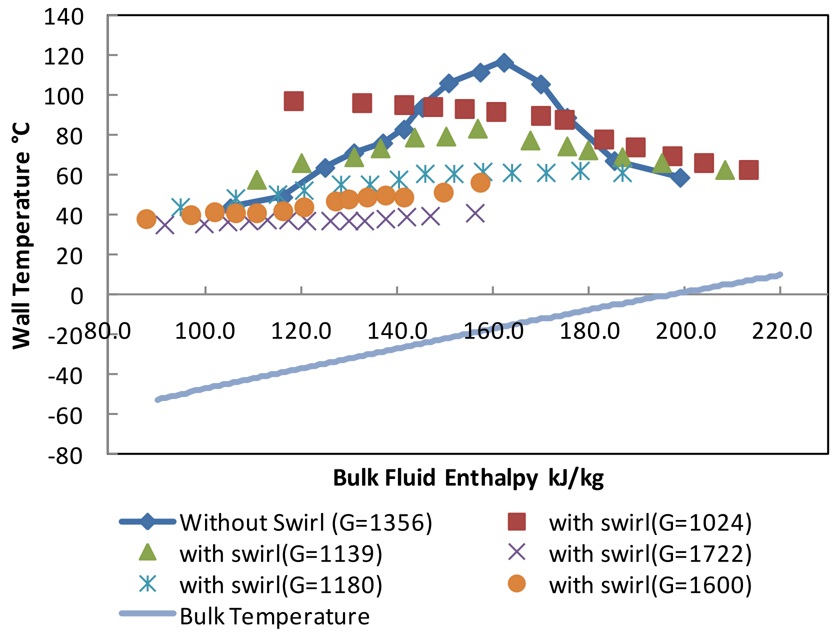

Figure 2.1: Variation in wall temperature with enthalpy at various mass fluxes for a bare tube and tube with a twisted tape: Carbon dioxide, P_{out} = 7.58 MPa, upward flow, ID = 6.35 mm, and H_{Pc} = 337.9 kJ kg^{-1} (Shiralkar and Griffith 1970).

Ackerman (1970) investigated heat transfer to water at supercritical pressures in vertical smooth and ribbed tubes over a wide range of pressure, mass flux, and heat flux, as given in Table 2.10. He observed that the heat transfer deterioration at supercritical pressures could occur due to “pseudo-film boiling” phenomenon, i.e. there is a large difference in density between the high-density bulk fluid (liquid-like) which is below the pseudo critical temperature, and the low-density fluid (gas-like) near the wall which is above the pseudo critical temperature. This is similar to film boiling at subcritical pressures. The author concluded that usage of ribs resulted in elimination of the heat transfer deterioration (HTD) at supercritical pressures as shown in Figure 2.2.

Lee and Haller (1974) observed similar results to those of Ackerman with no heat transfer deterioration at supercritical pressures for flow inside a ribbed tube. They attributed that to the higher turbulence level of the flow; hence the heavier density bulk fluid from the core can move towards the wall much faster than in smooth tubes. They were able to avoid the occurrence of HTD in the ribbed tubes at 50% - 100% higher heat fluxes than in smooth tubes.

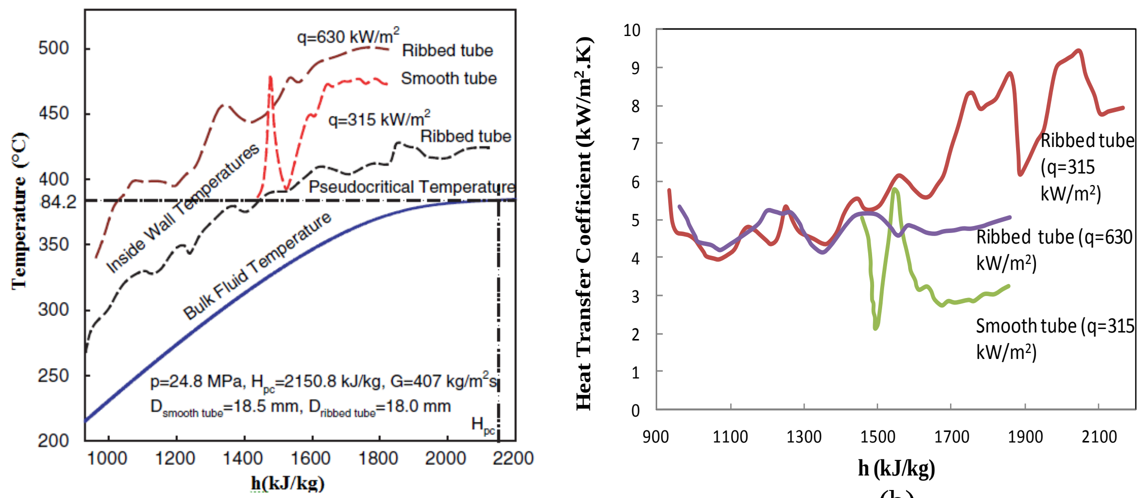

Figure 2.2: (a) Temperature variations along vertical smooth and ribbed tube cooled by supercritical water and (b) HTC variation for data given in Figure 2.2 (a) (Ackerman 1970).

Kamenetskii (1980), as reported by Pioro and Duffey (2007)**,** investigated the effect of the twisted tape on HTC in a horizontal tube at supercritical pressures. His results showed that the installation of the twisted tapes inside a bare tube reduced the flow stratification (where temperature difference between top and bottom tube surfaces was reduced compared to the bare tube); hence the heat transfer coefficient was increased as shown in Figure 2.3.

Fedorov *et al.* (1986), as reported by Pioro and Duffey (2007), found a significant heat transfer enhancement in hydrocarbons flow at supercritical pressures by installing internal circumferential ribs inside a smooth tube. The ribbed tube resulted in a more uniform wall temperature profile along the heated length and circumferentially compared to the smooth tube and the enhancement increases with increasing the heat flux.

Kalinin *et al.* (1998), as reported by Pioro and Duffey (2007)**,** conducted experiments in supercritical Kerosene flowing upward in a smooth and ribbed tube as shown in Figure 2.4. The effect of different Reynolds numbers and geometric parameters of the rib (height and pitch) have been studied as shown in Figure 2.5 to Figure 2.8. The results show that Nusselt number for a larger rib (*d/D*=0.85) is 35% - 90% higher than a smaller rib (*d/D*=0.95). As expected the pressure drop increases as *d/D* decreasing, where the friction factor ratio (ζ / ζ_{Smooth}) is three times higher than that associated with (*d/D*=0.95) as shown in Figure 2.5 and Figure 2.6. Figure 2.7 shows that Nu/Nu_{Smooth} decreases as rib pitch increases.

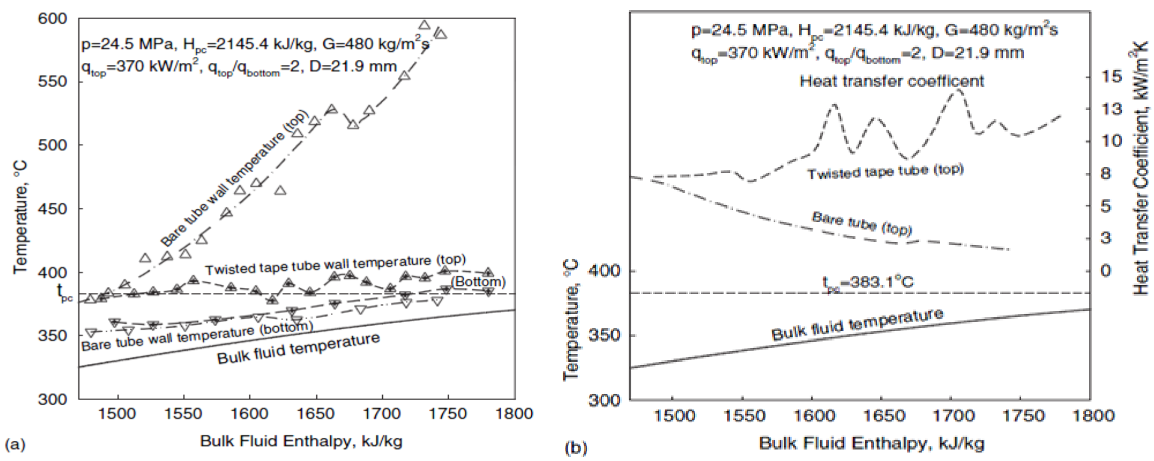

Figure 2.3: (a) Temperature variations along horizontal tubes with and without tape (non-circumferential heat flux) cooled by super-critical water (Kamenetskii 1980) and (b) HTC variation for data given in Figure 2.3 (a) calculated by Pioro and Duffy (2007).

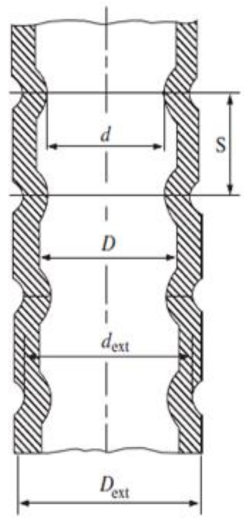

Figure 2.4: Schematic diagram of the ribbed tube where *d*, *S*, and *D* are minimum diameter, pitch, and internal smooth tube diameter, respectively (Kalinin *et al.*, 1998).

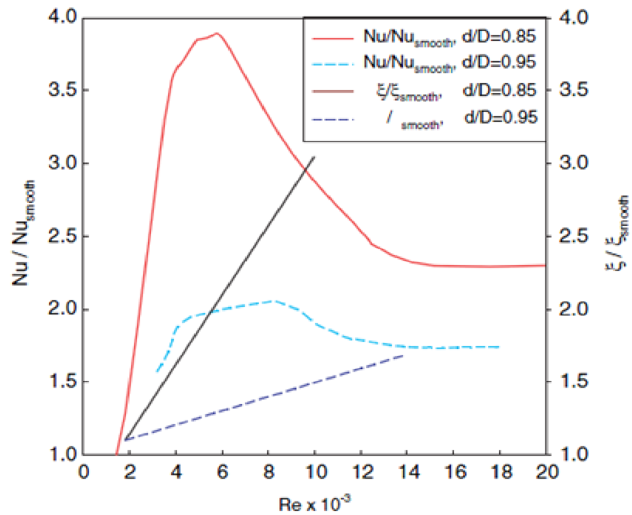

Figure 2.5: Effect of Re on the ratio of Nusselt number (Nu/Nu_{Smooth}) and the friction factor (ζ/ζ_{Smooth}) between the ribbed and smooth tubes for supercritical kerosene ("normal heat transfer") flowing in tubes: *S/D* = 1.5 (Kalinin *et al.*, 1998).

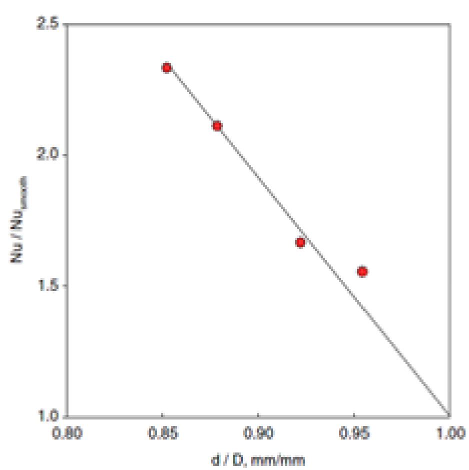

Figure 2.6: Effect of rib height on Nu/Nu_{Smooth} for supercritical kerosene flowing in tubes: Re = 10^4 and *S/D* = 1.5 (Kalinin *et al.*, 1998).

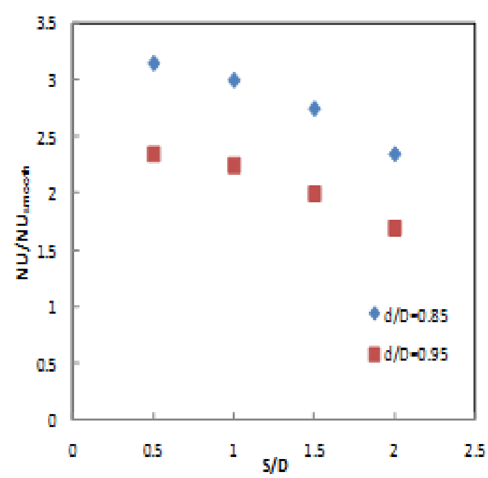

Figure 2.7: Effect of rib pitch on Nu/Nu_{Smooth} for supercritical kerosene flowing in tubes: Re = 10^4 (Kalinin *et al.*, 1998).

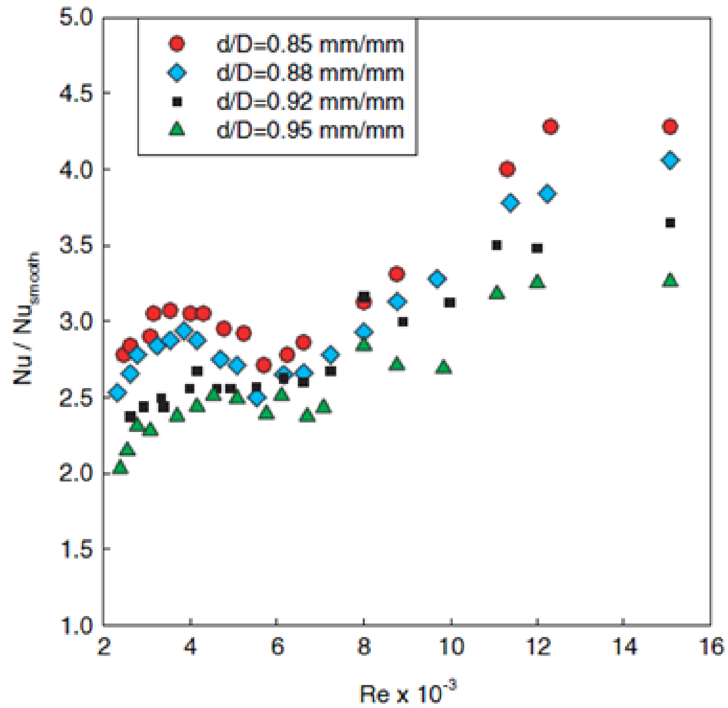

Figure 2.8: Effect of Re on Nu/Nu_{Smooth} for supercritical kerosene (deteriorated heat transfer) flowing in tube: *S/D* = 0.75 (Kalinin *et al.*, 1998).

Chen (2004), as reported by Pioro and Duffey (2007), investigated heat transfer to water flowing upwardly in a ribbed tube at supercritical pressures for a mass flux range of 400-1800 kg m^{-2} s^{-1}, a heat flux range of 200-800 kW m^{-2}, a pressure range of 23-27 MPa and a heated length of 1 m. He proposed the following correlations to calculate HTC for upflow water in a ribbed tube.

at $H_b<H_{Pc}$

$$Nu = 1.277\,\mathrm{Re}^{0.416}\left(\frac{H_w - H_b}{T_w - T_b}\,\frac{\mu_b}{k_w}\right)^{1.114}\left(\frac{v_b}{v_w}\right)^{0.458} \tag{2.45}$$

at $H_b>H_{Pc}$

$$Nu = 66.68\,\mathrm{Re}^{0.178}\left(\frac{H_w - H_b}{T_w - T_b}\,\frac{\mu_b}{k_w}\right)^{1.191}\left(\frac{v_b}{v_w}\right)^{1.706} \tag{2.46}$$

where $\dfrac{H_w - H_b}{T_w - T_b}$ represents the integrated specific heat across tube diameter ($\overline{C}p$).

Table 2.10: Parameters range for experiments investigating the flow obstacles effects on SC and near-critical heat transfer.

Reference	Heated Length (m)	Test section geometry details	Conditions			*P* MPa	*P/P$_c$*	Fluid
			Mass flux kg m^{-2} s^{-1}	Heat flux kW m^{-2}	Flow direction			
Shitsman 1967	1.5	Tube with a twisted tape, *D*=16 mm	600-690	90-370	Up	24.3-25.3	1.1-1.14	Water
Ackerman 1970	1.83	Ribbed tube (from rib valley to rib valley), Six helical ribs Pitch, *D*=21.8 and 18 mm	406.8	315.3-630.5	Up	24.8	1.13	Water
Kamenetsky Shitsman 1970	3	SS tube with a twisted tape, δ_w =0.8 mm, spiral shape with *S/D*=15; *D*=22 mm	540	190-1300	Up	24.5	1.11	Water
Lee and Haller (1974)	4.57	SS tube with ribs, *D*=38.1 mm	542- 2441	250-1570	Up	24.1	1.09	Water
Chen 2004	1	SS ribbed tube with rib specification (Height =0.81mm , Pitch= 20.5 mm, Width = 9mm); D_{avg}= 15.24 and D_{Ext}=28 mm	400	300	Up	24	1.086	Water
Shiralkar and Griffith 1968	1.524	Tube with a twisted tape, Twist is one turn of 360° in four diameters ,*D*=6.35 mm	Re 2.67×10^5 8.35×10^5	50.24-452.16	Up	7.58	1.03	CO_2
Ankudirov and Kurgarov 1981	1.84	Helical wire inside a tube, *D*= 8mm	2100-3200	Up to 1540	Up	7.7	1.04	CO_2
Bae *et al.* (2011)	2.65	1.3 mm OD Helical wire, 100 mm pitch, *D*=6.32 mm	400 to 1200	30-90	Up	7.75 and 8.12	1.05 and 1.1	CO_2
Wang *et al.* (2011,2012)	1.4	spiral spacer of 100 mm length inside an 4 and 6	350-1000	200-1000	Up	23-28	1.04-1.3	Water

		mm gap of annular channel, D_{hy}= 8 and 12 mm.						
Silin *et al.* 1993	-	Bundles, D_{rod}= 4 and 5.6mm, rod pitch=5.2 and 7mm.	350-5000	180-4500	Up	23.5-29.4	1.06-1.33	Water
Dyadyakin and Popov 1977	0.5	Tight bundle (7 rods), having D_{rod}=5.2mm and L=0.5 m; every rod has 4 helical fins with a height of 1 mm, helical pitch= 400 mm; located in a hexagonal pressure tube.	500-4000	<4700	-	24.5	1.11	Water
Mori *et al.* (2012)	2	Tube having an 4.4 mm ID	400-2000	215-440	Up and Down	5	1.1	HCF C-22
	1.95	7-rod bundle having a D_{hy}= 3.2 mm (No information about the grid spacers are available)	400-1000	230-455	Up and Down	5	1.1	HCF C-22
	1.45	3-rod bundle having a D_{hy}= 4.4 mm and 3 grid spacers (the first two spacers are separated from each other by a distance of 300 mm and the last one is 550 mm away from the second one.	400-1000	220-430	Up and Down	5	1.1	HCF C-22
Richards *et al.* (2013)	1	7-rod bundle having D_{rod} = 9.5 mm and 3 grid spacers having a pitch of 500 mm and (*P/D* =1.19).	440-1320	Power 2.5-25 (kW)	Up	4.65	1.12	Freon R-12
Hong-bo *et al.* (2013)	1.328	4-rod bundle equipped with 5 grid spacers having a pitch of 200 mm and (*P/D* =1.18, 1.3).	432-1775	425-1498	Up	23-26	1.04-1.18	Water

Hongzhi *et al.* (2009) investigated experimentally the SCHT characteristics of water flow in a test section having a heated rod (10 mm OD, 1.48 m heated length) equipped with a helical wire wrap (2.5 mm OD, 200 mm pitch) located inside a 15 mm wide square vertical channel. Flow parameters were, G = 500, 800, and 1200 kg m^{-2} s^{-1}, q = 400 kW m^{-2}, and a pressures of 23 and 25 MPa. As shown in Figure 2.9a (G = 1200 kg m^{-2} s^{-1}), the flow at 23 MPa has a more pronounced heat transfer enhancement compared to that at 25MPa. However, at a low mass flux of 500 kg m^{-2} s^{-1}, the flow at 23 MPa appears to experience an earlier onset of HTD and a more severe increase in the wall temperature than those associated with the flow at 25 MPa.

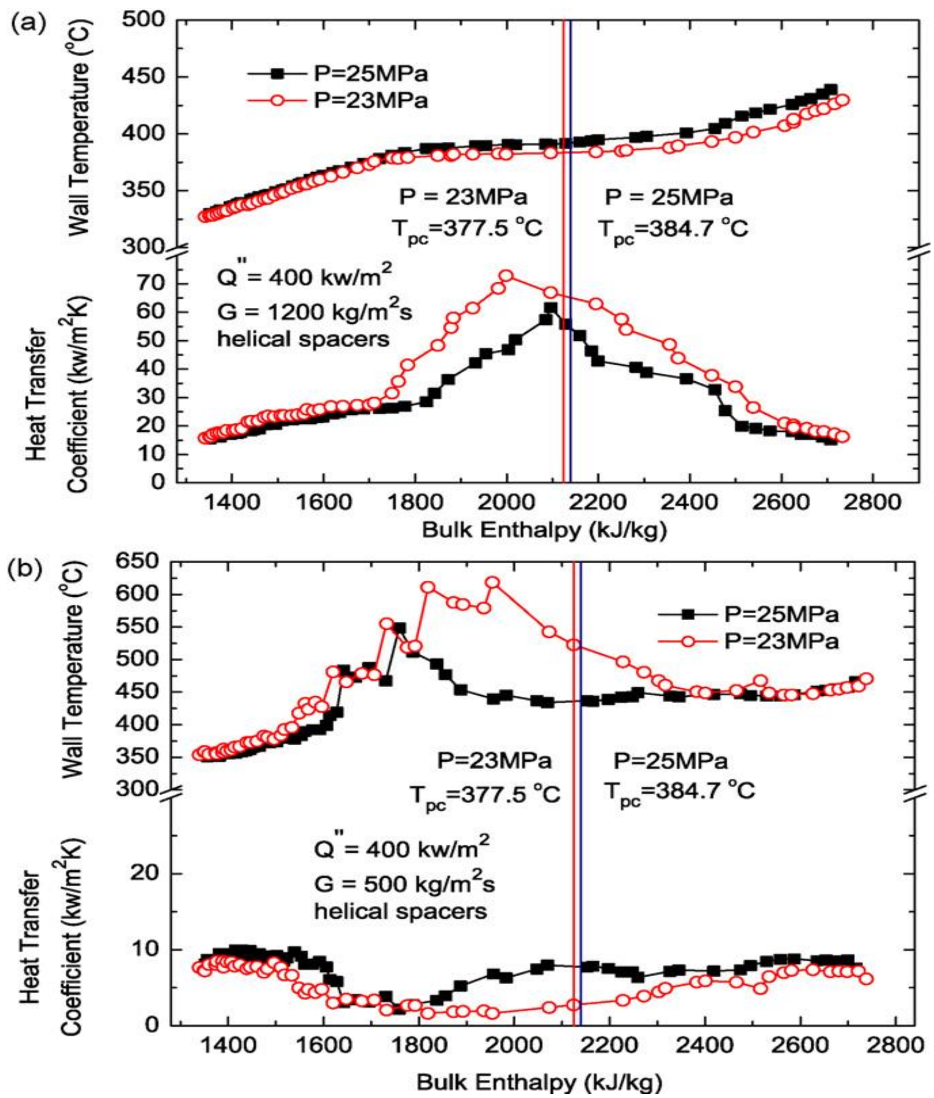

Figure 2.9: (a) Comparison of the heat transfer coefficients and wall temperatures at different pressures (high mass flux). (b) Comparison of the heat transfer coefficients and the wall temperatures at different pressures (low mass flux) **(**Hongzhi *et al.*, 2009).

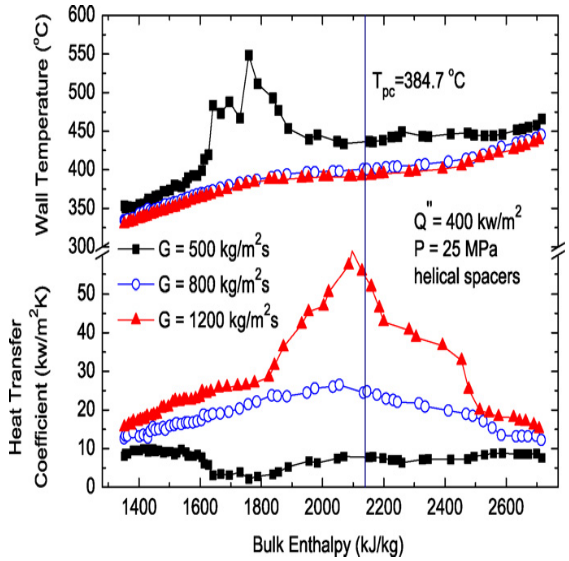

Figure 2.10: Comparison of the heat transfer coefficients and wall temperatures at different mass fluxes (Hongzhi *et al.*, 2009).

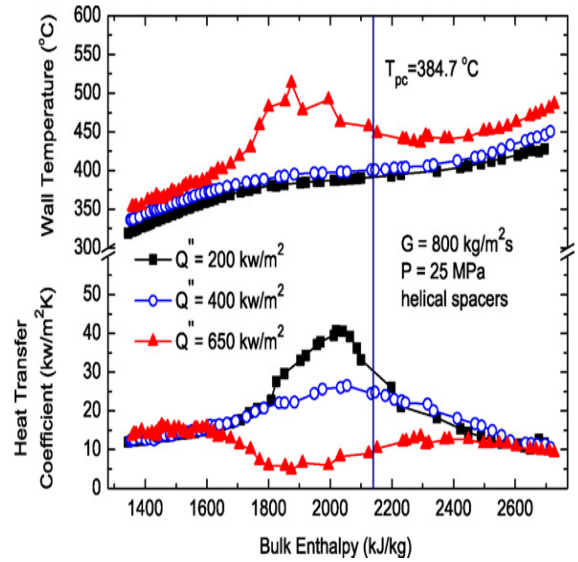

Figure 2.11: Comparison of the heat transfer coefficients and wall temperatures at different heat fluxes (Hongzhi *et al.*, 2009).

As shown from Figure 2.10, at a constant heat flux of 400 kW m^{-2}, the heat transfer coefficient increases significantly with increasing the mass flux. The maximum heat transfer coefficient enhancement occurs at 1200 kg m^{-2} s^{-1} with a 150 % increase in HTC in the pseudo-critical region (T_{bulk}~T_{pc}) compared to the HTC well away from T_{pc}. However, a significant deterioration in the heat transfer occurred at G = 500 kg m^{-2} s^{-1}, where the heat transfer coefficients are less than 5 kW m^{-2} K^{-1} when $T_w>T_{pc}>T_b$.

Figure 2.11 shows that the HTC depends strongly on heat flux in the vicinity of pseudo-critical region (when $T_w>T_{pc}>T_b$), while the heat transfer is almost independent of heat flux when $T_w<T_{pc}$ or when $T_{pc}<T_b$, (i.e. at conditions away from the pseudo-critical region). This figure suggests that the helical wire wrap is not effective in suppressing HTD.

Hongzhi *et al.* (2009) concluded that the helical wire does not provide a significant enhancement of the heat transfer under normal heat transfer conditions at supercritical pressures where by excluding the deterioration conditions (low Nusselt numbers) the two flow geometries with and without helical wires statistically have the same heat transfer, as shown in Figure 2.12.

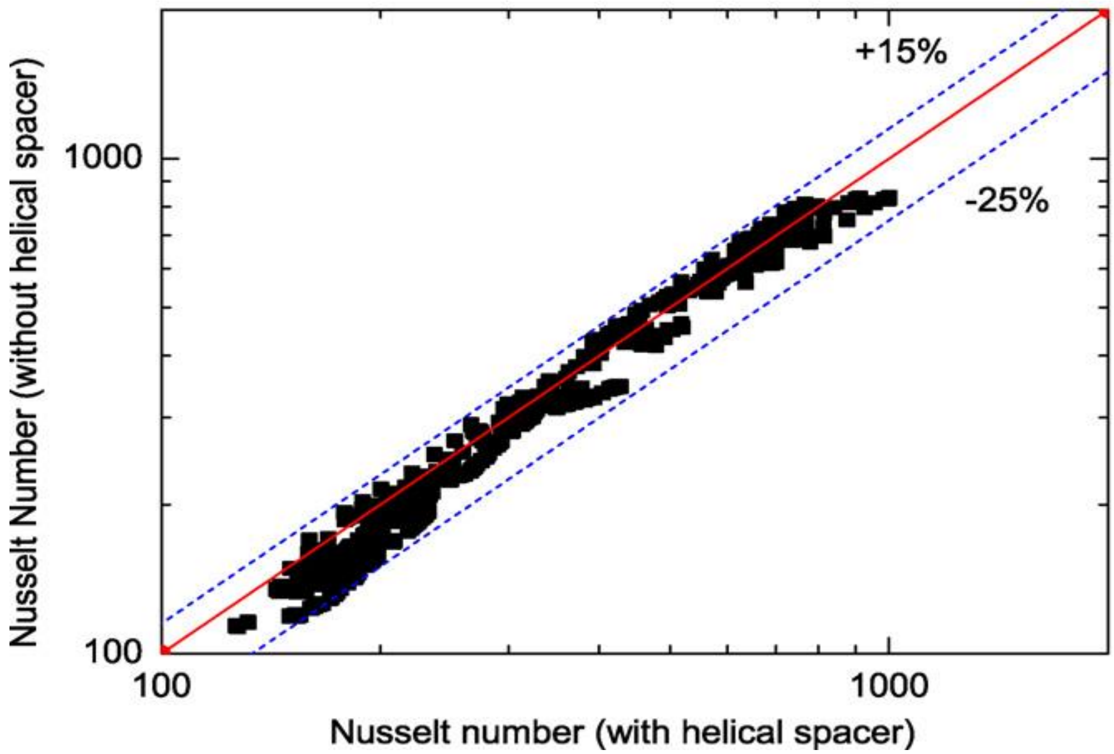

Figure 2.12: Comparison of the experimental Nusselt numbers of the square annular flow geometry with and without helical wire-wrapped spacer where HTD occurs only in the pseudo-critical region (Hongzhi *et al.,* 2009).

Bae et al. (2011) investigated the effect of a helical wire obstacle (1.3 mm OD, 100 mm pitch) on heat transfer to CO_2 flowing upward in a 6.32 mm ID tube having 2.65 m heated length. Experiments were carried out at various flow conditions (T_{in}: 5 - 37 °C, G: 400 - 1200 kg m^{-2} s^{-1}, corresponding to Re: 1.8*10^4 - 7.5*10^4, q: 30 - 90 kW m^{-2}, and P: 7.75 and 8.12 MPa, corresponding to P/P_c: 1.05 and 1.1). They observed a 100% heat transfer enhancement compared to the plain tube data predicted by Bae and Kim's correlation (2009). They used predicted data instead of measured data due to difficulties of matching the experimental conditions between the wired and plain tube. The maximum heat transfer enhancement occurred in a region where the bulk temperature was near the pseudo-critical temperature; the enhancement effect of the wire on HT decayed as the bulk temperature exceeded the pseudo-critical temperature. However, a local temperature drop at the contact point indicated a conduction heat transfer through the wire from the heated wall (fin effect). Figure 2.13 shows that for h > 400 kJ kg^{-1}, both the wall and the bulk temperatures were much higher than the pseudo-critical temperature, and the property variations across the channel no longer showed drastic changes. Consequently, the heat transfer can be predicted by the simple Dittus–Boelter correlation equation. Also, the Dittus–Boelter correlation can be applied in the region of h < 250 kJ kg^{-1} where both the wall and the bulk temperatures were well below the pseudo-critical temperature. The maximum heat transfer coefficient was 3.64 times the heat transfer coefficient of a plain tube, at h =300 kJ kg^{-1}, which is below the pseudo-critical point (h_{pc} = 340 kJ kg^{-1}).

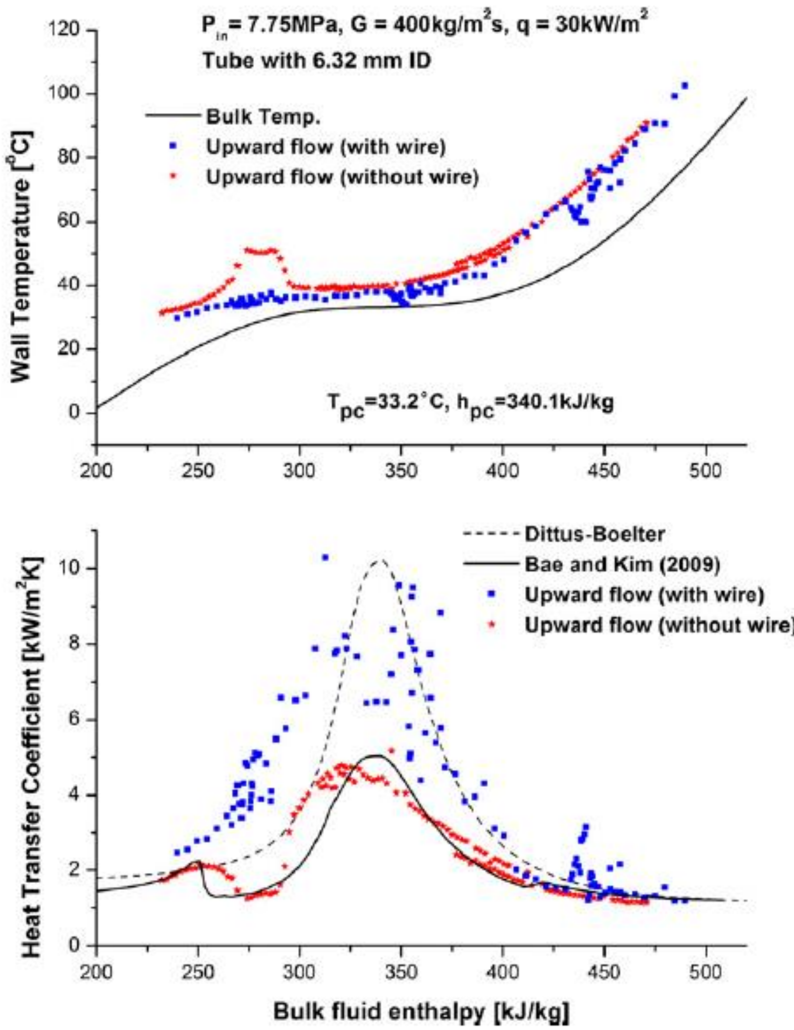

Figure 2.13: Comparison of wall temperature and heat transfer coefficient for a bare tube and a tube equipped with a helical wire; P = 7.75 MPa, G = 400 kg m^{-2} s^{-1}, q = 30 kW m^{-2} (Bae *et al.*, 2011).

Figure 2.14 shows a significant the heat transfer coefficient decrease with an increase in heat flux at a given pressure and mass flux. However, in the region where the enthalpy is higher than 450 kJ kg^{-1}, heat transfer coefficient was not sensitive to heat flux variation.

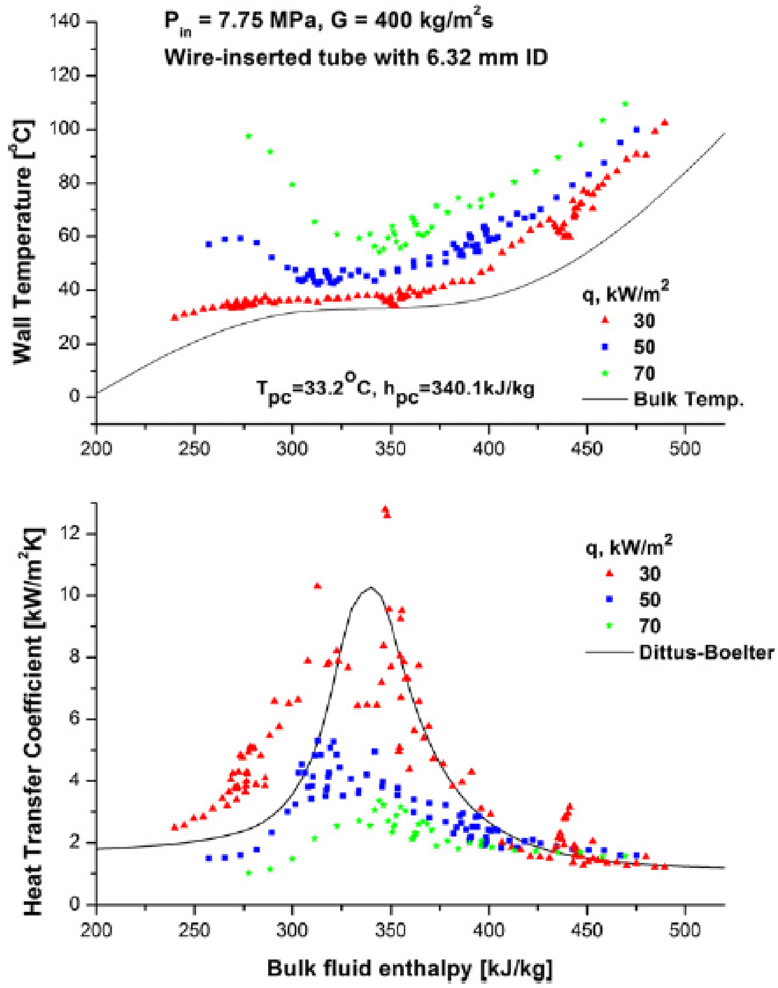

Figure 2.14: Effect of heat flux on SCHT in a tube with a helical wire insert (Bae *et al.*, 2011).

Figure 2.15 shows a large increase in HTC as the mass flux increases (at a given pressure and heat flux), which cannot be explained by the increased Re. However, in the region where the enthalpy is above 450 kJ kg^{-1}, heat transfer coefficient appears not sensitive to mass flux variations.

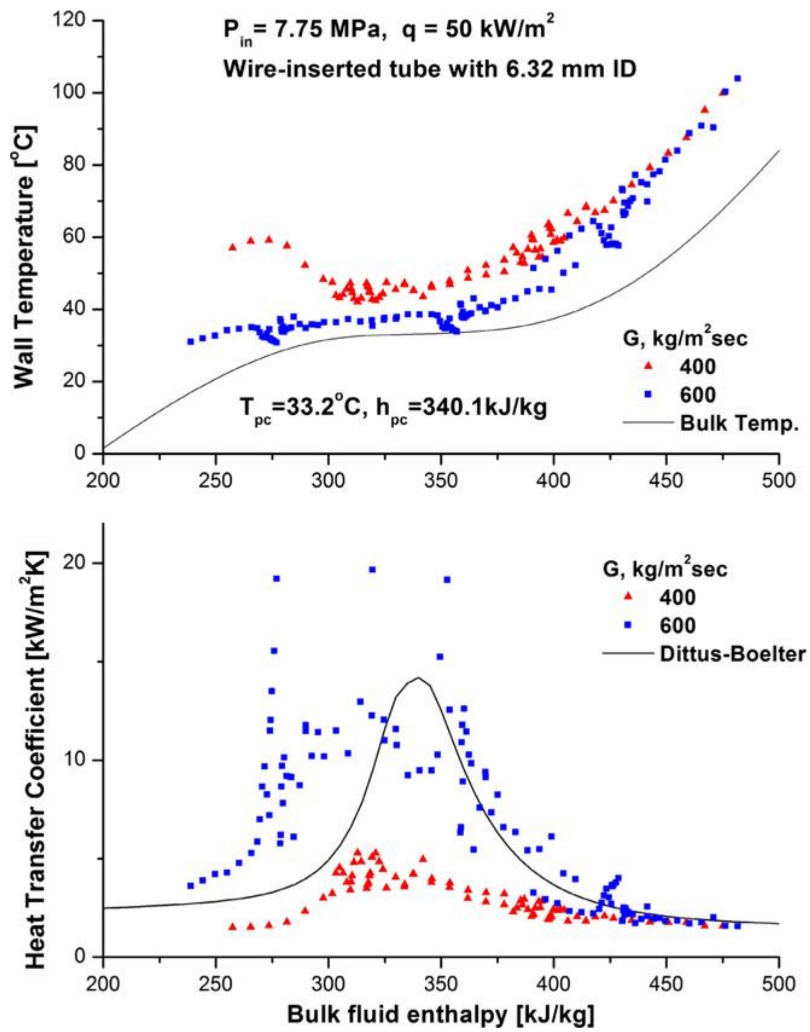

Figure 2.15: Effect of mass flux on SCHT in a tube with a helical wire insert, solid line was evaluated at G = 600 kg m^{-2} s^{-1} (Bae *et al.*, 2011).

Wang *et al.* (2011, 2012), investigated experimentally and numerically the heat transfer characteristics of supercritical water flowing in an annular channel. A spiral spacer having 3 mm OD and 100 mm length was installed inside an annular channel having a 6 and 4 mm gap; experiments were performed at various flow conditions (G: 350 - 1000 kg m^{-2} s^{-1}; q: 200-1000 kW m^{-2}; and P: 23-28 MPa. They observed that the axial distance, over which the spacer enhancement effect is effective, depends strongly on flow conditions. In addition, the spiral spacer had a positive effect on suppressing heat transfer deterioration which occurred at high q/G ratios. A comparison between the two annular channels was carried out over normal and deterioration heat transfer conditions. Figure 2.16 shows that, for normal conditions (q/G = 0.2 kJ kg^{-1}), the 6 mm gap annular channel had a higher HTC than the 4 mm gap annular channel while opposite trends are shown by the Dittus Boelter correlation, where HTC ~ $D^{-0.2}$ and which can be used to predict HTC at supercritical pressures over a normal conditions (q and G), while for the DTH conditions (q/G = 1.5 kJ kg^{-1}), the 6 mm and 4 mm gap results have almost the same HTCs. That means effect of the gap size strongly depends on flow conditions where the Dittus-Boelter correlation is no longer valid for deterioration conditions at supercritical pressures.

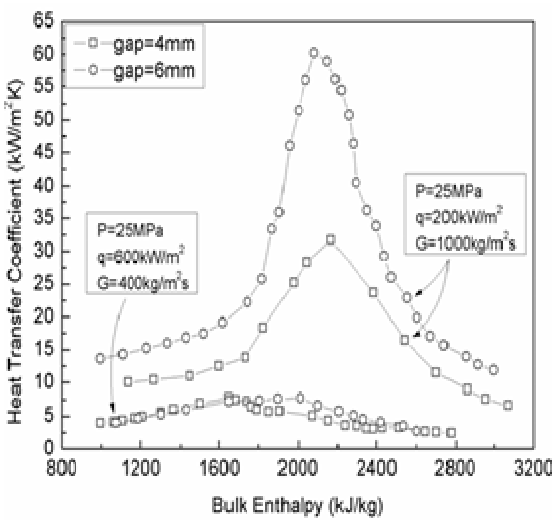

Figure 2.16: Effect of the gap size on the heat transfer coefficient (Wang *et al.*, 2011).

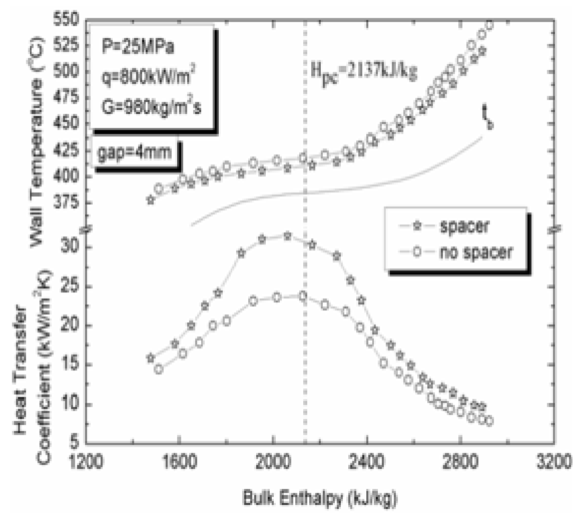

Figure 2.17: Comparison of the heat transfer characteristics with and without spacers for a 4 mm gap annular channel (Wang *et al.*, 2011).

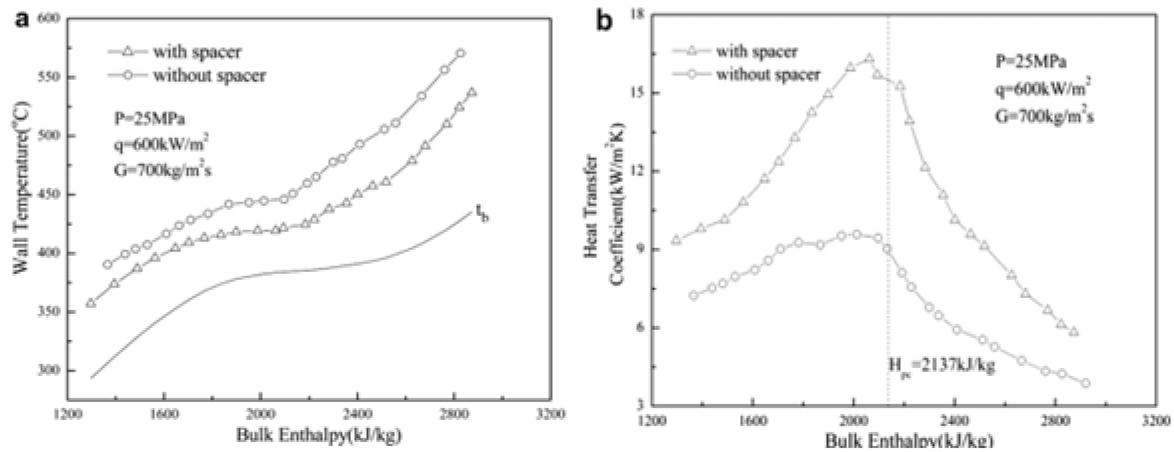

Figure 2.18: Comparison of the heat transfer characteristics with and without spacers for a 6 mm gap annular channel (a) wall temperature; (b) heat transfer coefficient (Wang *et al.*, 2012).

Wang *et al.* (2011, 2012) observed that the HTCs for the 4 mm gap bare annular channel were higher than those of the 6 mm gap bare annular channel at q/G = 0.86 and 0.82 kJ kg^{-1} for the 6 mm and 4 mm gap annular channels, respectively. This agrees with the reverse proportional relation between HTC and D as HTC ~ $D^{-0.2}$. However, the heat transfer coefficients for the spacer-equipped geometry are 25% - 80% higher than those of the geometry without spacer for the 6 mm gap annular channel with q/G = 0.86 kJ kg^{-1} as shown in Figure 2.18 (b) and 7% - 33% for the 4 mm gap annular channel q/G = 0.82 kJ kg^{-1} as shown in Figure 2.17. The following plausible explanation is followed. Although the blockage ratio is higher for the 4 mm gap which would give a higher heat transfer enhancement, but since the measuring locations are the same for both annular channels, L/D for the 6 mm gap is lower than that for the 4 mm gap by 50% which compensates for the difference in blockage ratio. Taking into consideration the two factors, blockage ratio and L/D, can result in a higher heat transfer enhancement for the 6 mm gap. As known from the knowledge of the heat transfer at subcritical pressures, heat transfer enhancement decays exponentially with L/D downstream from the obstacle, but increases with ε^2, see Table 2.5. At temperatures away from the pseudo-critical temperature, the enhancement is the lowest, which the authors attributed to the relatively minor variation in the thermo-physical properties of supercritical water at these conditions. However, at a bulk temperature close to the pseudo-critical temperature, the heat transfer enhancement is most effective; the HTC of the test section with a spacer has a maximum heat transfer coefficient of about 16 kW m^{-2} K^{-1}, which is 80% higher than those of the bare test section for the 6 mm gap annular channel.

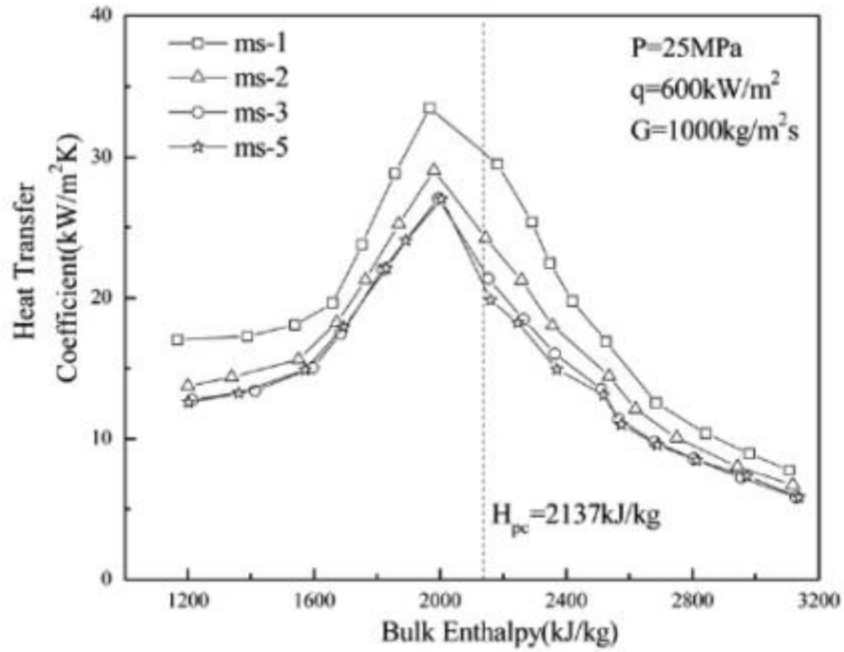

Figure 2.19: Effect of the spacer on the heat transfer coefficients at q/G = 0.6 kJ kg^{-1} for a 6 mm annular gap (Wang *et al.,* 2012).

Figure 2.19 shows heat transfer coefficients at different measuring positions (ms-1, ms-2, ms-3 and ms-5), corresponding respectively to L/D of 42, 58, 83, and 100, along the heated channel for the 6 mm gap. Measuring positions were at the same axial distances for the 4 mm gap annular channel as well. As shown in Figure 2.17, HTCs corresponding to ms-3 and ms-5 are nearly identical at mass flux of 1000 kg m^{-2} s^{-1} that means the effect of spacer on HT vanished when $L/D_{hy} \geq 58$. **Wang *et al.* (2012)** mentioned that this observation is consistent with the study of **Yao *et al.* (1982)** who found that the enhancement of heat transfer is relatively short-lived and decays with the increasing distance downstream of a spacer.

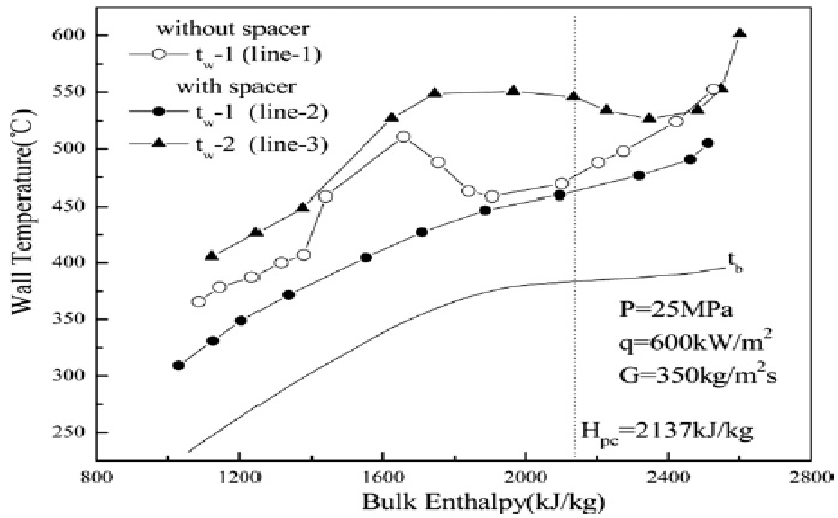

Figure 2.20: Comparison of wall temperature at deteriorated heat transfer condition for a 6 mm annular gap at different measuring location (Wang *et al.*, 2012).

At a constant pressure, heat and mass flux, the preheat power was increased to raise up the bulk enthalpy. In Figure 2.20, t_w-1 and t_w-2 represent the wall temperature at the axial locations along the heated test section corresponding respectively to *L/D* of 42 and 58. As shown from Figure 2.20, the spiral spacer suppressed HTD at high ratios of heat flux to mass flux (q/G = 1.71 kJ kg^{-1}) at a certain axial location t_w-1. However, the spacer effect on suppressing HTD was locally. So, at a downstream location of the spacer, HTD was observed as presented by (line-3).

Wang *et al.* (2012) also tested three turbulence models and compared their results with data of Yamagata *et al.* (1972). These three models are (i) the standard k-ε turbulence model, (ii) the RNG k-ε turbulence model and (iii) the realizable k-ε turbulence model. Figure 2.21 shows that the RNG k-ε turbulence model gives more reasonable predictions than the other tested models compared to the experimental data of Yamagata *et al.* (1972); this agrees very well with the findings of Kim's results.

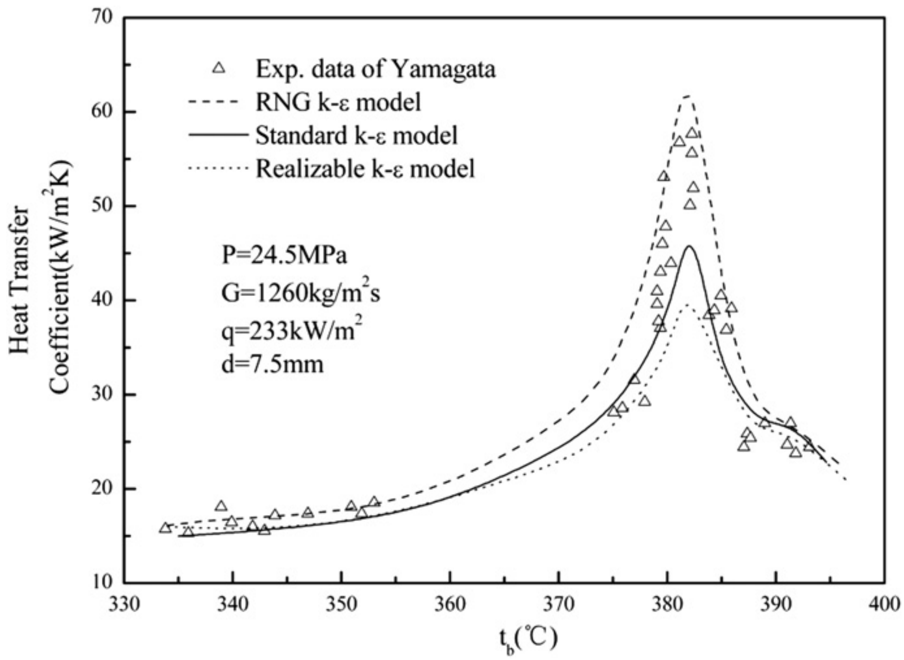

Figure 2.21: Comparison of the experimental and calculated heat transfer coefficient in a vertical upward circular tube. (Wang *et al.*, 2012).

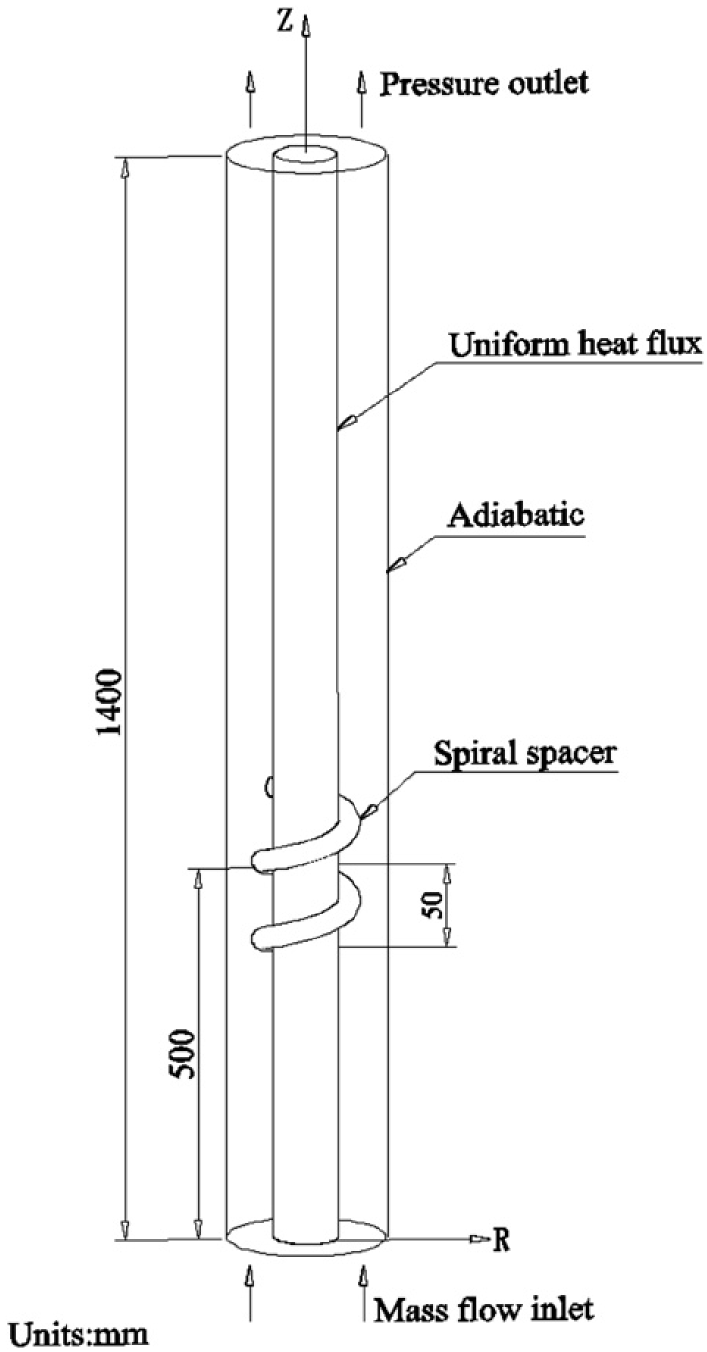

Figure 2.22: Geometry and boundary conditions of the annular test section used in the numerical study (Wang *et al.*, 2012).

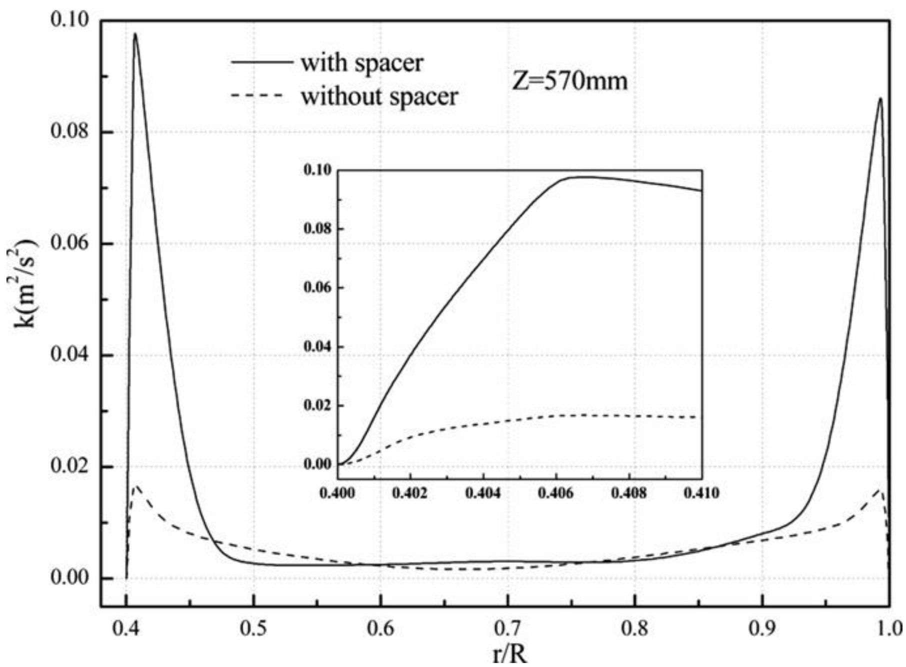

Figure 2.23: Radial distribution of turbulent kinetic energy (P = 25 MPa,G = 600 kg m^{-2} s^{-1}, q = 200 kW m^{-2}), (Wang *et al.*, 2012).

Based on the numerical results, **Wang *et al.* (2012)** suggested a mechanism that explains the effect of spacer on the heat transfer enhancement. The schematic diagram in Figure 2.22 represents the solved geometry by the CFD code FLUENT. The mechanism assumes that the fluid is subject to rotational forces due to the flow-swirling effect of the spacer. Therefore, the turbulence intensity near the spacer is expected to be higher than that without spacer. Figure 2.23 illustrates this mechanism numerically: at z = 570 mm which is 20 mm downstream of the spacer: it can be seen from the magnified picture inside Figure 2.23, that the near wall turbulent kinetic energy at this location with spacer is almost 5 times higher than that without spacer, which is probably the main reason of the heat transfer enhancement.

Zhao *et al.* (2013) have investigated the heat transfer characteristics of water flowing upward and downward through a 7.6 mm ID tube at supercritical pressures. Flow conditions were as follows: P = 23, 25 and 26 MPa, G = 450-1500 kg m^{-2} s^{-1}, q = 190-1400 kW m^{-2}, and T_{in} = 250-350 °C. His results showed that upward flows achieved higher heat transfer coefficients than downward flows at low heat fluxes. The authors observed that HTD is less pronounced in downward flow than upward flow where the buoyancy forces reduce bulk turbulence and hence heat transfer.

2.4.2 Experimental studies of supercritical heat transfer in rod bundles

Dyadyakin and Popov (1977), as reported by Pioro and Duffey (2007), carried out experiments using water at supercritical pressures in a tight 7-rod bundle; the flow conditions were as given in Table 2.10. The following correlations of Nusselt number and the coefficient of local resistance were formulated:

$$Nu_x = 0.021 \mathrm{Re}_x^{0.8}\, \overline{\mathrm{Pr}}_x^{0.7} \left(\frac{\rho_w}{\rho_b}\right)_x^{0.45} \left(\frac{\mu_b}{\mu_{in}}\right)_x^{0.2} \left(\frac{\rho_b}{\rho_{in}}\right)_x^{0.1} \left(1 + 2.5\frac{D_{hy}}{x}\right) \tag{2.47}$$

where x is the axial distance in meters.

This correlation fits the experimental data within $\pm 20\%$ except a few points within $\pm 30\%$

$$\xi_{frx} = \left(\frac{0.55}{\log_{10}\dfrac{\mathrm{Re}_x}{8}}\right)^2 \left(\frac{\rho_w}{\rho_b}\right)_x^{0.2} \left(\frac{\mu_b}{\mu_{in}}\right)_x^{0.2} \left(\frac{\rho_b}{\rho_{in}}\right)_x^{0.1} \tag{2.48}$$

where 94% of data points deviate from this correlation within $\pm 20\%$.

Bastron *et al.* (2005), as reported by Pioro and Duffey (2007), investigated different approaches to enhance heat transfer in a HPLWR (the HPLWR is the European version of the SCWR). Their results indicated that using of artificial surface roughness or staircase type grid spacer were efficient approaches to enhance the HTC by 100% compared to the HTC when these devices are not used.

Mori *et al.* (2012) investigated heat transfer characteristics of HCFC-22 flowing vertically upward and downward in a tube having a 4.4 mm ID and in sub-channels of a 3-rod bundle and a 7-rod bundle, having a sub-channel hydraulic diameter of 4.4 mm and 3.2 mm, respectively. The tube and rods in the three and seven-rod bundles have heated lengths of 2000 mm, 1450 mm and 1950 mm, respectively. In order to maintain the design of the pitch to diameter ratio in the bundle, grid spacers were used. The test conditions were G: 400 - 2000 kg m^{-2} s^{-1} for the tube and 400 - 1000 kg m^{-2} s^{-1} for both bundles; P = 5 MPa or P/P_c = 1.1; q : 215 - 440 kW m^{-2}, 220 - 430 kW m^{-2} and 230 - 455 kW m^{-2} in the tube, 3-rod, and 7-rod bundles, respectively. The 3-rod bundle results were expressed with a distance L from the downstream of the grid spacer, while the 7-rod bundle lacks information about the distance L. It is obvious from Figure 2.24 and Figure 2.25, the induced heat transfer characteristics for upflow are similar in the tube and the 3-rod bundle, where the heat transfer enhancement in the bundle is small at a low heat flux. However, at a high heat flux, the heat transfer characteristics are different due to deterioration that happens in the tube but disappears in the bundle near the grid spacer. With down-flow, no heat transfer deterioration was observed in either the tube or the bundle as shown in Figure 2.26. Figure 2.27 shows that the trends of the heat transfer for the 7-rod bundle up and down-flows are similar to those of the 3-rod bundle.

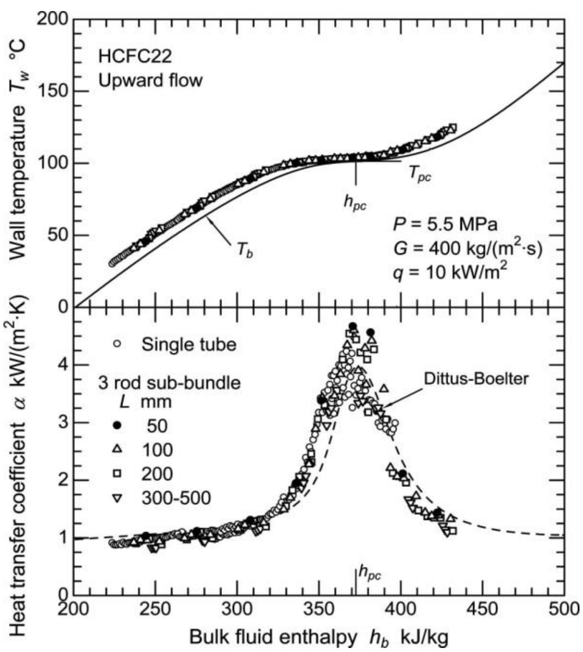

Figure 2.24: Heat transfer characteristics at a low heat flux for the tube and the 3-rod bundle, (Mori *et al.*, 2012).

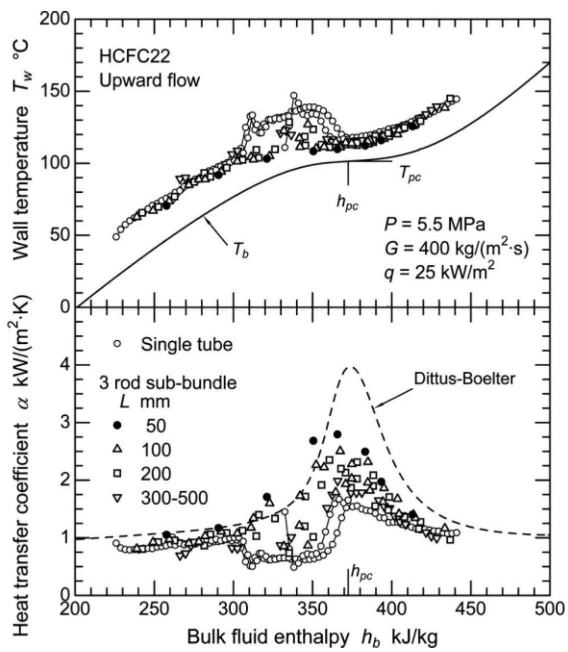

Figure 2.25: Heat transfer characteristics at a high heat flux for the tube and the 3-rod bundle, (Mori *et al.*, 2012).

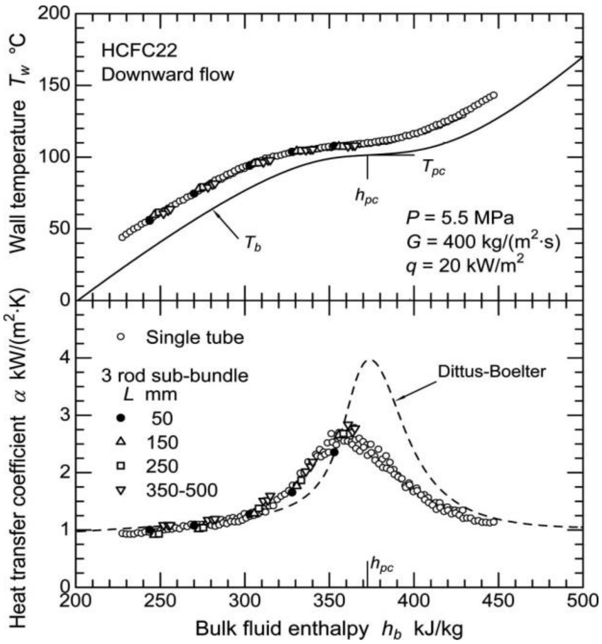

Figure 2.26: Heat transfer characteristics at a high heat flux for the tube and the 3-rod bundle down-flow, (Mori *et al.*, 2012).

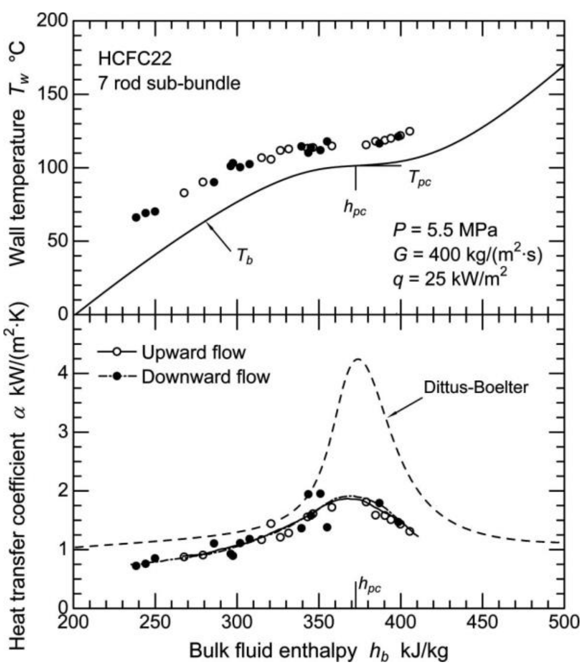

Figure 2.27: Heat transfer characteristics at a low mass velocity and a high heat flux for the 7-rod bundle up and down flows, (Mori *et al.*, 2012).

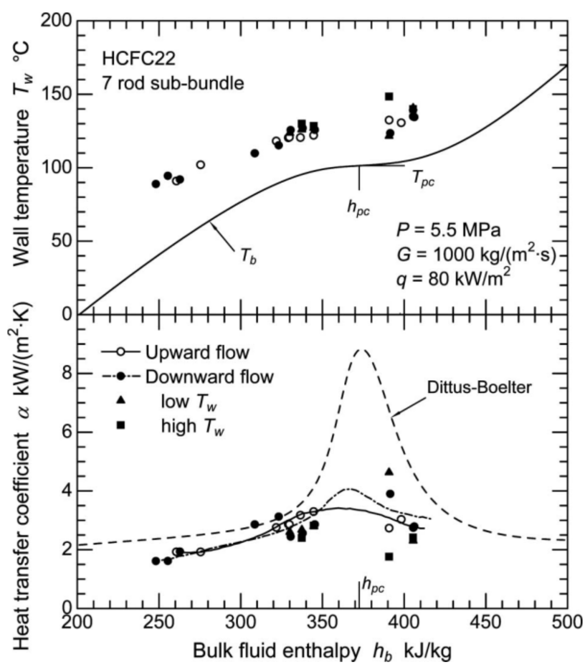

Figure 2.28: Heat transfer characteristics at a high mass velocity and a high heat flux for the 7-rod bundle up and down flows, (Mori *et al.*, 2012).

Mori *et al.* (2012), discussed the grid spacer effect on the heat transfer characteristics using the normalized heat transfer (H/H_o) for the up-flow; the results indicated that the heat transfer coefficients were enhanced just downstream the spacer and the enhancement decays gradually over a downstream distance of 60 to 70 D_h as shown in Figure 2.29. However, for down-flow, no significant spacer effect on the normalized heat transfer coefficients was observed. In fact, the normalized heat transfer coefficients downstream of the grid to the axial location of 60 D_h are slightly lower than those of locations over 60 D_h in up-flow. This could be attributed to the presence of the scatter data. Therefore, the heat transfer appears to become worse to some degrees unlike the case of up-flow. As a result of this investigation, **Mori *et al.* (2012)** developed a correlation representing the effect of the grid spacer on the heat transfer coefficient for up-flow within a limited range of heat flux for a given mass flux; this correlation is independent of mass flux as mentioned by the authors, as shown in Figure 2.30.

$$\frac{H}{H_o} = 1 + 5.55\varepsilon^2 e^{-0.05 L/D_h} \tag{2.49}$$

where:

H_o is the heat transfer coefficient unaffected by the spacer

H is the heat transfer coefficient affected by the spacer

ε is the blockage ratio

L/D_h is a distance downstream from the spacer

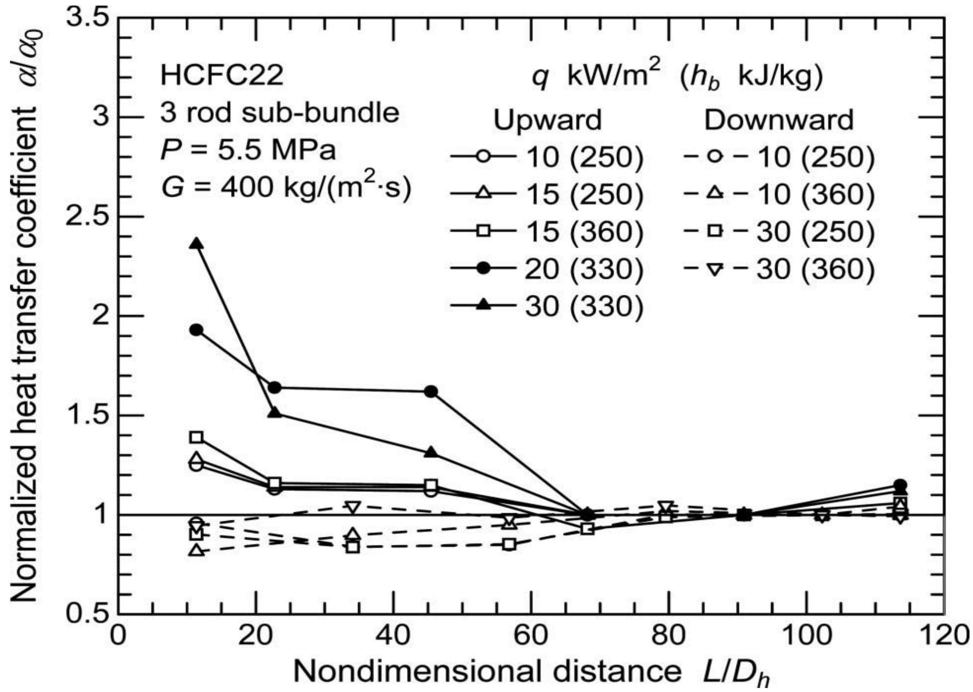

Figure 2.29: Effect of grid spacer on heat transfer at G = 400 kg m^{-2} s^{-1}, (Mori *et al.*, 2012).

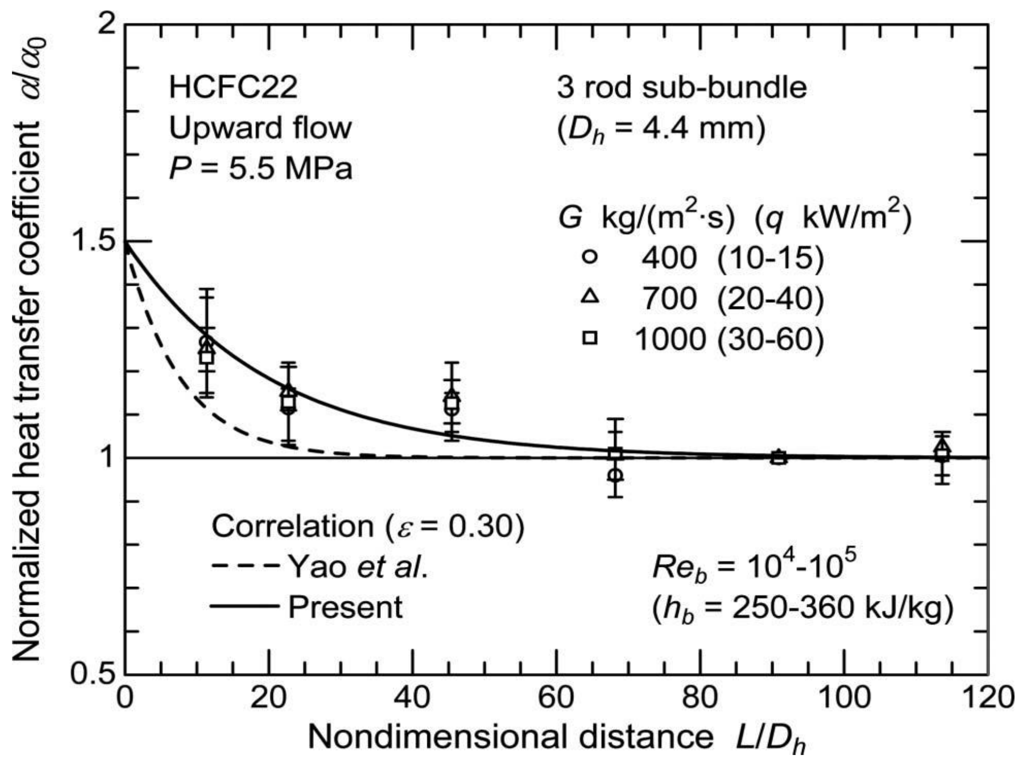

Figure 2.30: Effect of grid spacer on heat transfer with mass velocity as a parameter for the 3-rod sub-bundle upward flow, (Mori *et al.*, 2012).

Richards *et al.* (2013) have investigated experimentally the heat transfer characteristics of Freon (R-12) at a pressure of 4.65 MPa flowing upward through a 7-rod bundle having 1 m heated length and 9.5 mm rod OD. In order to keep rods apart from each other, 3 grid spacers have been installed along the heated length spaced by 500 mm and (*P/D* =1.19). Flow conditions have been sorted out into three groups according to the bulk temperature along the heated section as follows (I) below the pseudo critical point, (II) crossing the pseudo critical point and (III) above the pseudo critical point. At a pressure of 4.65 MPa, the pseudo critical temperature is 118.7 °C. Another classification has been used according to the mass flux; (I) low mass flux: 440–520 kg m^{-2} s^{-1}, (II) moderate mass flux: 990 – 1030 kg m^{-2} s^{-1} and (III) high mass flux: 1190–1320 kg m^{-2} s^{-1}. The results showed that although the 7-rod bundle is equipped with grid spacers, HTD was encountered in all tests; some cases encountered HTD once, while others encountered HTD twice. The effect of grid spacer was significant at the low mass flux 515 kg m^{-2} s^{-1} but not at the moderate or high mass flux. In addition, comparisons were made between the experimental data and predictions from 1-D dimensional empirical correlations based on a tube or annuli data. The results showed that predicted heat transfer coefficients deviate from the experimental ones by ±25% and ±50% when the bulk temperature is below and higher than the pseudo critical temperature, respectively.

Hong-bo et al. (2013) investigated SCHT of water flowing vertically upward through a 2 × 2 rod bundle. The test section contains four heated rods, having a heated length of 1328 mm. The flow conditions were: pressure: 23–26 MPa, mass-flux: 432–1775 kg m^{-2} s^{-1} and heat-flux: 425–1498 kW m^{-2}. Two different pitch to diameter ratios were tested (*P/D* = 1.18 and 1.3). The bundle was equipped with 5 grid spacers spaced by 200 mm. Results showed that the geometry of *P/D* = 1.3 experienced higher wall temperatures than the geometry of *P/D* = 1.18. The maximum wall temperature occurred at different corners with respect to the rod bundle geometry. Circumferential wall temperature found to be non-uniform but this non-uniformity decreased as the mass flux increased.

Wang *et al.* (2014) investigated SCHT of water flowing vertically upward through a 2 × 2 rod bundle. The test section contains four heated rods, having an 8 mm OD and heated length of 600 mm, installed inside a square channel with rounded corners. The flow conditions were: pressure: 23–28 MPa, mass-flux: 350–1000 kg m^{-2} s^{-1} and heat-flux:

200 – 1000 kW m^{-2}. The results revealed that (i) the maximum temperature occurred at the corner, (ii) effect of inlet temperature is minor, especially, at the corners where pseudo critical temperature axial location doesn't vary much, (iii) the circumferential temperature gradient increases as mass flux decreases and heat flux increases and (iv) heat transfer coefficient is sensitive to mass flux and heat flux variation but less sensitive to pressure variation.

2.5 Numerical studies

This section is dedicated for numerical studies of supercritical heat transfer in simple geometries and rod bundles.

2.5.1 Numerical studies of supercritical heat transfers in simple geometries

Chandra *et al.* (2009) investigated numerically the spacer effects on SCHT during up-flow of CO_2 for the following cases: (i) an annulus having 8 mm ID, 10 mm OD, and 1 m length, equipped with a square ring (Height/Diameter = 0.5) at distances of 50 mm and 200 mm from the inlet, (ii) the same annulus, equipped with a helical wire having a 1 mm OD and a pitch of 200 mm, and (iii) a tube having a 6.32 mm ID and 1050 mm length, equipped with a helical wire (1.3 mm OD, and 105 mm pitch). The flow conditions for the annulus were G = 400 kg m^{-2} s^{-1} and q = 120 kW m^{-2}, while q = 30 and 70 kW m^{-2} have been applied to the tube case with G = 400 kg m^{-2} s^{-1}. The results showed that a significant effect of the square ring on SCHT occurred over a short distance downstream of the ring, as shown in Figure 2.31 and Figure 2.32. It can be concluded that the ring location affects the heat transfer enhancement region: when the ring is located at 200 mm distance from the inlet, the heat transfer was enhanced up to L/D_{hy} =50 downstream from the ring, while in the case of 50 mm distance from the inlet it was up to L/D_{hy} =25 downstream the ring.

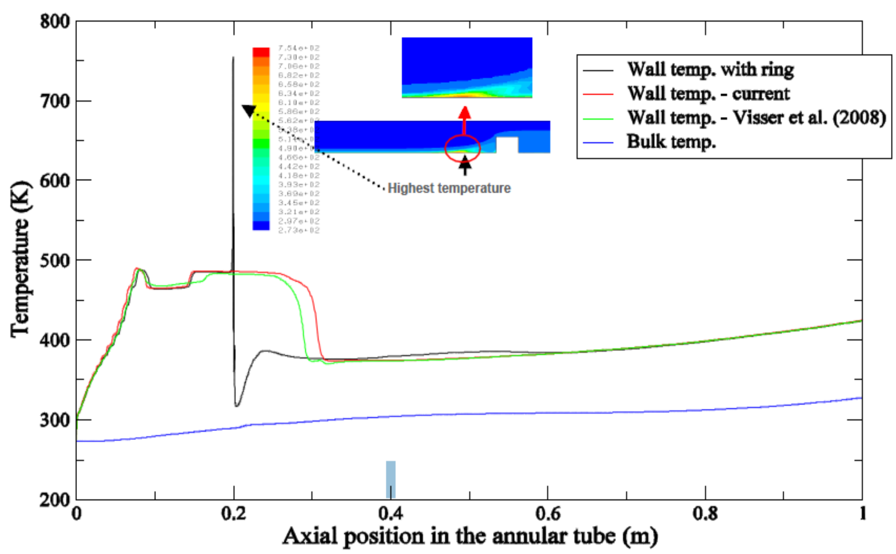

Figure 2.31: Computed axial heated inner wall and bulk fluid temperature for annulus without and with square ring placed at 200 mm, Chandra *et al.* (2009).

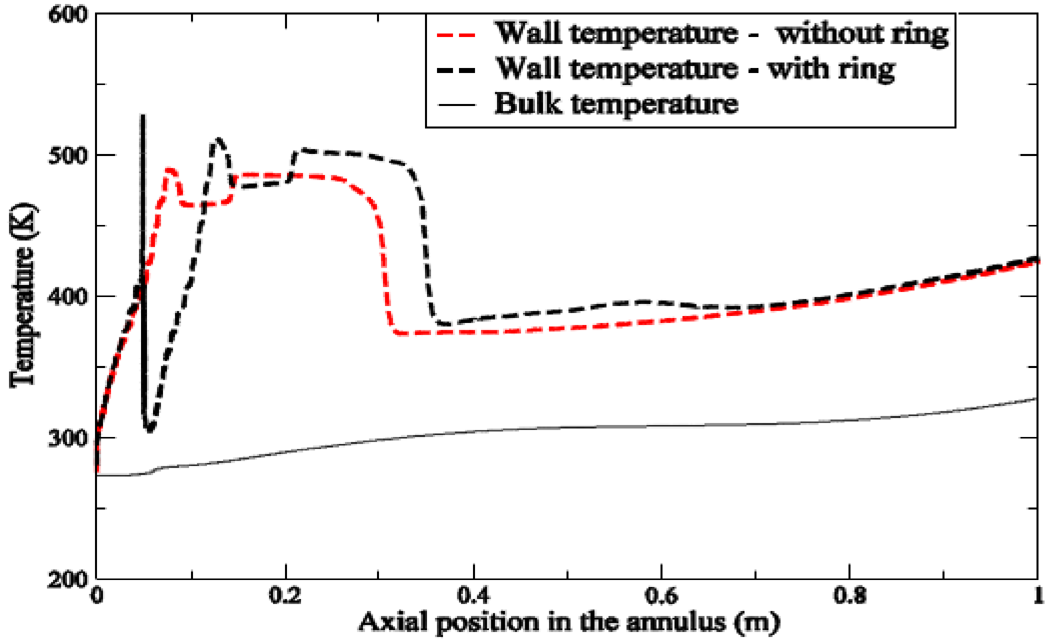

Figure 2.32: Computed axial heated inner wall and bulk fluid temperature for annulus without and with square ring placed at 50 mm from inlet, Chandra *et al.* (2009).

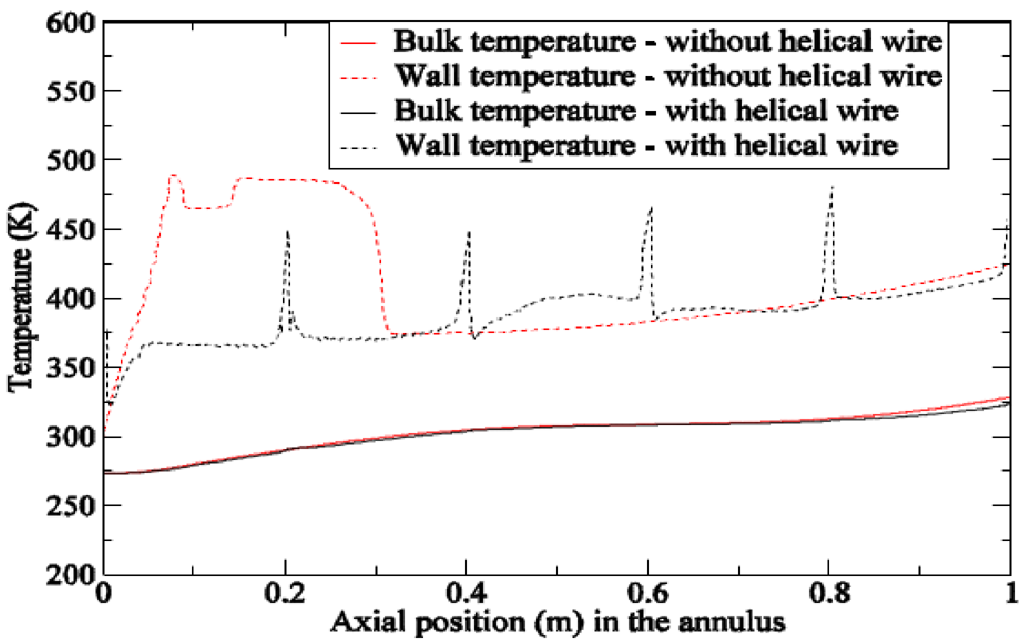

Figure 2.33: Computed axial heated inner wall and bulk fluid temperatures for annulus without and with a helical wire wrap, Chandra *et al.* (2009).

As shown from Figure 2.33, the helical wire suppressed the HTD by enhancing the heat transfer rate. This enhancement is due to the flow rotation around the helical wire which resulted in turbulent mixing enhancement. In summary, Chandra *et al.* (2009) concluded that, usage of obstacles such as helical wire and square ring inside annulus and tube is a very efficient heat transfer enhancing approach since it suppresses HTD or decreases the possibility of HTD occurrence.

Bae *et al.* (2010) investigated numerically the effect of inserting a helical wire spacer (1.3 mm OD, and 105 mm pitch) in an 6.32 mm ID tube (L_h = 2.65 m) on SCHT during upflow of CO_2 and compared the results with those obtained from KAERI's experiments. The flow parameters were: G = 400 kg m^{-2} s^{-1}, q = 30, 50, and 70 kW m^{-2}, and P = 8.12 MPa.

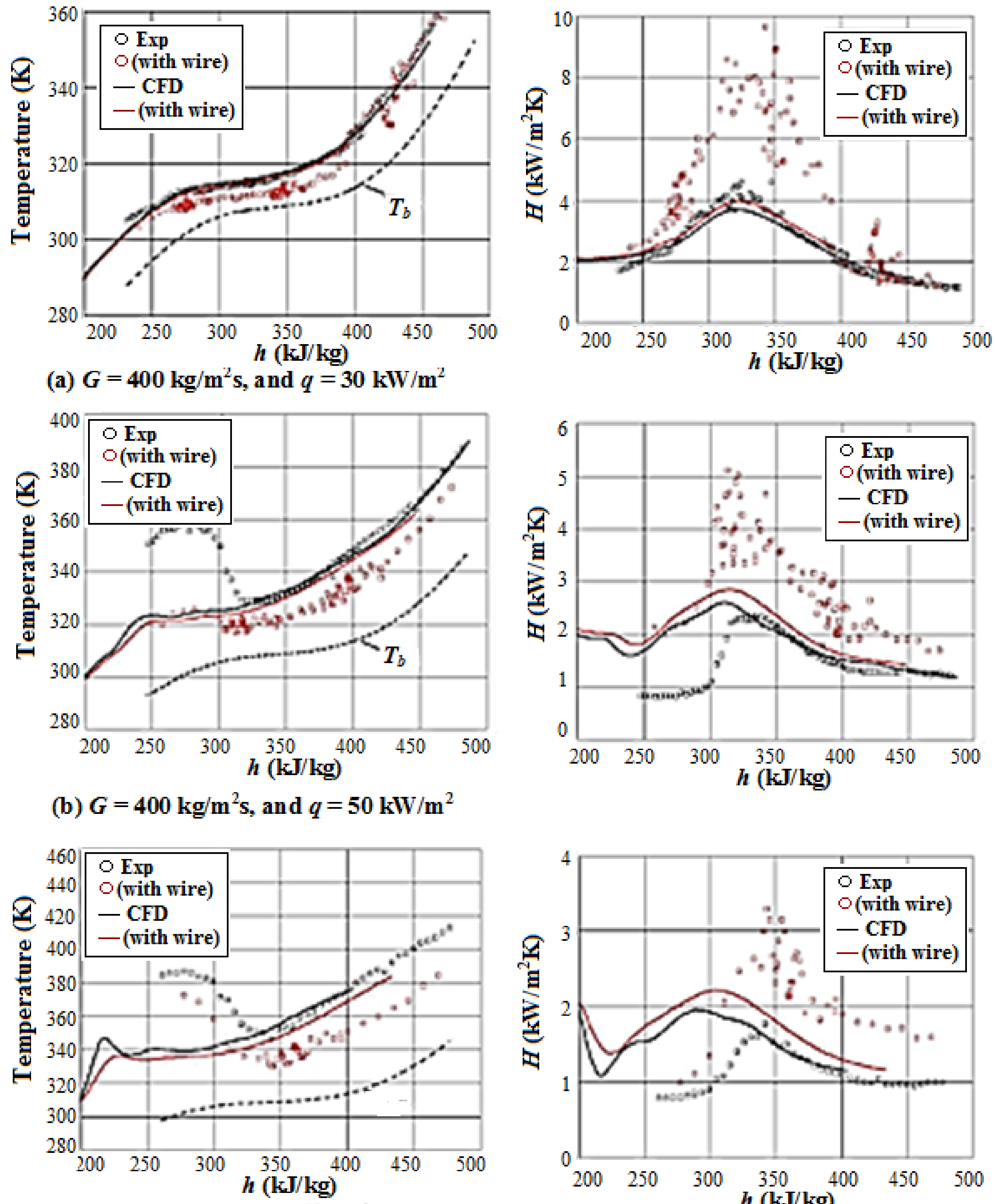

(a) G = 400 kg/m²s, and q = 30 kW/m²

(b) G = 400 kg/m²s, and q = 50 kW/m²

(c) G = 400 kg/m²s, and q = 70 kW/m²

Figure 2.34: Comparison between the experimental results (symbols) and the numerical results (lines) for the investigated cases. LHS figures are for the inner wall temperature vs. bulk fluid enthalpy; RHS figures are for HTC vs. bulk fluid enthalpy (Bae *et al.*, 2010).

Figure 2.34b and Figure 2.34c, show that deterioration of the heat transfer is encountered experimentally. However, the numerical model was unable to predict this deterioration. Although the experiments show that the helical wire is an efficient device to enhance heat transfer at supercritical pressures, where the HTD in plot (b) suppressed by using a helical wire, the CFD analyses show only a very small augmentation of the heat transfer rate due to the influence of the wire. The predicted HTC in the helical-wire obstructed tube flow increased about 10% compared to the bare tube flow while the measured increase in HTC could exceed 100%.

A numerical investigation of the effect of a 1 mm high ring on water SCHT located inside an 8 mm ID tube midway along the 1 m heated length was performed by **Yongliang *et al.* (2010)** using the RNG k-ε turbulence model and Scalable Wall Function in CFX10. The results show a significant reduction in the wall temperature over a distance of L/D = 62.5 downstream from the ring; after which the wall temperature gradually increases until it reaches the wall temperature of the bare tube as shown in Figure 2.35.

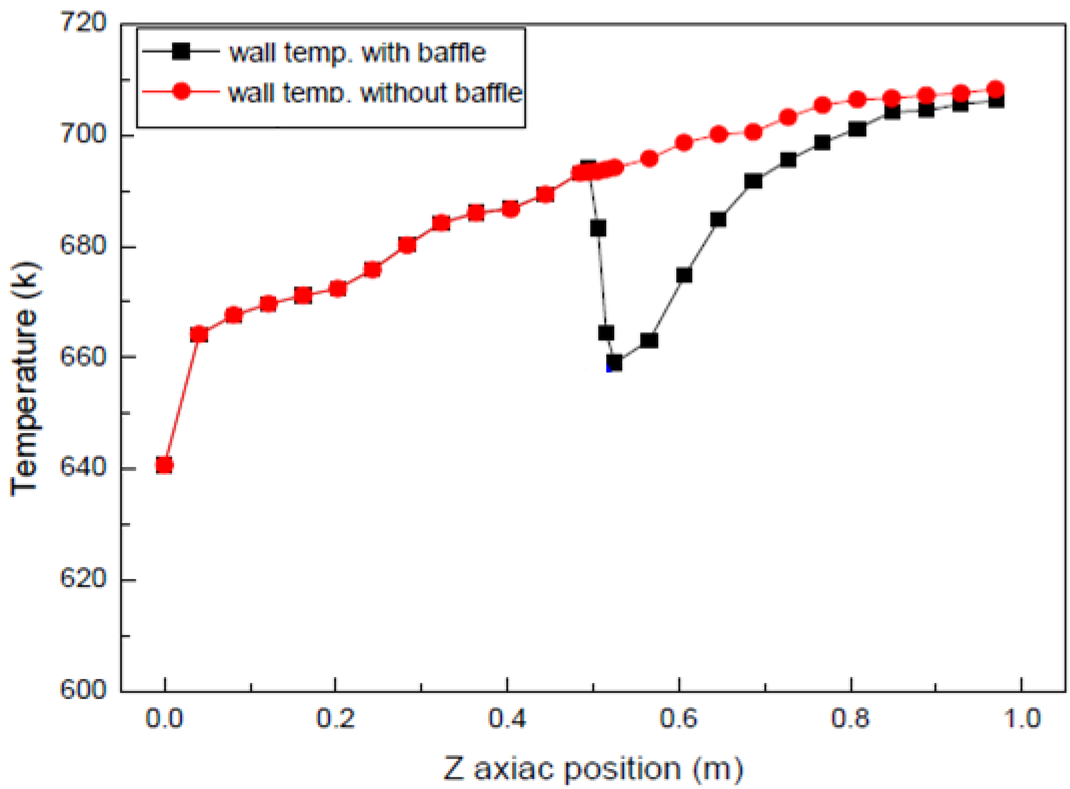

Figure 2.35: Axial wall temperature distribution with and without a ring (or baffle) midway along the tube (Yongliang *et al.*, 2010).

Niceno and Sharabi (2013) have used LES model to investigate the enhancement and deterioration of heat transfer for water flowing upward and downward through a tube having (6.28 mm ID and 0.6 m heated length preceded by 0.4 m entry length). The geometry has been simplified from a circular to a rectangular shape with more conditions applied to the region close to the walls to substitute for the differences in geometries. Flow conditions were as follows: P = 23.5 MPa, G = 509 kg m^{-2} s^{-1}, and q = 390 kW m^{-2}. The results showed good agreement with the corresponding experimental data. Moreover, this study showed that the downward flow did not have heat transfer deterioration but showed a monotonic increase of wall temperatures, while for upward flow heat transfer deterioration was encountered. The LES model allowed the authors to explain the physics behind the enhancement and deterioration of heat transfer which agrees with the explanation provided by Jackson (2013) and others. The heat transfer deterioration is due to a significant reduction in Reynolds stresses. When buoyancy changes dramatically in the vicinity of pseudo critical temperature, the Reynolds stresses decrease resulting in a reduction in the turbulence level which leads to a heat transfer deterioration. Afterwards, an M-shaped velocity profile develops close to walls due to acceleration that leads to a turbulence recovery; hence the enhancement of heat transfer can occur.

Many authors claimed that the RANS turbulence models are not the best choices to investigate heat transfer to fluids at supercritical pressures as mentioned earlier. To support this, **Ambrosini *et al.* (2013)** verified the inability of the RANS models at supercritical pressures to predict wall temperatures of circular channels. The lengths and diameters of these channels were varied according to real dimensions of different experiments. The results revealed that these models are not reliable: although a certain model can predict qualitatively wall temperatures at certain condition, it usually does not predict wall temperatures at different conditions even qualitatively.

2.5.2 Numerical studies of supercritical flows in rod bundles

Shan and Chen (2010) investigated numerically the effect of a wire-wrap spacer or a grid spacer inside a SCWR fuel bundle having 40 pins in a square arrangement with a total length of ~425 cm and an estimated grid spacer pitch of 30 cm. The flow conditions were T_{in} = 280 °C, G =780 kg m^{-2} s^{-1}, q = 614.2 kW m^{-2}, and P = 25 MPa. The numerical results suggested that the effect of the wire wrap is much better than the effect of the grid spacer based on cladding temperature, uniformity of coolant temperature and pressure drop. The peak cladding temperature was 587.6 °C when the wire wrap was used, while it was 603.5 °C when the grid spacer was used as shown in Figure 2.36. The coolant temperature became more uniform when the wire wrap spacer was used, due to more forced cross flow between sub-channels in the wire wrapped assembly. The maximum difference between the hottest and coldest sub-channel was 25.3 °C, while it was 40.2 °C when the grid spacer was used as shown in Figure 2.37. Pressure drops associated with the wire wrap spacer was lower than that associated with the grid spacer as shown in Figure 2.38. The effect of the wire wrap pitch was also investigated; as expected the most uniform temperature profile and the highest pressure drop occurred for the smallest wire pitch (H_{wire}/D_{rod} = 20) due to more cross flow (the maximum temperature difference between the hottest and the coldest sub-channels is 21.9 °C according to Figure 2.39). The effect of wire-wrap pitch on the axial pressure drop is shown in Figure 2.40.

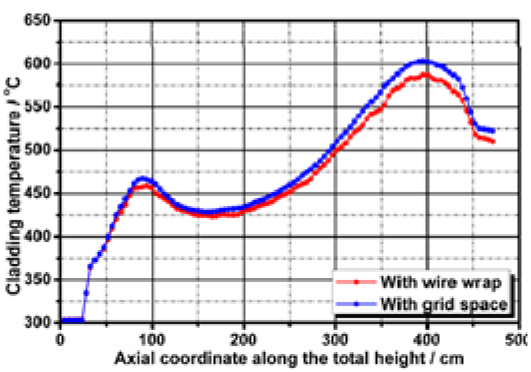

Figure 2.36: Axial cladding temperature profile in a hot channel (Shan and Chen, 2010).

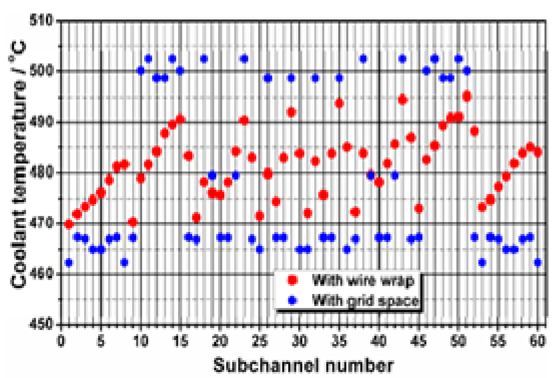

Figure 2.37: Coolant temperature profile at axial position where the peak cladding temperature occurs (Shan and Chen, 2010).

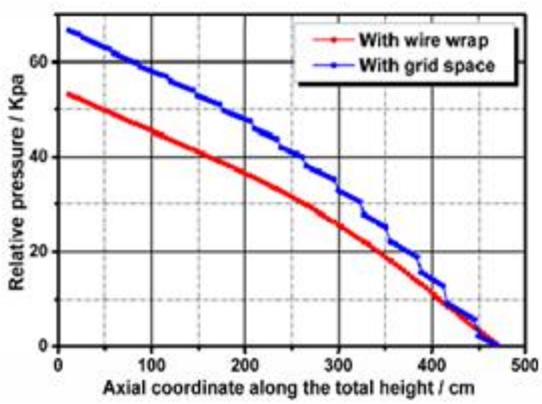

Figure 2.38: Pressure drop for the two assemblies (Shan and Chen, 2010).

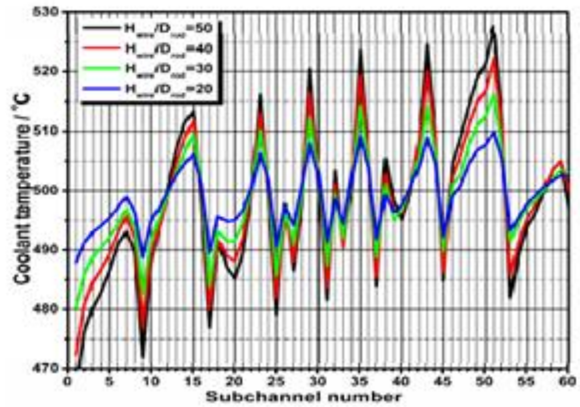

Figure 2.39: Exit coolant temperature profile with different pitch (H_{wire}/D_{rod}) values (Shan and Chen, 2010).

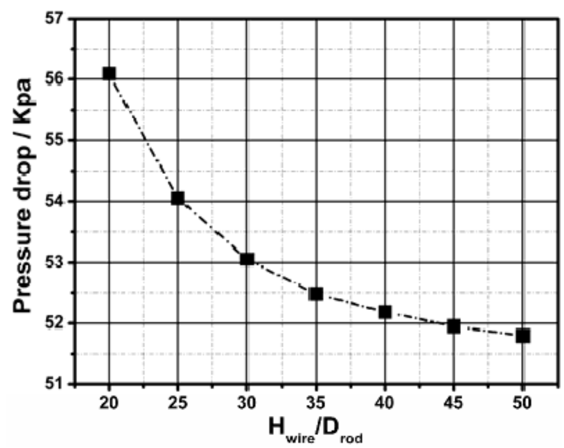

Figure 2.40: Pressure drop with different pitch (H_{wire}/D_{rod}) (Shan and Chen, 2010).

Jaromin *et al.* (2013) have used k-ω SST model, which is one of the RANS models; that is optimized by varying Pr values for water for wide ranges of mass flux, inlet enthalpy and heat flux at supercritical pressures. They determined the optimal Prandtl number for each individual coupled conditions (P, G, q, and T_{in}) which fitted the experimental data more accurate than those having a constant Prandtl number. Moreover, wall temperatures obtained using the best fit of Prandtl number have been compared to the wall temperatures obtained using turbulent Prandtl (Pr_t) models. This study concluded that none of the tested models provided a sufficiently wide range of the Prandtl number to satisfy all investigated experiments. **Podila and Rao (2016)** performed CFD simulation of SCHT into CO_2 flows through the 3-rod bundle equipped with wire wraps (University of Ottawa rod bundle). They tested different RANS models. None of the models was able to predict the experimental data. The simulation was not able to predict the experimental trend either.

Tables 2.11 and 2.12 summarize the experimentally observed and numerically predicted effects of the flow obstacles on SCHT, respectively.

Table 2.11: Experimentally observed effects of the flow obstacles on SCHT.

Reference	Obstacle type and geometry	Observed effect of the flow obstacles
Shiralkar and Griffith (1970)	Twisted Tape in a tube	At q = 146.59 kW m^{-2}, no HTD occurred at G > 1139 kg m^{-2} s^{-1}, while HTD occurred at $G \leq$ 1356 kg m^{-2} s^{-1} in the bare tube.
Ackerman (1970)	Ribs in a tube	At P =24.8 MPa and G = 407 kg m^{-2} s^{-1}, no HTD occurred at q = 630 kW m^{-2}, while HTD occurred at $q \geq$ 315 kW m^{-2} in the bare tube.
Lee and Haller (1974)	Ribs in a tube	Heat fluxes can be increased by 50%-100% over smooth tube values without occurrence of HTD.
Kamenetskii (1980)	Twisted Tape in a tube	Reduction in flow stratification in horizontal tubes.
Fedorov *et al.* (1986)	Ribs in a tube	More uniform wall temperature profile along the heated length and circumferentially compared to the smooth tube were observed. HT enhancement increased as heat flux increased.
Hongzhi *et al.* (2009)	Helical wire in a square annular channel	At P = 25 MPa and q = 400 kW m^{-2}, the maximum heat transfer enhancement occurred at G =1200 kg m^{-2} s^{-1}, while HTD occurred at G =500 kg m^{-2} s^{-1}. At P = 23 MPa, the heat transfer enhanced by 100% compared to that at P =25 MPa, but the HTD occurred at low mass fluxes compared to P =25 MPa.
Bae *et al.* (2011)	Helical wire in a tube	100% increase in HTC compared to that in the plain tube when T_b is very close to T_{pc}. At enthalpies much higher than h_{PC} , HTC becomes independent of the heat flux.
Wang *et al.* (2012)	Spacer in annulus	25%-80% increase in HTC compared to that in the annulus without a spacer. The least enhancement

		occurs when T_b is away from the pseudo-critical temperature, i.e. $T_w<T_{pc}$ or when $T_{pc}<T_b$
Mori *et al.* (2012)	Grid spacers in a 3 and 7 rod bundles	Downstream from the grid spacer, a significant HT enhancement was observed in the upward flow, but not in the downward flow.
Richards *et al.* (2013)	Grid spacers in a 7 rod bundles	Heat transfer deterioration occurred in all investigated cases regardless of grid spacers' existence.
Hong-bo *et al.* (2013)	2x2 rod bundle	(i) maximum temperature occurred at the corner, (ii) circumferential temperature gradient increases as mass flux decreases (iii) the larger *P/D* bundle experienced higher wall temperatures than the smaller *P/D* bundle.
Wang *et al.* (2014)	2x2 rod bundle	(i) maximum temperature occurred at the corner, (ii) circumferential temperature gradient increases as mass flux decreases and heat flux increases and (iii) heat transfer coefficient is sensitive to mass flux and heat flux variations but less sensitive to pressure variation.

Table 2.12: Numerically predicted effects of the flow obstacles on SCHT.

Reference	Obstacle type and geometry	Observed or predicted effect of the flow obstacles
Chandra *et al.* (2009)	Ring in an annulus, and helical wire in a tube and annulus (Numerical)	Effect of the ring was short-lived over a specific region downstream from the ring. However, In case where the ring is located at 200 mm distance from the inlet, the heat transfer was enhanced up to L/D_{hy} =50 downstream from the ring, while in the case of 50 mm distance from the inlet it was up to L/D_{hy} =25 downstream from the ring.
Bae *et al.* (2010)	Helical Wire in a tube (Numerical)	The HTD cannot be predicted by CFD at high heat fluxes compared to experiment. However, the predicted HTC in the wired tube increased about 10% compared to the bare tube.
Yongliang *et al.* (2010)	Ring in a tube (Numerical)	Reduction in the wall temperature for a distance downstream from the ring.
Shan and Chen (2010)	Wire wrap and grid spacer in a SCWR (Numerical)	Wire wrapped SCWR has a uniform coolant temperature; hence it has less cladding temperature compared to a SCWR with grid spacers. Moreover, it has less pressure drop which reduces the pumping power.

2.6 Conclusions and final remarks from literature review

The objective of this review is to understand the effect of the flow obstructions on SCHT and pressure drop. This review is carried out based on experimental investigations and numerical studies. The experimentally observed and numerically predicted effects of the obstacles are as follows:

Experimentally observed effects:

1. At SC conditions, the heat transfer coefficient, in both bare and helical wire equipped geometries, becomes almost independent of heat flux at very low and high enthalpies (away from the pseudo critical enthalpy).
2. The highest heat transfer enhancement due to a flow obstruction occurred near the pseudo-critical temperature where the enhancement can reach 100% compared to geometries without flow obstructions.
3. Heat transfer at subcritical pressures was enhanced over a distance L/D = 30-35 downstream from the flow obstruction, while at supercritical pressures, it is over L/D = 60-70; so, the enhancement of heat transfer at super-critical pressures due to flow obstructions is more efficient than that at subcritical pressures.
4. Heat transfer deterioration was encountered in upflow but not in downflow regardless of the geometry. Grid spacers can eliminate HTD partially in rod bundles as mentioned by Mori *et al.* (2012), or they could have no effect, as mentioned by Richards *et al.* (2013) at certain flow conditions.
5. The heat transfer enhancement downstream of a grid spacer decreases in upflow; however in downflow, the effect of grid spacers on heat transfer was less pronounced or was absent altogether.

Numerically predicted effects

1. Heat transfer at super-critical pressures was enhanced over a significant distance downstream the flow obstruction (L/D = 50 and 62.5).

2. Although numerical tools (CFD) do not always predict the HTD, they predict the experimental SCHTs with a reasonable accuracy away from the pseudo-critical temperature when spacers are not used. CFD prediction capability of SCHT in spacer-equipped geometries is poor.
3. The SCHT is almost independent of heat flux when $T_w<T_{pc}$ or when $T_{pc}<T_b$, i.e. at conditions away from the pseudo-critical region for both bare and spacer -equipped geometries.
4. Helical wires inside a SCWR lead to a more uniform fluid temperature, a lower cladding temperature, and a lower pressure drop than grid spacers.

It is tentatively concluded that numerical CFD results agree fairly well with the experimental results at normal flow conditions without spacers, while for deteriorated heat transfer conditions the agreement appears questionable. However, CFD underestimated the normal obstructed heat transfer and could not predict the deteriorated obstructed heat transfer, see Figure 2.34. Hence, CFD may be used as a first assessment tool for fuel bundle design at super critical pressures. The vast majority of the SCHT experiments were performed in tubes and annular channels instead of bundles. Therefore, more relevant experiments in bundles are still needed to get a better indication of the flow obstructions effects on SCHT and pressure drop.

Chapter 3

Experimental Facility

3.1 The flow loop

The Supercritical University of Ottawa loop (SCUOL) has been described in detail by Jiang (2015). Figure 3.1 shows its main components, while Figure 3.2 shows a schematic diagram of the loop. The maximum operating pressure is 10 MPa. The heat supplied to the test section was provided by a rectified DC power supply, capable of providing a maximum voltage of 60 V DC and a maximum current of 2833 A. The fluid inlet temperature to the test section is controlled by a 22 kW pre-heater. The CO_2 operating fluid was cooled in four heat exchangers connected in parallel; two of these units used centrally supplied chilled water as a secondary fluid, whereas the other two used ethylene glycol, that was circulated from a tank contained in an adjacent freezer room.

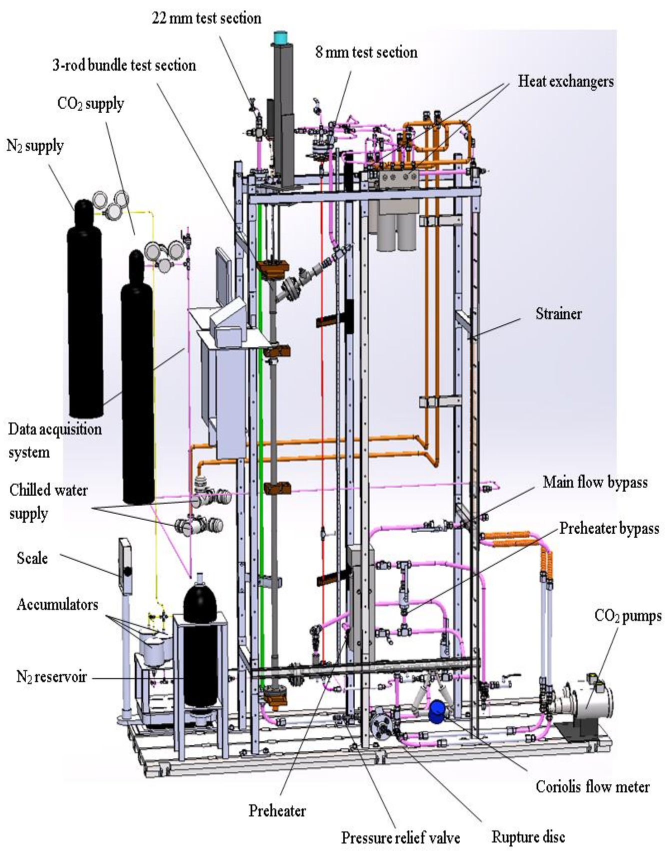

Figure 3.1: University of Ottawa multi-fluid supercritical loop (Jiang, 2015).

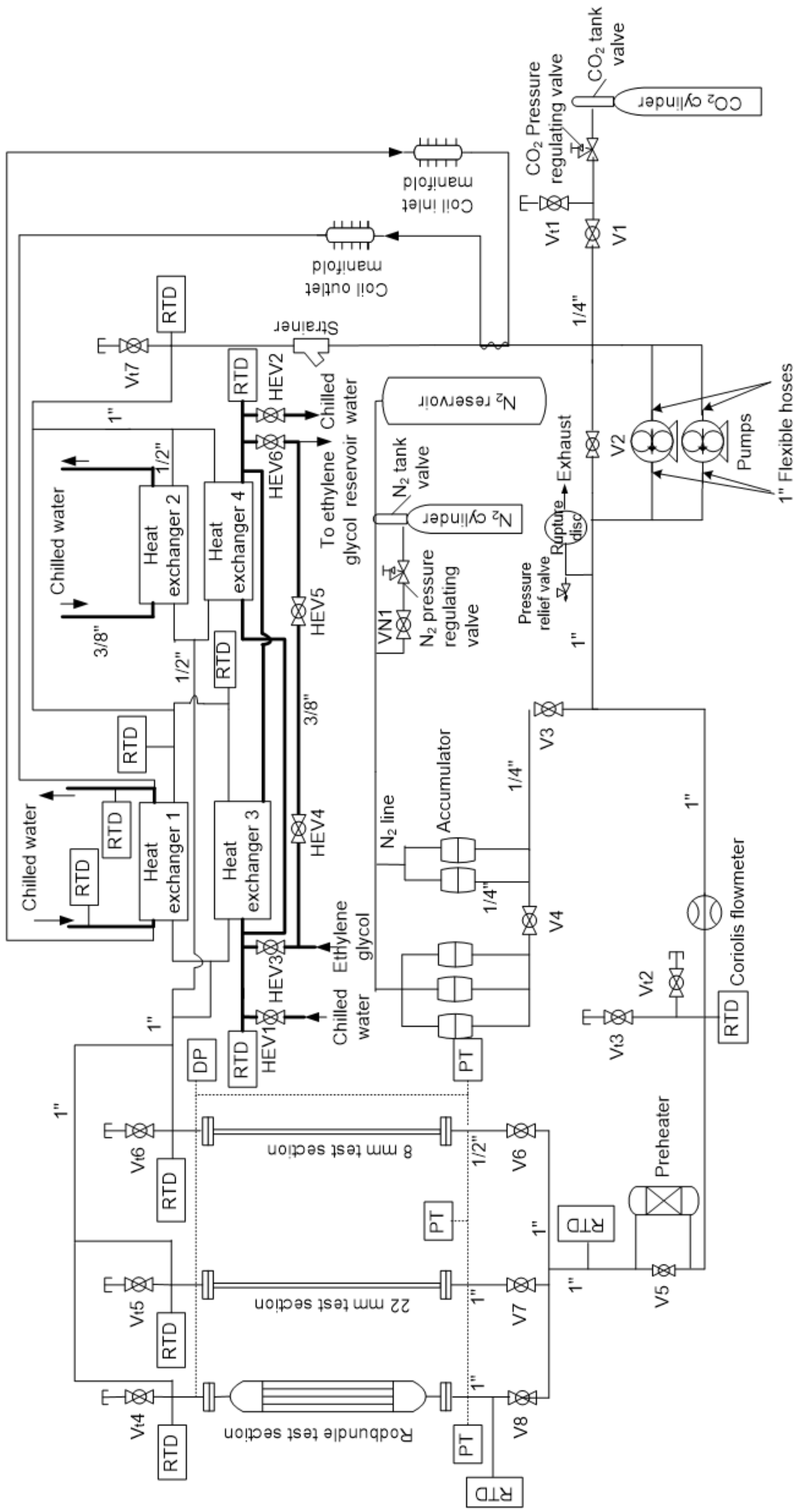

Figure 3.2: Schematic diagram of the loop and its components.

3.2 Rod bundle test section

The rod bundle was mounted vertically and was cooled by pressurized CO_2 flowing upwards. The rod bundle had a total length of 2500 mm and the heated section of each rod was made of Inconel 600 tubing with an outer diameter D = 10.0 mm and a length of 1500 mm. Figure 3.3 shows an overall view of the rod bundle and Figure 3.4 shows its cross section. The three rods were identified as Rod A, Rod B and Rod C. Circumferential positions around each rod were specified such that positions at 0° were facing the exterior of the rod bundle, positions at 180° were facing the axis of the rod bundle subassembly and positions at 90° and 270° were facing the gaps with the unheated rod fillers. More details about the unheated rod fillers have been provided by Jiang (2015). The bare rod bundle hydraulic diameter was D_h = 4.08 mm. The test section and the associated piping were insulated by a 2 mm thick layer of fiberglass and a 10 mm thick layer of insulating foam. The following two rod-spacer configurations were tested.

i) In the first configuration, the rods were separated from each other by four custom-made grid spacers, each having a blockage ratio of 5.3% and spaced by 500 mm (Figures 3.5-a,b). For each grid spacer, three thin shims made of stainless steel and having a thickness of 0.102 mm and a width of 4 mm were spot-welded on a short piece of stainless steel T304 tubing, having a length of 12 mm, an OD of 2.9 mm, and an ID of 2.4 mm, which served to separate the three heated rods. Each shim was wrapped around one rod and spot-welded on it. The heated rods were separated from the unheated rod fillers by an extra shim, having a total length L = 76 mm, as shown in Figure 3.5-a.

ii) In the second configuration, the rods were separated from each other by a “wire” (actually stainless steel T304 tubing) with a diameter of 1.3 mm that was wrapped around each rod with a pitch of 200 mm (Figure 3.5-c). The wire wrap pitch was 200 mm, except at the first 200 mm of the heated length, where it was 100 mm. The wire was fastened to the heater rods at the start of the heated section at a 0° location (facing the pressure tube, see Figure 3.4). The wire wrap resulted in a decrease in local flow area of 2.2 % from the unobstructed rod-bundle cross-sectional area just upstream of the start of the heated length, where no wire wraps were present. However the flow blockage of the wires projected on a plane normal to the axis was 32 %. The wire wrap had a resistance of 1.82 Ohm/m, which is much higher than the resistance of the heated rods, which was 0.036 Ohm/m.

3.2.1 Sliding thermocouple assembly

A convenient feature of this apparatus is the use of a sliding thermocouple system, which measured the inside wall temperature distributions of each of the three heated rods in the bundle. Each rod contained five thermocouples, positioned at three stations that were separated axially by a distance of 480 mm; two thermocouples were placed at diametrically opposite locations at each of the two upstream stations and a single thermocouple was placed at the farthest downstream station. Each thermocouple carrier is supported by two springs pressing the tips of the thermocouples against the heated wall. Each set of five thermocouples was attached to a push rod that could be traversed along the test section as well as rotated over the full 360° range by a step motor. These three step motors were mounted on a traversing system, which was advanced by a fourth step motor and permitted all thermocouples to be traversed axially over a distance of 500 mm (Figure 3.5-d).

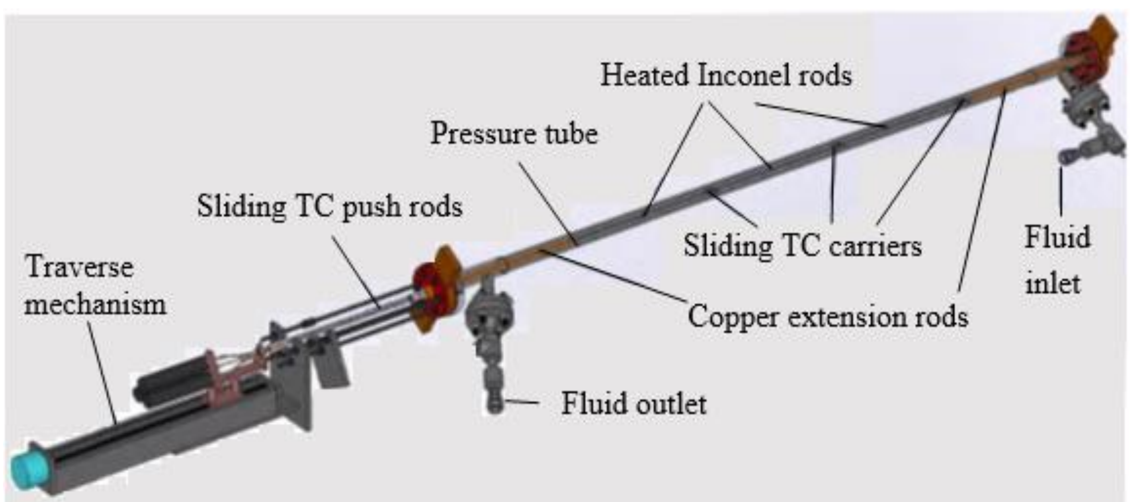

Figure 3.3: Overall view of the rod bundle and the thermocouple traversing mechanism (Jiang, 2015).

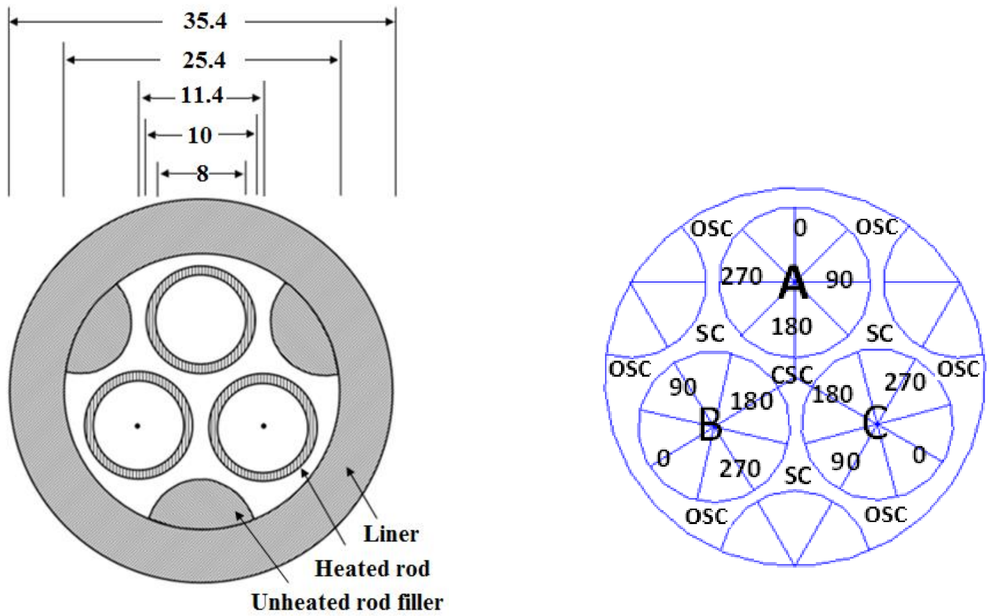

Figure 3.4: Left: Cross section of the rod bundle with dimensions in mm. Right: angular coordinate systems for temperature measurements around each of the three rods, marked as A, B and C, while viewed from downstream; CSC, SC and OSC denote the central subchannel, intermediate subchannels and outer subchannels, respectively.

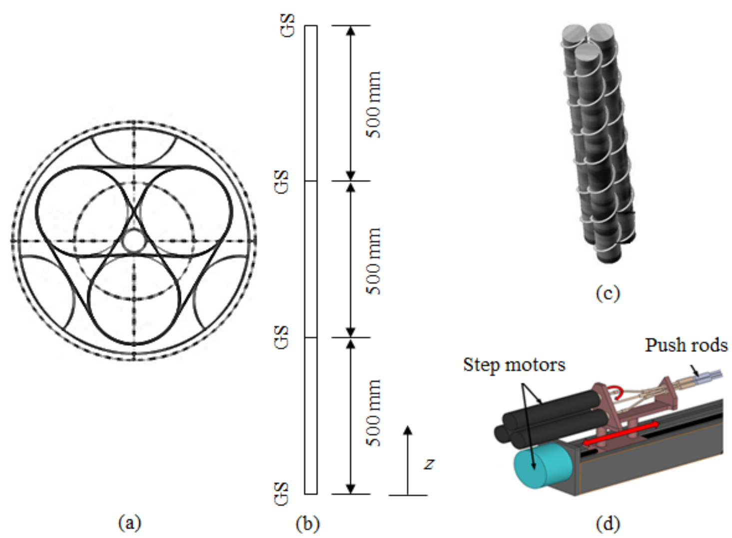

Figure 3.5: (a) Cross-section of the heated section equipped with grid spacers; (b) side view of the heated section equipped with grid spacers; (c) the wire-wrapped central rod assembly (not to scale); (d) thermocouple traversing system.

3.2.2 Instrumentation

The bulk fluid temperature at the inlet and outlet of the rod bundle, as well as temperatures at different locations of the loop, were measured with in-flow ultra-precise RTD sensors (Omega P-M-1/10-1/8-5-1/2-G-15). The range of these RTD sensors was from 0 to 100 °C and their uncertainty was 0.1 °C. J-type thermocouples were installed in the sliding thermocouple system; these thermocouples had an uncertainty of 1.0 K at the 95 % confidence level. Potentiometers were used to measure the axial and angular displacements of the thermocouples; the potentiometer measuring the axial displacement had a linearity of ±0.25% over its full moving range of 500 mm and the potentiometer measuring the angular displacement had an estimated uncertainty of 5°. The absolute pressure at the inlet of the rod bundle was measured with a pressure transducer (Rosemount, Model 3051T), having an uncertainty of 15.5 kPa. A Coriolis flow meter (Micro Motion® Elite®, Model CFM050M320N0A2E2ZZ) was used to measure the mass flow rate; this device was factory calibrated and had a specified uncertainty of 0.05 % for liquid flow. The instantaneous voltage drop across the heated length of the test section was measured with a 24-bit digital voltage measurement module (National Instrument NI 9225). The rectified voltage fluctuated at a frequency of 360 Hz and was sampled at a much higher sampling rate. The electrical power supplied to the test section was calculated from the measured time-averaged voltage drop across the rod bundle and the measured electrical resistance of the test section, which was measured prior to its installation. The measured voltage drop varied from 11.9 to 21.1 V, within a measurement uncertainty of 0.1 to 0.5%.

3.2.3 Data acquisition

All pressure and temperature measurements were acquired at a rate of 10 samples/s. After the operating conditions were stabilized, measurements were recorded continuously. During recording of the results, the traversing system was programmed to reposition the thermocouples, either axially or circumferentially, every 80 s. At the beginning, some tests were investigated at an angular displacement of 30 degrees and an axial displacement of 20 mm. Because of the many measurement locations, these experiments typically lasted for 12 hrs. For this long period of time, it was hard to maintain steady operating conditions because of system limitations. Therefore, subsequent experiments were investigated at an angular displacement of 45 degrees and an axial displacement of 50 mm, which reduced the test period to 3.5 hrs and allowed us to maintain fairly steady flow conditions. During data processing, each data set was divided into blocks, each of which contained data for a different position of the thermocouple assembly. The data collected during the last 10 s of each block were found to correspond to steady conditions. Data processing was done with the use of a code written in MATLAB. Spurious values in the data were removed. The data values used in the analysis of the results represent time averages over 10 s intervals.

3.3 8 mm test section

All measurements presented in this thesis were collected using a directly heated Inconel-600 tubular test section, mounted vertically with CO_2 flowing upwards. The test section had an internal diameter D = 8 mm, a wall thickness of 1 mm and a heated length L_h = 1940 mm. The heated part of the tube was preceded by an unheated section with a length of 890 mm, which ensured that the flow entering the heated section was fully developed. The test section was insulated thermally by layers of fiberglass cloth tape, with a thickness of 8 mm, surrounded by a rubber-foam insulation tube with a thickness of 50 mm. In order to study the flow obstacle effect on heat transfer, blunt or rounded cylindrical obstacles with a diameter of 4 mm (25% blockage ratio) and a length of 10 mm were inserted inside the test section, Subsequently, the effect of blockage ratio was investigated by using a blunt obstacle having a smaller diameter of 2.9 mm (13% blockage ratio). Because the blockage was located asymmetrically, the effect of circumferential blockage location on SCHT was also investigated. Figure 3.6 shows a schematic diagram of the test section with the locations of the thermocouples as well as cross sections of the test section with the main dimensions, definitions of azimuthal coordinates and an obstacle kept in place by a movable magnet. Note that the obstacles were located at 180° and the wall thermocouples at 0°. Tables 3.1 and 3.2 specify geometric details and axial positions of flow obstructions for the different configurations that were tested at supercritical and high subcritical pressures, respectively.

Table 3.1: Obstacle-equipped tube configurations for supercritical pressure tests

Configuration	Obstacle shape	Obstacle blockage ratio (%)	Number of obstacles	Distance of downstream end of obstacle from the inlet[1] (mm)		Obstacle pitch (mm)
				1st	Last	
1	Blunt	25	1	935	---	0
2			2	935	1935	1000
3			2	935	1435	500
4			8	935	2685	250
5	Rounded	25	2	935	1435	500
6	Blunt	13	8	935	2685	250

Table 3.2: Obstacle-equipped tube configurations for high subcritical pressure tests

Configuration	Obstacle shape	Obstacle blockage ratio (%)	Number of obstacles	Distance of downstream end of obstacle from the inlet[1] (mm)		Obstacle pitch (mm)
				1st	last	
1	Blunt	25	2	935	1935	1000
2			2	935	1435	500
3			8	935	2685	250

[1]Heated length starts at 890 mm.

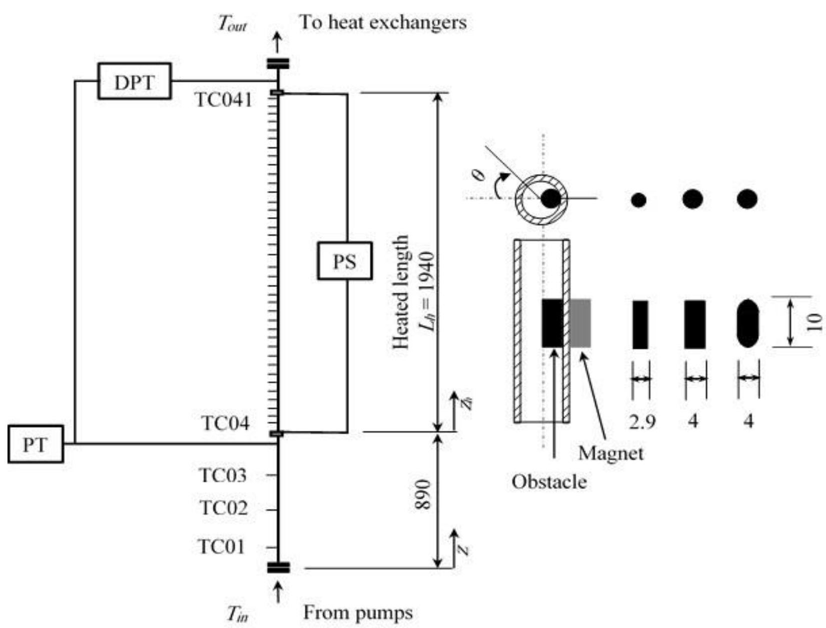

Figure 3.6: LHS: Schematic diagram of the 8 mm test section showing the locations of thermocouples; PS: power supply; PT: pressure transducer; DPT: differential pressure transducer; RHS: details of the obstacles and their locations; all dimensions are in mm.

3.3.1 Instrumentation

The temperature variation along the test section wall was measured with T-type (Copper-Constantan) thermocouples (Omega SA1XL-T-SRTC), having an uncertainty of 0.5 K (this and other reported uncertainties correspond to a 95% confidence level) and a time constant of less than 0.15 s. The thermocouples were attached to the exterior wall of the test section using a silicone-based adhesive, which has a temperature rating of 260˚C. The bulk fluid temperatures at the inlet and outlet of the test section and at other locations of the loop were measured with ultra-precise immersion RTD sensors (Omega P-M-1/10-1/8-5-1/2-G-15), having a maximum uncertainty of 0.1˚C between 0 and 100˚C. The test section inlet pressure was measured by a pressure transducer (Omega PX01C1-3KA5T) with a specified uncertainty of 21 kPa; it was calibrated in the range from 0 to 10342 kPa with a maximum uncertainty of 7.76 kPa. The pressure drop across the heated length of the test section was measured with a differential pressure transmitter (Omega PX771A-300DI), having an uncertainty of 75 Pa. The CO_2 mass flow rate was measured with a Coriolis flow meter (Micro Motion® ELITE® CFM050M320N0A2E2ZZ), having an uncertainty of 0.05% for liquid flow. The instantaneous voltage drop across the heated length of the test section was measured with a 24-bit digital voltage measurement module (National Instrument NI 9225), having a range of ±300 V and an uncertainty of 0.034 V. The rectified voltage fluctuated at a frequency of 360 Hz and was sampled at a much higher sampling rate. The electrical power supplied to the test section was calculated from the measured time-averaged voltage and the measured electrical resistance of the test section.

3.3.2 Data acquisition

A dedicated computerized data acquisition system was used to monitor and control different loop operations and to record the data. All pressure and temperature measurements were acquired at a rate of 10 samples/s. The measurements were recorded after the operating conditions had stabilized. Data processing was done with the use of a code written in MATLAB. Spurious values in the data were removed. The data values used in the analysis of the results represent time-average values over 60s intervals.

The ranges of the measured parameters and their uncertainties based on 2 sigma confidence interval are summarized in Table 3.3.

Table 3.3: Ranges of measured parameters and their uncertainties

Parameter	Unit	Range	Uncertainty
Wall temperature (8 mm ID tube, T-type thermocouple)	°C	(-73) – (+260)	0.5
Wall temperature (3-rod bundle, J-type thermocouple)	°C	0 – 750	1.0
Bulk temperature	°C	0 - 100	0.1
Mass flow rate	Kg s^{-1}	0 - 25	0.05 %
Voltage	Volt	(-300) – (+300)	0.034
Pressure (8 mm ID tube)	kPa	0 - 10342	7.76
Pressure (3-rod bundle)	kPa	0 - 10342	15.5
Obstruction position (8 mm ID tube)	mm	----	5
Axial displacement (thermocouple traversing system)	mm	0-500	1
Angular displacement (thermocouple traversing system)	degree	0-360	5

Chapter 4

An experimental investigation of supercritical heat transfer in a three-rod bundle equipped with wire-wrap and grid spacers and cooled by carbon dioxide

This chapter addresses the obstacles (wire wraps and grid spacers) effects on supercritical heat transfer in a 3-rod bundle. The results are presented in the form of the manuscript

> Eter, A., Groeneveld, D., Tavoularis, S., 2016. An Experimental Investigation of Supercritical Heat Transfer in a Three-rod Bundle Equipped with Wire-Wrap and Grid Spacers and Cooled by Carbon Dioxide. Nucl. Eng. Des. 303, 173-191.

The experimental results showed that heat transfer deterioration can occur for mass fluxes within the range of 200 and 700 kg m^{-2} s^{-1} near the start of the heated section of the rod bundle equipped with either type of spacers. The onset of heat transfer deterioration occurred at a higher heat flux for the wire-wrapped bundle than for the one with grid spacers, and at the lowest heat flux for the tube. Normal heat transfer in either of the rod bundles behaved similarly to the one in the tube for the same flow conditions and was also compatible with the predictions of the correlation of Jackson. Overall, hear transfer was somewhat better in the wire-wrapped bundle than in the one with grid spacers. For low mass fluxes (roughly 200 and 400 kg m^{-2} s^{-1}), normal heat transfer in the rod bundles was higher than in the tube for the same flow conditions; for an intermediate mass flux (700 kg m^{-2} s^{-1}), heat transfer in all three cases are comparable; and, rather surprisingly, at higher mass fluxes (1000 and 1200 kg m^{-2} s^{-1}), heat transfer in the tube appeared to be more efficient than in the rod bundles. The minimum SC heat transfer coefficient decreased somewhat with increasing heat flux (35% reduction as a result of a 100% increase in heat flux) and decreased strongly at a low mass flux (75% reduction as a result of 62% decrease in mass flux). The grid spacers introduced a strong local enhancement, but their effects disappeared only about 10 rod diameters downstream.

An Experimental Investigation of Supercritical Heat Transfer in a Three-rod Bundle Equipped with Wire-Wrap and Grid Spacers and Cooled by Carbon Dioxide

Ahmad Eter
Doctoral Student
Department of Mechanical Engineering
University of Ottawa
Ottawa, ON, Canada K1N 6N5
Aeter@uottawa.ca

Dé Groeneveld
Adjunct Professor
Department of Mechanical Engineering
University of Ottawa
Ottawa, ON, Canada K1N 6N5

Stavros Tavoularis[1]
Professor
Department of Mechanical Engineering
University of Ottawa
Ottawa, ON, Canada K1N 6N5
stavros.tavoularis@uottawa.ca

---

[1] Corresponding author

ABSTRACT

Heat transfer measurements in a three-rod bundle equipped with wire-wrap and grid spacers were obtained at supercritical pressures in the Supercritical University of Ottawa Loop (SCUOL). The tests were performed using carbon dioxide, as a surrogate fluid for water, flowing upwards for wide ranges of conditions, including conditions equivalent to the nominal and near-normal operating conditions of the proposed Canadian Supercritical Water-Cooled Reactor. The test section contained three heated rods and three unheated rod segments with an outer diameter of 10 mm and a pitch-to-diameter ratio of 1.14; the heated length was 1500 mm. Detailed surface temperature measurements along and around the three heated rods were collected using internally traversed thermocouples. The following ranges of test conditions were covered, with equivalent water conditions given inside parentheses: pressure from 6.6 to 8.36 MPa (19.7 to 25 MPa); inlet temperature from 11 to 30 °C (330 to 371 °C); mass flux from 200 to 1175 kg m^{-2} s^{-1} (340 to 1822 kg m^{-2} s^{-1}); and wall heat flux from 1 to 175 kW m^{-2} (11 to 1847 kW m^{-2}). For one set of tests, the heated rods were fitted with a 1.3 mm OD wire wrap, having an axial pitch of 200 mm along the entire heated length; for a second set, the heated rods were fitted with grid spacers having a 5.3% flow blockage and located at 500 mm axial intervals. The effects of spacer configuration on heat transfer at supercritical pressures were documented and analyzed. The observed experimental trends were compared to those obtained in an experiment in a heated tube at similar conditions and with predictions of a supercritical heat transfer correlation. Heat transfer was observed to deteriorate near the start of the heated section of the rod bundle equipped with either type of spacers as well as in a circular tube for mass fluxes between 200 and 700 kg m^{-2} s^{-1}. The onset of deterioration occurred at a higher heat flux for the wire-wrapped bundle than for the one with grid spacers, and at the lowest heat flux for the tube. Normal heat transfer in either of the rod bundles behaved similarly to the one in the tube and was also compatible with the predictions of the correlation of Jackson. The grid spacers introduced a strong local enhancement, but their effects disappeared only about 10 rod diameters downstream.

INTRODUCTION

The Super-Critical Water-Cooled Reactor (SCWR) is one of the candidate designs considered by the Generation IV International Forum as an innovative nuclear energy system with increased safety, more compact size, lower cost of energy production and reduced volume of nuclear waste, compared to existing systems. The present research is in support of the Canadian National Program for the development of the SCWR.

The supercritical heat transfer (SCHT) mode has distinct characteristics not present at subcritical pressures. When the fluid pressure and temperature are near their critical values, or when the pressure is supercritical (SC) and the temperature is near its pseudo-critical value, small changes in temperature can cause large changes in the thermo-physical properties and the heat transfer may undergo enhancement or deterioration. Of particular importance for the safety of SCWR is the phenomenon of heat transfer deterioration (HTD). HTD occurs when the supercritical heat transfer coefficient drops below the value that would be expected during normal forced convective heat transfer. HTD is characterized by wall temperature increase that is higher than normal can be encountered. Heat transfer deterioration is thought to be associated with the suppression of turbulence near the wall and is more likely to be encountered at low mass flows, high heat fluxes and in the vicinity of the pseudo-critical enthalpy.

Heat transfer in channels may be significantly affected by the presence of flow obstructions, including rod spacers in rod bundles. Eter *et al.* (2013) reviewed the literature of the spacer effect on SCHT. It has been observed that flow obstructions generally enhance heat transfer and that the highest heat transfer enhancement occurred when the flow temperature was near the pseudo-critical value; in such cases, the enhanced heat transfer coefficient was more than twice its value in channels without flow obstructions. Significant heat transfer enhancement was found to occur downstream of grid spacers in upflow; in downflow, however, the effect of grid spacers on heat transfer was less pronounced and it was sometimes absent altogether. Predictions of spacer effects on supercritical heat transfer using CFD codes were found to be in fair agreement with experimental observations for normal heat transfer conditions, but were deemed to be of questionable accuracy for HTD conditions.

Eter *et al.* (2013) found the vast majority of previous SCHT experiments were performed in tubes and, to a lesser degree, in annular channels. Very few experimental studies are available for SC flows in rod bundles. Dyadyakin and Popov (1977) conducted experiments in tight-lattice seven-rod bundles having different flow areas (102, 112, 113, 121, and 134 mm^2). A movable thermocouple installed in the central rod was used to measure the wall temperature. Significant pressure oscillations occurred (±5MPa with frequency of 0.04–0.033 Hz) at mass fluxes => 2000 kg m^{-2} s^{-1}) and high heat fluxes. The pressure oscillations appeared at an inlet bulk temperature of 260 °C and resulted in burnout of the test section. Silin *et al.* (1993) reported a database for water at supercritical pressures flowing in bundles; these data were obtained in the Russian Scientific Centre (RSC). They found that no heat transfer deterioration occurred in multi-rod bundles while HTD occurred in tubes at the same operating conditions. Wang *et al.* (2014) investigated SCHT of water flowing vertically upward through a 2 × 2 rod bundle. The test section contains four heated rods, having an 8 mm OD and a heated length of 600 mm, installed inside a square channel with rounded corners. The results revealed that (i) the maximum temperature occurred at the corner, (ii) effect of inlet temperature is minor, especially, at the corners where pseudo critical temperature axial location doesn't vary much, (iii) the circumferential temperature gradient increases as mass flux decreases and heat flux increases and (iv) heat transfer coefficient is sensitive to mass flux and heat flux variation but less sensitive to pressure variation. Gu *et al.* (2015) investigated the heat transfer characteristics of water flowing in a 2 × 2 bare rod bundle having a heated length of 800 mm. They found the circumferential wall temperature distribution to be non-uniform around the heated rod. In general, the operating conditions impacts on the water SCHT in the bundle are similar to those observed in tubes and annuli. Fewer experimental studies have addressed directly the spacer effect on SCHT. Mori *et al.* (2012) used HCFC-22 as a coolant. Upward and downward flows were investigated in a tube having a 4.4 mm ID and in sub-channels of a 3-rod bundle and a 7-rod bundle, having a sub-channel hydraulic diameter of 4.4 mm and 3.2 mm, respectively. The tube and rods in the three and seven-rod bundles have heated lengths of 2000 mm, 1450 mm and 1950 mm, respectively. Grid spacers were used to maintain the design of the pitch to diameter ratio in the bundle. A similar heat transfer trend among the tested sections was found at low heat fluxes, where the heat transfer enhancement in the bundle is small at a low heat flux. However, at a high heat flux, the heat transfer characteristics are different due to HTD that occurred in the tube but disappeared in the bundle near the grid spacer. They found the heat transfer enhancement decays gradually over a downstream distance of 60-70*D*. With down-flow, no HTD was observed in either the tube or the bundle and no significant spacer effect on the normalized heat transfer coefficients was observed. Richards *et al.* (2013) used Freon (R-12) as a coolant flowing in a 7-rod bundle having 1 m heated length and 9.5 mm rod OD. In order to keep rods apart from each other, 3 grid spacers have been installed along the heated length spaced by 500 mm and (pitch-to-diameter ratio =1.19). The results showed that although the 7-rod bundle is equipped with grid spacers, HTD was encountered in all tests; some cases encountered HTD once, while others encountered HTD twice. The effect of grid spacer was significant only at the low mass flux of 515 kg m^{-2} s^{-1}.

For SCWR development and safety analysis, relevant experiments in rod bundles are needed. The objective of the current study is to investigate experimentally SCHT in vertical upflow through a rod-bundle subassembly equipped with wire-wrap spacers and grid spacers. Of particular interest in this work is to investigate whether HTD is possible in this device.

EXPERIMENTAL FACILITY AND INSTRUMENTATION

The present SCHT investigation was conducted in the Supercritical University of Ottawa Loop (SCUOL), which was constructed especially for this purpose. Heat transfer measurements in upward flow through a three-rod bundle, equipped either with wire-wrap or with grid spacers, were obtained using a sophisticated thermocouple traversing system. This section describes the test facility, its instrumentation and the test section.

The flow loop

Figure 1 shows the major components of SCUOL, while Figure 2 shows a schematic diagram of the loop. The maximum operating pressure was 10 MPa. The heat supplied to the test section was provided by a rectified DC power supply, capable of providing a maximum voltage of 60 V DC and a maximum current of 2833 A. The fluid inlet temperature to the test section was controlled by a 22 kW pre-heater. The CO_2 operating fluid was cooled in four heat exchangers connected in parallel; two of these units used centrally supplied chilled water as a secondary fluid, whereas the other two used ethylene glycol, that was circulated from a tank contained in an adjacent freezer room.

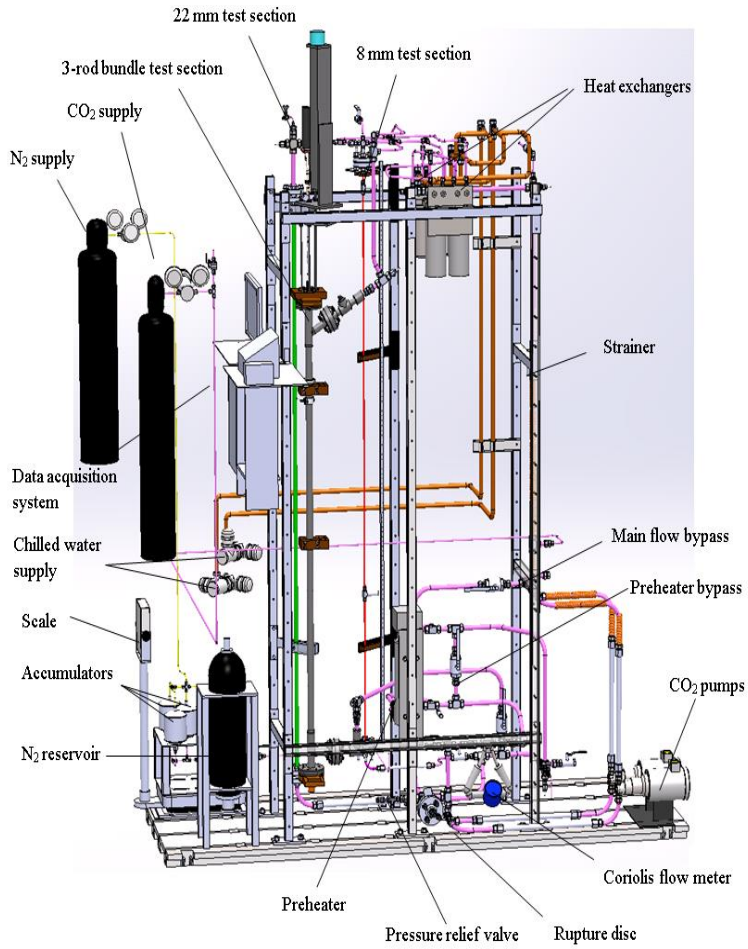

Fig. 1. University of Ottawa multi-fluid supercritical loop (Jiang, 2015).

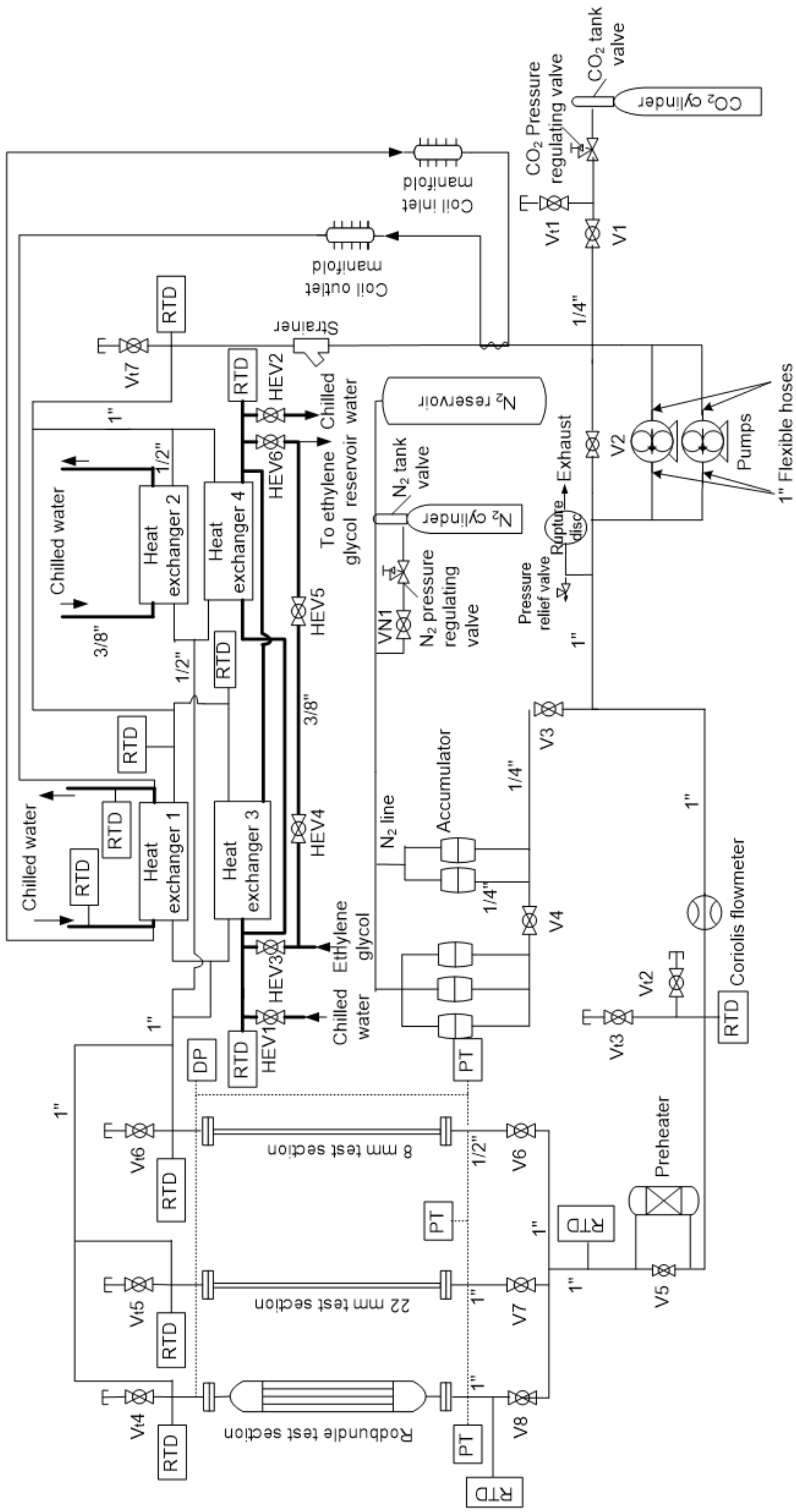

Fig. 2. Schematic diagram of the loop and its components.

Rod bundle test section

The rod bundle was mounted vertically and was cooled by pressurized CO_2 flowing upwards. The rod bundle had a total length of 2500 mm and the heated section of each rod was made of Inconel 600 tubing with an outer diameter D = 10.0 mm and a length of 1500 mm. Figure 3 shows an overall view of the rod bundle and Figure 4 shows its cross section. The three rods were identified as Rod A, Rod B and Rod C. Circumferential positions around each rod were specified such that positions at 0° were facing the exterior of the rod bundle, positions at 180° were facing the axis of the rod bundle subassembly and positions at 90° and 270° were facing the gaps with the unheated rod fillers. More details about the unheated rod fillers have been provided by Jiang (2015). The bare rod bundle hydraulic diameter was D_h = 4.08 mm. The test section and the associated piping were insulated by a 2 mm thick layer of fiberglass and a 10 mm thick layer of insulating foam. The following two rod-spacer configurations were tested.

i) In the first configuration, the rods were separated from each other by four custom-made grid spacers, each having a blockage ratio of 5.3% and spaced by 500 mm (Figures 5-a,b). For each grid spacer, three thin shims made of stainless steel and having a thickness of 0.102 mm and a width of 4 mm were spot-welded on a short piece of stainless steel T304 tubing, having a length of 12 mm, an OD of 2.9 mm, and an ID of 2.4 mm, which served to separate the three heated rods. Each shim was wrapped around one rod and spot-welded on it. The heated rods were separated from the unheated rod fillers by an extra shim, having a total length L = 76 mm, as shown in Figure 5-a.

ii) In the second configuration, the rods were separated from each other by a “wire” (actually stainless steel T304 tubing) with a diameter of 1.3 mm that was wrapped around each rod with a pitch of 200 mm (Figure 5-c). The wire wrap pitch was 200 mm, except at the first 200 mm of the heated length, where it was 100 mm. The wire was fastened to the heater rods at the start of the heated section at a 0° location (facing the pressure tube, see Figure 4). The wire wrap resulted in a decrease in local flow area of 2.2 % from the unobstructed rod-bundle cross-sectional area just upstream of the start of the heated length, where no wire wraps were present. However the flow blockage of the wires projected on a plane normal to the axis was 32 %. The wire wrap had a resistance of 1.82 Ohm/m, which is much higher than the resistance of the heated rods, which was 0.036 Ohm/m.

Sliding thermocouple assembly

A convenient feature of this apparatus is the use of a sliding thermocouple system, which measured the inside wall temperature distributions of each of the three heated rods in the bundle. Each rod contained five thermocouples, positioned at three stations that were separated axially by a distance of 480 mm; two thermocouples were placed at diametrically opposite locations at each of the two upstream stations and a single thermocouple was placed at the farthest downstream station. Each thermocouple carrier is supported by two springs pressing the tips of the thermocouples against the heated wall. Each set of five thermocouples was attached to a push rod that could be traversed along the test section as well as rotated over the full 360° range by a step motor. These three step motors were mounted on a traversing system, which was advanced by a fourth step motor and permitted all thermocouples to be traversed axially over a distance of 500 mm (Figure 5-d).

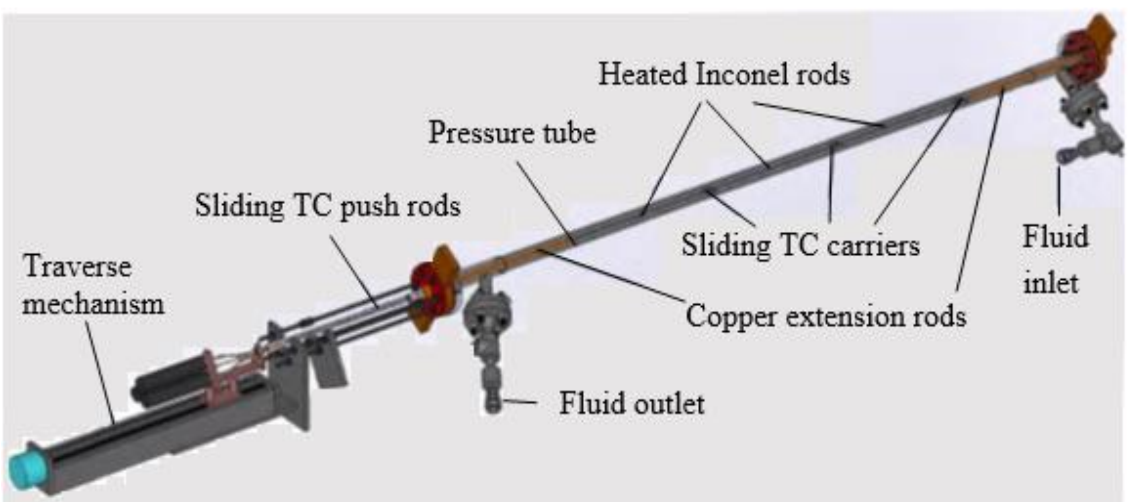

Fig. 3. Overall view of the rod bundle and the thermocouple traversing mechanism (Jiang, 2015).

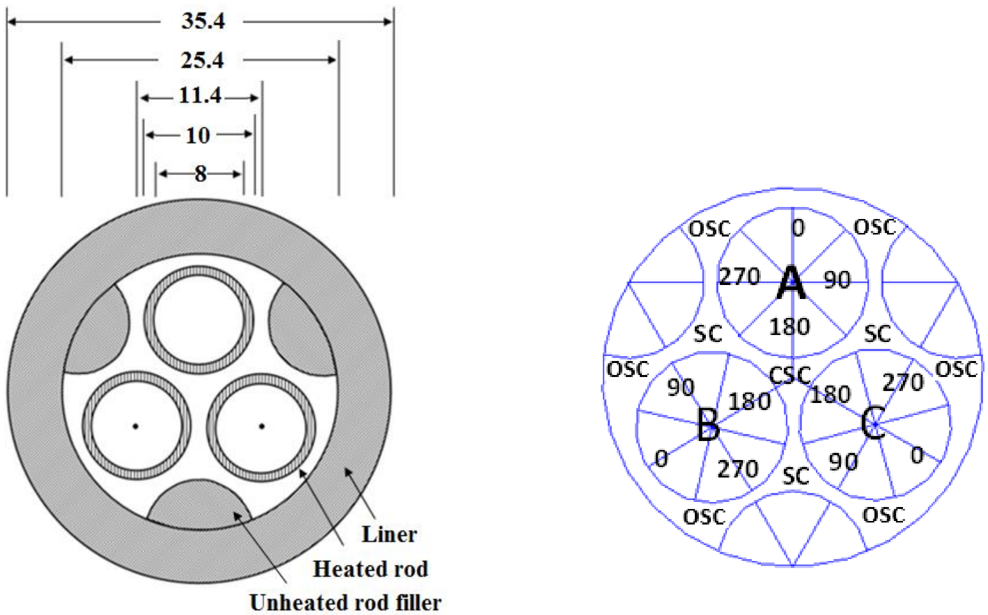

Fig. 4. Left: Cross section of the rod bundle with dimensions in mm. Right: angular coordinate systems for temperature measurements around each of the three rods, marked as A, B and C, while viewed from downstream; CSC, SC and OSC denote the central subchannel, intermediate subchannels and outer subchannels, respectively.

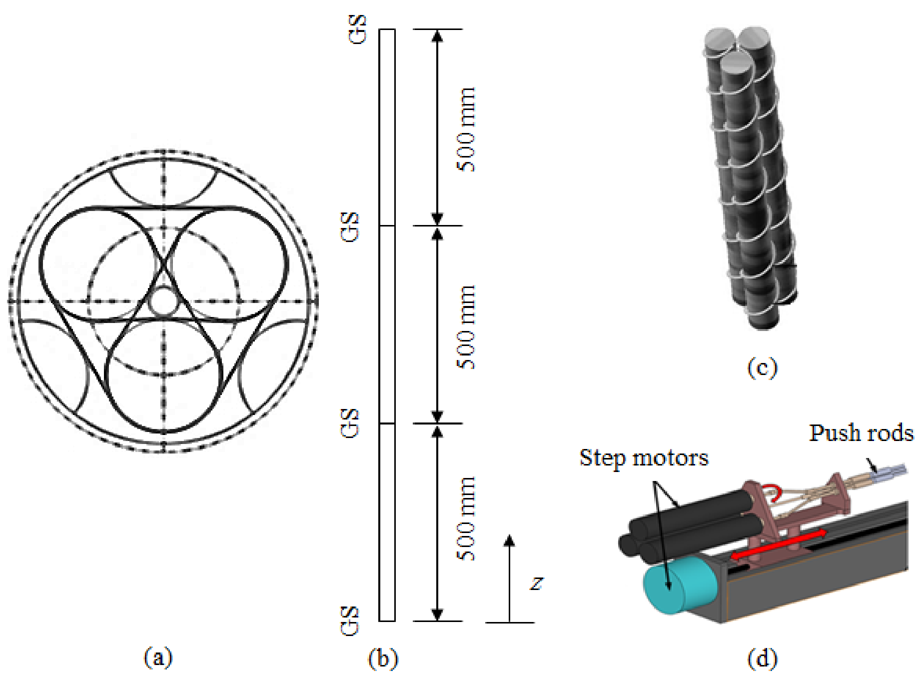

Fig. 5. (a) Cross-sections of the heated section equipped with grid spacers (GS); (b) the wire-wrapped central rod assembly; (c) thermocouple traversing system.

Instrumentation

The bulk fluid temperature at the inlet and outlet of the rod bundle, as well as temperatures at different locations of the loop, were measured with in-flow ultra-precise RTD sensors (Omega P-M-1/10-1/8-5-1/2-G-15). The range of these RTD sensors was from 0 to 100 °C and their uncertainty was (0.3 + 0.005 $|T|$) °C. J-type thermocouples were installed in the sliding thermocouple system; these thermocouples had an uncertainty of 1.0 K at the 95 % confidence level. Potentiometers were used to measure the axial and angular displacements of the thermocouples; the potentiometer measuring the axial displacement had a linearity of ±0.25% over its full moving range of 500 mm and the potentiometer measuring the angular displacement had an estimated uncertainty of 5°. The absolute pressure at the inlet of the rod bundle was measured with a pressure transducer (Rosemount, Model 3051T), having an uncertainty of 15.5 kPa. A Coriolis flow meter (Micro Motion® Elite®, Model CFM050M320N0A2E2ZZ) was used to measure the mass flow rate; this device was factory calibrated and had a specified uncertainty of 0.05 % within its full measurement range from 0 to 0.945 kg s^{-1}. The heating power was calculated from the voltage drop across the rod bundle and the electrical resistance of the test section, which was measured prior to its installation. The measured voltage drop varied from 11.9 to 21.1 V, within a measurement uncertainty of 0.1 to 0.5%.

TEST MATRIX, EXPERIMENTAL PROCEDURE AND DATA REDUCTION

Test matrix

Table 1 lists the test matrix of the tests performed with the rod bundle equipped with grid spacers and wire-wraps.

Table 1 Summary of test conditions

Rod bundle equipped with grid spacers						Rod bundle equipped with wire wraps					
P (MPa)	P/P_c (-)	G kg m^{-2} s^{-1}	T_{in} (°C)	q (kW m^{-2})	Date	P (MPa)	P/P_c (-)	G kg m^{-2} s^{-1}	T_{in} (°C)	q (kW m^{-2})	Date
7.69	1.04	200	15.0	1-50	15-06-11	7.69	1.04	200	15.0	1-50	15-01-08
8.41	1.14	714	10.9	89.9	15-06-17	8.41	1.14	711	11.0	89.9	14-02-24
						8.42	1.14	743	11.2	174.4	14-04-30
						8.37	1.13	1006	11.1	124.7	14-02-25
						8.59	1.16	1175	10.9	124.4	14-05-08
8.37	1.13	731	20.2	89.8	15-06-18	8.31	1.12	731	20.2	89.9	14-05-02
8.41	1.14	713	20.1	119.5	15-06-18	8.39	1.14	717	20.2	119.3	14-05-08
						8.35	1.13	338	11.0	84.0	14-09-26
						8.38	1.13	337	30.0	84.0	14-09-25
						8.37	1.13	334	11.0	55.9	14-09-08
						8.36	1.13	339	30.0	55.9	14-09-25
						8.36	1.13	444	11.1	109.9	14-09-09
						8.42	1.14	445	30.0	109.7	14-09-22
						8.40	1.14	442	11.1	73.3	14-09-09
						8.39	1.14	446	30.0	73.1	14-09-19
7.66	1.04	339	11.5	83.9	15-06-16	7.66	1.04	337	11.4	83.6	14-09-03
7.72	1.04	334	29.9	84.0	15-06-15	7.66	1.04	335	30.2	84.1	14-09-24
7.65	1.04	339	11.0	56.0	15-06-15	7.66	1.04	336	11.1	56.0	14-09-04
7.71	1.04	336	30.8	55.9	15-06-16	7.73	1.05	336	30.9	55.9	14-09-24
7.74	1.05	443	11.0	109.9	15-06-08	7.68	1.04	444	11.1	110.0	14-09-04
7.74	1.05	443	29.8	109.6	15-06-09	7.69	1.04	443	30.0	109.8	14-09-23
7.86	1.06	453	10.9	73.1	15-06-08	7.75	1.05	451	11.0	72.9	14-09-05
7.71	1.04	441	29.9	73.1	15-06-09	7.73	1.05	445	29.9	73.3	14-09-23
						6.58	0.89	548	20.4	65.9	14-05-13
						6.66	0.90	572	20.2	60.2	14-05-14
						6.58	0.89	548	20.4	65.9	14-08-12

Data acquisition

All pressure and temperature measurements were acquired at a rate of 10 samples/s. After the operating conditions were stabilized, measurements were recorded continuously. During recording of the results, the traversing system was programmed to reposition the thermocouples, either axially or circumferentially, every 80 s. At the beginning, some tests were investigated at an angular displacement of 30 degrees and an axial displacement of 20 mm. Because of the many measurement locations, these experiments typically lasted for 12 hrs. For this long period of time, it was hard to maintain steady operating conditions because of system limitations. Therefore, subsequent experiments were investigated at an angular displacement of 45 degrees and an axial displacement of 50 mm, which reduced the test period to 3.5 hrs and allowed us to maintain fairly steady flow conditions. During data processing, each data set was divided into blocks, each of which contained data for a different position of the thermocouple assembly. The data collected during the last 10 s of each block were found to correspond to steady conditions. Data processing was done with the use of a code written in MATLAB. Spurious values in the data were removed. The data values used in the analysis of the results represent time averages over 10 s intervals.

Thermocouple and RTD calibration check

To check the accuracy of the thermocouples, a zero-power test at a high mass flux was performed for every run. Figure 6 shows that all sliding thermocouples measured the same wall temperature within $\pm$0.1 K and were in excellent agreement with the RTDs (within 0.1 K), even at the relatively low mass flux of 502 kg m^{-2} s^{-1}.

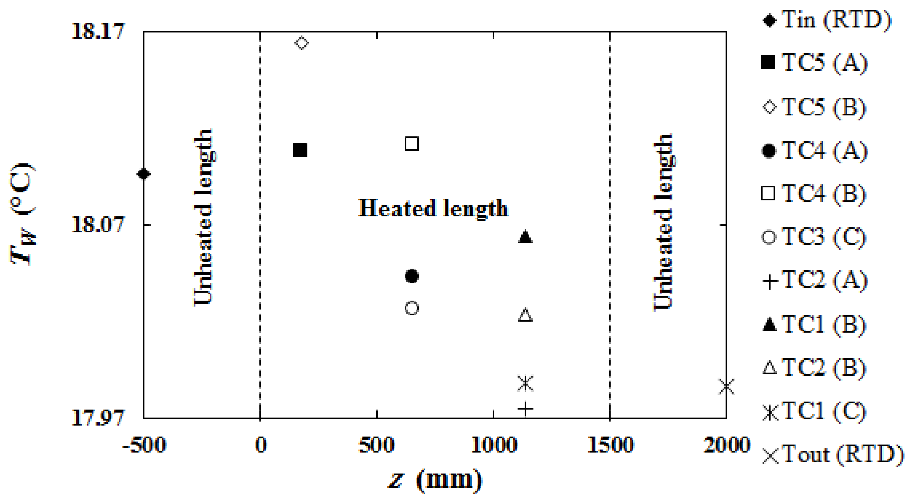

Fig. 6. Temperature readings along the unheated rod bundle; G = 548 kg m^{-2} s^{-1}.

Heat balance check

As an overall check of the accuracy of the measured flow rate, the inlet and outlet RTD measurements and the NIST code property values, we compared the electric power N supplied to the test section to the power $\dot{m}(h_{out} - h_{in})$ absorbed by the fluid. The heat balance error was calculated as

$$\Delta N(\%) = 100\frac{N - \dot{m}(h_{out} - h_{in})}{N}\% \qquad (1)$$

The specific enthalpies at the inlet h_{in} and the outlet h_{out} of the test section were calculated from the corresponding measured bulk temperatures and the measured pressure at the inlet. The heat balance error was about 3%, except for cases for which the specific bulk enthalpy at the outlet of the rod bundle was close to the pseudo-critical enthalpy, in which cases it was about 5% (Figure 7a). This is because of the strong property variation in the vicinity of the pseudo-critical enthalpy h_{pc}; here, a slight variation in the outlet temperature, due to a slight increase in q or decrease in G or due to the uncertainty of the measuring device can have a significant effect on h_{out} and consequently the heat balance error. If one assumes that the heat balance error is due to the heat loss only, a monotonic increase in heat loss with an increase in bundle wall temperature would have been expected. However, no such trend was observed in Figure 7b.

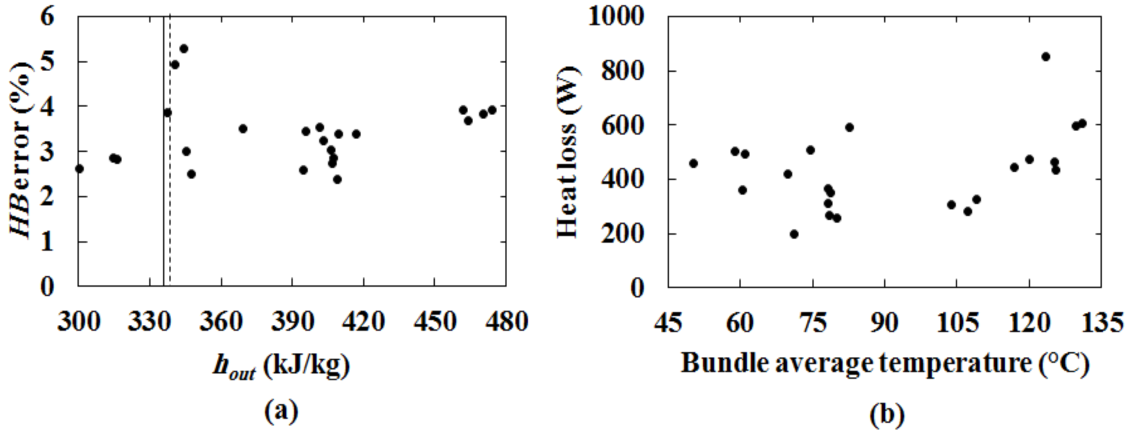

Fig. 7. (a) Percentage error in heat balance error *vs.* h_{out} (kJ kg^{-1}) and (b) Heat loss (W) vs. the bundle-average temperature (°C); solid and dotted lines indicate the pseudocritical specific enthalpies for P/P_c = 1.04 and 1.13, respectively.

Repeatability checks

We performed two types of repeatability checks, a classical one, in which we compared measurements for nominally the same test conditions at roughly the same time, and a second one, in which we compared corresponding measurements taken after a long period on inactivity or after making changes to the loop. The second type would indicate the appearance of errors in measuring devices due to instrument drift or due to changes made to the loop. Figure 8 shows an example of a test of the first type of repeatability, performed within a time interval of 3 hrs; it can be seen that the wall temperatures were in excellent agreement for the two trials. An example of the second type of test, performed with a time separation of 3 months, is shown in Figure 9; in this case as well, the measurement repeatability was excellent.

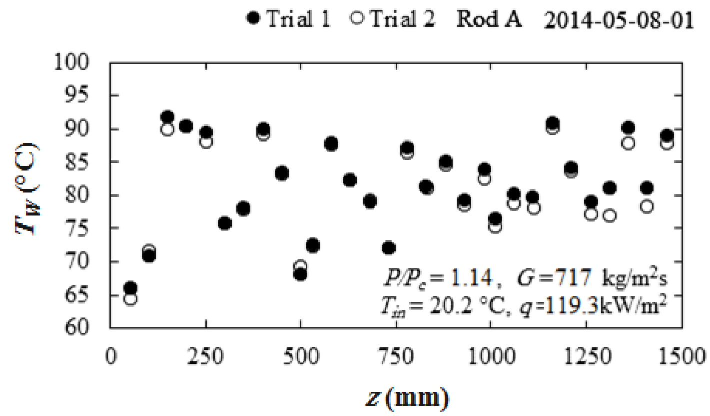

Fig. 8. Repeatability test results for 0° angle (trial 1), and 360° angle (trial 2, obtained 3 hrs later, with the thermocouple rotated by 360°).

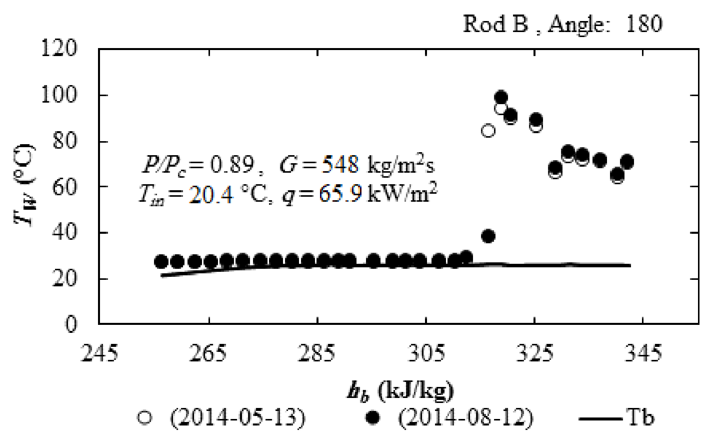

Fig. 9. Comparison of test results taken with a separation of three months.

CALCULATION OF THE ROD OUTER WALL TEMPERATURE AND THE LOCAL HEAT TRANSFER COEFFICIENT

The bulk specific enthalpy h_b at an axial location having a distance z_h from the inlet of the heated test section was calculated as

$$h_b = h_{in} + \frac{N}{\dot{m}} \frac{z}{L_h}, \tag{2}$$

where h_{in} is the specific enthalpy at the inlet, N is the measured electrical power supplied to the test section, $\dot{m}$ is the mass flow rate and L_h is the heated length. The corresponding local bulk fluid temperature T_b and the bulk thermo-physical properties of carbon dioxide for each value of h_b and a specified pressure P were calculated using NIST software (Lemonn *et al.*, 2002). Considering that the thermal resistivity coefficient of Inconel 600 is very small, one may assume that the volumetric heat generation Q for each of the three heated rods was uniform and equal to

$$Q = \frac{N}{3\pi(r_o^2 - r_i^2)L_h}, \tag{3}$$

where r_o and r_i are, respectively, the rod outer and inner radii. The nominal, or average, heat flux from each rod to the fluid was computed as

$$q = \frac{N}{6\pi L_h r_o}. \tag{4}$$

The nominal heat flux was uniform in the entire heated section, but the local heat flux to the fluid varied because of heat conduction in the rod walls as a consequence of wall temperature non-uniformity in the circumferential and axial directions. To determine the local heat transfer coefficient accurately, one would need accurate estimates of the local outer wall temperature and the local heat flux, but obtaining such estimates is a complex matter, as will be illustrated in the following.

In cylindrical coordinates r, φ, z, the heat conduction equation in the rod wall is described by the equation

$$\frac{1}{r}\frac{\partial}{\partial r}\left(r\frac{\partial T}{\partial r}\right) + \frac{1}{r^2}\frac{\partial^2 T}{\partial \varphi^2} + \frac{\partial^2 T}{\partial z^2} + \frac{Q}{k} = 0\,, \tag{5}$$

where k is the local thermal conductivity of Inconel 600, which, for convenience, may be evaluated at the local measured inner wall temperature $T_{w,i}$. This equation is subjected to two boundary conditions. First that $T(r_i, \varphi, z)$ must match the measured local $T_{w,i}$ and second that the inner wall should be adiabatic, which implies that $k\frac{\partial T}{\partial r}\,|_{r=r_i} = 0$. This equation can be easily solved numerically, but it requires specification of $T_{w,i}$ at all locations, which would require measurements with a very fine spatial resolution, as necessary for an accurate determination of second order temperature derivatives. This was unattainable in the present setup, because it would mean that each run would extend over several days, making it impossible to maintain constant operating conditions. For this reason, we adopted a simplified approach, which was deemed to be suitable for rough estimates of the local outer wall temperature and the local heat transfer coefficient, especially at locations where temperature changes were sharp, as in the vicinity of spacers.

The simplest means of calculating the outer wall temperature $T_{w,o}$ from the measured inner wall temperature $T_{w,i}$ would be to neglect circumferential and axial heat conduction through the rod wall and solve the one-dimensional (*i.e.*, radial) heat conduction equation instead of the 3D equation (5). This would give (Incropera *et al.*, 2007) the 1D estimate

$$T_{w,o}^{1D} = T_{w,i} - \frac{Qr_i^2}{2k} \ln \frac{r_i}{r_o} + (r_i^2 - r_o^2) \frac{Q}{4k} \quad . \tag{6}$$

Following this procedure, the 1D estimate of the local wall heat flux to the fluid would be uniform and equal to the nominal heat flux q and the 1D estimate of the local heat transfer coefficient would be

$$H^{1D} = \frac{q}{T_{w,o}^{1D} - T_b} \tag{7}$$

This approach, although adopted by many previous investigators, would introduce significant error at locations having strong circumferential and/or axial wall temperature variations. An alternative approach may be based on the analysis by Huang *et al.* (1996), which neglects the radial variations of the circumferential and axial temperature derivatives and solves equation (5) to estimate the local wall heat flux to the fluid as

$$q^{3D} = q + k(r_o - r_i)\left(\frac{1}{r_o r_i} \frac{\partial^2 T_{w,i}}{\partial \theta^2} + \frac{\partial^2 T_{w,i}}{\partial z^2} \right) \quad . \tag{8}$$

It must also be noted that this solution was based on the approximation $\ln \frac{r_o}{r_i} \approx \frac{r_o - r_i}{r_i}$, which, for the current ratio $\frac{r_o}{r_i} = 1.1$, introduces an error of less than 5%. Huang *et al.* (1996) compared the values of local wall heat flux calculated from equation (8) by neglecting axial conduction to exact solutions of equation (5) for a representative circumferential variation of inner wall temperature and found them to be close to each other for the diameter ratio value used presently. In view of these findings, one may be confident that equation (8) would provide a good estimate of the local wall heat flux, except possibly at locations with strong axial wall temperature variations (as would likely occur in the vicinity of spacers) and provided that inner wall temperature measurements allow for fair estimates of second order derivatives. This still leaves the task of calculating the outer wall temperature. The literature provides no approximate method for this calculation and one would need to solve equation (5), which would be impractical in the present setup because of the coarse spacing of inner wall temperature measurements. As will be demonstrated shortly by example, it was found that conduction effects can be significant for calculation of the wall heat flux and, consequently, for the heat transfer coefficient, but they are generally small for the calculation of the outer wall temperature, because of the small rod wall thickness. In turn, an error in outer wall temperature would introduce a much smaller error in the heat transfer coefficient, because of the relatively large difference between wall and bulk temperatures. For this reason, we decided to estimate the outer wall temperature by using the 1D conduction equation, having first substituted the actual volumetric heat flux by its portion that was transferred to the fluid. Thus,

$$T_{w,o}^{3D} = T_{w,i} - \frac{r_o q^{3D} r_i^2}{(r_o^2 - r_i^2)k} \ln \frac{r_i}{r_o} - \frac{r_o q^{3D}}{2k}. \tag{9}$$

Finally, the local heat transfer coefficient was estimated as

$$H^{3D} = \frac{q^{3D}}{T_{w,o}^{3D} - T_b}. \tag{10}$$

Before showing some examples of the application of the present method, it seems necessary to review its advantages and limitations. An important observation is that the error in the local heat transfer coefficient estimate would mainly depend on the error in the local wall heat flux estimate, and to a much lesser degree on the error in the outer wall temperature estimate. Another important point is that circumferential heat conduction corrections of the local wall heat flux and the local outer wall temperature would even out when averaged circumferentially. For this reason, we content that a fairly good estimate of the average HTC would be obtained as

$$H^{av} = \frac{q}{T_{w,o}^{1Dav} - T_b}. \tag{11}$$

where $T_{w,o}^{1Dav}$ is the circumferentially averaged 1D outer wall temperature. The accuracy in the H^{3D} estimate would depend mainly on the accuracy of determination of second derivatives (curvature) of inner wall temperature variations. Curvature would be most significant at local minima and maxima of $T_{w,i}$. At a $T_{w,i}$ maximum, H^{3D} would have a local minimum and the 3D correction for wall heat flux would be such as to further diminish the H^{3D} value. On the opposite, at a $T_{w,i}$ minimum, H^{3D} would have a local maximum and the 3D correction would be such as to further increase the H^{3D} value. As a result, if heat conduction had not been considered, the estimates of HTC would have been systematically distorted: minima would have been overestimated and maxima would have been underestimated, although average values may not have had significant errors. In practice, because the curvature of $T_{w,i}$ must be determined from coarsely spaced measurements, additional errors, both of precision and bias type, would be introduced. Huang *et al.* (1996) demonstrated by example that precision error in $T_{w,i}$ introduced significant scatter on the wall heat flux estimates, which would then propagate into HTC. The coarseness of $T_{w,i}$ measurements would likely result in underestimation of the curvature magnitude at maxima and minima, which means that the results would be under-corrected at such locations. Close circumferential and axial spacings (*e.g.*, 5 degrees and 10 mm, respectively) would have improved the accuracy of the estimates, but were unattainable for the reason mentioned previously.

In the present tests, we measured $T_{w,i}$ at evenly spaced circumferential and axial intervals. For a small number of early runs, the axial spacing was set to 20 mm and the circumferential spacing was set to 30 degrees. Because, however, even such runs required a relatively long time to complete, the spacings were increased to 50 mm and 45 degrees for the majority of runs. This axial spacing was not sufficient to resolve local extrema and the axial conduction correction that was based on the available data was, in general, found to be negligible. For this reason, axial conduction effects were not accounted for in our results. On the other hand, circumferential conduction effects, even when estimated from relatively coarsely spaced measurements, were found to be substantial and were accounted for to the degree that was possible.

Figure 10 shows comparisons between 1D, 2D (this means that axial conduction was neglected) and 3D estimates of the outer wall temperature and the heat transfer coefficient for a case with a rather extreme circumferential variation of measured wall temperature around one rod. The largest wall temperature correction for this case was found to be 1.1 °C, whereas the largest correction for H was 37%. The largest differences for $T_{w,o}$ and H occurred at locations at which the circumferential profile of the inner wall temperature had a strong curvature, which in most cases occurred near a minimum or a maximum of $T_{w,i}$. Near a maximum $T_{w,i}$, the 2D estimate of $T_{w,o}$ was typically larger than the 1D estimate, whereas the 2D estimate of H was smaller than the 1D estimate; the reverse was observed at locations with a maximum $T_{w,i}$. Figure 11 shows representative axial variations of the uncorrected and corrected maximum heat transfer coefficients along a wire-wrapped rod and the corresponding axial variations of the average heat transfer coefficients in the central subchannel, where H was higher than the circumferentially averaged values. These plots clearly demonstrate that the 2D estimates of the minimum H were generally lower than the 1D estimates, and, on the opposite, the 2D estimates of H in the central subchannel were in most cases higher than the 1D values. The previous discussion may serve as a warning when analyzing heat transfer data in tightly-packed (*i.e.*, with a pitch-to-diameter ratio that is lower than 1.2) rod bundles, in which temperature may change significantly in the circumferential direction. We also found that, despite the use of a sophisticated method for measuring the rod inner temperature distribution and the application of corrections for 2D conduction effects, the estimated local HTC may still be subject to appreciable errors, both of precision and bias types. Such errors would be much higher, if, instead, one had used the 1D method for evaluating the local HTC, as this method would underestimate significantly the spread in HTC around the rod circumference, which could affect adversely the accuracy of SCWR safety analyses.

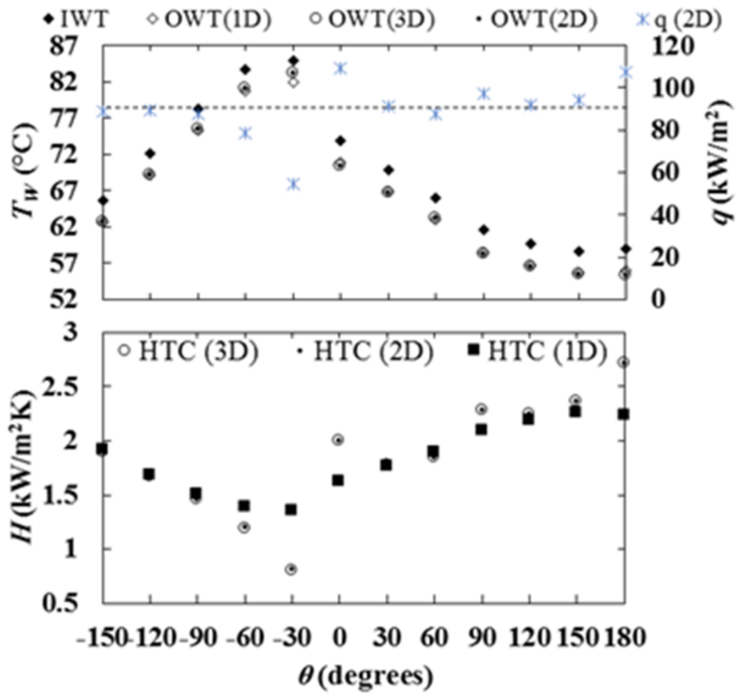

Fig. 10. Circumferential variations of the inner wall temperature (IWT), the outer wall temperature (OWT) and the heat transfer coefficient (HTC), estimated by 1D, 2D and 3D analyses; the variation of the wall heat flux estimated by a 2D analysis is also shown; these results correspond to rod C of the wire-wrapped rod bundle at z = 184 mm; P = 8.36 MPa, G = 700 kg m^{-2} s^{-1}, T_{in} = 11 °C and q = 89.9 kW m^{-2} (plotted as a dashed line); in this run, inner wall temperature was measured at circumferential increments of 30 deg and axial increments of 20 mm.

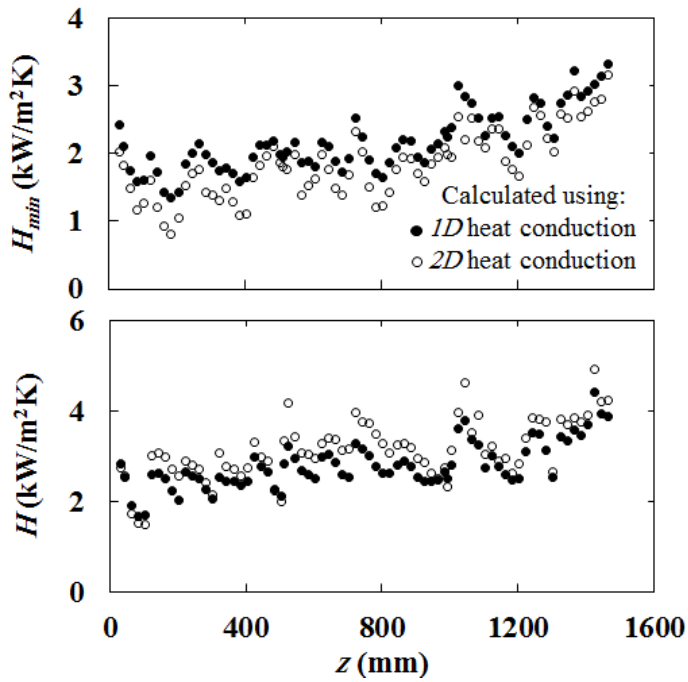

Fig. 11. Axial variation of the minimum heat transfer coefficient along the heated section (top) and the average heat transfer coefficient in the central subchannel (bottom) of a wire-wrapped rod bundle; conditions as in Figure 10.

EXPERIMENTAL RESULTS AND DISCUSSION

In this section, the results are presented graphically as plots of the outer rod wall temperature and the heat transfer coefficient against the local bulk enthalpy. In some cases, the heat transfer coefficient has also been plotted against axial location.

Axial and circumferential variations of wall temperature and heat transfer coefficient

Representative plots of the wall temperature at different circumferential and axial positions and the corresponding heat transfer coefficient along one of the three rods are presented in Figures 12 and 13. One may observe a significant spread in temperatures around the rod at each axial location and an irregular axial temperature variation. Although wall temperature and HTC variations may appear to be random to a casual view, they were actually found to be systematic and repeatable. The complexity of these variations is such, however, that it is impossible to identify their causes, or connect consistently the specific local temperature values to local geometrical features, including the local wire-wrap patterns. The only clear observation in both figures is the local enhancement of heat transfer at the grid spacers and just downstream of them. Among the factors that could affect the wall temperature and HTC variations are (i) possible imperfections in the fabrication or the materials of the device and possible local distortions from the unheated shape as the result of thermal expansion, (ii) the distance from the nearest wire-wrap location or grid spacer, (iii) the orientation of the measurement position, namely whether the thermocouple faces an open subchannel, an unheated wall, or a heated wall, (iv) the enthalpy and flow imbalances between the different types of subchannels. In addition, for certain flow conditions, HTD may have occurred in one sub-channel but not another, and this would have given rise to further increases in the temperature spread. Indeed, in some cases, the results near the entrance of the heated wire-wrapped rod bundle show evidence of local HTD in the form of a peak in wall temperature and a minimum in HTC. This was, for example, the case shown in Figure 12, for runs with a relatively small mass flux and a relatively large heat flux. In contrast, Figure 13, which shows cases at a higher mass flux and somewhat lower heat flux, bears no signs of HTD. It is noteworthy that, in this respect, results obtained with either wire-wraps or grid spacers had similar overall characteristics. Tube results under the same conditions, also shown in Figures 12 and 13, provide further evidence for HTD near the heated section entrance for the first runs and lack of HTD for the second runs. The important lesson we learned from these observations is that one may not exclude the presence of HTD in wire-wrapped rod bundles under some conditions, in contradiction to some statements in the literature. The issue of HTD will be discussed in more detail in a later section.

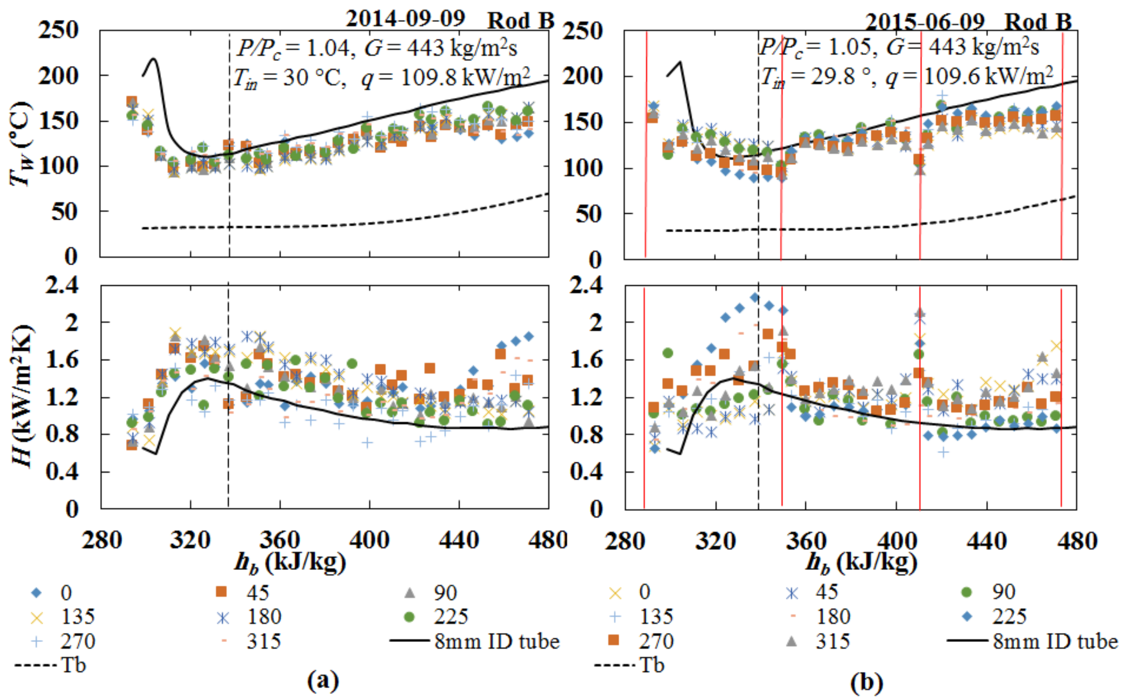

Fig. 12. Wall temperature and heat transfer coefficient at various circumferential positions along rod B of the rod bundle equipped with (a) wire-wraps and (b) grid spacers; dashed vertical lines represent the pseudo-critical enthalpy (h_{pc}) and red vertical lines mark grid spacer locations.

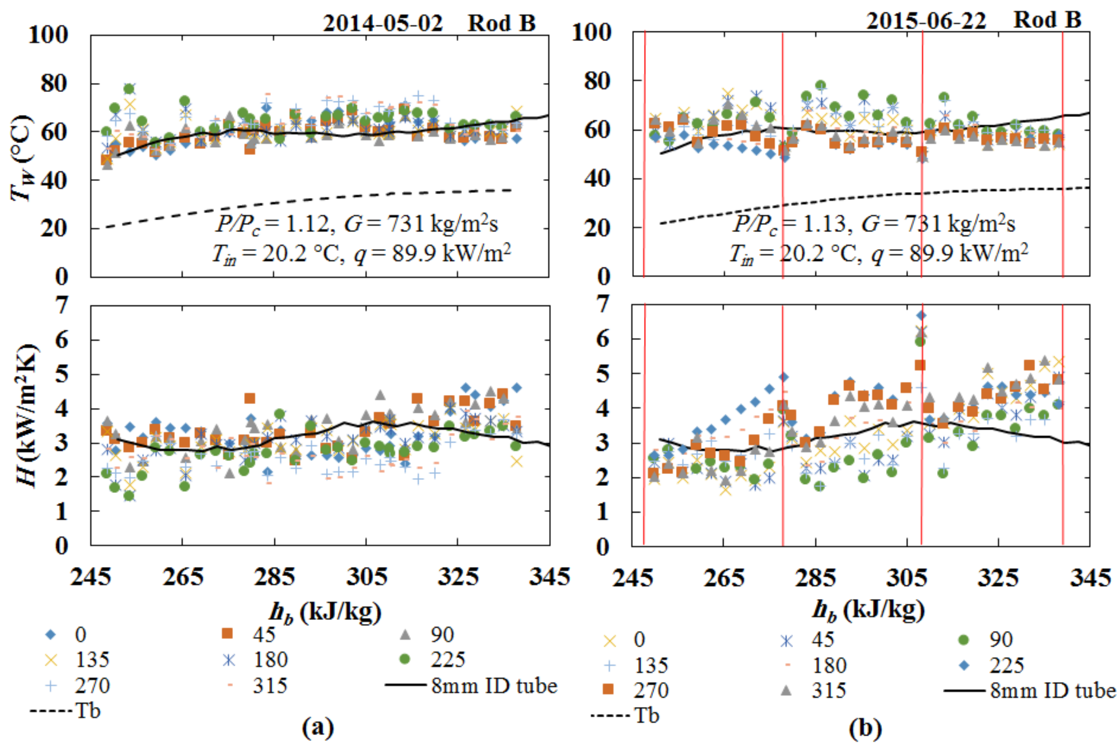

Fig. 13. Wall temperature and heat transfer coefficient vs. bulk enthalpy at different circumferential positions along Rod B of the rod bundle equipped with (a) wire-wraps and (b) grid spacers; red vertical lines mark grid spacer locations.

Parametric trends of maximum wall temperature and minimum HTC

In this section, we present representative axial profiles of the maximum wall temperature T_{max} and the corresponding minimum heat transfer coefficient H_{min}, as these properties are of primary concern in nuclear safety analysis. In particular, we examine the dependence of these extremes upon the values of the imposed heat flux, mass flux, pressure, inlet temperature and spacer type. We present mostly measurements obtained for the wire-wrapped bundle, but note that corresponding data for the bundle equipped with grid spacers showed similar effects.

Heat flux effect: Figure 14 shows the axial variations of T_{max} and H_{min} for four representative pairs of runs; each pair had the same pressure, mass flux and inlet temperature but two different heat fluxes. Note that H_{min} generally decreased with increasing heat flux, but this dependence was much weaker than the dependence of T_{max} on heat flux. For example, in one case an increment of 100 % in heat flux corresponded to a decrement of H_{min} by 35%. A comparison between the measurements and the corresponding predictions of Jackson's correlation (Jackson, 2011) is shown in Figure 15. Although this correlation was based on bare-tube data, it predicted approximately the observed trends of the heat flux effect on the rod-bundle wall temperature and heat transfer coefficient. The predicted heat transfer coefficients were roughly 25 to 150% higher than the experimental values.

Mass flux effect: The effects of mass flux on T_{max} and H_{min} for nearly constant pressure, inlet temperature and heat flux are shown in Figure 16 for the fairly wide mass flux range from 440 to 1175 kg m^{-2} s^{-1}. As expected, a decrease in mass flux resulted in an increase in wall temperature and a decrease in HTC. The overall decrease of 62% in mass flux caused a decrease of H_{min} by 75%. These results do not show any clear evidence of HTD, although it seems possible that some mild form of HTD may have occurred near the inlet of the heated section at the lowest considered mass flux.

Pressure effect: Figure 17 shows a comparison of T_{max} and H_{min} for P/P_c = 1.04 and P/P_c = 1.13. It appears that the pressure value within this SC range had little effect on these two parameters. In addition, one can see that the corresponding data points for the two pressures nearly coincided, which provides further proof that the variation of wall temperature was systematic and repeatable.

Inlet temperature effect: The effect of inlet temperature on T_{max} and H_{min} for the same values of other flow conditions is shown in Figure 18. For the range of 10 - 30 C° no significant effect was observed, thus providing support for using h_b as the main independent parameter affecting the wall temperature and heat transfer coefficient.

Effect of type of rod spacer: Figure 19 shows axial profiles of T_w and H_{min} in the rod bundle equipped with wire-wrap spacers (WR) and grid spacers (GS). It is evident that the spread in H_{min} was greater for the GS bundle than for the WR bundle, which indicates that wire-wrapping was more effective in mixing the flow in the entire rod bundle. Both the lowest and the highest values of H_{min} occurred in the GS bundle, with the latter appearing at the locations of the spacers and shortly downstream of them. The grid spacer effect is discussed and analyzed in more detail later in this paper.

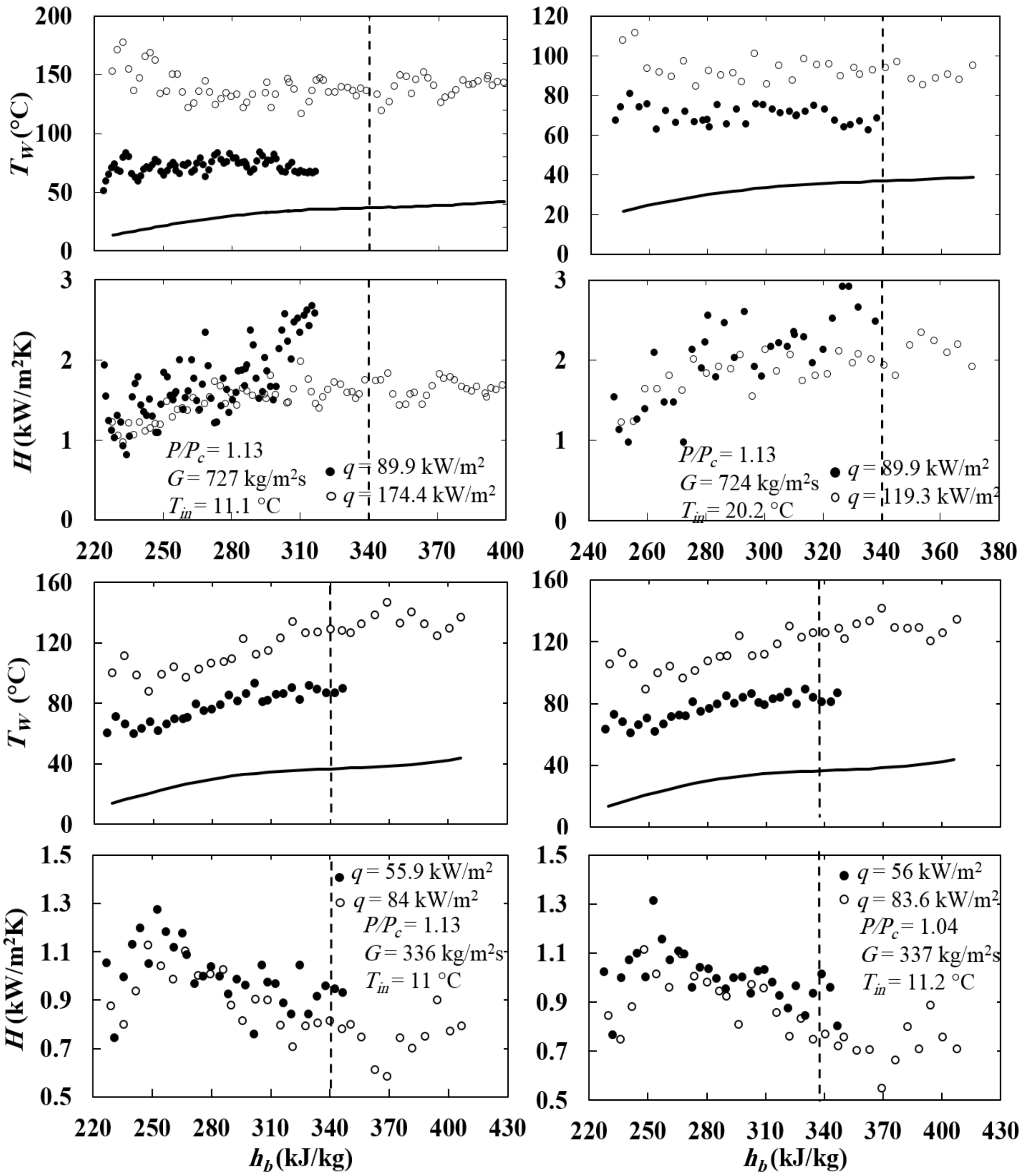

Fig. 14. Effect of heat flux on the maximum wall temperature and the minimum heat transfer coefficient for the wire-wrapped rod bundle.

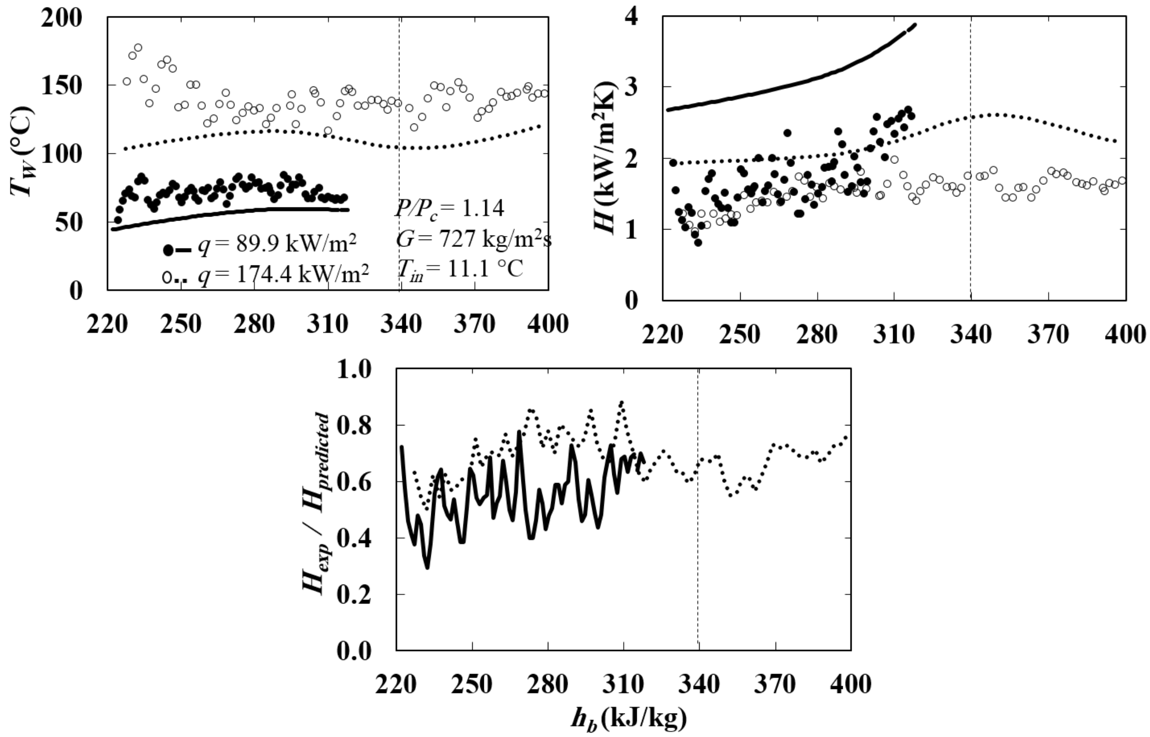

Fig. 15. Maximum wall temperature and minimum heat transfer coefficient (circles), together with predictions of Jackson's correlation (solid and dotted lines) against bulk enthalpy for the wire-wrapped rod bundle; dashed vertical lines indicate the pseudocritical specific enthalpy.

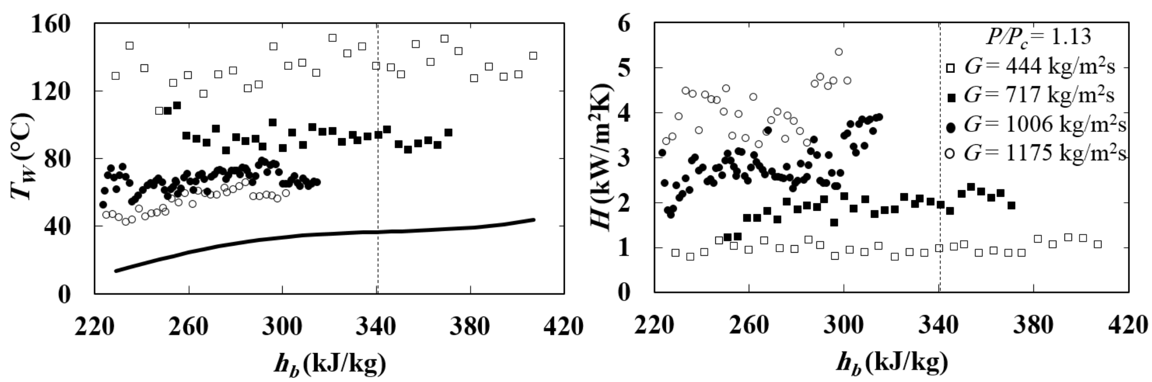

Fig. 16. Effect of mass flux on the maximum wall temperature and the minimum heat transfer coefficient for the wire-wrapped rod bundle; the four sets of conditions were as follows: i) G = 444 kg m^{-2} s^{-1}, q =109.9 kW m^{-2} and T_{in} =11.1 °C; ii) G = 717 kg m^{-2} s^{-1}, q =119.3 kW m^{-2} and T_{in} =20.2 °C; iii) G = 1006 kg m^{-2} s^{-1}, q = 124.6 kW m^{-2} and T_{in} = 11.1°C; iv) G = 1175 kg m^{-2} s^{-1}, q=124.6 kW m^{-2} and T_{in} =11.1 °C.

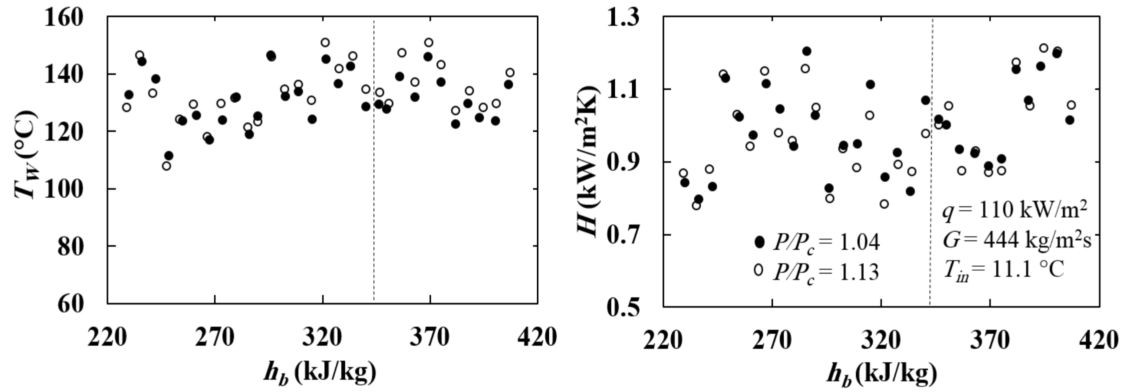

Fig. 17. Effect of pressure on the maximum wall temperature and the minimum heat transfer coefficient for the wire-wrapped rod bundle.

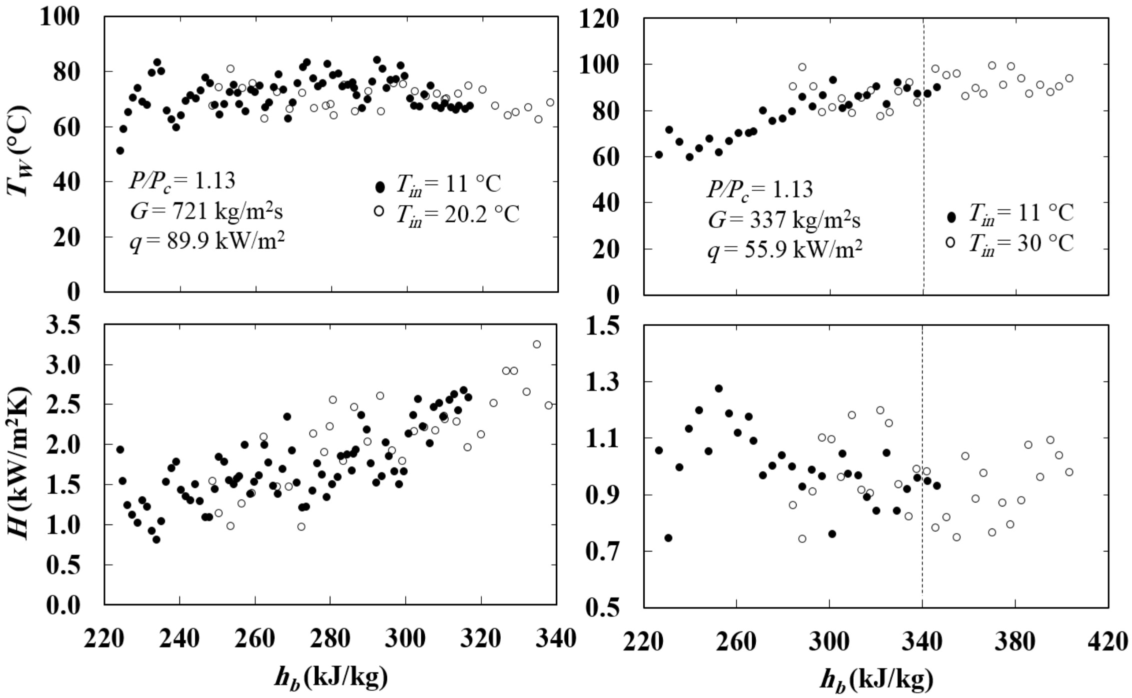

Fig. 18. Effect of inlet temperature on the maximum wall temperature and the minimum heat transfer coefficient for the wire-wrapped rod bundle.

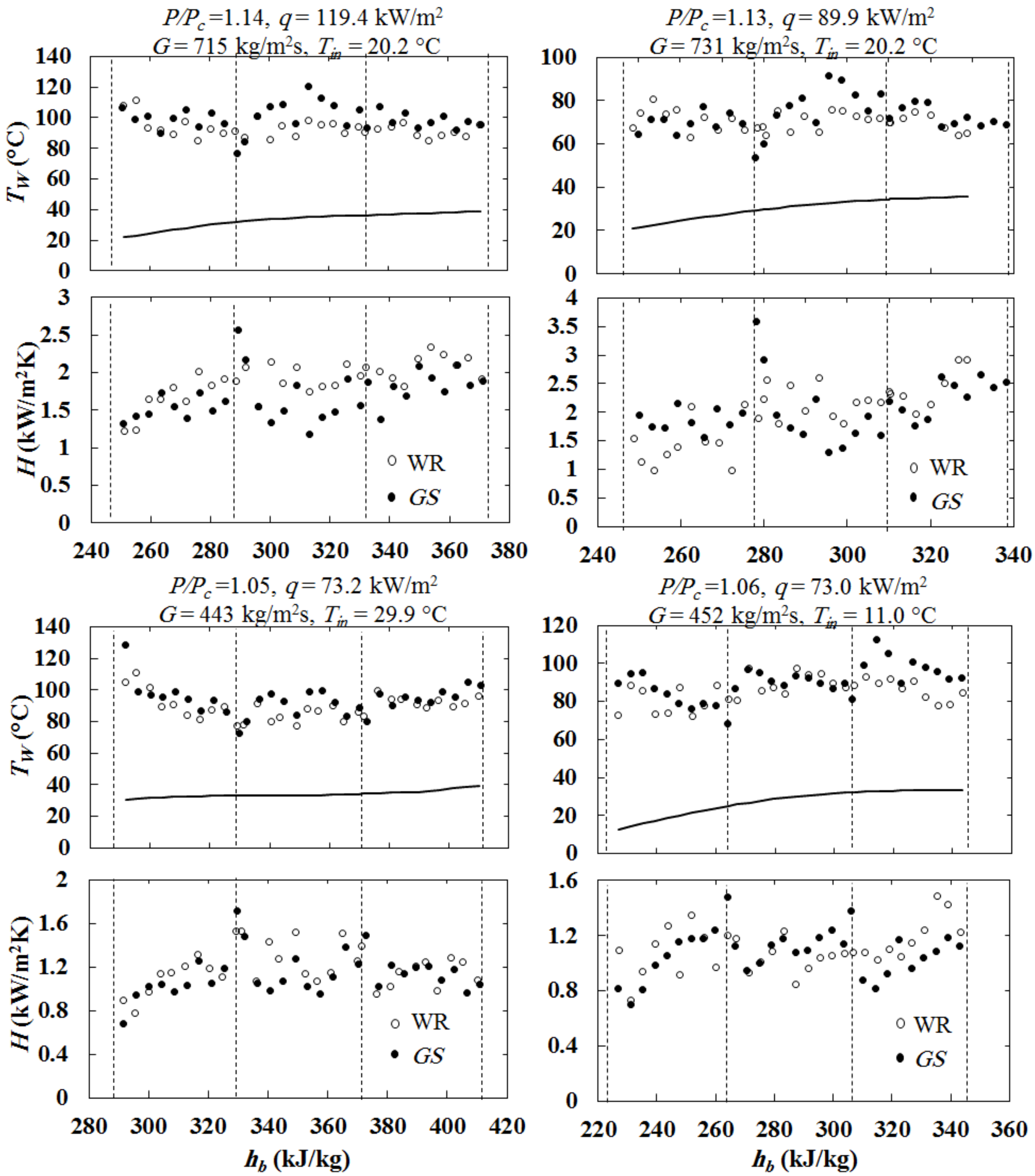

Fig. 19. Effect of spacer type on the maximum wall temperature and the minimum heat transfer coefficient; dashed vertical lines indicate the grid spacer locations.

Normal heat transfer in the rod bundle and comparison with tube measurements and predictions of a correlation

In this section, we are concerned only with cases having normal heat transfer in the rod bundle equipped with either type of spacers, as well as in the 8 mm tube that was used as a reference. We examined results within the full range of mass fluxes (G = 200 to 1175 kg m^{-2} s^{-1}) and, for each mass flux, we selected cases for which the heat flux was sufficiently low for the heat transfer to show no signs of deterioration. Representative measurements of the wall temperature and the corresponding heat transfer coefficient are presented in Figure 20, together with predictions of Jackson's correlation for supercritical normal heat transfer in tubes. Because our tests with grid spacers (GS) in place were more limited in scope than tests with wire-wraps (WR), some plots are missing GS results. Moreover, in view of the strong circumferential variation of wall temperature in the rod bundle, we considered the average wall temperature in the central subchannel (CSC) formed by the three rods, rather than local values.

For very rough purposes, one may assert that the results in the two rod bundles and the tube, as well as the predictions, show similar trends and that differences among the corresponding values are relatively small or moderate. The most notable differences may be observed for the lowest mass flux (G = 200 kg m^{-2} s^{-1}), in which case the HTC in the WR bundle was clearly higher than that in the GS bundle and the HTC in the tube was significantly lower than the two others. Based on this observation, one may conclude that grid spacers act as to enhance normal heat transfer at low mass fluxes and that wire-wraps are more efficient in this respect than grid spacers. At moderate mass fluxes (G = 713 kg m^{-2} s^{-1}), all results fell within the experimental scatter and so one may conclude that spacers had a small effect on normal heat transfer in this range. Surprisingly, however, at the higher mass fluxes (G = 1006 and 1175 kg m^{-2} s^{-1})[2], the HTC in the tube was measurably higher than that in the WR bundle and the difference seems to increase

[2] The reason why the tube has a higher HTC than the bundle at high mass flows is not clear but it may be related to variations in bulk temperatures. Figure 20 is based on the central subchannel (CSC) which has the largest heated perimeter and hence is the hottest subchannel of our geometry. So, using the cross-sectional average bulk temperature will under-estimate the fluid temperature in the CSC and thus under-estimate the true CSC HTC.

with increasing mass flux. This reversal agrees with the observations of Miller *et al.* (2013) and Tanase and Groeneveld (2015) that heat transfer enhancement by obstructions was diminished at higher mass fluxes; Eq. 8 of Miller *et al.* (2013) in fact quantifies this diminishing heat transfer enhancement effect at higher mass fluxes. This observation may act as caution against the intuitive presumption that heat transfer in rod bundles with spacers would always be stronger than that in tubes. Another surprising observation is that the HTC predicted by Jackson's correlation was in very good agreement with the WR measurements, although it deviated from the tube results. In view of the fact that this correlation was based on tube data, themselves subjected to large scatter, we consider the level of its agreement with the rod bundle data as rather fortuitous.

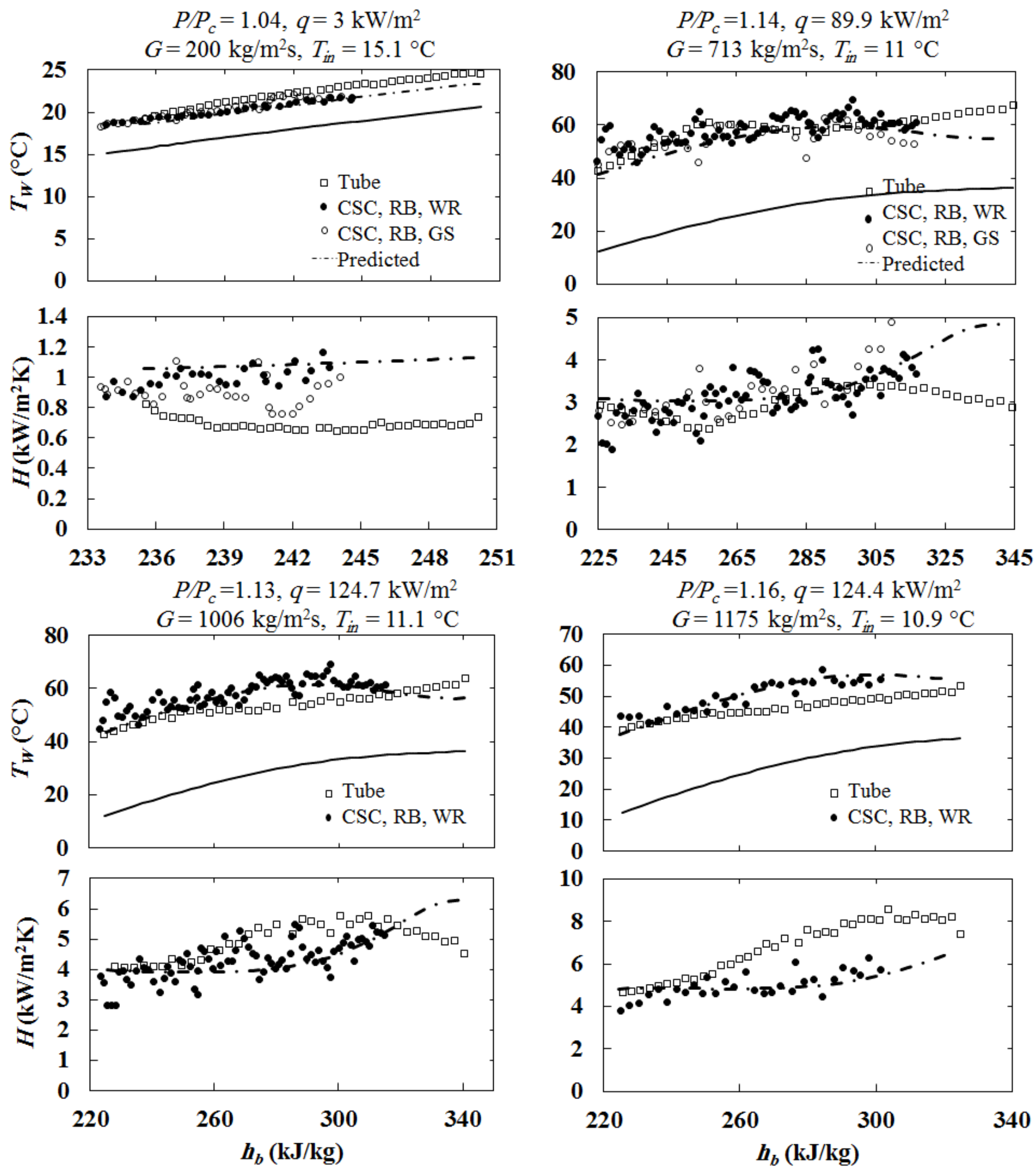

Fig. 20. Comparisons of wall temperatures and heat transfer coefficients at normal heat transfer conditions in the central subchannel (CSC) of the rod bundle equipped with wire-wraps (WR) or grid spacers (GS) and in a 8 mm ID bare tube; predictions of Jackson's correlation are also shown in the plots (dotted lines), solid lines represent the bulk temperature.

Heat transfer deterioration in the rod-bundle

Although a significant volume of data under presumably HTD conditions have been published over several decades, this phenomenon lacks a clear definition and its occurrence, even for flows in circular tubes, remains largely unpredictable. A plausible explanation is that HTD is caused by buoyancy and acceleration effects (Jackson, 2011). Pioro and Duffey (2007) reviewed SCHT in channels having flow obstructions and speculated that HTD is unlikely to occur in rod bundles equipped with spacers. This conjecture was supported by the work of Mori *et al.* (2012), who did not observe any HTD in a spacer-equipped bundle at SC conditions. In contrast, Richards *et al.* (2013) showed that HTD occurred in a grid-spacer-equipped seven-rod bundle at SC pressures. As already shown in Figure 12, HTD was observed to occur under certain conditions near the inlet of the heated section of the present rod bundle equipped with either wire-wraps or grid spacers, as well as in a tube. In these cases, the onset of HTD was demonstrated by a peak in wall temperature, or, equivalently, by a significant local decrease in HTC. The issue of HTD in the present rod bundle will be discussed in more detail in this section. As for the normal heat transfer, HTD plots will present the average wall temperature in the central subchannel.

First, let us examine the onset of HTD for cases with the lowest considered mass flux (G = 200 kg m^{-2} s^{-1}), which is most likely for HTD to occur at relatively low heat fluxes. Figure 21 shows comparisons between measurements in the rod bundle equipped with the two types of spacers and the tube. The only significant difference among the conditions applying to the four shown plots is the heat flux, which was gradually increased. At the lowest heat flux of q = 3 kW m^{-2}, heat transfer was normal in all cases, although the HTC for the tube was visibly lower than those in either rod bundle. An increase to q = 5.1 kW m^{-2} triggered HTD in the tube, as indicated by a peak in wall temperature near the inlet; heat transfer in both rod bundles remained normal. Further increase to q = 7.2 kW m^{-2} resulted in HTD in the GS bundle, but not in the WR bundle. Finally, at q = 12.4 kW m^{-2}, all three test sections contained HTD regions near their inlets. These observations demonstrate that, as in tubes, heat transfer in rod bundles at low mass fluxes deteriorates when the heat flux exceeds a certain threshold. The level of this threshold is apparently higher for wire-wraps than for the present low K-factor grid spacers. The HTC in the WR bundle under normal heat transfer conditions was in all cases in good agreement with predictions of Jackson's correlation, which was, nevertheless, unable to predict the onset of HTD.

Additional evidence for the occurrence of HTD near the inlet of the rod bundle for mass fluxes in the range from 334 to 740 kg m^{-2} s^{-1} is presented in Figure 22. The two cases with relatively high inlet temperature, which have been included in this figure, are qualitatively compatible with cases having low inlet temperature and indicate that HTD occurred under wide ranges of conditions. The results presented in this figure also demonstrate that the change of spacers from one type to the other had a rather small effect on the heat transfer, except at locations near the grid spacers. Measurements in the 8 mm tube under the same conditions showed similar trends, but also made it clear that heat transfer in the tube was less efficient than in the rod bundle and that the difference increased with decreasing mass flux. Inspection of our measurements in both rod bundles and the tube at mass fluxes higher than 1000 kg m^{-2} s^{-1} did not identify any cases with HTD, but it must be noted that it was not in the scope of this work to assert conclusively whether or not HTD could be induced at high flow rates.

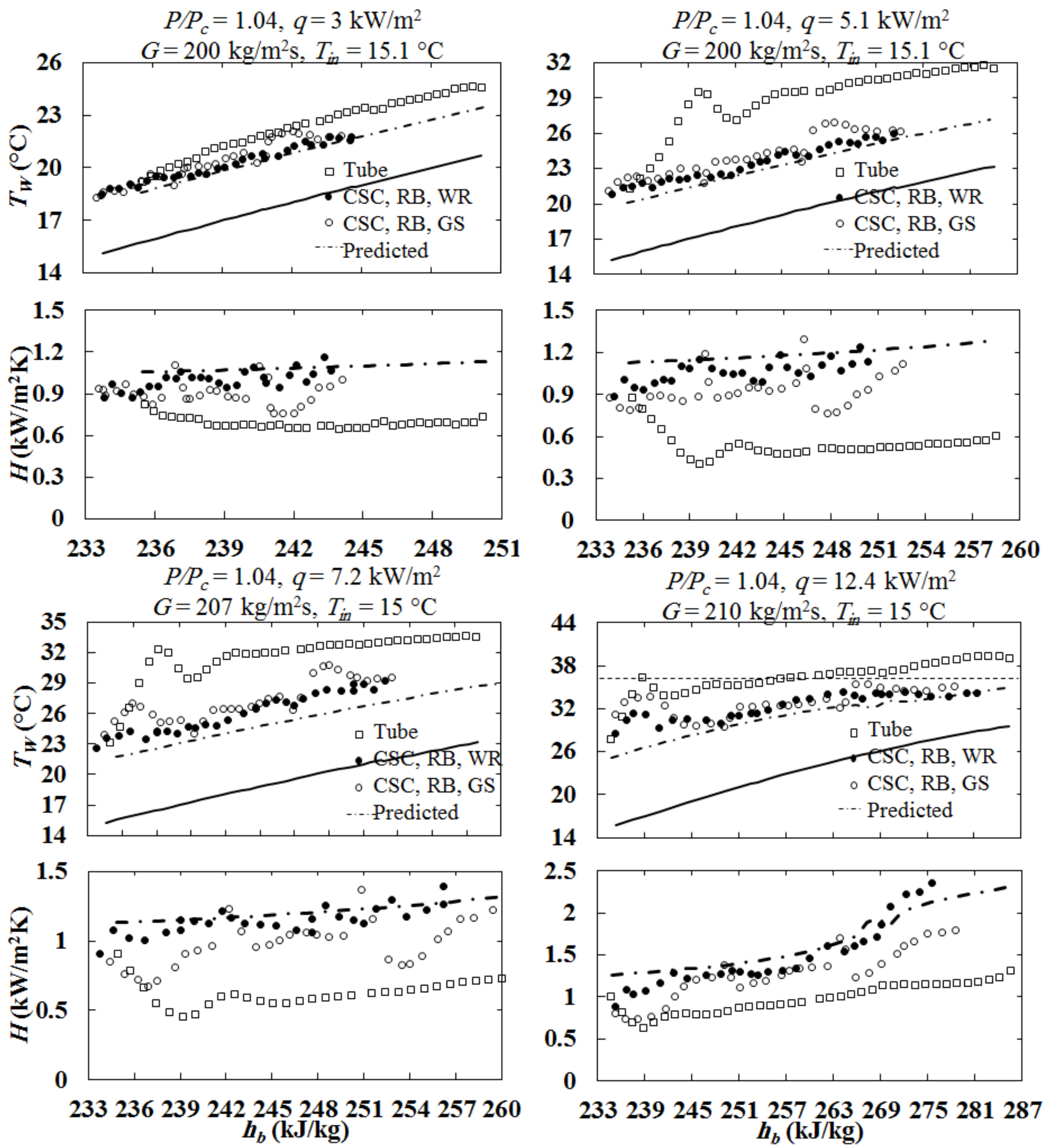

Fig. 21. Onset of heat transfer deterioration in a flow with a low mass flux (G = 200 kg m^{-2} s^{-1}); WR and GS refer to rod bundles with wire wraps and grid spacers, respectively; predictions of Jackson's correlation are also shown in the plots (dotted lines), solid lines represent the bulk temperature.

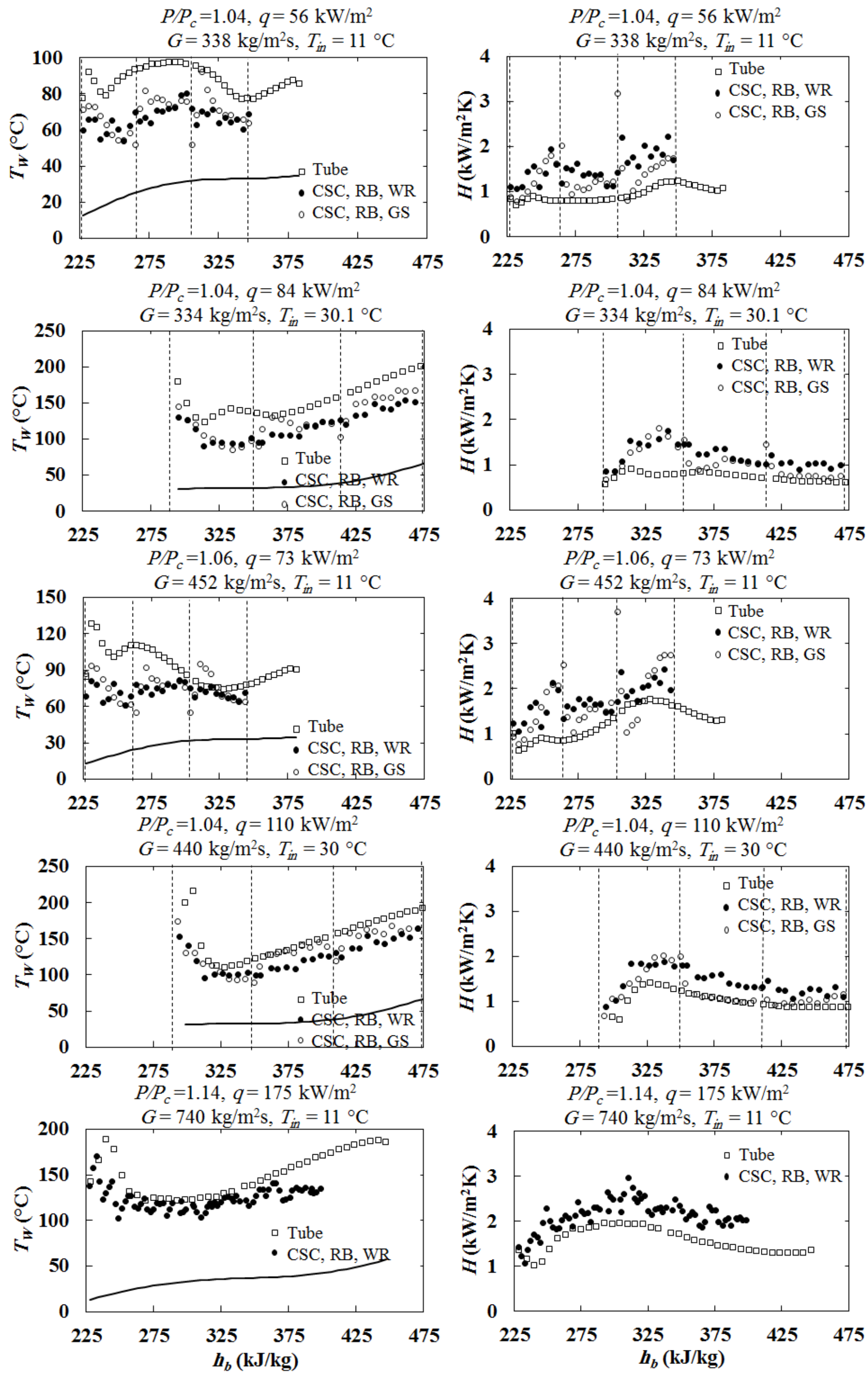

Fig. 22. Evidence for heat transfer deterioration in the central subchannel of the rod bundle equipped with two types of spacers; measurements in a tube are also presented; vertical lines mark the grid spacer locations.

Effects of grid spacers and wire-wraps on wall temperature and heat transfer coefficient

To illustrate the effect of grid spacers on the local heat transfer in the rod bundle, Figure 23 shows representative variations of wall temperature and HTC along one of the rods at two circumferential positions: one facing the central subchannel (180 deg) and another in the gap with another rod (135 deg). The first observation from this figure is that the differences between values at these two circumferential locations were not very significant, which implies that the spacers were effective in mixing the flow at least in the core of the rod bundle. The patterns of axial temperature variation were similar for the three spacers. A wall temperature minimum appeared at the spacer location; this was followed by a rapid temperature increase to a local maximum at a downstream distance of very roughly 10*D* (*D* is the rod diameter), beyond which the temperature decreased gradually and settled at approximately 30 to 40*D* downstream of the spacer. The local extrema at the spacers would be subjected to larger uncertainty than values elsewhere, because of (i) significant axial heat conduction corresponding to the sharp axial temperature gradient, (ii) distortion of the electric current at the points of contact between the rods and spacer material, and (iii) additional heat dissipation due to heat conduction to the spacer. Therefore, the wall temperature and HTC values at the spacers should be considered for qualitative purposes rather than quantitative ones. The decaying trend in HTC with distance downstream of the spacer is only noticeable over the typical distance of 10*D*, which is much shorter than distances observed in other SCHT experiments (typically 30 to 70*D*, see Eter *et al.*, 2013). This can be partially explained by the very small blockage ratio (only 5.3%) of the present spacers. The decaying trend is qualitatively similar to the exponentially decaying trend of sub-critical heat transfer correlations for bundles equipped with spacers (Yao *et al.*, 1982; Miller *et al*., 2013); it is noted, however, that such correlations predicted corrections in the local Nusselt number closely downstream of spacers that were two or more orders of magnitude smaller than the present observations. A peculiar pattern of decreasing temperature following the post-spacer maximum may be noticed for all three spacers at the particular conditions of Figure 23. This pattern was at its strongest downstream of the last spacer, where the specific enthalpy crossed its pseudo-critical value of about 315 kJ kg^{-1};

this may be attributed to an improvement in heat transfer due to the drastic change of thermophysical properties in the pseudo-critical region.

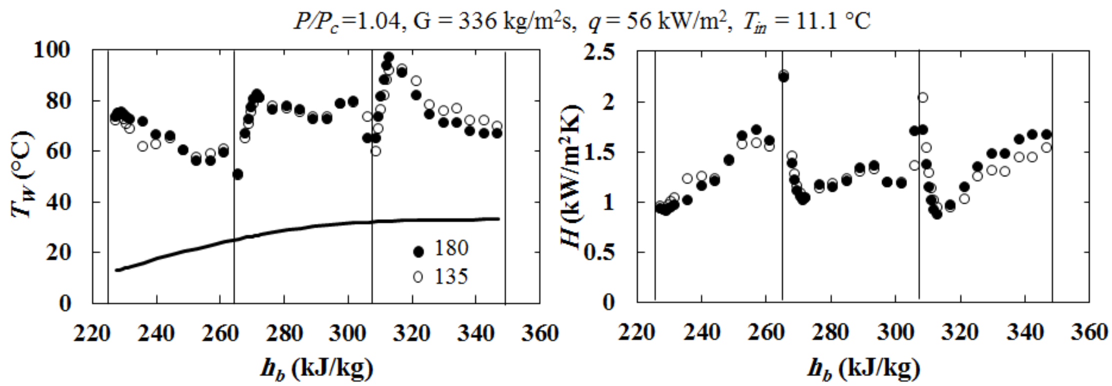

Fig. 23. Axial variations of wall temperature and local heat transfer coefficient along a rod at circumferential locations facing the axis of the rod-bundle subassembly (180° angle) and a gap between two heated rods (135° angle); grid spacer locations are indicated by solid lines.

To help visualize the effect of the wire-wrap spacers on the local heat transfer, Figure 24 shows the axial variations of the measured three-rod-average wall temperature and HTC at 180° (facing the axis of the central subchannel). These variations are quite complex, but, when all runs are considered together, a pattern appears to emerge with frequent mild minima in wall temperature and corresponding local maxima in HTC at the locations of the wire-wraps, which had a pitch of 200 mm (as mentioned previously, the pitch was shorter in the first 200 mm of the heated lengths of the rods). A direct comparison of the effects of grid spacers and wire-wraps on wall temperature and heat transfer is shown in Figure 25. The rather mild, if any, local increase in local heat transfer caused by the wire-wraps, by comparison to the sharp increase by grid spacers, is not surprising in view of the facts that (i) wire-wraps deflected the flow by the small angle of 9° and were not placed normal to the flow like the grid spacers; (ii) the wire-wrap pitch was much shorter than the grid spacer pitch (200 mm *vs*. 500 mm), and so the wire-wrap effect was distributed more evenly along the rod bundle; and (iii) heat transfer on each rod was affected by wire-wraps on adjacent rods, unlike heat transfer in the grid-spacer geometry, in which the obstruction was placed at the same location for all rods. All these effects tended to even out any large changes in HTC along the heated length of the wire-wrapped rod bundle.

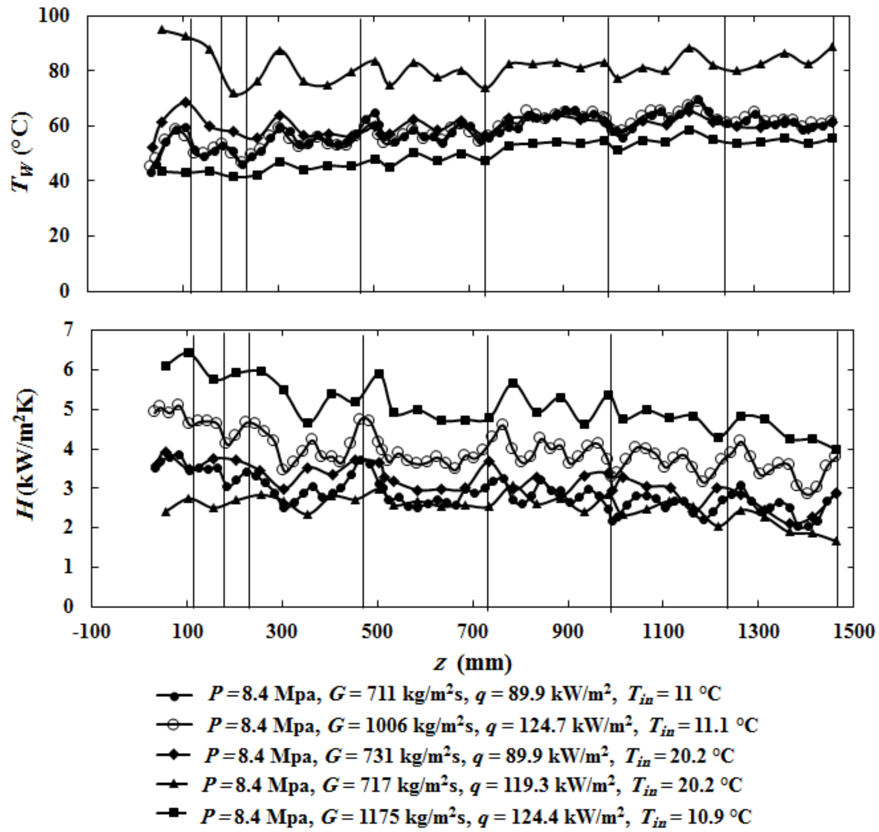

Fig. 24. Axial variation of the three-rod average wall temperature and heat transfer coefficient at circumferential locations facing the center of the three-rod bundle subassembly (180° angles); wire-wrap locations are indicated by solid vertical lines.

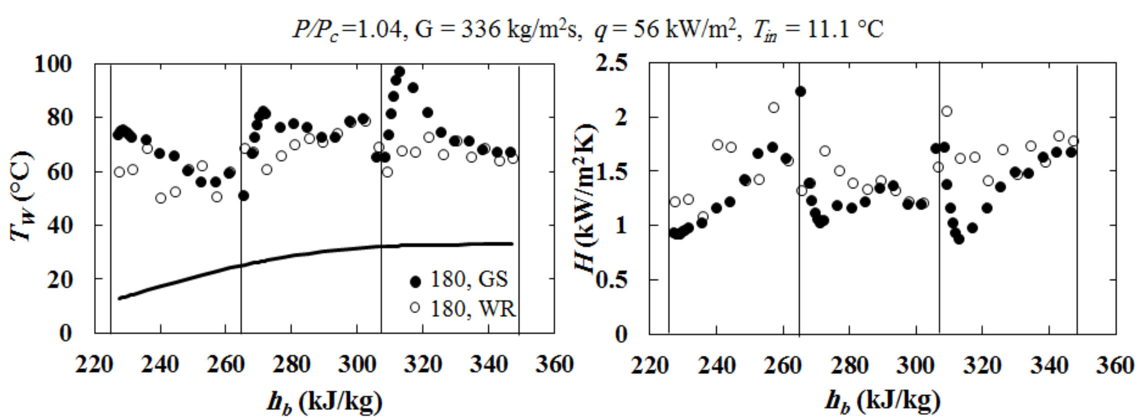

Fig. 25. Comparison between wire-wrap and grid spacer effects on wall temperature and HTC at circumferential locations facing the axis of the rod-bundle subassembly (angle of 180°); grid spacers locations are indicated by solid lines.

CONCLUSIONS

Our comparative study of heat transfer at supercritical pressures in a three-rod bundle equipped with either wire-wrap spacers or low-blockage-ratio grid spacers has led to the following main conclusions.

1. The circumferential and axial variations of wall temperature were quite complex but systematic and reproducible. It was shown that some of these measurements were subjected to significant uncertainty, and corrections were applied to the measurements to compensate for the effects of circumferential heat conduction in the heated wall.
2. Heat transfer deterioration appears to have occurred for mass fluxes in the approximate range between 200 and 700 kg m^{-2} s^{-1} near the start of the heated section of the rod bundle equipped with either type of spacers as well as in a circular tube under the same flow and heating conditions. The onset of deterioration occurred at a higher heat flux for the wire-wrapped bundle than for the one with grid spacers, and at the lowest heat flux for the tube.
3. For rough purposes, normal heat transfer in either of the rod bundles behaved similarly to the one in the tube and was also compatible with the predictions of the correlation of Jackson. Overall, hear transfer was somewhat better in the wire-wrapped bundle than in the one with grid spacers. For low mass fluxes (roughly 200 and 400 kg m^{-2} s^{-1}), normal heat transfer in the rod bundles was stronger than in the tube; for an intermediate mass flux (700 kg m^{-2} s^{-1}), heat transfer in all three cases had comparable strengths; rather surprisingly, at higher mass fluxes (100 and 1200 kg m^{-2} s^{-1}), heat transfer in the tube appeared to be more efficient than in the rod bundles.
4. The minimum super critical heat transfer coefficient decreased somewhat with increasing heat flux (35% reduction as a result of a 100% increase in heat flux) and decreased strongly at a low mass flux (75% reduction as a result of 62% decrease in mass flux). The effects of pressure and inlet temperature were weak.
5. The grid spacers introduced a strong local enhancement, but their effects disappeared only about 10 rod diameters downstream.

ACKNOWLEDGMENT

This project is part of the Canadian Gen-IV National Program. Funding for this program was provided by Natural Resources Canada through the Office of Energy Research and Development, Atomic Energy of Canada Limited, and Natural Sciences and Engineering Research Council of Canada.

NOMENCLATURE

D	rod diameter, mm
D_h	hydraulic diameter of the rod bundle, mm
G	mass flux, kg m^{-2} s^{-1}
H	heat transfer coefficient, kW m^{-2} K^{-1}
H_{av}	circumferentially averaged heat transfer coefficient, kW m^{-2} K^{-1}
H_{min}	minimum heat transfer coefficient at an axial location, kW m^{-2} K^{-1}
h	specific enthalpy, kJ kg^{-1}
h_b	bulk specific enthalpy, kJ kg^{-1}
h_{in}	specific enthalpy at inlet, kJ kg^{-1}
h_{out}	specific enthalpy at outlet, kJ kg^{-1}
h_{pc}	pseudo-critical specific enthalpy, kJ kg^{-1}
k	thermal conductivity, kW m^{-1} K
L	length of grid spacer material
L_h	heated length, mm
$\dot{m}$	mass flow rate, kg s^{-1}
P	pressure, MPa
P_c	critical pressure, MPa
Q	volumetric heat generation, kW m^{-3}
Q_e	electric power to the test section, kW
q	heat flux, kW m^{-2}
q^{3D}	heat flux, kW m^{-2}
r_i	rod outer radius, mm
r_o	rod inner radius, mm

T_b	bulk temperature, °C
T	temperature, °C
T_{in}	test section inlet temperature, °C
T_{max}	maximum wall temperature across an axial location, °C
$T_{w,o}$	outer wall temperature, °C
$T_{w,o}^{1D}$	outer wall temperature, estimated by 1D analysis, °C
$T_{w,o}^{3D}$	outer wall temperature, estimated by 3D analysis, °C
$T_{w,o}^{1Dav}$	circumferentially averaged outer wall temperature, estimated by 1D analysis, °C
$T_{w,i}$	measured rod inner wall temperature, °C
t	rod wall thickness, mm
z	axial distance, mm
z_h	axial distance from the start of the heated section, mm
φ	angular coordinate, deg

REFERENCES

Chandra, L., Lycklama, J.A., Dirk, C.V., Roelofs, F., 2009. CFD analysis on the influence of wire wrap spacers on heat transfer at supercritical conditions. Proc. 4^{th} Intern. Symp. On Supercritical Water-Cooled Reactors, ISSCWR-4, Heidelberg, Germany, March 8-11, 2009.

Dyadyakin, B.V., Popov, A.S., 1977. Heat transfer and thermal resistance of tight seven-rod bundle, cooled with water flow at supercritical pressures. Trans. VTI (11), 244–253 (in Russian).

Eter, A., Groeneveld, D., Tavoularis, S., Onder, N., 2013. Heat transfer enhancement at supercritical pressures. Proc. 12th International Conference on CANDU Fuel, September 15-18, Kingston, Ontario, Canada.

Gu, H.Y., Li, H.B., Hu, Z.X., Liu, D., Zhao, M., 2015. Heat transfer to supercritical water in a 2 X 2 rod bundle. Annals of Nuclear Energy. 83,114–124.

Huang, X.C., Cheng, S.C., Groeneveld, D.C., Rudzinski, K.F., 1996. Analysis of the conjugation effect during convective flow film boiling in an eccentric annular test section. Nucl. Eng. Des. 163, 177-190.

Incropera, F.P., DeWitt, D.P., Bergman, T.L., Lavine, A.S., 2007. Fundamentals of Heat and Mass Transfer, 6th ed., John Wiley and Sons, Hoboken, USA.

Jackson, J.D., 2011. A model of developing mixed convection heat transfer in vertical tubes to fluids at supercritical pressure. Proc. 5th International Symposium on Supercritical Water-Cooled Reactors, ISSCWR-5, Vancouver, Canada, March 13-16, 2011.

Jiang, K., 2015. An experimental facility for studying heat transfer in supercritical fluids. M.A.Sc. Thesis, Department of Mechanical Engineering, University of Ottawa, Ottawa, Canada.

Miller, D.J., Cheung, F.B., Bajorek, S.M., 2013. On the development of a grid-enhanced single-phase convective heat transfer correlation. Nucl. Eng. Des. 264, 56-60.

Mori, H., Kaida, T., Ohno, M., Yoshida, S., Hamamoto, Y., 2012. Heat transfer to a supercritical pressure fluid flowing in sub-bundle channels. Nucl. Sci. Technol. 49, 373–383.

Pioro, I. L., Duffey, R.B., 2007. Heat Transfer and Hydraulic Resistance at Supercritical Pressures in Power-Engineering Applications. ASME Press, New York, USA.

Richards, G., Harvel, G.D., Pioro, I.L., Shelegov, A.S., Kirillov, P.L., 2013. Heat transfer profiles of a vertical, bare, 7-element bundle cooled with supercritical Freon R-12. Nucl. Eng. Des. 264, 246-256.

Silin, V.A., Voznesensky, V.A., Afrov, A.M., 1993. The light water integral reactor with natural circulation of the coolant at supercritical pressure B-500 SKDI. Nucl. Eng. Des. 144, 327–336.

Tanase, A., Groeneveld, D.C., 2015. An experimental investigation on the effects of flow obstacles on single phase heat transfer. Nucl. Eng. Des. 288, 195-207.

Wang, H., Qincheng B., Linchuan W., Haicai L., Laurence K.H., 2014. Experimental investigation of heat transfer from a 2 × 2 rod bundle to supercritical pressure water. Nucl. Eng. Des. 275, 205–218.

Yao, S.C., Hochreiter, W.J., Leech, W.J., 1982. Heat transfer augmentation in rod bundles near grid spacers. J. Heat Transfer. 104, 76-81.

Chapter 5

Convective heat transfer in supercritical flows of CO_2 in tubes with and without flow obstacles

This chapter addresses the obstacles effects on supercritical heat transfer in an 8 mm ID tube at supercritical pressures. The results are presented in the form of a manuscript that has been submitted for publication.

> Eter, A., Groeneveld, D., Tavoularis, S., 2016. Convective heat transfer in supercritical flows of CO_2 in tubes with and without flow Obstacles. Under review by Nucl. Eng. Des.

This paper presents a new database of CO_2 heat transfer measurements at low, moderate and high mass fluxes, and supercritical pressures obtained in an 8 mm ID tube with and without flow obstructions. At low flows and low heat fluxes HTD-like phenomena were observed near the start of the heated length at supercritical pressure (in the liquid-like phase). This new data set has improved our understanding of the various heat transfer modes at supercritical pressures and the effect of flow obstructions on these heat transfer modes. These data can be used to improve fluid-to-fluid scaling methods or enhance the accuracy of available correlations to predict the heat transfer. Some of the novel observations described in this paper are (i) mass flux has insignificant effect on SCHT at HTD conditions and the same bulk enthalpy, and (ii) spacers can trigger heat transfer deterioration (HTD) under certain conditions.

Convective Heat Transfer in Supercritical Flows of CO_2 in Tubes with and without Flow Obstacles

Ahmad Eter
Doctoral Student
Department of Mechanical Engineering
University of Ottawa
Ottawa, ON, Canada K1N 6N5
Aeter@uottawa.ca

Dé Groeneveld
Adjunct Professor
Department of Mechanical Engineering
University of Ottawa
Ottawa, ON, Canada K1N 6N5

Stavros Tavoularis[3]
Professor
Department of Mechanical Engineering
University of Ottawa
Ottawa, ON, Canada K1N 6N5
stavros.tavoularis@uottawa.ca

[3] Corresponding author Tel.: 613 562 5800 ext. 6271

ABSTRACT

Heat transfer measurements to CO_2-cooled tubes with and without flow obstacles at supercritical pressures were obtained at the University of Ottawa's supercritical pressure test facility. The effects of obstacle geometry (obstacle pitch, obstacle shape, flow blockage) on the wall temperature and heat transfer coefficient were investigated. Tests were performed for vertical upward flow in a directly heated 8 mm ID tube for a pressure range from 7.69 to 8.36 MPa, a mass flux range from 200 to 1184 kg m^{-2} s^{-1}, and a heat flux range from 1 to 175 kW m^{-2}. The results are presented graphically in plots of wall temperature and heat transfer coefficient *vs.* bulk specific enthalpy of the fluid. The effects of flow parameters and flow obstacle geometry on supercritical heat transfer for both normal and deteriorated heat transfer are discussed. A comparison of the measurements with leading prediction methods for supercritical heat transfer in bare tubes and for spacer effects is also presented. The optimum increase in heat transfer coefficient was found to be for blunt obstacles, having a large flow blockage, and a short obstacle pitch.

Keywords:
Convective heat transfer
Supercritical pressure
Experimental data
Carbon dioxide
Heat transfer deterioration
Obstacles

1. INTRODUCTION

The supercritical heat transfer (SCHT) mode has distinct characteristics not present at subcritical pressures. When the fluid pressure and temperature are near their critical values, or when the pressure is supercritical and the fluid temperature is near its pseudo-critical value, small changes in temperature can cause large changes in the thermo-physical properties, and the heat transfer may undergo enhancement or deterioration. Of particular importance in the safety analysis of the super-critical water reactor (SCWR) is the phenomenon of heat transfer deterioration (HTD), during which the supercritical (SC) heat transfer coefficient (HTC) drops below the value that would be expected during normal forced convective heat transfer, thus resulting in a rise in surface temperature. Peaks in wall temperature have been encountered closely downstream of the beginning of the heated length and this has been attributed to heat transfer degradation associated with the development of the thermal boundary layer (Pioro and Duffey, 2007). Peaks in wall temperature have also been encountered within the developed thermal boundary layer and this may be attributed to buoyancy effects in mixed convection flow (Fewster and Jackson, 2004). Investigations of heat transfer to supercritical fluids using CO_2 as a modeling fluid have been performed by several research groups, because, compared to SC water, CO_2 has lower critical pressure (7.4 MPa *vs.* 22.1 MPa) and temperature (31°C *vs.* 374 °C) and lower power requirements. Many researchers, including Jackson (2008), Zwolinski *et al.* (2011), Cheng *et al.* (2011) and Zahlan *et al.* (2015) have developed fluid-to-fluid scaling laws based on the similarity in the thermalhydraulic behaviours of water and CO_2 at supercritical pressures. Supercritical heat transfer in fuel channels is affected by the presence of flow obstructions, such as spacer grids in rod bundles. Eter *et al.* (2013) reviewed the literature of the spacer effect on SCHT. They found that flow obstructions generally enhance heat transfer and that the highest heat transfer enhancement (sometimes exceeding 100%) occurred when the coolant temperature was near its pseudo-critical value. Significant heat transfer enhancement was found to occur downstream of grid spacers in upflow; in downflow, however, the effect of grid spacers on heat transfer was less pronounced and was sometimes absent altogether (Mori *et al.*, 2012). Predictions of spacer effects on supercritical heat transfer using CFD codes were found to be in fair agreement with experimental observations for normal heat transfer conditions, but were deemed to be of questionable accuracy for HTD conditions.

The present experimental investigation is a continuation of the experimental program at the University of Ottawa, following the article by Zahlan et al. (2015b) on CO_2-cooled directly heated tubes. Whereas that investigation was primarily designed to provide supplementary data for a trans-critical multi-fluid look-up table (Zahlan et al., 2015a) for heat transfer coefficients, the present study was designed to investigate systematically the effects of flow obstructions on supercritical heat transfer. The results of this investigation fill the present gap in our knowledge concerning supercritical heat transfer downstream of obstructions and can be used for assessing the thermalhydraulic impact of fuel bundle spacers in SCWRs.

2. EXPERIMENTAL FACILITY AND INSTRUMENTATION

The present SCHT investigation was conducted in the University of Ottawa Supercritical CO_2 loop (SCUOL). This section describes the test facility, its instrumentation and the test section configurations.

2.1 Test facility

Figure 1 shows the major components of SCUOL. The maximum operating pressure is 10 MPa. The heat supplied to the test section was provided by a rectified DC power supply having a maximum voltage of 60 V DC and a maximum current of 2833 A. The main power supply draws power from the university's AC power grid (380 V, 60 Hz, 3-phase) and provides a rectified current with a frequency of 360 Hz, which is sufficiently high to maintain a steady heating of the test section. Four parallel cables were used to transmit the current across the test section; power loss due to heating of the cables was kept at acceptable levels. The fluid inlet temperature to the test section was controlled by a 22 kW pre-heater. Cooling of the loop was achieved by passing the operating fluid through four heat exchangers connected in parallel; two of these units used centrally supplied chilled water as a secondary fluid, whereas the other two used ethylene glycol, that was circulated from a tank contained in a freezer room. More details have been provided by Jiang (2015).

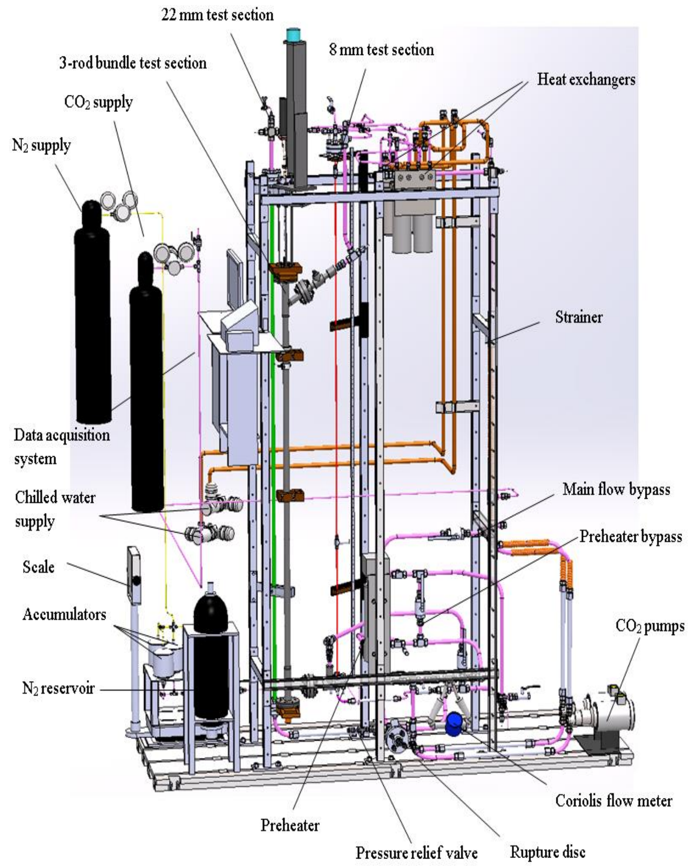

Figure 1: 3-D view of University of Ottawa CO_2 supercritical loop (Jiang, 2015).

2.2 Test section

All measurements presented in this paper were collected using a directly heated Inconel-600 tubular test section, mounted vertically with CO_2 flowing upwards. The test section had an internal diameter D = 8 mm, a wall thickness of 1 mm and a heated length L_h = 1940 mm. The heated part of the tube was preceded by an unheated section with a length of 890 mm, which ensured that the flow entering the heated section was fully developed. The test section was insulated thermally by layers of fiberglass cloth tape, with a thickness of 8 mm, surrounded by a rubber-foam insulation tube with a thickness of 50 mm. In order to study the flow obstacle effect on heat transfer, blunt or rounded cylindrical obstacles with a diameter of 4 mm (25% blockage ratio) and a length of 10 mm were inserted inside the test section. Subsequently, the effect of blockage ratio was investigated by using a blunt obstacle having a smaller diameter of 2.9 mm (13% blockage ratio). Because the blockage was located asymmetrically, the effect of circumferential blockage location on SCHT was also investigated. Figure 2 shows a schematic diagram of the test section with the locations of the thermocouples as well as cross sections of the test section with the main dimensions, definitions of azimuthal coordinates and an obstacle kept in place by a movable magnet. Note that the obstacles were located at 180° and the wall thermocouples at 0°. Table 1 specifies the pertinent geometric details and axial positions of the flow obstructions for the six different configurations that were tested.

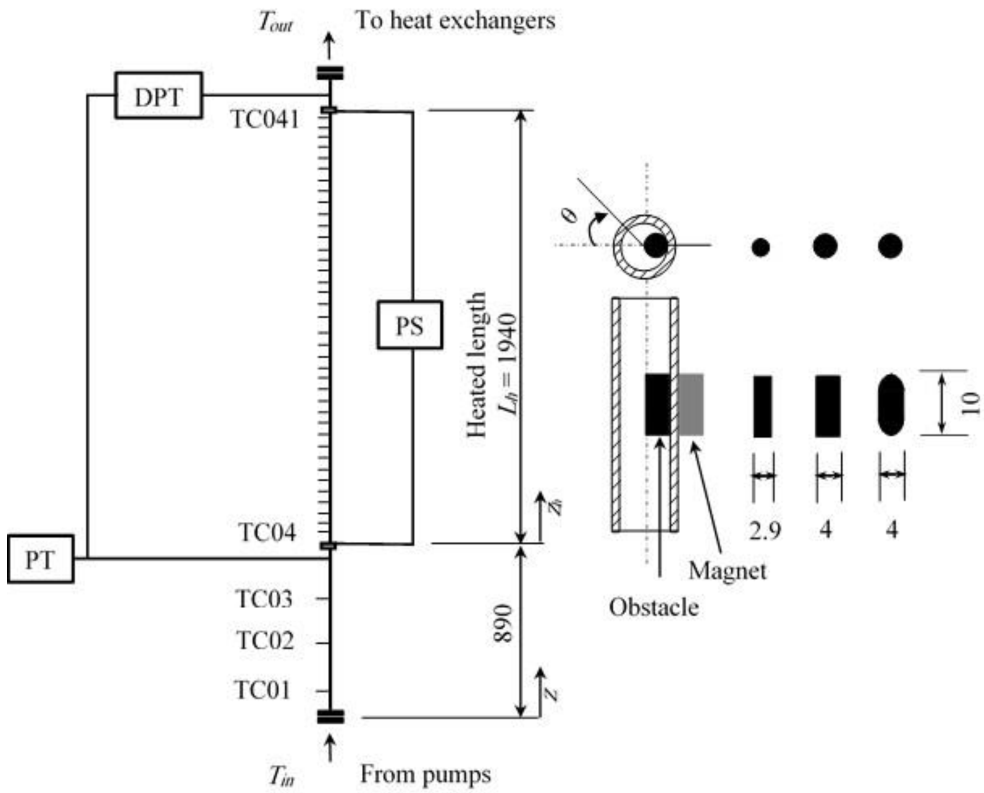

Figure 2: LHS: Schematic diagram of the 8 mm test section showing the locations of thermocouples; PS: power supply; PT: pressure transducer; DPT: differential pressure transducer; RHS: details of the obstacles and their locations; all dimensions shown are in mm.

Table 1: Obstacle-equipped tube configurations

<table>
<tr><th rowspan="2">Configuration</th><th rowspan="2">Obstacle shape</th><th rowspan="2">Obstacle blockage ratio (%)</th><th rowspan="2">Number of obstacles</th><th colspan="2">Distance of downstream end of obstacle from the inlet[1] (mm)</th><th rowspan="2">Obstacle pitch (mm)</th></tr>
<tr><th>First</th><th>Last</th></tr>
<tr><td>1</td><td rowspan="4">Blunt</td><td rowspan="4">25</td><td>1</td><td>935</td><td>---</td><td>0</td></tr>
<tr><td>2</td><td>2</td><td>935</td><td>1935</td><td>1000</td></tr>
<tr><td>3</td><td>2</td><td>935</td><td>1435</td><td>500</td></tr>
<tr><td>4</td><td>8</td><td>935</td><td>2685</td><td>250</td></tr>
<tr><td>5</td><td>Rounded</td><td>25</td><td>2</td><td>935</td><td>1435</td><td>500</td></tr>
<tr><td>6</td><td>Blunt</td><td>13</td><td>8</td><td>935</td><td>2685</td><td>250</td></tr>
</table>

[1]Heating started at 890 mm.

2.3 Instrumentation

The temperature variation along the test section wall was measured with T-type (Copper-Constantan) thermocouples (Omega SA1XL-T-SRTC), having an uncertainty of 0.5 K (this and other reported uncertainties correspond to a 95% confidence level) and a time constant of less than 0.15 s. 41 thermocouples were attached to the exterior wall of the test section (38 on the heated section and 3 on the unheated section) using a silicone-based adhesive, which has a temperature rating of 260˚C. The thermocouples were attached to the exterior wall of the test section using a silicone-based adhesive, which has a temperature rating of 260˚C. The bulk fluid temperatures at the inlet and outlet of the test sections and at other locations of the loop were measured with ultra-precise immersion RTD sensors (Omega P-M-1/10-1/8-5-1/2-G-15), having a maximum uncertainty of 0.1˚C between 0 and 100˚C. The test section inlet pressure was measured by a pressure transducer (Omega PX01C1-3KA5T) with a specified uncertainty of 21 kPa; it was calibrated in the range from 0 to 10342 kPa with a maximum uncertainty of 7.76 kPa. The pressure drop across the heated length of the test section was measured with a differential pressure transmitter (Omega PX771A-300DI), having an uncertainty of 75 Pa. The CO_2 mass flow rate was measured with a Coriolis flow meter (Micro Motion® ELITE® CFM050M320N0A2E2ZZ), having an uncertainty of 0.05% for liquid flow. The instantaneous voltage drop across the heated length of the test section was measured with a 24-bit digital voltage measurement module (National Instrument NI 9225), having a range of ±300 V and an uncertainty of 0.034 V. The rectified voltage fluctuated at a frequency of 360 Hz and was sampled at a much higher sampling rate. The electrical power supplied to the test section was calculated from the measured time-averaged voltage and the measured electrical resistance of the test section. A dedicated computerized data acquisition system was used to monitor and control different loop operations and to record the data. All pressure and temperature measurements were acquired at a rate of 10 samples/s. Once the test conditions were set (pressure, inlet temperature, mass flux, and heat flux), we waited for the wall temperature to reach a constant level. Then the system was considered steady state and the measurements were recorded. The measurements were recorded after the operating conditions had stabilized. Data processing was done with the use of a code written in MATLAB. Spurious values in the data were removed. The data values used in the analysis of the results represent time-average values over 60s intervals. The ranges of the measurement devices and their uncertainties (90% confidence) are summarized in Table 2.

Table 2: Ranges of measured parameters and their uncertainties

Parameter	**Unit**	**Range**	**Uncertainty**
Wall temperature	°C	(-73) – (+260)	0.5
Bulk temperature	°C	0 - 100	0.1
Mass flow rate	Kg s^{-1}	0 - 25	0.05 %
Voltage	Volt	(-300) – (+300)	0.034
pressure	kPa	0 - 10342	7.76
Obstruction position	mm	----	5

3. TEST MATRIX, EXPERIMENTAL PROCEDURE AND DATA REDUCTION

3.1 Test matrix

Table 3 lists the ranges of flow conditions covered in the experiments with the bare and obstructed tube test section. Supplementary data associated with this article can be found, in the online version, at http://dx.doi.or.

Table 3: Conditions for investigated flows in a bare and an obstructed 8 mm ID tube

P (MPa)	P/P_c	G (kg m^{-2} s^{-1})	q (kW m^{-2})	T_{in} (°C)	Re	Pr	Gr
7.69	1.04	200 -1000	1.0 – 92.4	9 - 30	19,400 – 240,000	1 - 24	$6.7*10^6$ - $3.7*10^8$
8.36	1.13	200 -1184	1.0 – 229	9 – 30	18,950- 356,000	1 - 21	$5.5*10^6$ - $3.7*10^8$

3.2 Heat transfer calculation procedures

The volumetric heat generation in the test section wall was calculated as

$$q^v = \frac{Q_e}{\pi(r_o^2 - r_i^2)L_h} \quad , \tag{1}$$

where Q_e is the measured electrical power supplied to the test section, r_o and r_i are the tube outer and inner radii, respectively, and L_h is the heated length. The inner wall temperature T_w was calculated from the measured outer wall temperature $T_{w,o}$ using the heat diffusion equation with uniform internal energy generation in cylindrical coordinates (Incropera *et al*., 2007), as

$$T_w = T_{w,o} + \frac{2q_{loss}r_o - q^v r_o^2}{2k} \ln\frac{r_o}{r_i} + (r_o^2 - r_i^2)\frac{q^v}{4k} \quad , \tag{2}$$

where k is the thermal conductivity of Inconel 600 evaluated at the local $T_{w,o}$ and q_{loss} is the heat loss to the surroundings, which was neglected for this calculation. The wall heat flux was calculated as

$$q = \frac{Q_e}{\pi D L_h}, \tag{3}$$

under the assumption of no heat loss to the surroundings and no heat conduction to the test section supports. Under the same assumption, the bulk fluid enthalpy along the heated test section was calculated using the simplified energy equation

$$h_b = h_{in} + \frac{Q_e}{\dot{m}} \frac{z_h}{L_h} \quad , \tag{4}$$

where h_{in} is the specific enthalpy at the inlet, $\dot{m}$ is the mass flow rate, and z_h is the axial distance along the heated section. The corresponding local bulk fluid temperature T_b and the thermo-physical properties of carbon dioxide were calculated using NIST software (Lemonn *et al.* 2002). Finally, the local heat transfer coefficient (HTC) was calculated as

$$H = \frac{q}{T_w - T_b}. \tag{5}$$

3.3 Checks of measurement accuracy

To check the accuracy of the thermocouples, a zero-power test at a high mass flux was performed for every run. In all cases, differences in the readings of all test section thermocouples and the RTD were less than 0.1 K, which is deemed to be the temperature measurement uncertainty. In order to confirm that the performance of the loop and the instrumentation remained stable and that no changes occurred to the calibrated measuring devices during the course of these experiments, repeat tests were performed occasionally. Figure 3 shows an example of a pair of repeat test, performed with a time separation of two years; it can be seen that the wall temperatures and heat transfer coefficients were in excellent agreement for the two trials. It is further noted that Zahlan *et al.* (2015b) performed comparisons of SCHT data obtained in SCUOL with previous SC CO_2 data obtained by various authors and found good agreement, thus confirming the reproducibility of data obtained in SCUOL.

As an overall check of the accuracy of the measured flow rate, the inlet and outlet RTD measurements and the NIST code property values, we computed the imbalance between the electrical power Q_e supplied to the test section and the thermal power $\dot{m}(h_{out} - h_{in})$ absorbed by the fluid as

$$\Delta Q_e = Q_e - \dot{m}(h_{out} - h_{in}) \, . \tag{6}$$

The specific enthalpies at the inlet h_{in} and the outlet h_{out} of the test section were calculated from the corresponding measured bulk temperatures and pressures. This imbalance includes measurement errors and heat losses to the surrounding air and the test section supports. It is expected that heat losses would be relatively low for tests for which the axially averaged test section temperature $T_{w,av}$ was not much higher than the room temperature, but would increase with increasing $T_{w,av}$. We verified this hypothesis by conducting a series of tests with different wall heat fluxes, while keeping the pressure, mass flux and inlet temperature constant. We performed these tests at the lowest mass flux of 200 kg m^{-2} s^{-1}, for which the relative imbalance $\Delta Q_e/Q_e$ was found to be the highest. As figure 4 shows, the imbalance ΔQ_e was very small for $T_{w,av}$ < 100°C and increased monotonically with increasing $T_{w,av}$ for higher average temperatures. For the lowest tested heat fluxes, the power imbalance appeared to be negative, which we attribute to measurement errors. With the exception of tests at the lowest mass and heat fluxes, the relative imbalance $\Delta Q_e/Q_e$ was found to be less than 5% in magnitude, which is deemed to be acceptable, especially when considering that in the vast majority of tests the relative imbalance would be significantly lower. It is noted that the number of measurements obtained in the obstructed tube at low flows was very small.

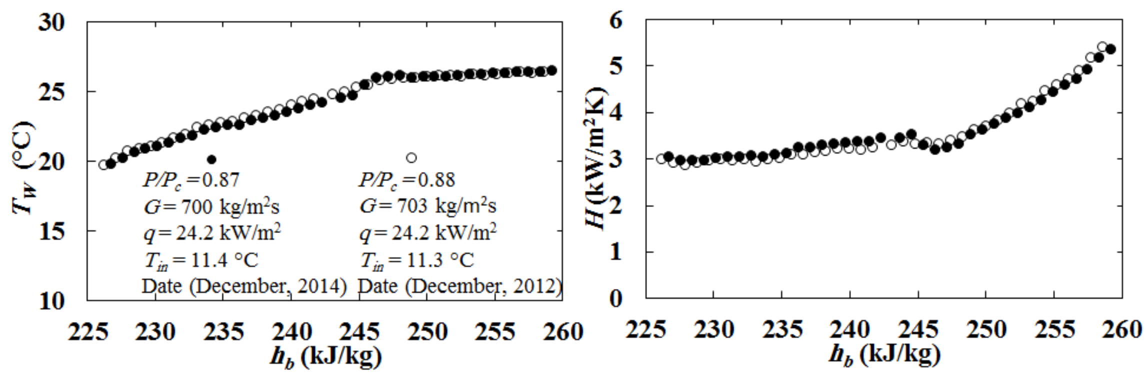

Figure 3: Repeatability check with a time separation of two years.

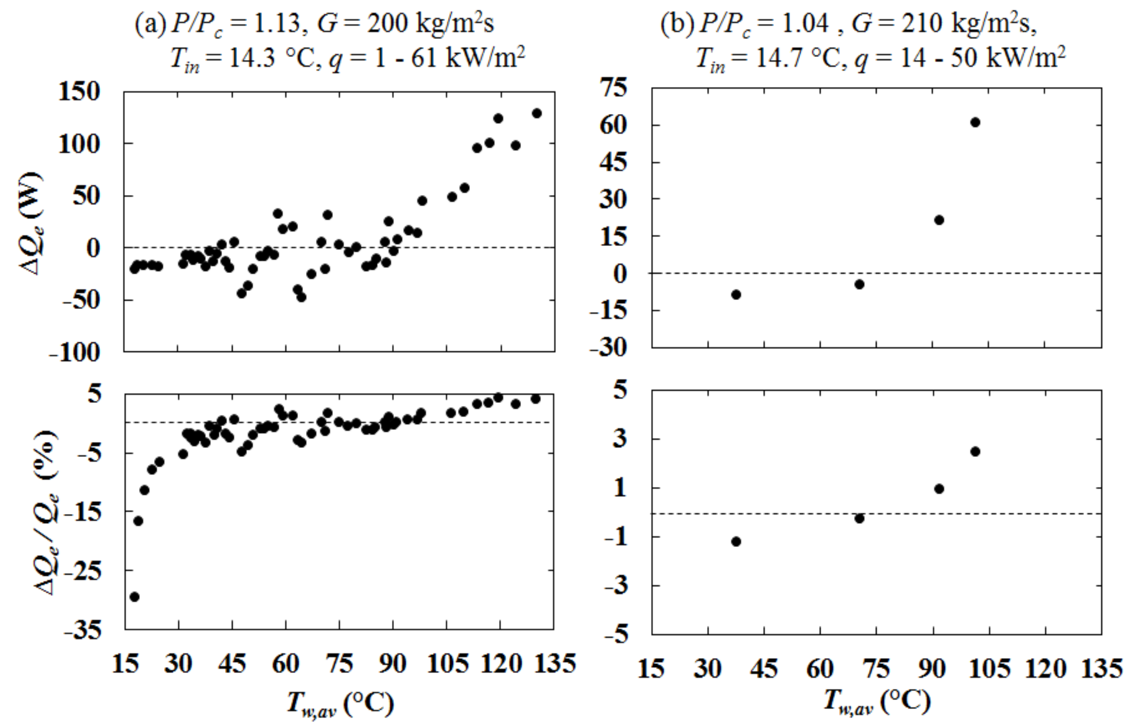

Figure 4: Measured power imbalance *vs.* axially averaged test section wall temperature for a low mass flux and a range of heat fluxes, (a) bare tube and (b) obstructed tube with 8 obstacles.

4. SUPERCRITICAL HEAT TRANSFER IN A BARE TUBE

In this section, the bare tube results are presented graphically as plots of the wall temperature T_w and the corresponding heat transfer coefficient H against the specific bulk fluid enthalpy h_b. The solid and dashed lines in these plots represent respectively the bulk fluid temperature and the pseudo-critical enthalpy. Flow conditions reported in the plots are averaged values and it is noted that the pressure, mass flux and heat flux could vary by up to 1% during the course of each test; similarly, the inlet temperature could vary by up to 0.5°C.

4.1 Heat transfer types

Figures 5 to 7 show examples of the bare tube results obtained at low mass fluxes, which cover a much wider range of bulk enthalpies than the higher mass flux results to be discussed later. This permits us to distinguish among three SCHT types.

(i) Heat transfer to liquid-like CO_2: this happens when $h_b << h_{pc}$ and $T_w < T_{pc}$. For relatively low heat fluxes, *e.g.*, q = 2.9 kW m^{-2} in Figures 5a,b and q = 9.2 kW m^{-2} in Figure 5c, T_w increased monotonically along the heated test section, which indicates that heat transfer was normal. At higher heat fluxes, the wall temperature underwent one or more peaks, which is evidence of heat transfer deterioration (HTD). HTD in the bare tube will be discussed in the following subsection.

(ii) Near-critical heat transfer: this happens when h_b is close to h_{pc}. Figure 6 shows examples of near-critical heat transfer. The heat transfer was enhanced significantly in the vicinity of the pseudo-critical point for G =300 kg m^{-2} s^{-1}, but less so for G = 200 kg m^{-2} s^{-1}. Figures 6c and 7c also show that, at lower heat fluxes, the heat transfer improvement was more pronounced. This improvement is primarily attributed to the large changes in heat transport properties, especially in specific heat.

(iii) Heat transfer to gas-like CO_2: this happens when $h_b >> h_{pc}$. Figure 7 shows examples of gas-like heat transfer type. In this range, the heat transfer resembles single-phase, subcritical heat transfer, especially at conditions that are far away from the pseudo-critical values.

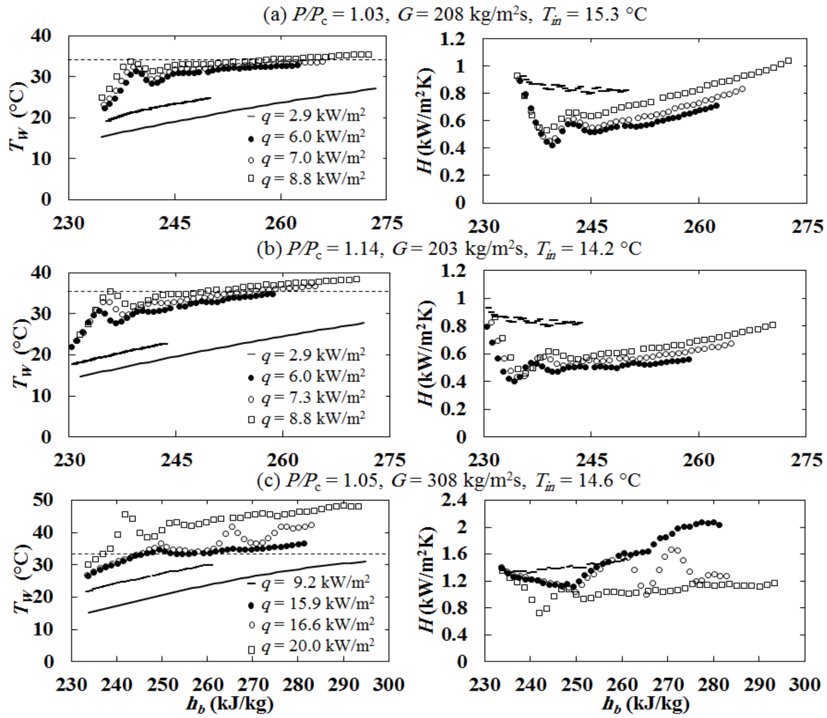

Figure 5: Wall temperature and heat transfer coefficient *vs.* specific bulk enthalpy for low heat fluxes and low mass fluxes. The horizontal dashed line indicates the pseudo-critical temperature.

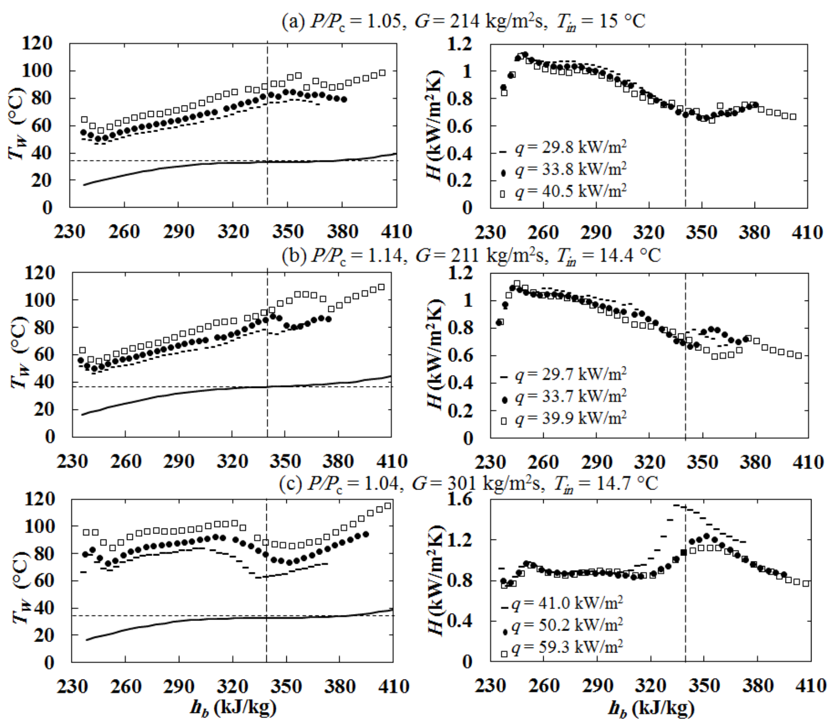

Figure 6: Wall temperature and heat transfer coefficient *vs.* specific bulk enthalpy for moderate heat fluxes and low mass fluxes. The solid line indicates the bulk specific enthalpy, the horizontal dashed line indicates the pseudo-critical temperature and the vertical dashed line indicates the pseudo-critical specific enthalpy.

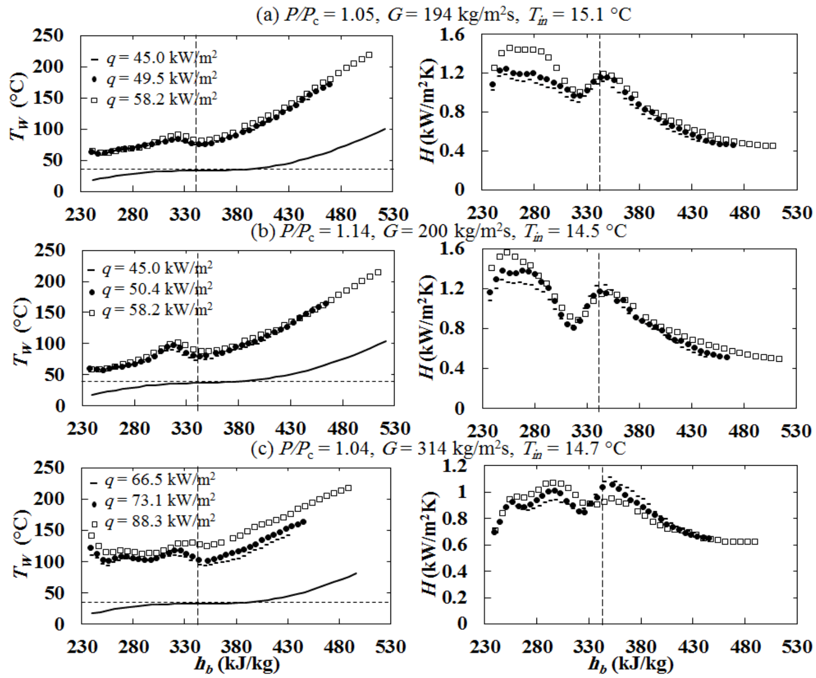

Figure 7: Wall temperature and heat transfer coefficient *vs.* specific bulk enthalpy for high heat fluxes and low mass fluxes. The solid line indicates the bulk specific enthalpy, the horizontal dashed line indicates the pseudo-critical temperature and the vertical dashed line indicates the pseudo-critical specific enthalpy.

4.2 Parametric trends

The effects of pressure, mass flux and heat flux on the wall temperature and HTC profiles are shown in Figures 8 - 10 and are discussed below. The inlet temperature effect was not investigated in detail, because previous investigations by Zahlan *et al.* (2015b) and Eter *et al.* (2015) have indicated that, away from the inlet, the local T_w and H were not sensitive to the inlet temperature but were primarily dependent on the local bulk enthalpy. Several sets of the present measurements were used to test the predictions of Jackson's SCHT correlation (2002), which provides the bulk Nusselt number as

$$\mathrm{Nu}_b = 0.0183\mathrm{Re}_b^{0.82}\mathrm{Pr}_b^{0.5}\left(\frac{\rho_w}{\rho_b}\right)^{0.3}\left(\frac{\overline{C_p}}{C_{pb}}\right)^n, \quad (7)$$

where Re_b and Pr_b are, respectively, the bulk Reynolds and Prandtl numbers, ρ_w and ρ_b are, respectively, the density at wall and bulk temperatures, and $\overline{C_p}$ and C_{pb} are, respectively the average and bulk specific heats; Jackson suggested empirical values for the exponent *n* that depended on the relative values of the bulk, wall and pseudo-critical temperatures. Jackson's correlation was based on CO_2 data and was recommended by Pioro and Duffey (2003) and Zahlan et al. (2015), among others. This correlation accounts for changes in thermo-physical properties but not for buoyancy forces or acceleration effects, and is therefore meant to apply only to normal SCHT.

Pressure effect: Figure 8 contains representative plots of T_w and *H vs.* h_b for two pressures for heat transfer to liquid-like, near-critical, and gas-like CO_2. These plots indicate that the pressure effect is small, regardless of the enthalpy range. For the few cases shown, predictions of Jackson's correlation showed that the pressure effect on SCHT would be small and that the difference would increase as the specific enthalpy approached the pseudocritical value 340 kJ kg^{-1}. The HTC was measurably higher for the lower pressure ratio, an effect attributed to the higher specific heat at pressures closer to the critical pressure.

Mass flux effect: Figure 9 shows four pairs of plots of T_w and *H vs*. h_b for different mass fluxes. For normal heat transfer conditions or recovery from HTD, *H* generally increased as the mass flux was increased. An important observation in this figure is that the mass flux effect on HTC appears to be suppressed at HTD conditions, with the exception of the highest mass flux. The explanation offered for this is that the buoyancy effect at HTD conditions is sufficiently strong to suppress the convection effects for low to medium mass fluxes, while at high mass fluxes the convection effects are too strong to be suppressed by buoyancy forces. None of the SCHT correlations predicts this trend. At higher enthalpies, the data show trends expected for normal heat transfer and Jackson's correlation predicts qualitatively a similar trend. In the vicinity of the pseudo-critical enthalpy (h_{pc} = 340 kJ kg^{-1}), Jackson's correlation over-predicted the SCHT. This behavior was reported previously by Bae and Kim (2009) for CO_2 data obtained in tubes having different diameters at different operating conditions.

Heat flux effect: The effects of heat flux on *H*, presented earlier in Figures 5-7, are shown collectively in Figure 10. It can be seen that, in the liquid-like region and at very low heat fluxes, normal heat transfer was characterized by a small drop in *H* for the same h_b as *q* increased, until the onset of HTD. At HTD conditions, *H* decreased significantly compared to normal SCHT. Interestingly, further increases in heat flux led to a higher *H* than for normal SCHT in the liquid-like region for low mass fluxes. In the near-critical and gas-like regions, *H* increased with an increase in heat flux only for the low mass fluxes, while for all other mass fluxes the opposite is true.

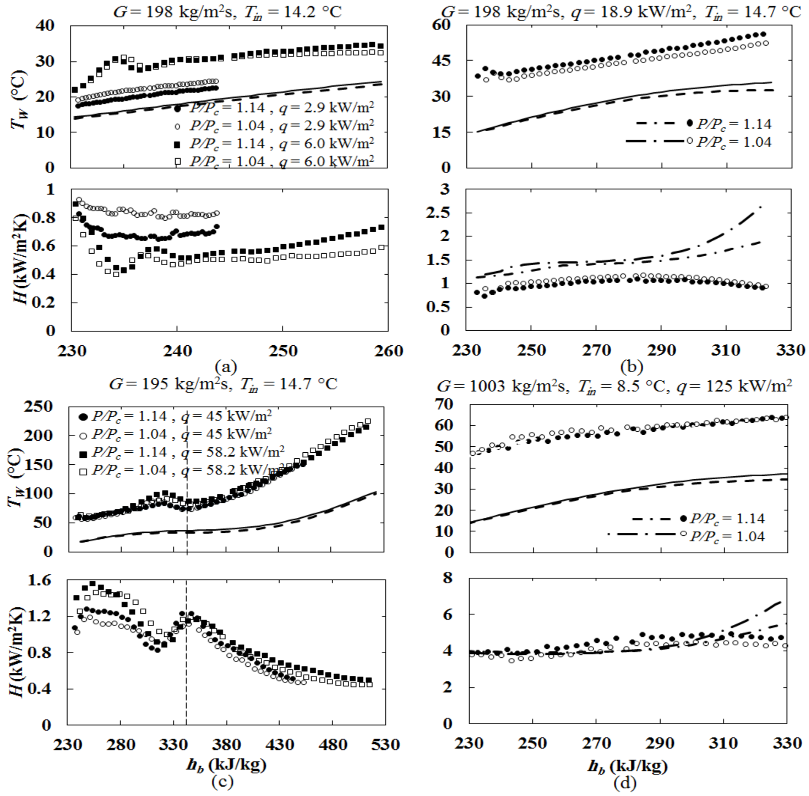

Figure 8: Variations of T_w and H *vs*. h_b for two supercritical pressures; solid and dashed curves in the wall temperature plots represent the bulk temperature evolutions for P/P_c = 1.14 and 1.04, respectively; dash-dot lines in b and d show predictions of Jackson's correlations for the pressures indicated in the corresponding legends; vertical dashed lines mark the pseudo-critical specific enthalpy for P/P_c = 1.14, whereas for P/P_c = 1.04 this value is 2 kJ kg^{-1} lower.

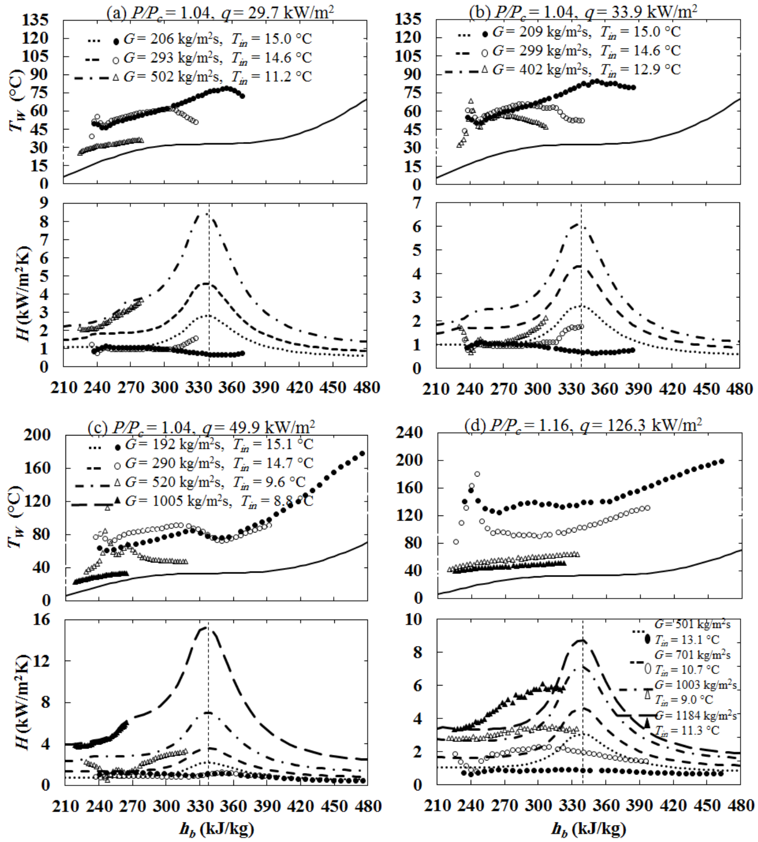

Figure 9: Variations of T_w and H *vs*. h_b at a supercritical pressure and different mass fluxes; vertical dashes lines mark the pseudo-critical specific enthalpy; solid lines show the bulk temperature variation; other lines represent predictions of Jackson's correlation.

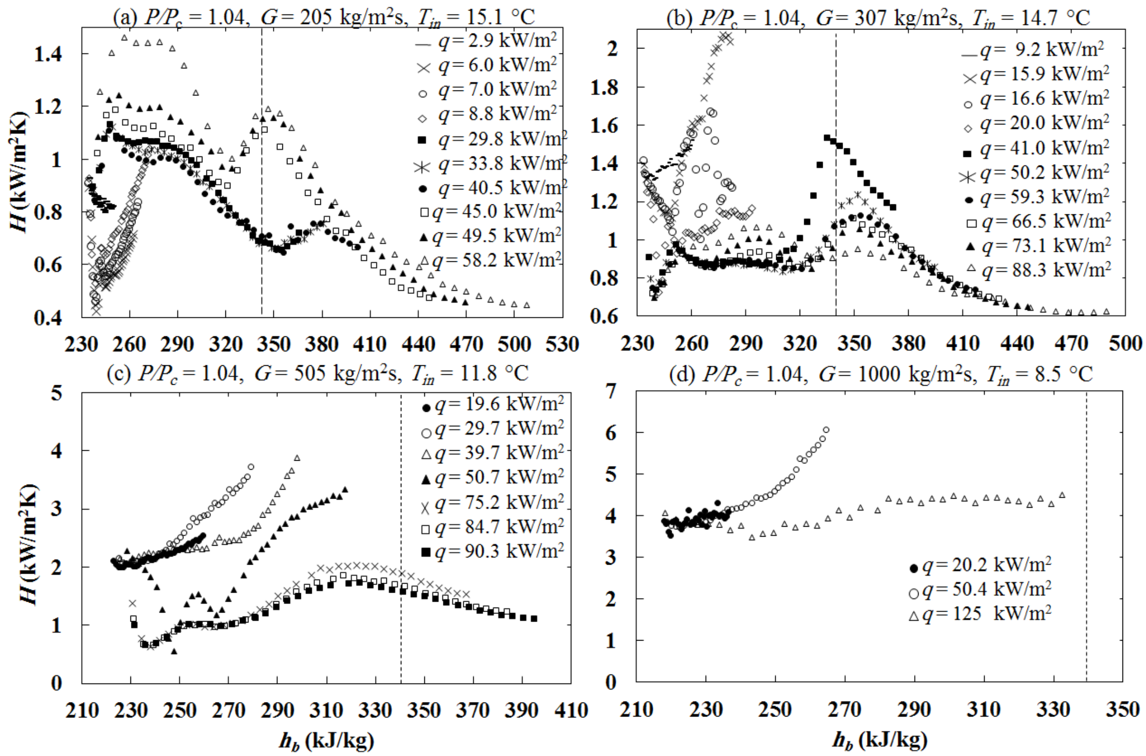

Figure 10: Effect of heat flux on H for different mass fluxes; vertical lines mark the pseudo-critical specific enthalpy.

4.3 Heat transfer enhancement in the pseudo-critical region

We now focus on heat transfer under conditions for which the bulk specific enthalpy increased beyond the pseudo-critical value. At relatively low mass and heat fluxes (Figure 6a,b), the HTC passed through a mild minimum in the pseudo-critical region, but, at higher mass and/or heat fluxes (Figures 6c and 7a-c), the HTC had a clear peak in this region, which is evidence for heat transfer enhancement due to the favourable variation of the thermo-physical properties. The anomaly at low mass and heat fluxes indicates that there is a distinct HTD mechanism under such conditions, which is not present at higher mass and heat fluxes. Jackson's correlation generally shows a very significant increase in HTC in the near-pseudo-critical region, with prominent peaks in HTC even for conditions for which low peaks, or none at all, were seen in the measurements (Figure 9).

5. SUPERCRITICAL HEAT TRANSFER IN A TUBE EQUIPPED WITH FLOW OBSTRUCTIONS

This section describes the SCHT test results for the obstacle-equipped tube configurations listed in Table 1. The test results are presented as plots of T_w and H $vs.$ h_b. The obstacles were located at an angle $\theta = 0°$ (see Figure 2), unless otherwise specified. The impact of various obstacle parameters at different flow conditions on SCHT is described first. A more detailed discussion of the impact of obstacles on SCHT and the interpretation of the results are given in subsequent subsections.

5.1 Effects of obstacle shape, location and pitch

Obstacle shape effect: The effect of obstacle shape, namely whether it was blunt or rounded, on SCHT was examined for a wide range of flow conditions by comparing results for configurations 3 and 5 in Table 1. Both configurations consisted of two obstacles, each with a 25% flow blockage, installed inside the 8 mm ID tubular test section; the first obstacle was located at the beginning of the heated length and the second obstacle was located at a distance $\Delta z = 500$ mm downstream from the first one ($\Delta z/D$ = 62.5; for comparison, the entire heated test section was 242.5D long and was preceded by an unheated section that was 111D long). Figure 11 shows some typical results. For both obstacle shapes, the HTC had a peak closely downstream of the obstacle and then decreased rapidly. As observed in previous single-phase flow studies (*e.g.*, Tanase and Groeneveld, 2015), the blunt obstacles were found to have a stronger impact on the HTC than the rounded obstacles. For the low mass flux of 200 kg m^{-2} s^{-1} (Figure 11a), the first obstacle of either type delayed, rather than eliminating, the mild HTD that occurred near the bare tube inlet. For a higher mass flux (Figure 11b), both obstacles suppressed HTD at the inlet, but the second obstacle (at 500 mm from the inlet) did not suppress HTD at locations well downstream from itself. In Figure 11b, the second obstacle also had the effect of shifting the wall temperature peaks that occurred in the bare tube to higher bulk enthalpies. Additional measurements at even higher flows showed that the first obstacle suppressed the strong near-inlet HTD that was observed in the bare tube. Subsequent measurements in the obstructed tube were performed using only blunt obstacles, because these were found to have a stronger impact on the HTC than rounded ones.

Obstacle pitch effect: As a first step for this study, the results of tests with two 25% blockage ratio blunt obstacles spaced by 500 mm were compared with those from tests with the same obstacles spaced by 1000 mm. The effect of second obstacle location on the HTC at normal and deteriorated heat transfer conditions can be seen in Figure 12. First of all, Figures 12a and b show that the first obstacle (at the start of the heated length) appears to have eliminated the mild HTD present for the bare tube case. Figure 12c shows two temperature peaks for the bare tube case, which are shifted downstream by the presence of the obstacles over a distance of 40-60D. These figures demonstrate that the effectiveness of obstacles in suppressing near-inlet HTD is very sensitive to flow and power conditions. Figure 12b further shows that the second obstacle actually created additional peaks in temperature which were not present in the bare tube case. The multiple peaks in temperature for the bare tube case in Figure 12c were affected, but not eliminated by the obstacles. The previous results make it evident that the use of two obstacles with pitches equal to 500 and 1000 mm cannot be considered as an effective strategy for suppressing HTD under different test conditions. Next, we performed tests using 8 obstacles spaced by the shorter pitch of 250 mm ($\Delta z/D = 31$; configuration 4 in Table 1). Figure 13 shows that this configuration was generally effective in improving H over most of the heated section, although some mild HTD was also observed to occur at about 20-30D downstream of the obstacles, primarily in the liquid-like region, as shown in Figure 13b. Figure 13 also shows that, for the higher bulk enthalpies, the enhanced HTC did not approach the bare tube value within the 250 mm pitch, but heat transfer enhancement by the obstacle appeared to maintain a cumulative excess. An inspection of plots of the measured HTC for all three obstacle pitches (not all of which are shown in the present article) demonstrated that, although in general obstacles enhanced SCHT, especially for higher flows and in the gas-like region, there were also conditions and configurations for which the opposite was true, as will be discussed further in the next subsection. This adverse effect of obstacles was observed for all obstacle pitches. Another observation is that, for higher flows and in the gas-like region, the enhancement effect of each obstacle persisted over a relatively long downstream distance. A more detailed discussion on the obstacle effect on the HTC is presented in following subsections.

<u>Flow blockage effect</u>: Figure 14 shows an example of the effect of obstacle blockage ratio on the HTC. Two sets of blunt obstacles with blockage ratios 25% and 13%, respectively, and both with a pitch of 250 mm were investigated. As expected, the obstacles with the higher blockage ratio always had a stronger overall impact on SCHT.

<u>Obstacle circumferential location effect</u>: All previous results were obtained with the obstacles located at an angle θ = 180°, whereas all wall thermocouples were located at θ = 0° (see Figure 2). Considering that the blockage was non-axisymmetric, we investigated the effect of circumferential blockage location on SCHT. This was done for configuration 4 (blunt obstacle, 25% blockage, 250 mm pitch), with the first two obstacles relocated circumferentially to four positions in steps of 90°, while the remaining obstacles were left in place to confirm the repeatability of the measurements. The results for four values of the angle θ of the obstacles are shown in Figure 15. Although the spatial resolution of our temperature measurements is inadequate to show circumferential differences in wall temperature in the close vicinity of the first two obstacles, it is clear that, at all locations of shown measurements, the impact of changing the alignment of the first two obstacles with respect to the wall thermocouples and the downstream obstacles was small and in many cases barely noticeable. It is also noted that the shown differences could be partially attributed to small inaccuracies in the location the obstacles and to slight variations in pressure, heat flux, and inlet temperature during the course of the experiment.

<u>Obstacle streamwise location effect:</u> Figure 16 shows representative examples of normal heat transfer enhancement by an obstacle located near the heated inlet and a second one located 500 or 1000 mm downstream (configurations 2 and 3). Both the liquid-like and gas-like regions are represented in these examples. It can be seen that the first obstacle induced a mild localized enhancement, which was relatively short lived (*i.e.*, it was negligible beyond 15*D* downstream of this obstacle); the second obstacle also resulted in a mild enhancement in SCHT, which however persisted over longer distances. These examples suggest that in general the HT enhancement decay length downstream from an obstacle would be shorter with the obstacle placed near the inlet than away from it; it also appears that the enhancement by the inlet obstacle was in general less prominent. A plausible explanation for these observations is that, because near the inlet the thermal boundary layer was developing but remained thin, the vigorous mixing downstream of the obstacle had a relatively weak effect on the overall thermal field inside the tube.

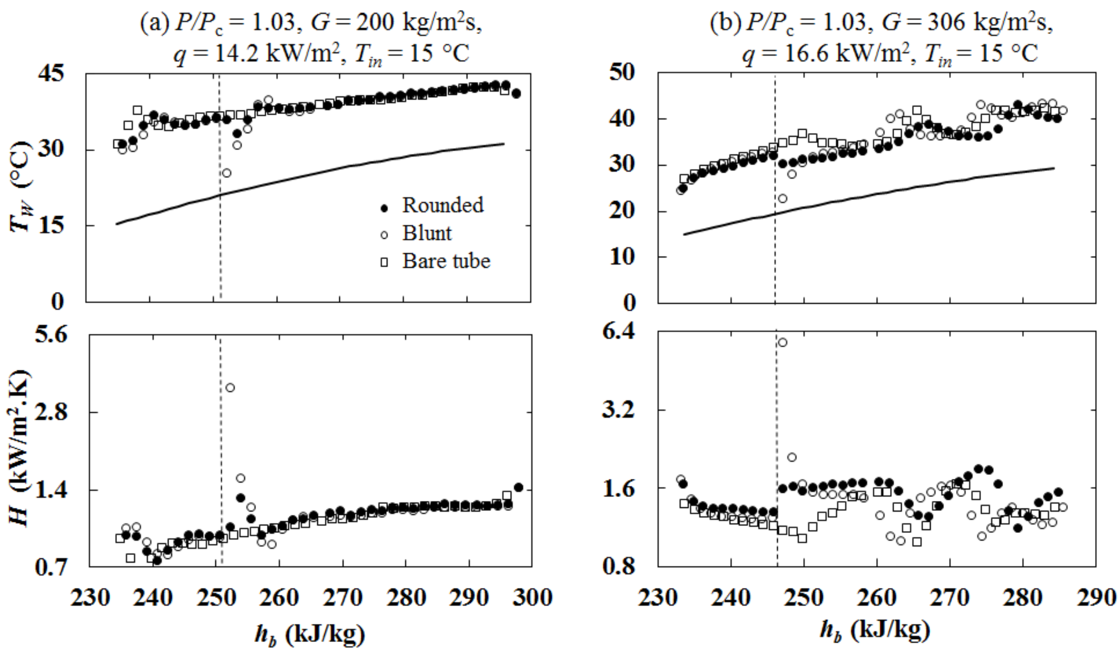

Figure 11: Effect of obstacle shape on SCHT; results for two pairs of blunt and rounded obstacles are presented; in all cases the blockage ratio was 25 % and the obstacle pitch was 500 mm; H is plotted in semi-logarithmic axes; the first obstacle was placed at the start of the heated section, whereas dashed vertical lines show the location of the second obstacle.

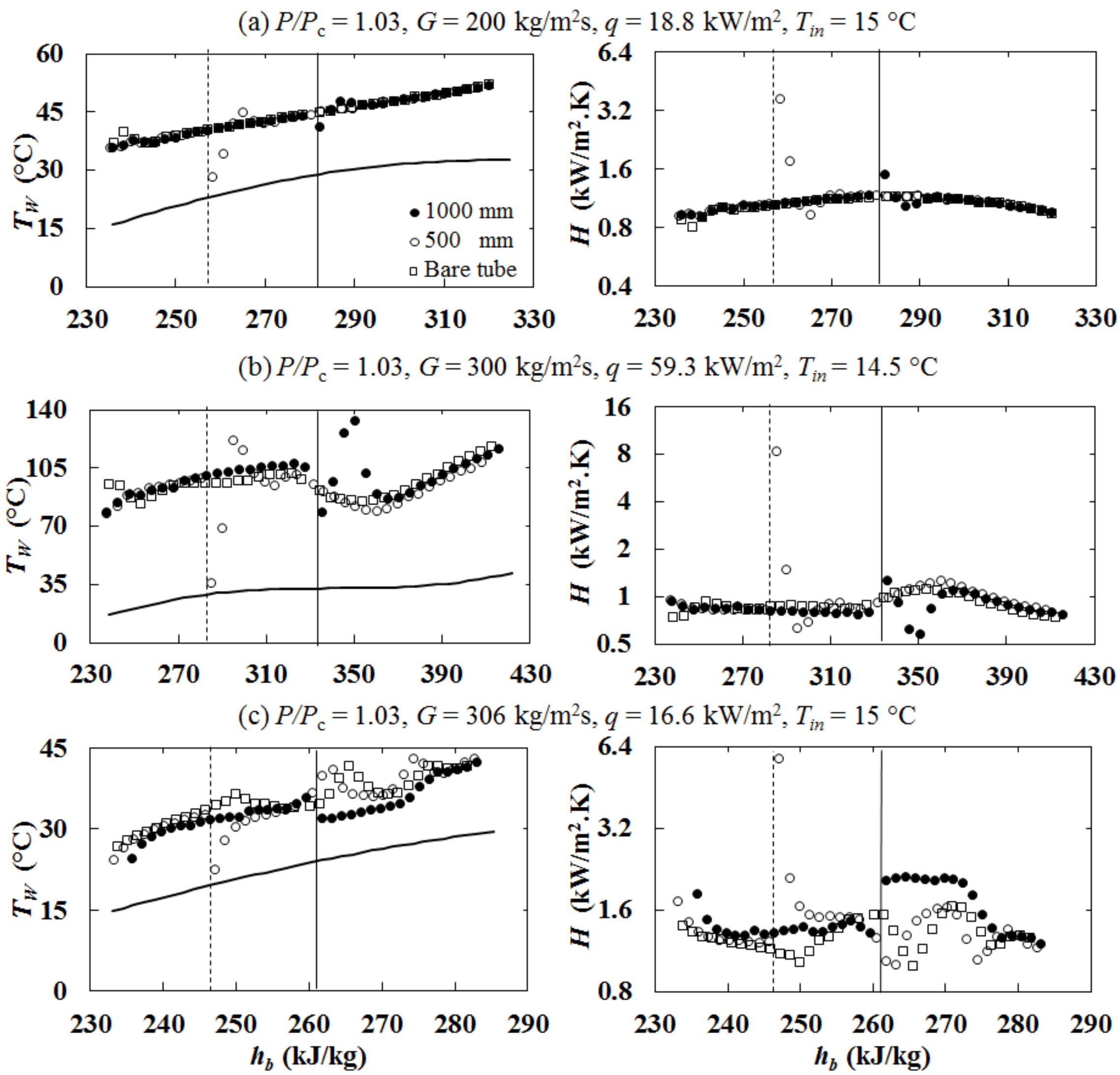

Figure 12: Effect of obstacle pitch on SCHT; results for two pairs of blunt obstacles are presented, with blockage ratios of 25 % for both pairs and obstacle pitches of 500 and 1000 mm, respectively; H is plotted in semi-logarithmic axes; the first obstacle was placed at the start of the heated section, whereas dashed and solid vertical lines show the location of the second obstacle.

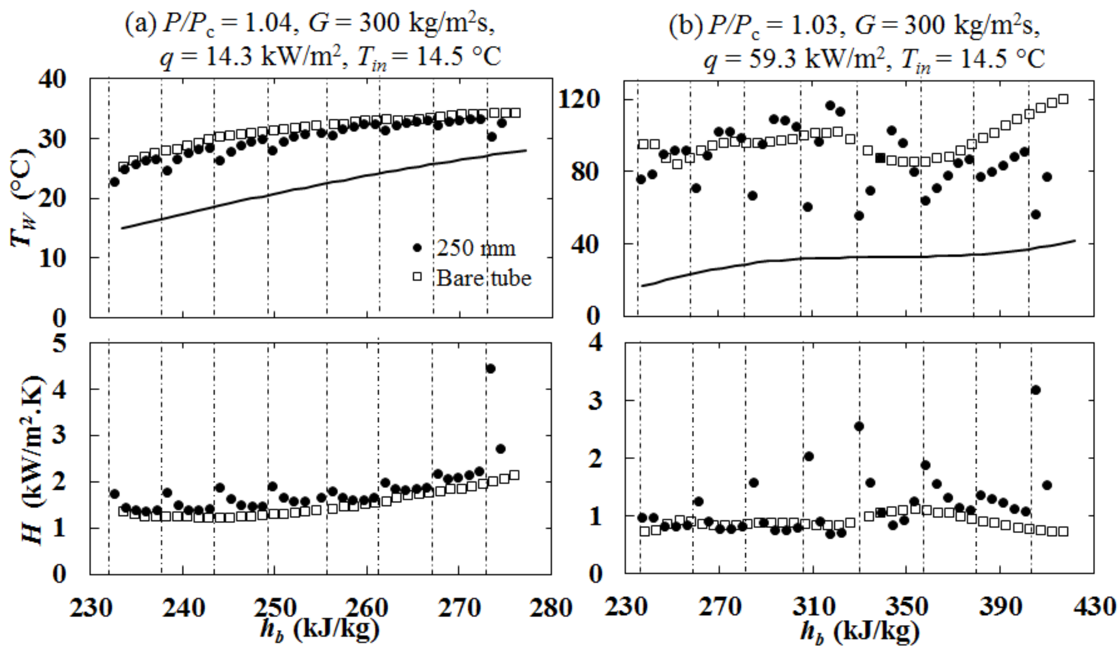

Figure 13: Effect of blunt obstacles with a blockage ratio of 25 % and a pitch of 250 mm on SCHT; vertical lines mark obstacle locations.

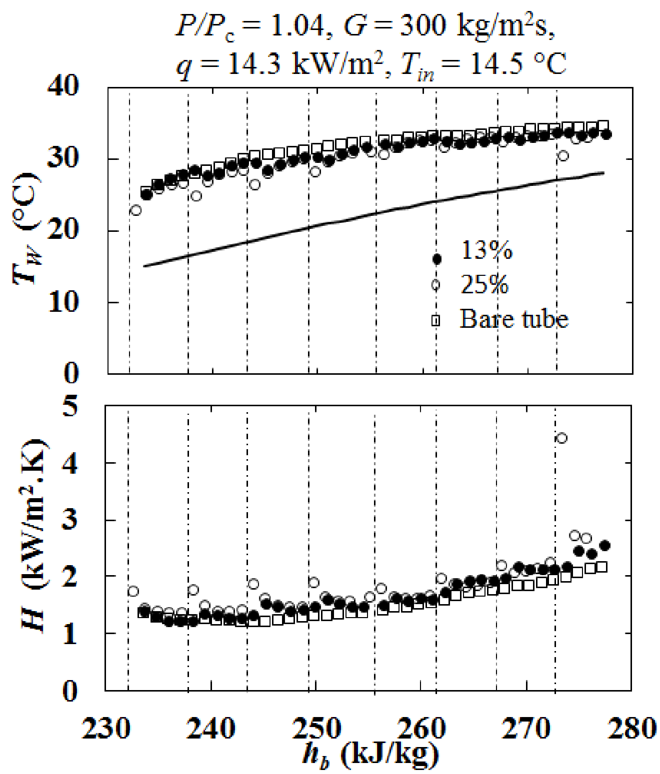

Figure 14: Effect of obstacle blockage ratio on SCHT for blunt obstacles with a 250 mm pitch; vertical lines mark obstacle locations.

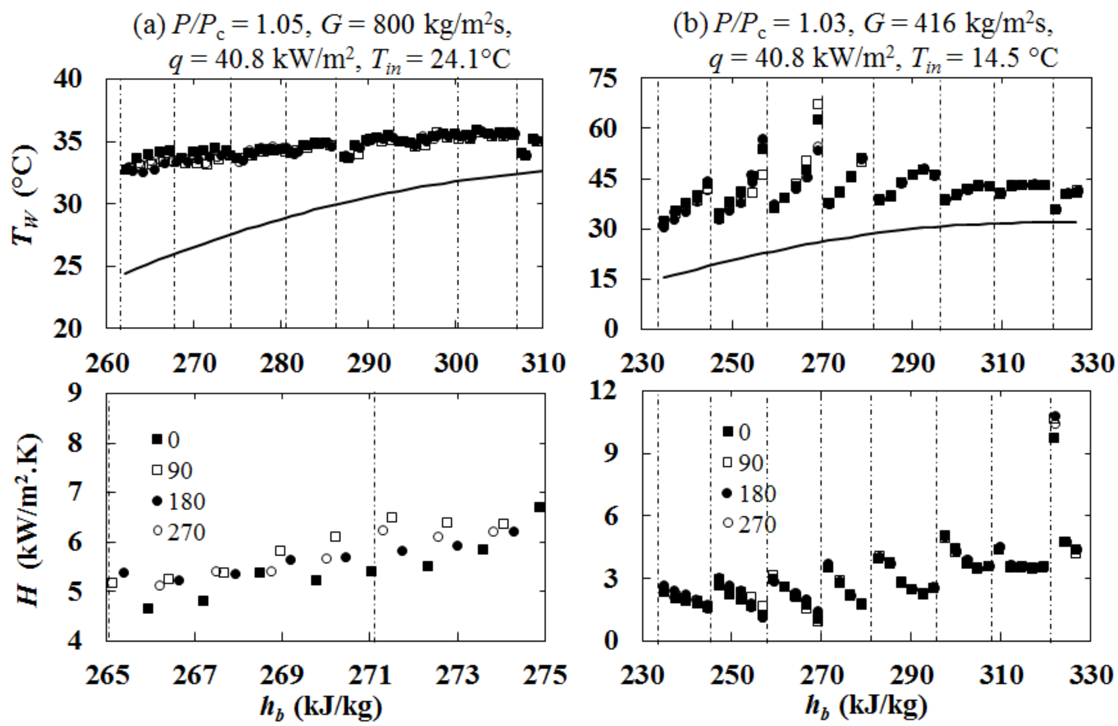

Figure 15: Effect of the circumferential locations of the first two obstacles on SCHT; blunt obstacles with a 25% flow blockage and a 250 mm pitch were used; vertical lines mark obstacle locations; numbers in the legends indicate obstacle angle (in degrees) with respect to the axis of the thermocouples.

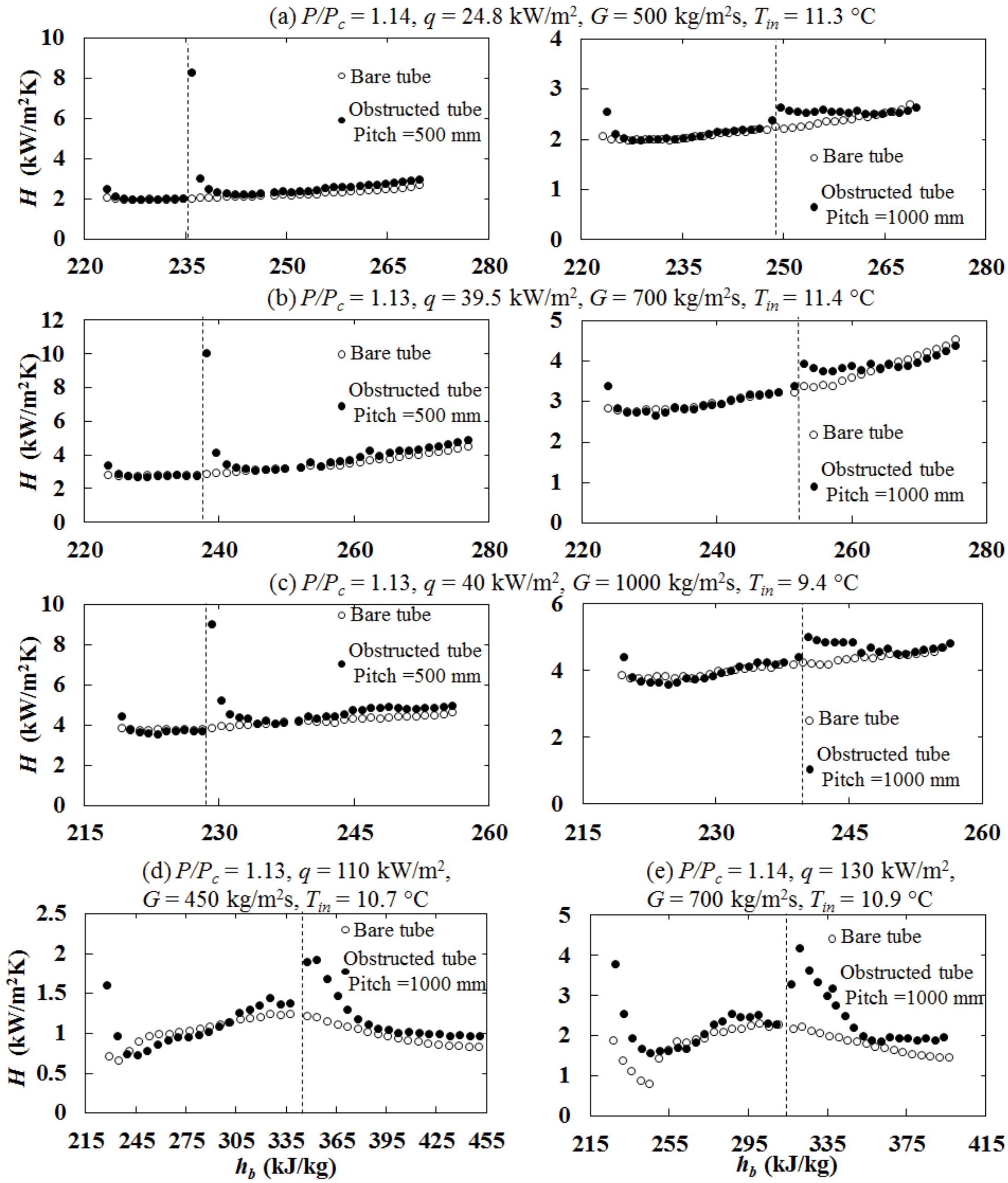

Figure 16: Normal heat transfer enhancement in a tube equipped with a blunt obstacle at its heated inlet and a second one at the location indicated by a dashed vertical line; in plots a-c, the fluid was in the liquid-like region, whereas, in plots d-e, the fluid was mostly in the gas-like region.

5.2 Heat transfer deterioration caused by flow obstacles

It was noticed earlier that, under a variety of conditions, HTD may occur in a tube equipped with cylindrical flow obstacles, although its intensity and location of occurrence may be different from those in the bare tube. One of the surprising results of the present experiments is that the SC HTC downstream of obstacles dropped below the bare tube value before rising again to match the latter. An example of this phenomenon for the low mass flux of 200 kg m^{-2} s^{-1} is shown in Figure 11a (blunt obstacle). Another example for a higher flow rate is shown in Figure 17. This observation is contrary to findings in subcritical studies, in which obstacles always had either an enhancing or a neutral effect on the HTC (*e.g.*, Groeneveld and Yousef, 1980).

A qualitative explanation for the occurrence of HTD closely downstream of obstacles may be based on a possible analogy of this phenomenon and the occurrence of HTD close to the inlet of heated tubes at supercritical pressures. The latter has been associated with the development of a thermal boundary layer and the associated strong temperature gradient near the wall. Thorough mixing of the flow by an obstacle would tend to make the fluid temperature more uniform than upstream of the obstacle, so that a new thermal boundary layer would start forming near the continuously heated tube wall, similar to the entrance thermal boundary layer. Fluid in this layer would be susceptible to HTD under certain flow and heating conditions. It is noted that the development of a new thermal boundary layer downstream of obstacles in deterioration-free subcritical heat transfer in tubes was earlier conjectured by Yao *et al.* (1982).

Considering the difficulty in predicting HTD even in unobstructed tubes, it seems rather unlikely that obstacle-induced HTD would be predicted by relatively simple means. An exploration of various approaches to quantify this phenomenon has been attempted by Eter (2016). In the following, we summarize our efforts to correlate HTD downstream of obstacles to the buoyancy parameter, which is a measure of the strength of buoyancy effects. This parameter has been defined by Bae and Kim (2009) in terms of the bulk Grashof number Gr_b, Reynolds number Re_b and Prandtl number Pr_b as

$$\mathrm{Bu} = \frac{\mathrm{Gr_b}}{\mathrm{Re}_b^{2.7}\,\mathrm{Pr}_b^{0.5}} \;, \tag{8}$$

where $\mathrm{Gr_b} = \dfrac{\rho_b(\rho_b - \bar{\rho})gD^3}{\mu_b^2}$. Figure 18 shows values of the ratio R_{SCHT} of the heat transfer coefficients in obstructed and bare tubes for a wide range of values of Bu under conditions for which an adverse effect of obstacles on the HTC is more likely to occur. No specific relationship between these two parameters can be discerned from this figure, except that, for the conditions of our tests, a significant adverse effect of obstacles was not observed for Bu < 4×10^{-6}. For higher values of this parameter, obstacle-induced HTD was absent from the majority of tested cases, but present in a sizeable number of others. This finding seems to suggest that, within the ranges of tested conditions, the value Bu = 4×10^{-6} is a threshold below which buoyancy forces would not be sufficient to induce HTD closely downstream of obstacles.

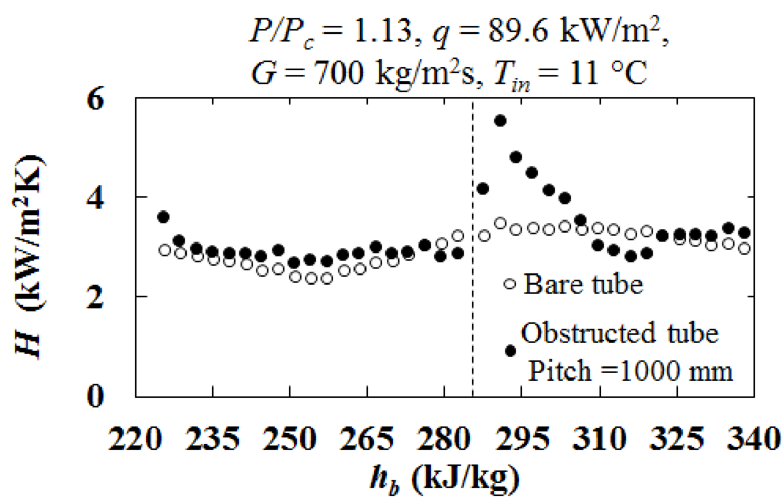

Figure 17: Example showing local heat transfer deterioration caused by an obstacle; vertical line marks obstacle location.

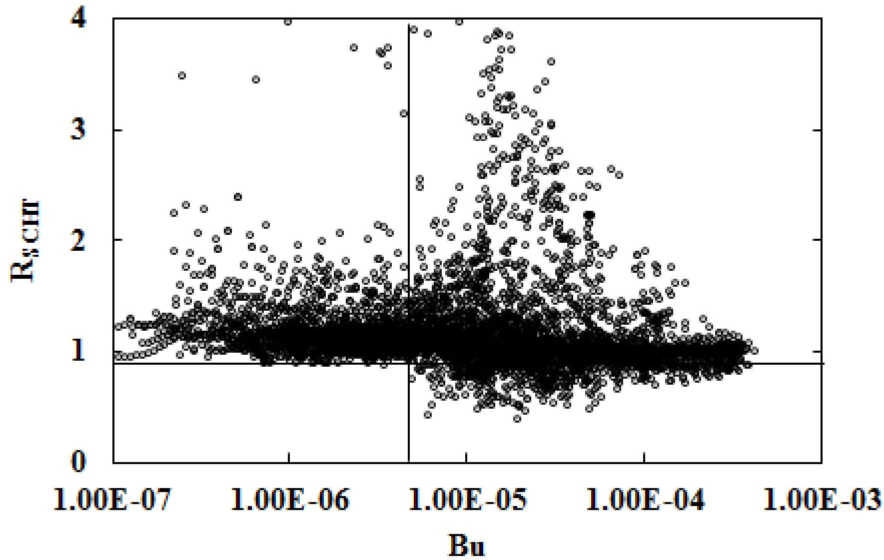

Figure 18: Effect of buoyancy parameter Bu on the ratio R_{SCHT} of the heat transfer coefficients in obstructed and bare tubes at P/P_c = 1.04 and 1.13 and G = 200 – 1000 kg m^{-2} s^{-1}; the horizontal line marks the threshold R_{SCHT} = 0.9, below which heat transfer deterioration caused by obstructions is considered to be significant; the vertical line marks the value Bu = 4×10^{-6}.

5.3 Quantification of obstacle-induced heat transfer enhancement

Correlations that describe the effect of single obstacles on the heat transfer coefficient in single-phase flows have been proposed, among others, by Yao *et al.* (1982), Mori *et al.* (2012), Miller *et al.* (2013) and Tanase and Groeneveld (2015). These correlations were generally of the form

$$\frac{\mathrm{Nu_{obs}}}{\mathrm{Nu_{bare}}} = 1 + A\varepsilon^2 e^{-B\Delta z_0/D_h} \tag{9}$$

where Nu_{obs} and Nu_{bare} are, respectively, the Nusselt numbers in the obstructed and the bare tubes under the same conditions; A and B are positive empirical constants; ε is the blockage ratio; Δz_0 is the axial distance downstream of the downstream edge of the obstacle; and D_h is the hydraulic diameter of the heated channel. These types of correlations predict a sudden increase of Nusselt number at the downstream edge of the obstacle and subsequent exponential decay of this parameter with distance from this edge. The coefficient A is a measure of the maximum enhancement, whereas the coefficient B is a measure of the extent of the enhancement zone. For comparative purposes, we will define the enhancement decay length as the distance over which the Nusselt number ratio drops to 1.05; this decay length is approximately equal to $3D_h/B$. As a reference, both the Yao *et al.* and Mori *et al.* correlations had A = 5.55, however, the former had a decay length of $23D_h$ (B = 0.13), whereas the latter had a decay length of $60D_h$ (B = 0.05).

Figure 19 shows the experimental ratio $\mathrm{Nu}_{obs}/\mathrm{Nu}_{bare}$, plotted *vs.* $\Delta z_o/D$ for a few cases with different obstacle pitches, two flow blockage ratios, different mass fluxes in the range 200 - 1000 kg m^{-2} s^{-1} and different pressures. Only cases with normal heat transfer in either the bare or the obstructed tube have been considered. Focusing first on the liquid-like data, it is apparent that the heat transfer enhancement downstream of obstacles placed near the entrance of the heated section was much milder and had a much shorter duration than that downstream of obstacles placed far away from the inlet. As was discussed in section 5.1, the enhancement characteristics near the inlet, where the thermal boundary layer is in a developing state, would not be truly representative of the obstacle-induced heat transfer enhancement. It is also apparent that obstacle-induced enhancement was stronger and had a longer duration in the gas-like region than the liquid-like region. The same figure shows that predictions by correlations of Yao *et al*. and Mori *et al*. fell between the two sets of liquid-like data. For comparative purposes, we have fitted different values of the coefficients A and B to each of the three sets of data; these values are shown in the legend of figure 19. The corresponding decay lengths were approximately 15D for the near-entrance obstacle, 35D for the downstream obstacle in the liquid-like region and 60D for the gas-like region. In view of the relatively small number of measurements used for these fits and the possible dependence of obstacle-induced enhancement on the local Reynolds number and other parameters, the values mentioned previously should be treated as tentative.

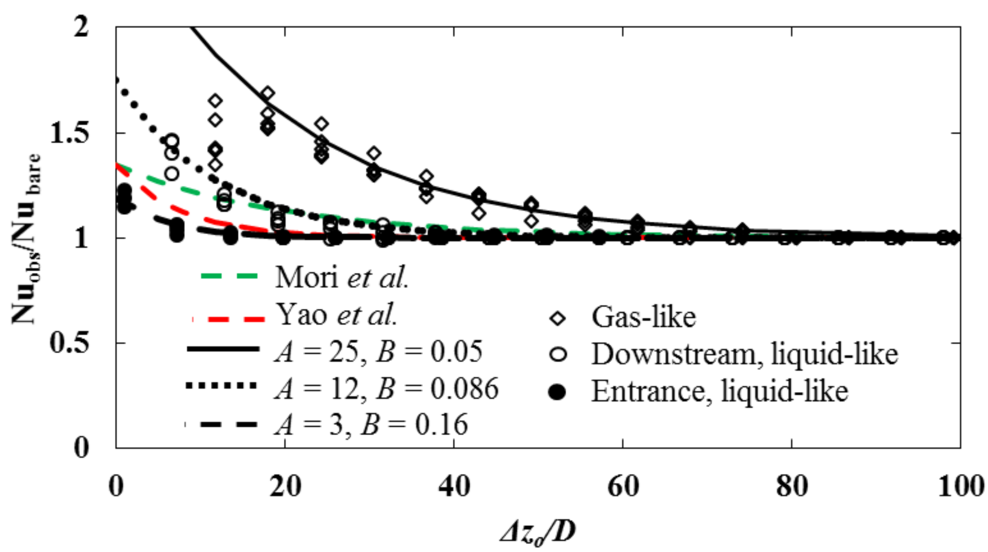

Figure 19: Measured normal heat transfer enhancement downstream of obstacles and comparison with predictions of previous correlations and present fits.

6. CONCLUSIONS

This article presents and discusses heat transfer measurements obtained in CO_2 flowing upwards in a 8 mm ID tube with and without flow obstructions at supercritical pressures and wide ranges of heat and mass fluxes. Heat transfer deterioration (HTD) was observed under certain conditions for both the bare tube and the obstacle-equipped tube. An examination of the parametric trends has shown that the SC heat transfer coefficient variation with bulk enthalpy was fairly insensitive to inlet temperature and pressure changes, while it was strongly affected by changes in mass and heat fluxes. An important finding of the bare tube experiments is that the dependence of SCHT on mass flux appears to be suppressed at HTD conditions. This may be explained by a conjecture that at HTD conditions the buoyancy effect is sufficiently strong to suppress the dependence of heat transfer on convection effects, which would normally increase with increasing mass flux. The increase in heat transfer coefficient (HTC) was most pronounced for blunt than rounded obstacles and for those having a larger flow blockage. In this respect, the effectiveness of obstacles increased when they were spaced with a relatively short pitch, but this would also result in higher pressure losses. Keeping the obstacle pitch short was found to be the most effective method of suppressing HTD. For certain flow conditions and obstacle locations, obstacles suppressed HTD or shifted its occurrence to downstream locations. An obstacle placed at the beginning of the heated section shifted the HTD to a higher bulk enthalpy at relatively low flows (300 - 500 kg m^{-2} s^{-1}) and suppressed HTD at a relatively high flow (700 kg m^{-2} s^{-1}). The enhancement effectiveness of the obstacles depended strongly on bulk enthalpy: the highest increases were obtained at the high enthalpies in the liquid-like region. The HTC enhancement decayed exponentially with distance from the obstacle. For normal heat transfer in liquid-like fluid, the decay length was short (typically 15D) when the obstacle was placed near the heated test section inlet and increased (to about 35*D*) when the obstacle was placed downstream; the decay length was significantly longer (typically 60*D*) in the gas-like region. For most conditions, the flow obstacles reduced the maximum wall temperatures or had a neutral effect. However, for certain conditions (low flows and enthalpies in the vicinity of the pseudo-critical enthalpy or lower than that), flow obstacles resulted in higher wall temperatures than those in the bare tube reference case, and triggered heat transfer deterioration.

ACKNOWLEDGMENTS

This study is part of the Canadian Gen-IV National Program. Funding for this program was provided by Natural Resources Canada through the Office of Energy Research and Development, Atomic Energy of Canada Limited, and Natural Sciences and Engineering Research Council of Canada.

NOMENCLATURE

Bu	buoyancy parameter
c_{pb}	specific heat at bulk temperature, kJ kg^{-1} K^{-1}
$\bar{c}_p$	average specific heat, kJ kg^{-1} K^{-1}
D	inside diameter of the tube, mm
Gr	Grashof number
g	gravitational acceleration, m s^{-2}
H	heat transfer coefficient, kW m^{-2} K^{-1}
h_b	specific bulk enthalpy, kJ kg^{-1}
h_{in}	specific enthalpy at inlet, kJ kg^{-1}
h_{pc}	pseudo-critical specific enthalpy, kJ kg^{-1}
k	thermal conductivity, kW m^{-1} K^{-1}
L_h	heated length, mm
$\dot{m}$	mass flow rate, kg s^{-1}
Nu	Nusselt number
$\mathrm{Nu_b}$	bulk Nusselt number
$\mathrm{Nu_{bare}}$	Nusselt number in a bare tube
$\mathrm{Nu_{obs}}$	Nusselt number in an obstructed tube
n	exponent in Jackson’s correlation
P	pressure, MPa
P_c	critical pressure, MPa
$\mathrm{Pr_b}$	bulk Prandtl number
Q_e	nominal electrical power supplied to the test section, kW
q	wall heat flux, kW m^{-2}
q_{loss}	heat flux to surroundings (heat losses), kW m^{-2}
q^v	volumetric heat generation, kW m^{-3}
$\mathrm{Re_b}$	bulk Reynolds number
r_i	test section inner radius, mm
r_o	test section outer radius, mm
T_{in}	test section inlet temperature, °C

T_{pc}	pseudo-critical temperature, °C
T_w	corrected wall temperature, °C
$T_{w,o}$	tube outer wall temperature (measured by thermocouple), °C
z	axial distance from the unheated test section inlet, mm
z_h	axial distance from the heated test section inlet, mm
	Greek symbols
ΔQ_e	power imbalance, W
Δz	axial distance between obstacles (pitch), mm
Δz_O	axial distance from the downstream end of an obstacle, mm
θ	angle of thermocouple location relative to the obstacles, °
μ_b	bulk dynamic viscosity, Pa s
ρ_b	fluid density at bulk temperature, kg m^{-3}
ρ_w	fluid density at wall temperature, kg m^{-3}
$\bar{\rho}$	average of densities at bulk and wall temperatures, kg m^{-3}

	Acronyms
DPT	differential pressure transducer
HTC	heat transfer coefficient
HTD	heat transfer deterioration
LHS	left hand side
PS	power supply
PT	pressure transducer
RHS	right hand side
R_{SCHT}	ratio of the SCHT of the obstructed to the bare tube
SC	super-critical
SCHT	super-critical heat transfer
SCUOL	University of Ottawa supercritical CO_2 loop
SCWR	super-critical water reactor

REFERENCES

Bae, Y. Y., Kim, H. Y., 2009. Convective heat transfer to CO_2 at a supercritical pressure flowing vertically upward in tubes and an annular channel. Exp. Therm. Fluid Sci. 33, 329-339.

Cheng, X., Liu, X.J., Gu, H.Y., 2011. Fluid-to-fluid scaling of heat transfer in circular tubes cooled with supercritical fluids. Nucl. Eng. Des. 241, 498–508.

Eter, A., Groeneveld, D., Tavoularis, S., Onder, N., 2013. Heat transfer enhancement at supercritical pressures. Proc. 12t^{h} Intern. Conf. On CANDU Fuel, September 15-18, Kingston, Ontario, Canada.

Eter, A., Groeneveld, D., Tavoularis, S., 2016. An experimental investigation of supercritical heat transfer in a three-rod bundle equipped with wire-wrap and grid spacers and cooled by carbon dioxide. Nucl. Eng. Des. 303, 173-191.

Fewster, J., Jackson, J.D., 2004. Experiments on supercritical pressure convective heat transfer having relevance to SPWR. Proc. ICAPP'04, Paper 4342, June 13−17. Pittsburgh, PA, USA.

Groeneveld, D.C. Yousef, W.W., 1980. Spacing devices for nuclear fuel bundles: A survey of their effect on CHF, Post-CHF heat transfer and pressure drop. Proc. ANS/ASME/NRC Intern. Topical Meeting on Nuclear Reactor Thermal-Hydraulics, October 5-8. Saratoga springs, N.Y., NUREG/CP-0014, Vol. 2, 1111-1130.

Incropera, F.P., DeWitt, D.P., Bergman, T.L., and Lavine, A.S., 2007. Fundamentals of Heat and Mass Transfer. 6th edition, John Wiley and Sons.

Jackson, J. D., 2002. Consideration of the heat transfer properties of supercritical pressure water in connection with the cooling of advanced nuclear reactors. Proc. 13th Pacific Basin Nuclear Conference Shenzhen City, China.

Jackson, J. D., 2008. A semi-empirical model of turbulent convective heat transfer to fluids at supercritical pressure. Proc. 16th Intern. Conf. On Nuclear Engineering, Orlando, USA, Jiang, K., 2015. An experimental facility for studying heat transfer in supercritical fluids. M.A.Sc. Thesis, Department of Mechanical Engineering, University of Ottawa, Ottawa, Canada.

Lemonn, E.W., M'cLinden, M.O., Friend, D.G., 2002. Thermophysical properties of fluid systems. NIST Standard Reference Database Number 69, REFPROP: Version 7.0.

Miller, D.J., Cheung, F.B., Bajorek, S.M., 2013. On the development of a grid-enhanced single-phase convective heat transfer correlation. Nucl. Eng. Des. 264, 56-60.

Mori, H., Kaida, T., Ohno, M., Yoshida, S., and Hamamoto, Y., 2012. Heat transfer to a supercritical pressure fluid flowing in sub-bundle channels. Nucl. Sci. Techn. 49, 373–383.

Pioro, I. L., Duffey, R.B., 2003. Literature survey of heat transfer and hydraulic resistance of water, carbon dioxide, helium and other fluids at supercritical and near-critical pressures. Chalk River Laboratories, Chalk River, Ontario Canada.

Pioro, I. L., Duffey, R.B., 2007. Heat transfer and hydraulic resistance at supercritical pressures in power-engineering applications. ASME Press, New York.

Tanase, A., Groeneveld, D., 2015. An experimental investigation on the effects of flow obstacles on single phase heat transfer. Nucl. Eng. Des. 288, 195-207.

Yao, S.C., Hochreiter, W.J., Leech, W.J., 1982. Heat transfer augmentation in rod bundles near grid spacers. J. Heat Transfer. 104, 76-81.

Zahlan, H., Groeneveld, D., Tavoularis, S., 2015. Fluid-to-fluid scaling for convective heat transfer in tubes at supercritical and high subcritical pressures. Int. J. Heat Mass Transfer 73, 274–283.

Zahlan, H., Tavoularis, S., Groeneveld, D., 2015a. A look-up table for trans-critical heat transfer in water-cooled tubes. Nucl. Eng. Des. 285, 109-125.

Zahlan, H., Groeneveld, D., Tavoularis, S., 2015b. Measurements of convective heat transfer to vertical upward flows of CO_2 in circular tubes at near-critical and supercritical pressures. Nucl. Eng. Des. 289, 92-107.

Zwolinski, S., Anderson, M., Corradini, M., Licht, J., 2011. Evaluation of fluid-to-fluid scaling method for water and carbon dioxide at supercritical pressure. Proc. 5th Intern. Symp. On Supercritical Water-Cooled Reactors (SCWR5), Vancouver, Canada.

Chapter 6

Convective heat transfer to CO_2 - cooled tubes with and without Flow obstacles at high sub-critical pressures

This chapter addresses the obstacles effects on near-critical heat transfer in an 8 mm ID tube. The results are presented in the form of the manuscript

> Eter, A., Groeneveld, D., Tavoularis, S., 2016. Convective heat transfer to CO_2 - cooled tubes with and without Flow obstacles at high sub-critical pressures. To be submitted to Nucl. Eng. Des.

This paper shows that the bare-tube single phase (liquid) results are in good agreement with Gnielinski's correlation. The obstacle effect decays rapidly at single phase conditions. Gnielinski’s correlation with Yao's correction may be used for predicting the decaying flow obstruction effect. The bare-tube CHF data at P/P_c = 0.90, after conversion into water-equivalent conditions, are found to be under predicted by the CHF look-up table. Obstacles suppressed the CHF occurrence locally and shifted the CHF location to a downstream location. The increase in CHF depends strongly on the distance from the nearest upstream obstacle and ranged from 0 - 300 %. Available correlations for the effect of flow obstructions on CHF could not provide a satisfactory prediction. No reliable prediction for the film boiling for our test data could be identified. Increasing the pressure from P/Pc = 0.9 to 0.95 reduced the maximum film boiling temperature; a further increase in pressure to supercritical conditions (for the same inlet temperature, heat flux and mass flux) resulted in a significant decrease in the maximum wall temperature. The obstacle reduced the maximum wall temperature noticeably at all pressures.

Convective Heat Transfer to CO_2 -Cooled Tubes With and Without Flow Obstacles at High Subcritical Pressures

Ahmad Eter
Doctoral Student
Department of Mechanical Engineering
University of Ottawa
Ottawa, ON, Canada K1N 6N5
Aeter@uottawa.ca

Dé Groeneveld
Adjunct Professor
Department of Mechanical Engineering
University of Ottawa
Ottawa, ON, Canada K1N 6N5

Stavros Tavoularis[4]
Professor
Department of Mechanical Engineering
University of Ottawa
Ottawa, ON, Canada K1N 6N5
stavros.tavoularis@uottawa.ca

[4] Corresponding author

ABSTRACT

Heat transfer measurements to CO_2-cooled tubes with and without flow obstacles at high subcritical pressures were obtained at the University of Ottawa's supercritical test facility. Tests were performed for vertical upward flow in a directly heated 8 mm ID tube for a pressure range from 6.6 to 7.2 MPa, a mass flux range from 115 to 1000 kg m^{-2} s^{-1}, and a wall heat flux range from 1 to 122 kW m^{-2}. Cases with spacing between obstacles equal to 250, 500 and 1000 mm were investigated. The results are presented in plots of wall temperature and heat transfer coefficient vs. bulk fluid enthalpy. The effects of flow conditions and obstacle geometry and spacing on high subcritical heat transfer have been discussed. Obstacles were found to suppress nucleate boiling, increase the CHF and lower the maximum post-CHF temperature. The maximum increases in CHF and in post-dryout heat transfer coefficient were observed for the obstacles having a spacing of 250 mm. Comparisons of the experimental data with prediction methods for single-phase heat transfer, CHF and post-dryout heat transfer are also presented.

Keywords:
Convective heat transfer
High subcritical pressure
Carbon dioxide
CHF
Obstacles

1. Introduction

During startup or postulated accidents, fuel elements of supercritical water-cooled reactors (SCWR) would experience cooling at high sub-critical pressures. Therefore, the accurate prediction of heat transfer and critical heat flux (CHF) characteristics at high subcritical pressures is essential for SCWR design. Knowledge of the effects of flow obstructions such as fuel rod spacers under such conditions is also important. Past literature has shown that, at low and moderate sub-critical pressures, CHF occurrence generally leads to a sudden rise in the wall temperature, whereas, at high subcritical pressures, this temperature rise is relatively small and gradual. Considering that, as a rough approximation, CHF is proportional to the latent heat, which vanishes at the critical pressure P_c, CHF is expected to be relatively low and the post-dryout heat transfer coefficient is expected to be elevated because of more efficient heat transport at near-critical pressures.

Several early studies have investigated experimentally heat transfer to flow of water in upward vertical, uniformly heated round tubes at high subcritical pressures; these include the studies by Schmidt (1960), Swenson *et al.* (1962), Miropol'skiy (1962), Bishop *et al.* (1965) and Herkenrath *et al.* (1967). Renewed interest on this topic was received in recent years. Some of the main results of the relevant studies will be summarized in the following paragraphs.

Schmidt (1960) performed experiments at high subcritical and supercritical pressures in the range from 17 to 30 MPa for water flows in vertical and horizontal tubes with 8 mm ID. He noted a significant decrease in CHF as the pressure approached the critical value. As a result of this, the CHF location and the maximum temperature location shifted towards lower enthalpies, as pressure was increased under constant wall heat flux. Further increases of the system pressure above the critical pressure at the same heat flux and mass flux led to a gradual disappearance of a maximum in the wall temperature profile at a pressure of 30 MPa (P/P_c =1.36).

Swenson *et al.* (1962) investigated heat transfer to upwards vertical flow of water in a stainless steel tube with 10.4 mm ID at a pressure of 20.7 MPa, mass fluxes of 994 and

1356 kg m^{-2} s^{-1}, and inlet specific enthalpies in the range 1760 – 2220 kJ kg^{-1}. They also investigated the case of an internally ribbed carbon-steel tube having an ID of 10.4 mm. Their results showed that, by comparison to the bare tube, the ribbed tube suppressed CHF and maintained nucleate boiling at higher bulk enthalpies. The film boiling data obtained from the bare tube were described within 10% by the modified form $\mathrm{Nu} = 0.076\,\mathrm{Re}^{0.8}\,\mathrm{Pr}^{0.4}$ (Nu, Re and Pr are, respectively, the Nusselt, Reynolds and Prandtl numbers) of the Dittus-Boelter (1930) correlation.

Bishop *et al.* (1965) performed heat transfer experiments in water flowing in tubes made of hastelloy C and stainless steel 316 with 5.08 and 2.54 mm ID. Their pressure P was in the range 16.69 – 21.51 MPa (P/P_c = 0.76 – 0.98), the mass flux G was in the range 678 – 3390 kg m^{-2} s^{-1}, and the exit quality varied from 7 to 100 %. With the exception of results at their lowest mass flux of 678 kg m^{-2} s^{-1}, their film boiling data were described within 19% by the expression $\mathrm{Nu} = 0.0193\,\mathrm{Re}^{0.8}\,\mathrm{Pr}^{1.23}\left(\frac{\rho_g}{\rho_b}\right)^{0.68}\left(\frac{\rho_g}{\rho_l}\right)^{0.068}$, where the bulk density was calculated from the gas and liquid densities as $\rho_b = \rho_g(\alpha) + \rho_l(1-\alpha)$ and the void fraction α was calculated by the homogenous model.

Chen *et al.* (2015) conducted CHF tests for subcooled water at high subcritical pressures in tubes made of Inconel 625 having ID of 4.62, 7.98 and 10.89 mm. The operating conditions were: P = 1 – 20 MPa (P/P_c = 0.05 – 0.90), G = 454 - 4055 kg m^{-2} s^{-1}, and inlet subcooling T_s - T_{in} = 53 – 361 K. Their data showed that CHF was inversely proportional to $D^{0.35}$, where D is the internal diameter of the tube. The authors correlated their CHF data as $\mathrm{CHF} = Cq_s$, where $q_s = (h_s - h_{in})GD/(4L_h)$ was the heat flux that resulted in saturation temperature at the end of the heated length, and

$C = \mathrm{Min}[2350(1-0.0307P)(G(H_s - H_{in}))^{-0.35}(D/0.008)^{-0.35}, 1.0]$.

This correlation predicted the high subcritical data with an error ranging from -15 to 20%.

The experiments in water require expensive high pressure test facilities operating at high temperatures and powers. A more convenient approach for investigating high-pressure subcritical heat transfer is by means of using modelling fluids. Recent studies using refrigerant R-134a as a modelling fluid include the ones by Hong *et al.* (2004), Vijayarangan *et al.* (2005), and Chun *et al.* (2007).

Hong *et al.* (2004) investigated CHF occurrence for R-134a upward flows in an internally heated vertical annular channel made of Inconel 601. They performed CHF tests at both steady and transient pressures through the critical pressure. The operating conditions were as follows: P = 0.63 – 3.98 MPa (P/P_c = 0.16 – 0.98), G = 501, 1002 and 1502 kg m^{-2} s^{-1}, and inlet subcooling T_s - T_{in} = 14.5, 24.8, 34.5, and 44.3 K. For steady pressures, the CHF value decreased as the pressure approached the critical pressure. Mass flux and inlet subcooling had small effects on the CHF at near-critical pressures. The sharp decrease in the CHF near the critical pressure was attributed to the dramatic decrease in the latent heat h_{fg}. During transient tests with the pressure being reduced from supercritical to high subcritical values, the CHF occurred as soon as the pressure dropped below the critical value.

Vijayarangan *et al.* (2005) conducted CHF experiments in a vertical stainless steel tube having an ID of 12.7 mm and cooled by R-134a. The operating conditions were as follows: P = 1 – 3.97 MPa (P/P_c = 0.25 – 0.98), G = 200 - 2000 kg m^{-2} s^{-1}, and exit quality in the range 0.17 – 0.94. They compared their CHF data with predictions based on the look-up table of Groeneveld *et al.* (1996) and the correlation of Katto and Ohno (1984). The prediction methods were in good agreement with experimental values for low pressures (P/P_c < 0.5). At high reduced pressures (P/P_c= 0.6 - 0.94), however, the prediction error varied between 20 and 250% for the correlation of Katto and Ohno (1984) and between 50% and 350% for the look-up table. Vijayarangan *et al.* (2005) modified the correlation of Katto and Ohno (1984) to the following form

$$\frac{\mathrm{CHF}}{Gh_{fg}} = \frac{0.0051(\rho_g/\rho_l)^{0.133}(\sigma\rho_l/G^2L_h)^{1/3}(P/P_c)^{0.147}\,\mathrm{Re}^{0.25}}{1+0.0031(L_h/D)},$$

where σ is the surface tension. This correlation predicted their experimental CHF within ±30 % at low reduced pressures (P/P_c < 0.5); however, the prediction error increased to a range from -30% to 70%, when the reduced pressure range was from 0.6 – 0.94.

Chun *et al.* (2007) conducted CHF tests in R-134a at high subcritical pressures in a 5×5 rod bundle. The heated rods were made of Inconel 601 with an OD of 9.5 mm and a heated length of 2000 mm. Grid spacers without mixing vanes were located every 564 mm to maintain a rod pitch of 12.85 mm. The authors claimed that the grid spacers had no effect on the CHF, but presented no justification for this claim and performed no bare bundle tests. The operating conditions were: P = 3 – 4.03 MPa (P/P_c = 0.74 – 0.99), G = 50 - 2000 kg m^{-2} s^{-1}, and T_s - T_{in} = 40 – 84 K. They noted that the CHF was only slightly affected by the pressure at the very low mass flux of 50 kg m^{-2} s^{-1}. However, the effect of pressure became significant when the mass flux increased to 2000 kg m^{-2} s^{-1}. At high subcritical pressures, CHF was found to shift to a negative quality (subcooled liquid). CHF at high subcritical pressures was found to be affected by changes in the mass flux but not by inlet subcooling. As expected, they found that CHF no longer occurred when the pressure was increased to just above the critical pressure.

Recently, Zahlan *et al.* (2015) reported the results of experiments at high subcritical pressures in vertical Inconel tubes having 8 and 22 mm ID and cooled by CO_2. The operating conditions were as follows: P = 5.91 – 7.17 MPa (P/P_c = 0.80 – 0.97), G = 193 - 2041 kg m^{-2} s^{-1}, q = 2.9 – 280 kW m^{-2} and T_{in} = 7.3 – 12.2 °C. Their results showed that the heat transfer coefficient (HTC) in the 8 mm ID tube was slightly higher than that in the 22 mm ID tube for single-phase liquid flow. During nucleate boiling, the impact of diameter was negligible, whereas the impact of diameter on CHF was not discussed. Pressure and inlet temperature were found to have negligible impact on the HTC during single phase liquid flow while mass flux was found to have a significant impact on the HTC. As the mass flux was increased, the HTC was found to increase. As the heat flux was increased under constant other conditions, the heat transfer mode changed from single-phase liquid to nucleate boiling and eventually film boiling. Zahlan *et al.* noticed a decrease in the HTC at low mass and heat fluxes in the 22 mm ID tube, which was similar to heat transfer deterioration at supercritical pressures.

In the present investigation, CO_2 was chosen as a modelling fluid because of its lower critical pressure (7.4 MPa) and critical temperature (31°C) and lower power requirements compared to water, in which the critical pressure and temperature are 22.1 MPa and 374 °C, respectively. This is the first systematic investigation of the flow obstacle effect on heat transfer and CHF at high sub-critical pressures. The present experimental investigation is a continuation of the supercritical heat transfer investigation at the University of Ottawa by Zahlan *et al.* (2015) on CO_2-cooled directly heated tubes and by Eter *et al.* (2016a, 2016b) on CO_2-cooled 3-rod bundles and tubes with and without flow obstructions.

2. Experimental facility, instrumentation and measuring procedures

The present investigation was conducted in the University of Ottawa Supercritical CO_2 loop (SCUOL). Figure 1 shows the main components of this loop, with additional details provided by Eter *et al.* (2016). The maximum operating pressure was 10 MPa. The test section wall was heated by the Joule power generated by electric current provided by a rectified power supply rated at a maximum voltage of 60 V and a maximum current of 2833 A. The fluid inlet temperature to the test section was controlled by a 22 kW pre-heater. Cooling of the loop was achieved by passing the operating fluid through four heat exchangers connected in parallel; two of these units used centrally supplied chilled water as a secondary fluid, whereas the other two used ethylene glycol, which was circulated from a tank contained in a freezer room.

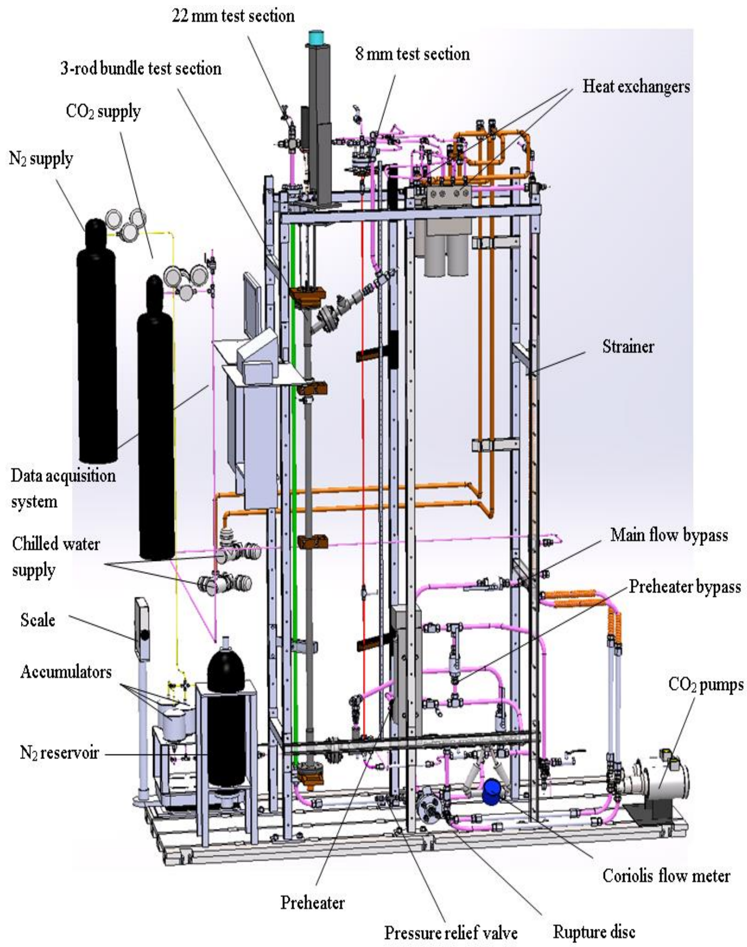

Figure 1: 3-D view of the University of Ottawa multi-fluid supercritical loop (Jiang, 2015).

The test section used for all measurements presented in this paper was an Inconel-600 tube, mounted vertically with CO_2 flowing upwards. This tube had an ID D = 8 mm, a wall thickness of 1 mm and a heated length L_h = 1.94 m. The heated part of the tube was preceded by an unheated section with a length of 0.89 m, which ensured that the flow entering the heated section was fully developed and free of entrance effects. The test section was insulated thermally by layers of fibreglass cloth tape, with a thickness of 8 mm, surrounded by a tube made of rubber foam with a thickness of 50 mm. Cylindrical obstacles with a diameter of 4 mm (25% blockage ratio) and a length of 10 mm were inserted inside the test section and kept in place by movable magnets positioned in the exterior of the tube (Figure 2).

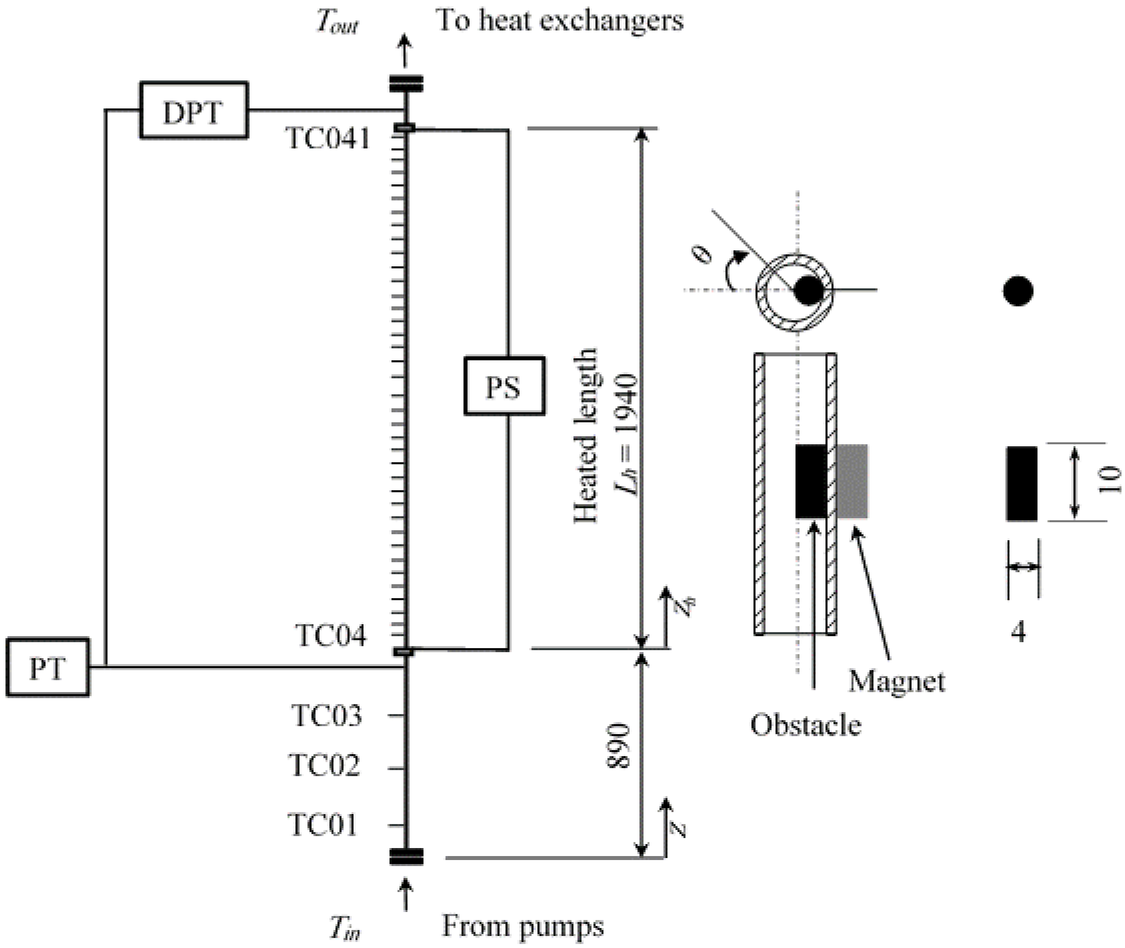

Figure 2: LHS: Schematic diagram of the test section showing the locations of thermocouples (TC), the power supply (PS), the pressure transducer (PT), and the differential pressure transducer (DPT); RHS: details of the obstacles and their locations; dimensions are in mm.

The wall temperature along the test section was measured with T-type (Copper-Constantan) thermocouples (Omega SA1XL-T-SRTC), having an uncertainty of 0.5 K and a time constant of less than 0.15 s. The thermocouples were attached to the exterior wall of the test section using a silicone-based adhesive, which has a temperature rating of 260˚C. The contact lines of the obstacles and the thermocouples were at diametrically opposite locations (0° and 180°, respectively, in the sketch shown in Figure 2). The bulk fluid temperatures at the inlet and outlet of the test sections and other locations of the loop were measured with ultra-precise immersion RTD sensors (Omega P-M-1/10-1/8-5-1/2-G-15), having an uncertainty of 0.1°C within the range between 0 and 100°C. The test section inlet pressure was measured by a pressure transducer (Omega PX01C1-3KA5T) with a specified uncertainty of 21 kPa, which was calibrated in the range of 0 to 10342 kPa so that its uncertainty was reduced to 8 kPa. The pressure drop across the heated length of the test section was measured with a differential pressure transmitter (Omega PX771A-300DI), having an uncertainty of 75 Pa. The CO_2 mass flow rate was measured with a Coriolis flow meter (Micro Motion® ELITE® CFM050M320N0A2E2ZZ), having an uncertainty of 0.05% for liquid flow. The instantaneous voltage drop across the heated length of the test section was measured with a 24-bit digital voltage measurement module (National Instruments NI 9225), having a range of ±300 V and an uncertainty of 0.034 V. The rectified voltage fluctuated at a frequency of 360 Hz and was sampled at a much higher sampling rate. The electrical power supplied to the test section was calculated from the measured rms voltage and the measured electrical resistance of the test section. A dedicated computerized data acquisition system was used to monitor and control different loop operations and to record the data. All pressure and temperature measurements were acquired at a rate of 10 samples/s. The measurements were recorded after the operating conditions had stabilized. Data processing was done with the use of a code written in MATLAB. Spurious values in the data were removed. The data values used in the analysis of the results represent time-average values over 60 s intervals.

As an overall check of the accuracy of the measured flow rate, the inlet and outlet RTD measurements and the NIST code property values, we compared the electrical power Q_e

supplied to the test section to the thermal power $\dot{m}(h_{out} - h_{in})$ absorbed by the fluid. The heat balance error was calculated as

$$\Delta Q_e = Q_e - \dot{m}(h_{out} - h_{in}) \,. \tag{1}$$

The specific enthalpies at the inlet h_{in} and the outlet h_{out} of the test section were calculated from the corresponding measured bulk temperatures and pressures. The average heat balance error for single-phase liquid flows was less than 5%.

3. Experimental conditions and calculation of reported properties

Experiments were performed in the bare tube and in the obstructed tube with the obstacles positioned in three different configurations, as listed in Table 1.

Table 1: Obstacle-equipped tube configurations

Configuration	Number of obstacles	Distance of downstream end of obstacle from the inlet[1] (mm)		Obstacle pitch (mm)
		First	Last	
1	2	935	1935	1000
2	2	935	1435	500
3	8	935	2685	250

[1]Heated length starts at 890 mm.

Table 2 lists the ranges of flow conditions covered in the experiments. In the online version, the new data can be found at http://dx.doi.or. In addition, some earlier data obtained by Zahlan *et al.* (2015) were taken into consideration.

Table 2: Flow conditions during measurements in the bare and obstructed tubes

P (MPa)	P/P_c	G (kg m^{-2} s^{-1})	q (kW m^{-2})	T_{in} (°C)
6.6 7.2	0.89 0.97	115, 130, 200, 500, 600, 700, 1000, 1500, 2000	2.5 – 122	9, 11, 20.2

The volumetric heat flux in the test section wall was calculated as

$$q^{v} = \frac{Q_e}{\pi(r_o^2 - r_i^2)L_h} \quad , \tag{2}$$

where r_o and r_i are the tube outer and inner radii,. The inner wall temperature T_w was calculated from the measured outer wall temperature $T_{w,o}$ using the heat diffusion equation with uniform internal energy generation in cylindrical coordinates (Incropera *et al*., 2007), as

$$T_w = T_{w,o} + \frac{2q_{loss}r_o - q^{v}r_o^2}{2k}\ln\frac{r_o}{r_i} + (r_o^2 - r_i^2)\frac{q^{v}}{4k} \quad , \tag{3}$$

where k is the thermal conductivity of Inconel 600 evaluated at the local $T_{w,o}$ and q_{loss} are the heat losses to the surroundings, which were neglected as being within the measurement uncertainty.

The wall heat flux was calculated as

$$q = \frac{Q_e}{\pi D L_h} \quad , \tag{4}$$

under the assumptions that no losses to the environment and no axial heat conduction occurred.

The bulk fluid enthalpy along the heated test section was calculated using the simplified energy equation

$$h_b = h_{in} + \frac{Q_e}{\dot{m}}\frac{z_h}{L_h} \quad , \tag{5}$$

where $\dot{m}$ is the mass flow rate and z_h is the axial distance along the heated section. The corresponding local bulk fluid temperature T_b and the thermo-physical properties of carbon dioxide were calculated using NIST software (Lemmon *et al.* 2002). Finally, the local heat transfer coefficient (HTC, *H*) was calculated as

$$H = \frac{q}{T_w - T_b} \ , \tag{6}$$

A discussion of heat losses, repeatability, and thermocouple and RTD calibration checks was provided by Eter *et al*. (2016b).

4. Measurements in the bare tube

This section presents the subcritical heat transfer results obtained in the bare tube for the conditions specified in Table 2. The experimental results are generally presented as plots of wall temperature and heat transfer coefficient vs. specific bulk enthalpy. The overall trends in the data will be presented first before discussing the specific trends for each heat transfer type and comparing them with predictions of correlations and trends at supercritical pressures. Single-phase results will be compared with predictions of Gnielinski's (1976) equation, which was found to provide the best fit over a wide range of conditions (Zahlan *et al.*, 2011). This equation is

$$\mathrm{Nu}_b = \frac{(f/8)(\mathrm{Re}_b - 1000)\mathrm{Pr}_b}{1 + 12.7(f/8)^{1/2}\left(\mathrm{Pr}_b^{2/3} - 1\right)} \tag{7}$$

where Re_b and Pr_b are the Reynolds and Prandtl numbers evaluated at the local bulk conditions and

$$f = \frac{1}{(1.82\log_{10}(\mathrm{Re}_b) - 1.64)^2}\,. \tag{8}$$

4.1 Typical wall temperature variations

Figure 3 shows some typical wall temperature measurements for different mass and heat fluxes at high subcritical pressures. Each plot contains results obtained by gradually increasing the heat flux. In all cases, single-phase conditions existed along part or all of the test section for sufficiently low heat fluxes. At higher heat fluxes, the wall temperature reached the saturation temperature and nucleate boiling occurred. As heat flux was further increased, nucleate boiling was replaced consecutively by transition and film boiling, which were accompanied by a sudden rise in local wall temperature. This phenomenon, which is commonly referred to as the "Critical Heat Flux condition" or "boiling crisis", occurred first at the test section outlet and advanced towards the inlet as the heat flux was increased (Figures 3c-f).

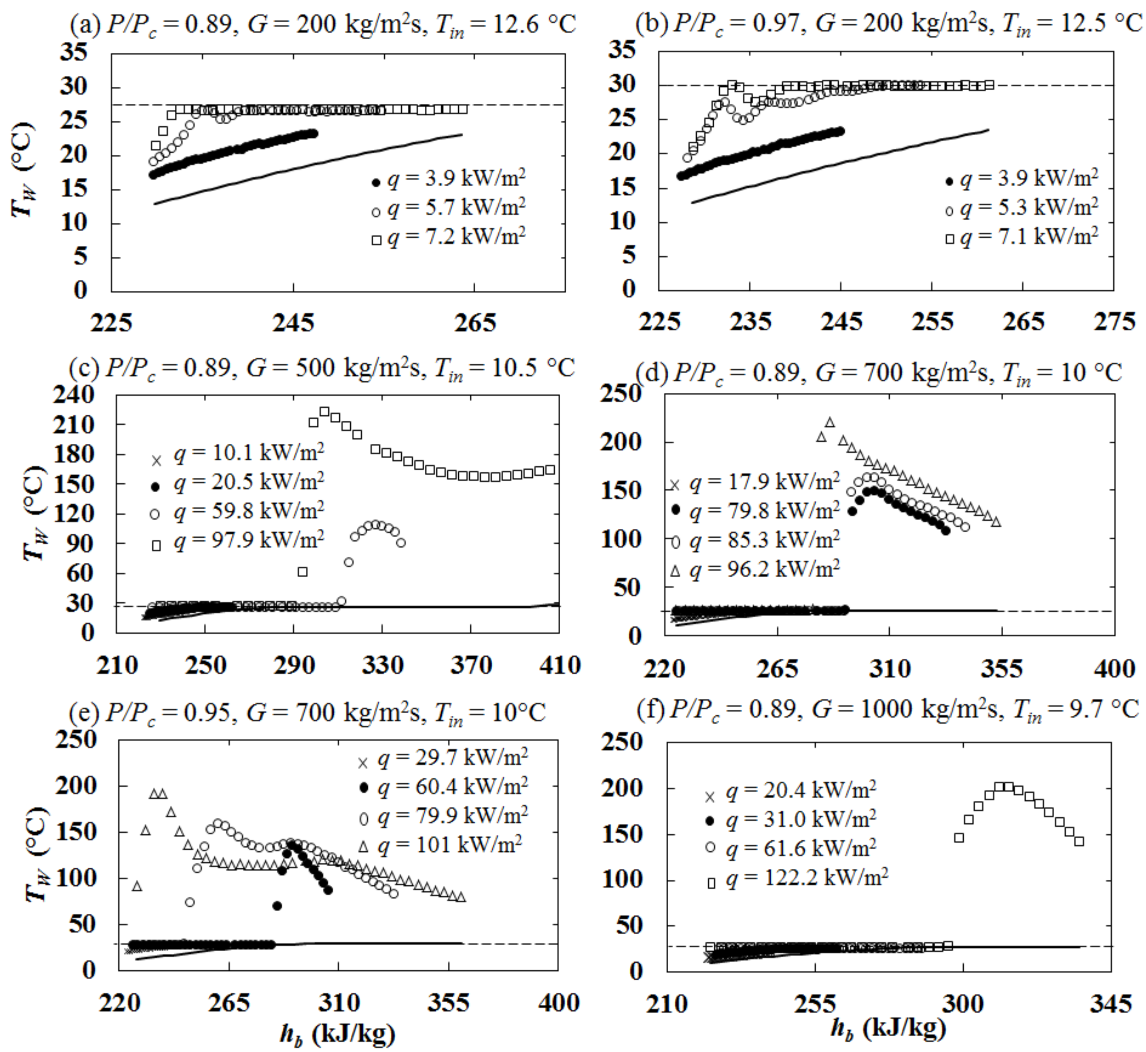

Figure 3: Wall temperature *vs.* specific bulk enthalpy at high subcritical pressures; horizontal dashed lines represent the saturation temperature and solid lines represent the bulk temperature variation.

4.2 Pre-CHF (single-phase and nucleate boiling) heat transfer

First, we will discuss some measurements at the lowest examined mass flux of approximately G = 200 kg m^{-2} s^{-1}. Results for comparable heat fluxes at both high subcritical and supercritical pressures (liquid-like region; Eter *et al.*, 2016b), shown in Figure 4, follow similar trends. At very low heat fluxes (q < 5 kW m^{-2}), the wall temperature T_w followed monotonically increasing trends but remained lower than the corresponding saturation temperature T_s or pseudo-critical temperature T_{pc} along the entire test section. The corresponding HTC was fairly constant for these conditions and had comparable values for both the subcritical and the supercritical pressures. Gnielinski's equation over-predicted the experimental HTC by 30-50%. When, however, the heat flux exceeded approximately 5 kW m^{-2}, a marked deterioration in heat transfer took place for both high subcritical and supercritical pressures. This led to a minimum in the HTC with roughly half the value for normal heat transfer, followed by a second, weaker, minimum and then a gradual monotonic increase. The striking similarity in the behaviour of the HTC, for both normal and deteriorated heat transfer on both sides of the critical pressure is a novel and somewhat surprising observation. In particular, the short-lived return of heat transfer to an apparently single-phase mode (Figure 4a,b) is very similar to the short-lived HTC relative enhancement at supercritical pressures (Figure 4c,d). This disturbed heat transfer profile was not observed at high mass fluxes.

The inaccuracy of Gnielinski's equation for the low mass flux G = 200 kg m^{-2} s^{-1} may be possibly attributed to the strong effect of buoyancy forces, which becomes negligible when the mass flux is increased. Indeed, as Figures 5 and 6 show, agreement of this equation with normal heat transfer measurements under high subcritical and supercritical (liquid-like region) pressures was quite fair for 500 kg m^{-2} s^{-1} $\leq G \leq$ 1500 kg m^{-2} s^{-1}. The exceptional case in these figures is the subcritical flow with q = 125 kW m^{-2} (Figure 6b), in which the subcritical wall temperature exceeded T_s and the more efficient nucleate boiling became the primary heat transfer mode. Under these conditions, the supercritical wall temperature remained lower than the pseudo-critical value, heat transfer remained normal and the HTC was in fair agreement with values from Gnielinski's equation.

Figure 7 illustrates the effect of mass flux on heat transfer for a high subcritical pressure and several heat fluxes. When single-phase heat transfer was the predominant mode, the local wall temperature decreased with increasing G, whereas the local HTC increased; these trends are in agreement with the predictions of Gnielinski's equation. Beyond the onset of nucleate boiling, however, T_w was close to T_s (in fact, a small superheat of up to 2 K was observable) and the heat transfer coefficient became insensitive to the mass flux.

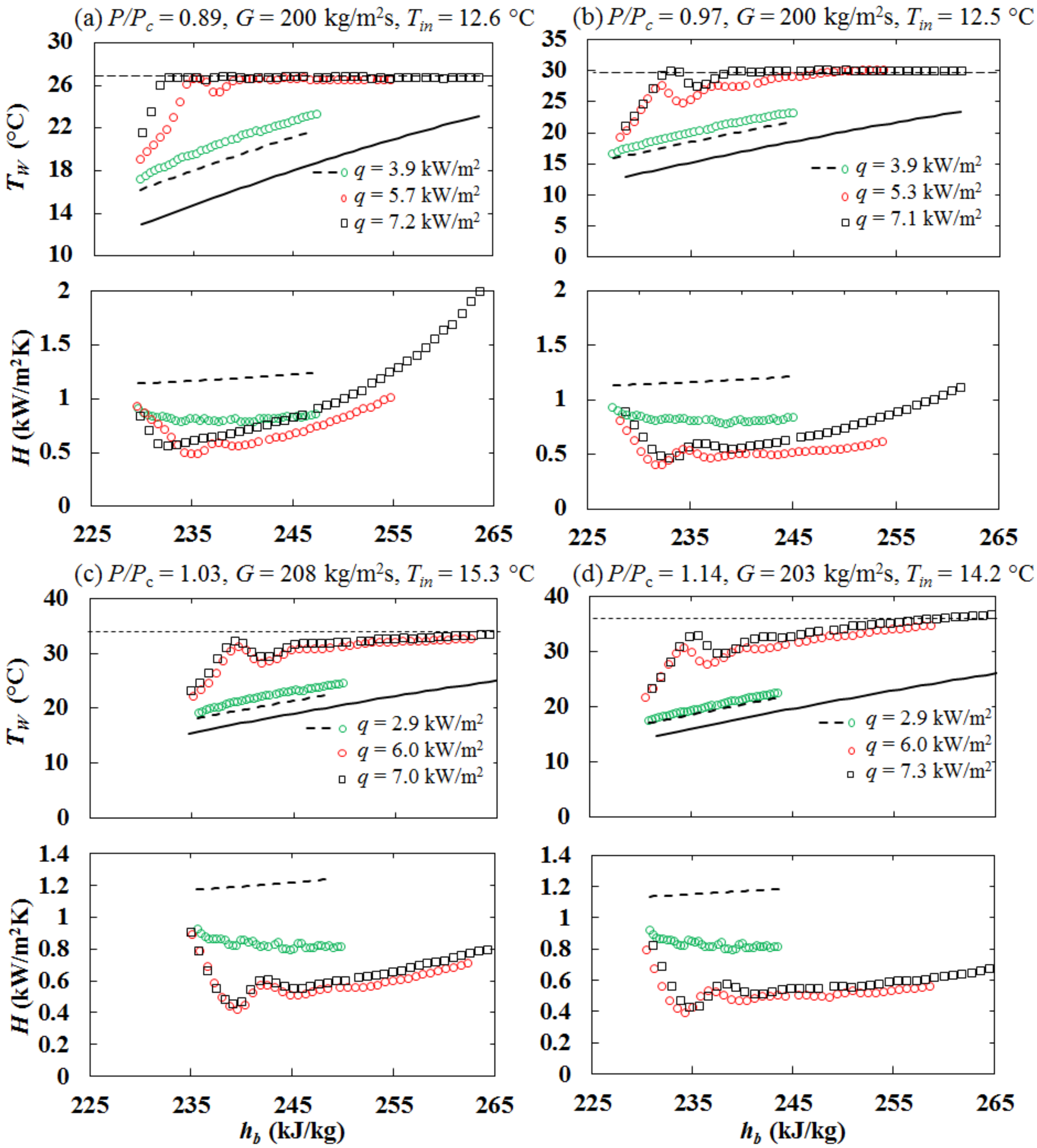

Figure 4: Wall temperature and heat transfer coefficient variations *vs.* specific bulk enthalpy for low heat fluxes and low mass fluxes at high subcritical and supercritical pressures; horizontal dashed lines represent the corresponding saturation or pseudo-critical temperatures; dashed lines represent predictions of Gnielinski's (1976) correlation and solid lines represent the bulk temperature.

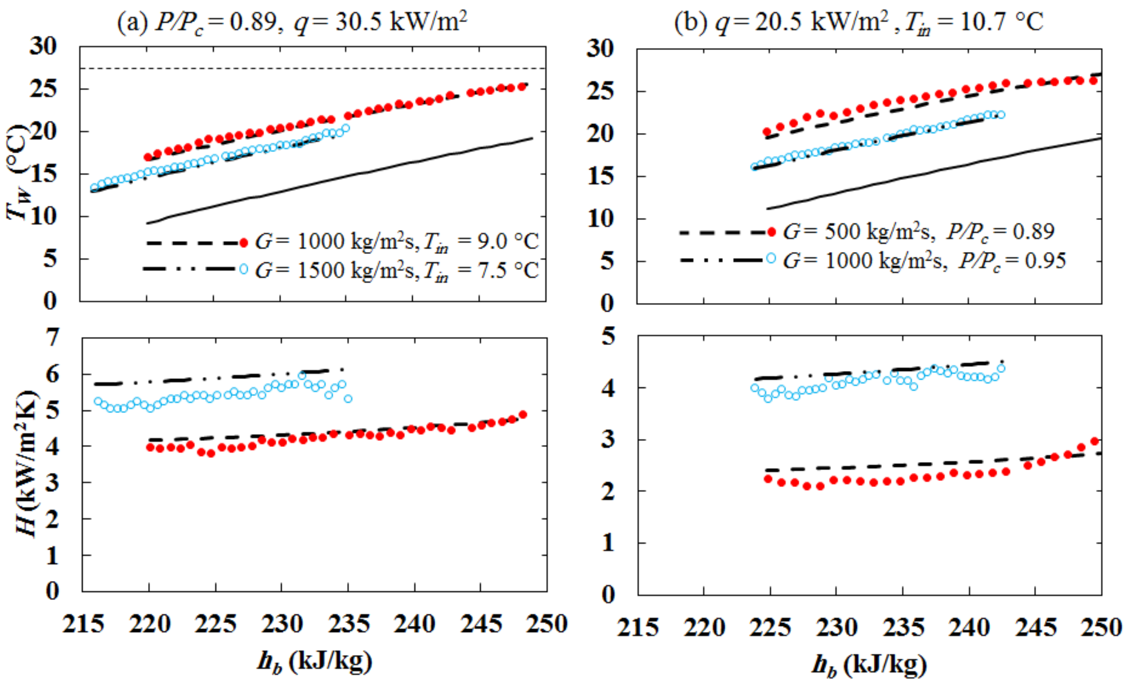

Figure 5: Comparison of measured wall temperatures and heat transfer coefficients (symbols) and predictions of Gnielinski's (1976) correlation (dashed and dot-dot-dashed lines); solid lines represents bulk temperature.

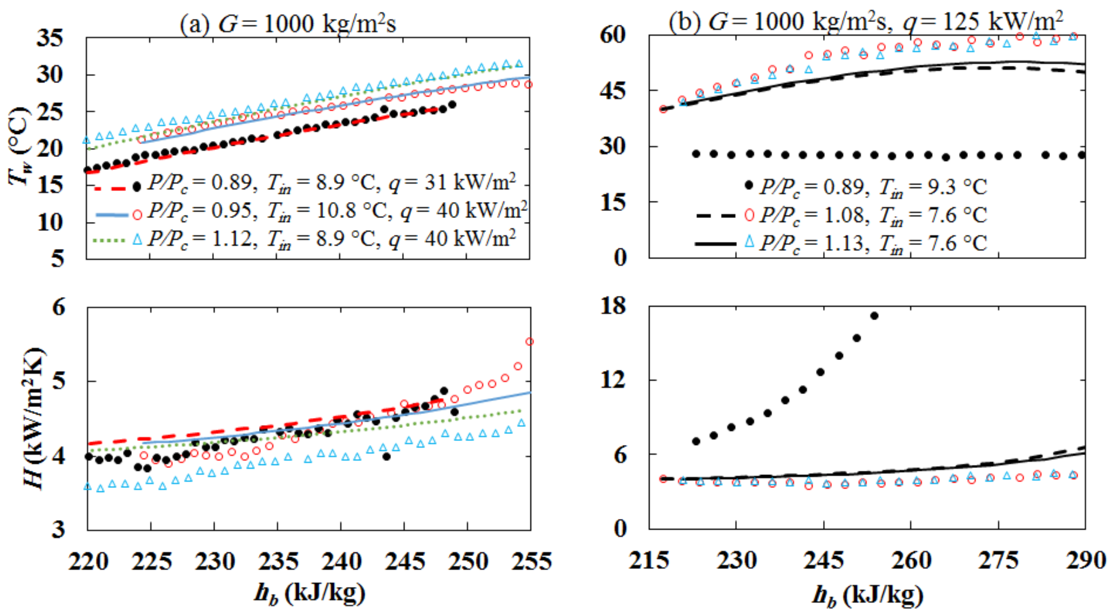

Figure 6: Comparison of single-phase and pre-CHF heat transfer measurements at high subcritical pressures to heat transfer measurements at supercritical pressures; solid and dashed lines represent predictions of Gnielinski's (1976) correlation.

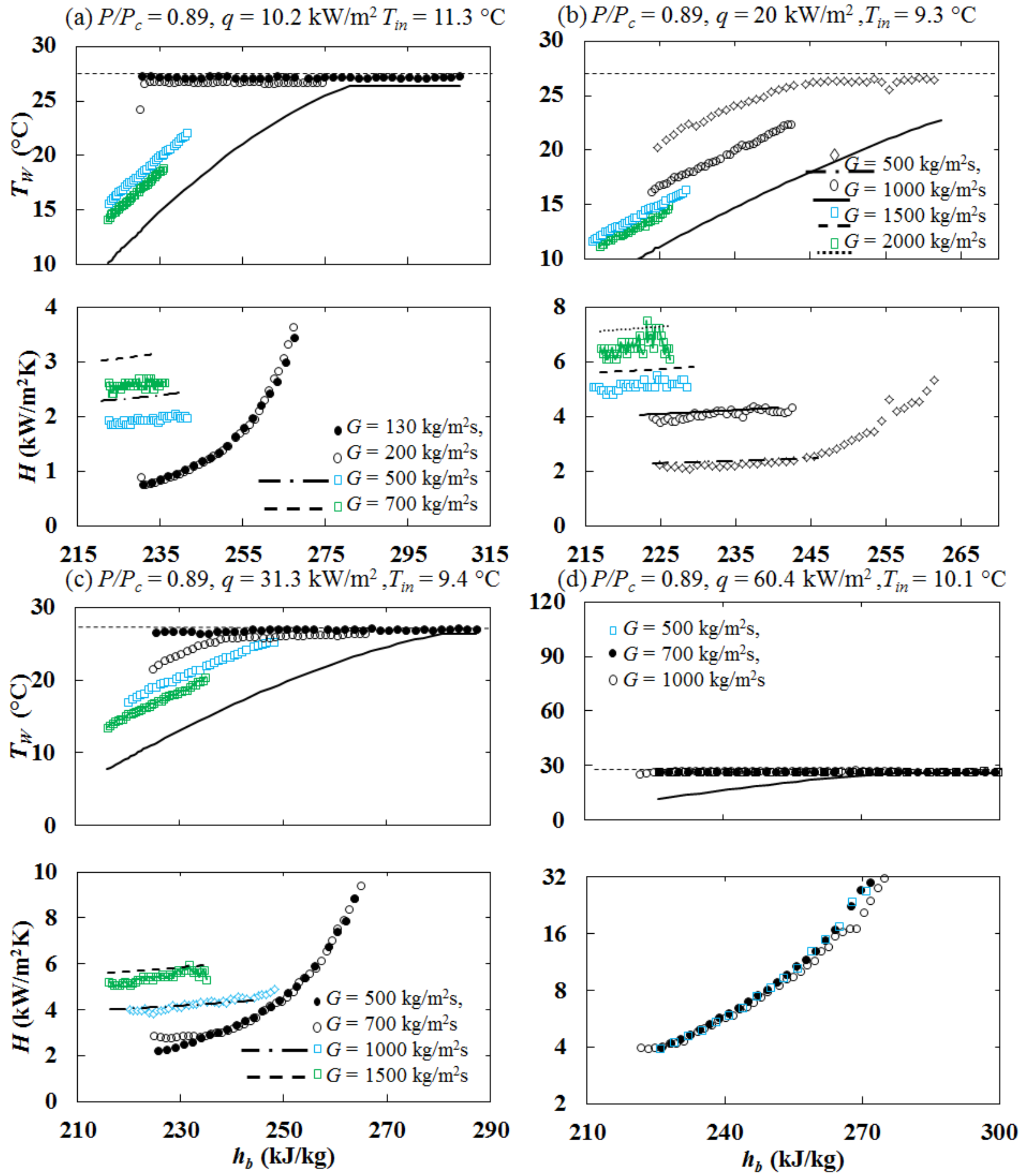

Figure 7: Effect of mass flux on T_w and HTC at a high subcritical pressure for pre-CHF heat transfer.

4.3 CHF

As shown in Figures 3c-f, an increase in heat flux under constant other conditions resulted in boiling crisis and dry-out first at the downstream end of the test section, followed by spreading of dry-out in the upstream direction as the heat flux was increased. The location of boiling crisis, which in past literature has also been referred to as the location of CHF, was defined to be midway between the most downstream thermocouple showing nucleate boiling and the adjacent downstream thermocouple showing the first occurrence of post-CHF conditions, which was characterized by a sudden temperature excursion. Note that the axial temperature profile at the highest examined subcritical pressure (P/P_c = 0.95) did not show a significant temperature excursion, especially at the higher flow rates; this increased the uncertainty in the determination of the CHF location at these conditions.

Table 3 presents a list of experimental conditions for which boiling crisis was observed, the boiling crisis location and the corresponding bulk specific enthalpy h_b and thermodynamic quality X_{th}. These values were extracted from the database of Zahlan *et al.* (2015), which were obtained in an 8 mm ID bare tube at the University of Ottawa. The same table also presents the predicted CHF_{corr} using the correlation given in Appendix B (B-1).

The CHF has been plotted *vs*. the thermodynamic quality in Figures 8-11, along with predictions of the CHF look-up table for water (Groeneveld *et al.*, 2006), after conversion into CO_2 equivalent conditions, as described in Appendix A. The CHF look-up table cannot be used to predict CO_2 data for P/P_c = 0.95, because its equivalent density ratio in water corresponds to P/P_c = 0.97, which is outside the table's range. In the following analysis, we examined the effects of specific parameters on the CHF, while keeping all other parameters constant. Because, however, the various test conditions could not be matched precisely from one run to another, comparisons were made for various sets of nominal flow conditions and the experimental CHF values were normalized to the nominal flow conditions, as described in Appendix B. Figures 8 and 9 show that the CHF decreased with increasing quality, in conformity with past experience. Note that in Figure 8 (P/P_c = 0.90) the CO_2-equivalent CHF lookup table significantly over-predicted the experimental data. The reason for this may be that the fluid-to-fluid modelling relationships used for converting the water-based CHF into CO_2-equivalent values were validated only for lower pressures (Groeneveld *et al.*, 1997) and may not be sufficiently accurate for high subcritical pressures.

The predicted and measured effects of pressure on the CHF *vs.* X_{th} curves are shown in Figure 10. This figure shows that, as the pressure increases, CHF decreases; this is attributed to a reduction in the latent heat h_{fg}. CHF correlations of Katto and Ohno (1984), Mishima (1984), and Sudo *et al.* (1985) are of the form CHF = $A\ h_{fg}\ fn(P,G,X)$, where A is an empirical coefficient and $fn(\ldots)$ is an empirical multi-variate function. Such correlations predict that CHF would decrease as the critical pressure is approached and vanish at the critical point. Figure 11 shows that the CHF increased with an increase in mass flux. This is in agreement with predictions of the look-up table (Figure 8) and the present CHF correlation (Equation B-1 of Appendix B).

Table 3 Boiling crisis in the bare tube

Experimental conditions					Conditions at boiling crisis			CHF$_{corr}$* (kW m^{-2})
P/P_c	P (MPa)	G (kg m^{-2} s^{-1})	q (kW m^{-2})	T_{in} (°C)	z_h (m)	h_b (kJ kg^{-1})	X_{th}	
0.943	6.98	508	53.6	10.4	0.803	265	-0.333	52.2
0.881	6.52	495	97.9	10.3	0.703	292	0.131	88.3
0.874	6.47	494	92.2	10.3	0.803	298	0.186	87.6
0.885	6.55	503	74.6	10.3	1.134	307	0.250	71.1
0.878	6.50	498	75.1	10.3	1.134	308	0.271	72.9
0.885	6.55	500	59.8	10.3	1.484	312	0.294	64.6
0.946	7.00	713	80.0	10.5	0.453	248	-0.549	69.9
0.953	7.05	708	60.4	10.8	1.434	284	-0.148	52.7
0.884	6.54	707	100.9	9.7	0.803	279	0.006	118.1
0.884	6.54	707	96.2	9.7	0.903	283	0.041	114.3
0.882	6.53	698	85.3	9.7	1.184	293	0.136	103.4
0.880	6.51	693	79.8	9.7	1.284	295	0.155	102.0
0.900	6.66	998	122.2	8.9	1.284	298	0.149	108.3
0.889	6.58	993	113.0	8.9	1.434	301	0.191	109.6
0.888	6.57	1001	102.0	8.9	1.684	305	0.230	102.4
0.923	6.83	990	94.9	9.1	1.784	307	0.204	79.3
0.947	7.01	1018	84.0	11.4	1.134	272	-0.276	89.3
0.932	6.90	1511	135.6	10.0	0.653	251	-0.435	161.6
0.947	7.01	1509	114.3	10.3	1.484	278	-0.196	126.3
0.889	6.58	1464	169.4	7.7	1.334	293	0.125	156.4
0.949	7.02	2002	169.6	11.6	0.153	232	-0.771	174.7
0.932	6.90	2013	150.9	11.0	1.334	274	-0.175	181.8
0.901	6.67	2041	225.2	8.5	1.034	275	-0.068	217.6
0.900	6.66	1937	220.4	8.4	1.184	285	0.032	194.1
0.907	6.71	1962	201.1	8.4	1.434	291	0.075	177.7
0.899	6.65	2005	180.2	8.3	1.634	291	0.088	184.6
0.891	6.59	2012	160.4	8.3	1.934	295	0.143	176.2
0.836	6.19	1897	169.3	9.2	1.834	302	0.260	153.8

* CHF$_{corr}$ is the prediction of the CHF at the corresponding experimental conditions by the fitted correlation (B-1) in Appendix B.

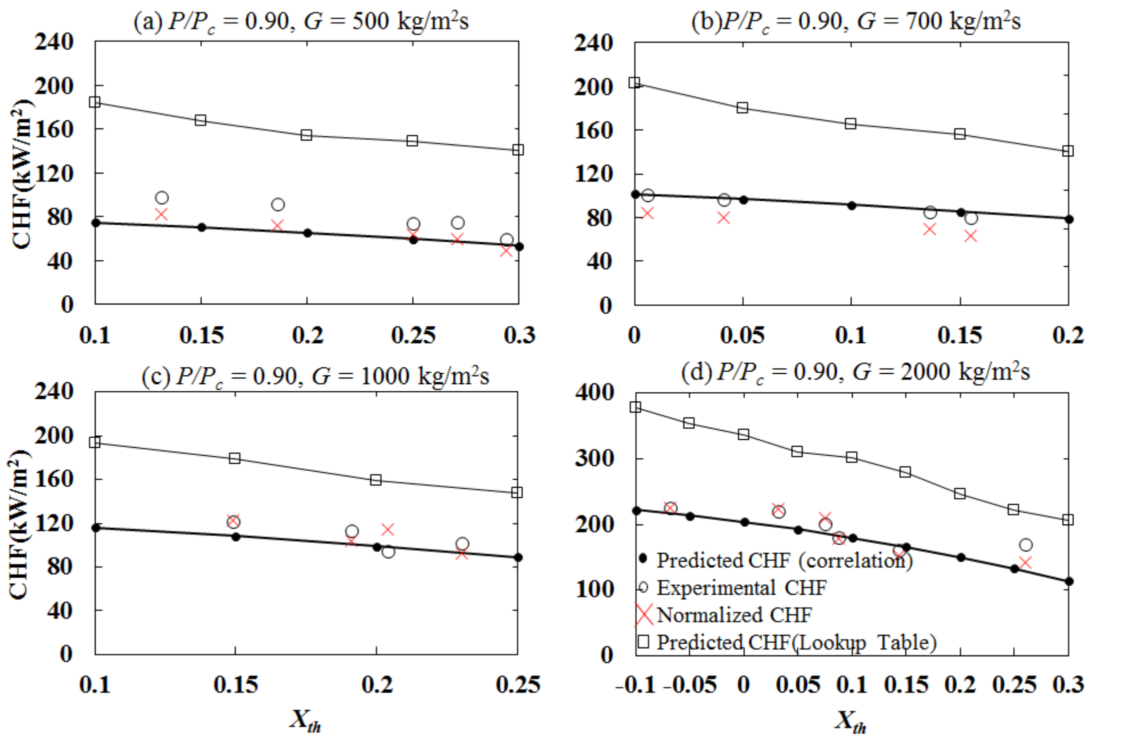

Figure 8: Comparison of experimental and predicted CHF using the CHF correlation of Appendix B and the CHF lookup table (Groeneveld *et al.*, 2006); P/P_c = 0.90.

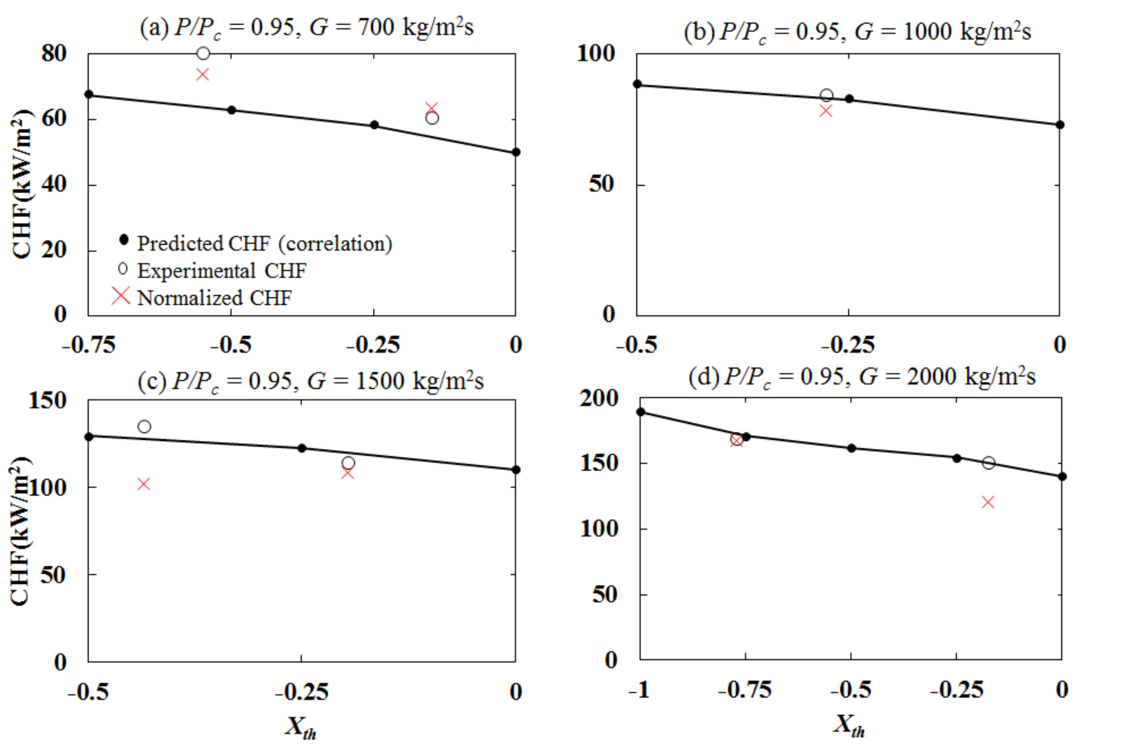

Figure 9: Comparison of experimental CHF and its prediction by the CHF correlation of Appendix B; P/P_c = 0.95.

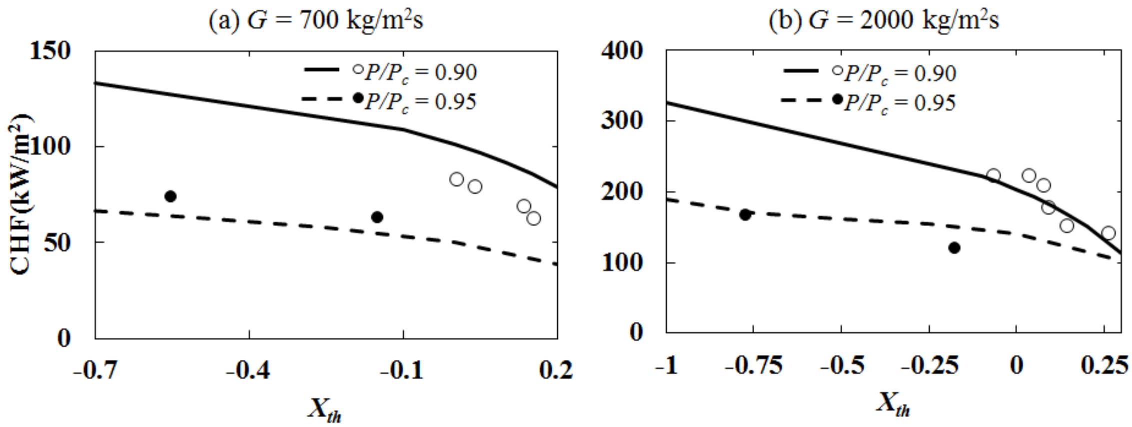

Figure 10: Effect of pressure variation on CHF at high subcritical pressures; symbols denote the normalized CHF and lines denote the CHF correlation of Appendix B.

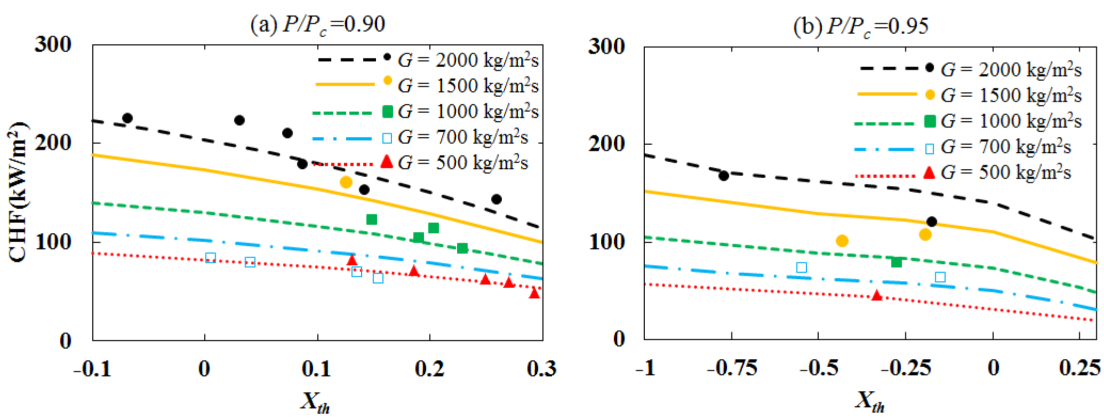

Figure 11: Effect of mass flux variation on CHF at high subcritical pressures; symbols denote the normalized CHF and lines denote the CHF correlation of Appendix B.

4.4 Post-CHF or Film Boiling Heat Transfer

As discussed in Section 4.1 and shown in Figures 3 and 12a-c, as the heat flux was gradually increased to fairly large values, boiling crisis was first encountered at the outlet of the test section and then spread upstream with a continuing increase in heat flux. In general, the highest wall temperature occurred closely downstream from the CHF location, at a location where the vapour quality and thus the vapour velocity were the lowest. Further downstream, the quality increased, and so did the vapour velocity and vapour Reynolds number, which resulted in a higher heat transfer coefficient and a lower wall temperature. However, at very high heat fluxes and moderate flows (or moderate heat fluxes in the case of a low mass flux) the thermodynamic quality at the outlet would exceed 100%, which means that the bulk fluid would become superheated; under such conditions, the wall temperature would start to rise again, following the increase in bulk temperature, as shown in Figure 12c. It is noted that the rise in wall temperature just downstream of the CHF location and the occurrence of a subsequent peak are similar to the trend observed for supercritical heat transfer (Figure 12d), in which case they have been attributed to the occurrence of heat transfer deterioration (HTD). Ackerman (1970) referred to this HTD as "pseudo-film boiling" phenomenon, because of its similarity to film boiling at subcritical pressures.

Film boiling heat transfer has been predicted using Dougall-Rohsenow's (1963) modification of the Dittus Boelter equation

$$Nu_f = 0.023\, Re^{0.8}\, Pr_f^{0.4} \qquad (8)$$

where $Re = \rho_g U_g D / \mu_g$ and the subscript f refers to the vapour film temperature, which is the average of the wall and vapour temperatures. The homogeneous vapour velocity, based on the assumption of zero slip between liquid and vapour, is given by

$$U_g = G\left(\frac{X_{th}}{\rho_g} + \frac{1 - X_{th}}{\rho_l}\right) \quad . \qquad (9)$$

Pressure Effect The heat transport properties changed with pressure, especially in the vicinity of the critical point, where both the thermal conductivity and the specific heat increased significantly. Therefore, for near-critical pressures, and for the same conditions (G, X_{th}, q), the film boiling HTC would tend to increase with an increase in pressure, which would result in a lower wall temperature. This is shown in Figure 13, in which the corresponding supercritical values are added for comparison; one should note the significant increase in HTC when exceeding the critical pressure. Figure 14 shows poor agreement between the Dougall-Rohsenow (1963) equation (Eq. 8) and the experimental data; this correlation only predicts accurately the pressure and quality trends in the positive quality region.

Mass Flux Effect The observed effect of mass flux on film boiling heat transfer is shown in Figure 15, along with the corresponding predictions of Eq 8. The results show the expected trend of increasing HTC with an increase in Reynold number; Figure 15b, however, shows that for G = 700 and 1000 kg m^{-2} s^{-1}, the curves seem to be much closer than the trend predicted by Eq. 8. The qualities are also shown in Figure 15.

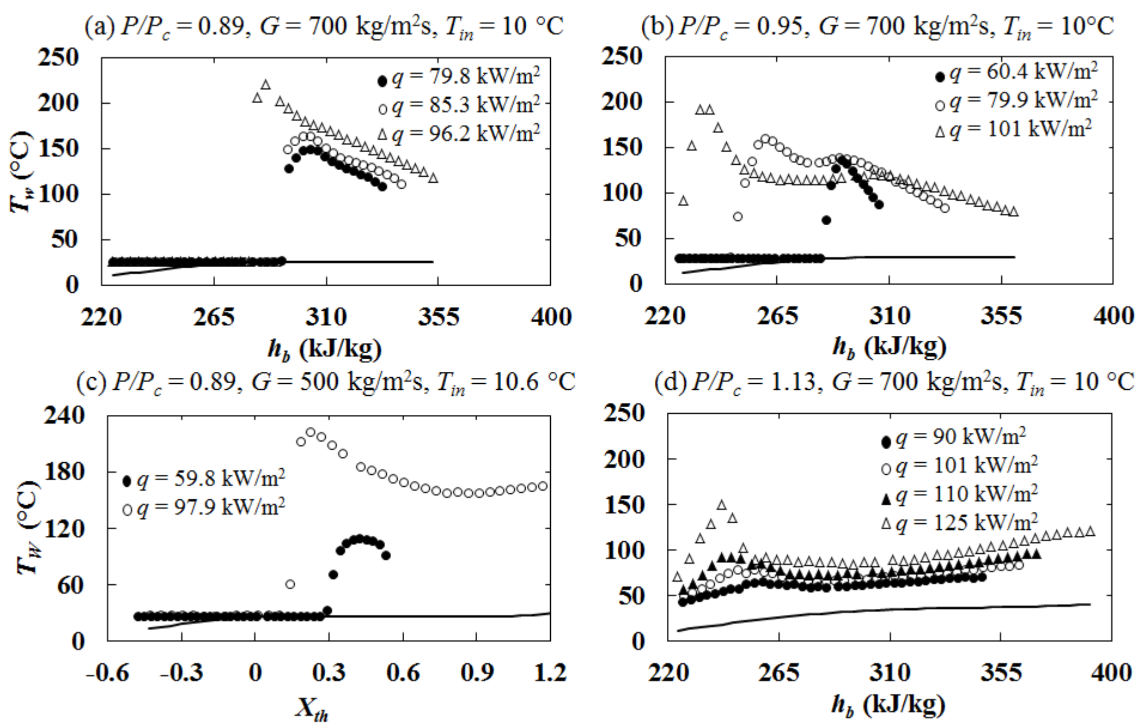

Figure 12: Wall temperature profiles at high sub-critical and supercritical pressures; solid lines denote the bulk temperature and it continues to be the saturation temperature during the film boiling.

Heat Flux Effect Figures 3c-e and Figure 12 show that, with an increase in heat flux, the film boiling zone spread upstream. Figures 16 and 17 show more detailed views of the heat flux effect on film boiling heat transfer for P/P_c = 0.89 and 0.95, respectively. Both figures show that the heat transfer coefficient at film boiling conditions generally decreased with an increase in heat flux at the same flow conditions. This appears counter-intuitive, if one consider the increase in the near-wall thermal conductivity at the higher heat flux.

Quality Effect Figures 13c,d, 14c,d, 15b,d and 17a,b all show a minimum in HTC *vs.* quality or HTC *vs.* h_b plots. This minimum tended to occur in the range $-0.2 \leq X_{th} \leq 0$. For higher thermodynamic qualities, the HTC is expected to increase because of a higher vapour velocity, as explained above. However, when the thermodynamic quality is negative, film boiling is characterized by the inverted annular flow regime (IAFB), in which a thin vapour film separates the subcooled core of liquid from the heated wall. Under such conditions, the predominant heat transfer mode is conduction across the thin vapour film; for higher subcoolings (or lower negative qualities), the film becomes thinner thus increasing the HTC (Hammouda *et al.*, 1996). For thermodynamic qualities greater than 1.0, only single-phase vapour would be present and the HTC would be roughly constant (see Fig. 15a) because the Reynolds number in Equation 8 reverts back to $\rho_g U_g D/\mu_g = GD/\mu_g$ and is no longer dependent on quality; then, any change in HTC would be due solely to changes in the fluid properties.

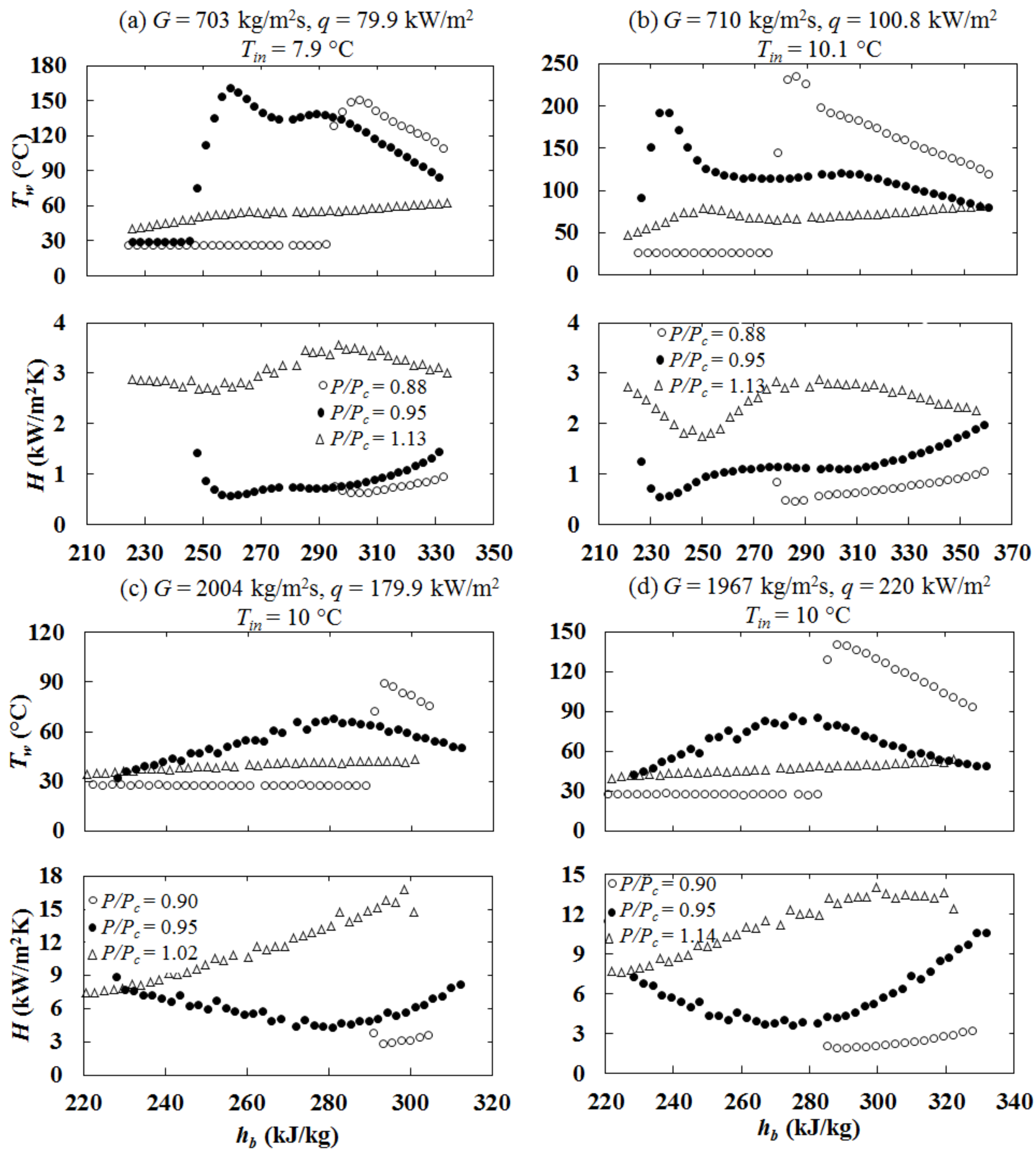

Figure 13: Effect of pressure on film boiling heat transfer and comparison with supercritical heat transfer results.

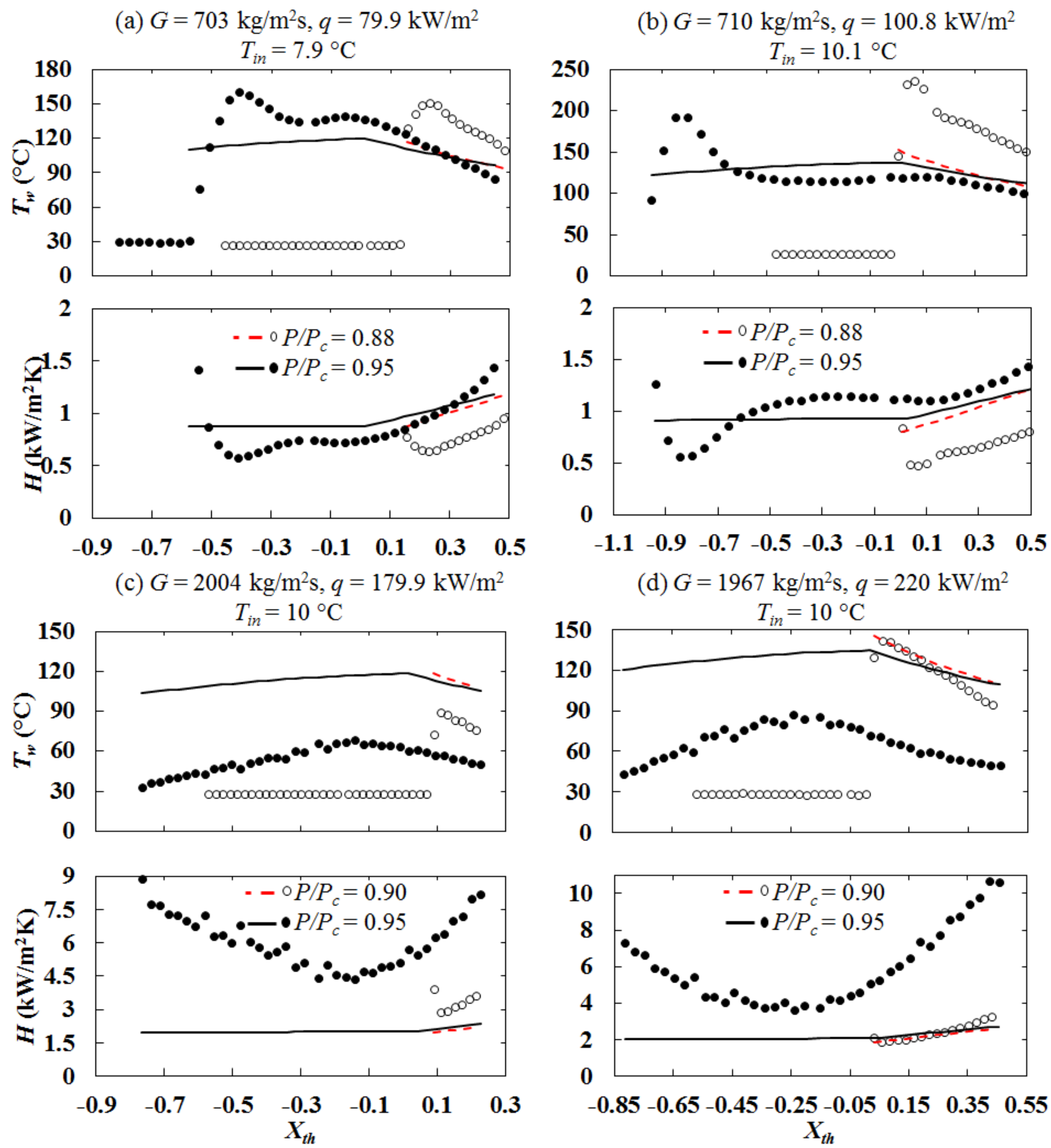

Figure 14: Effect of pressure on film boiling heat transfer at high subcritical pressures; solid and dashed lines mark predictions of the Dougall-Rohsenow correlation.

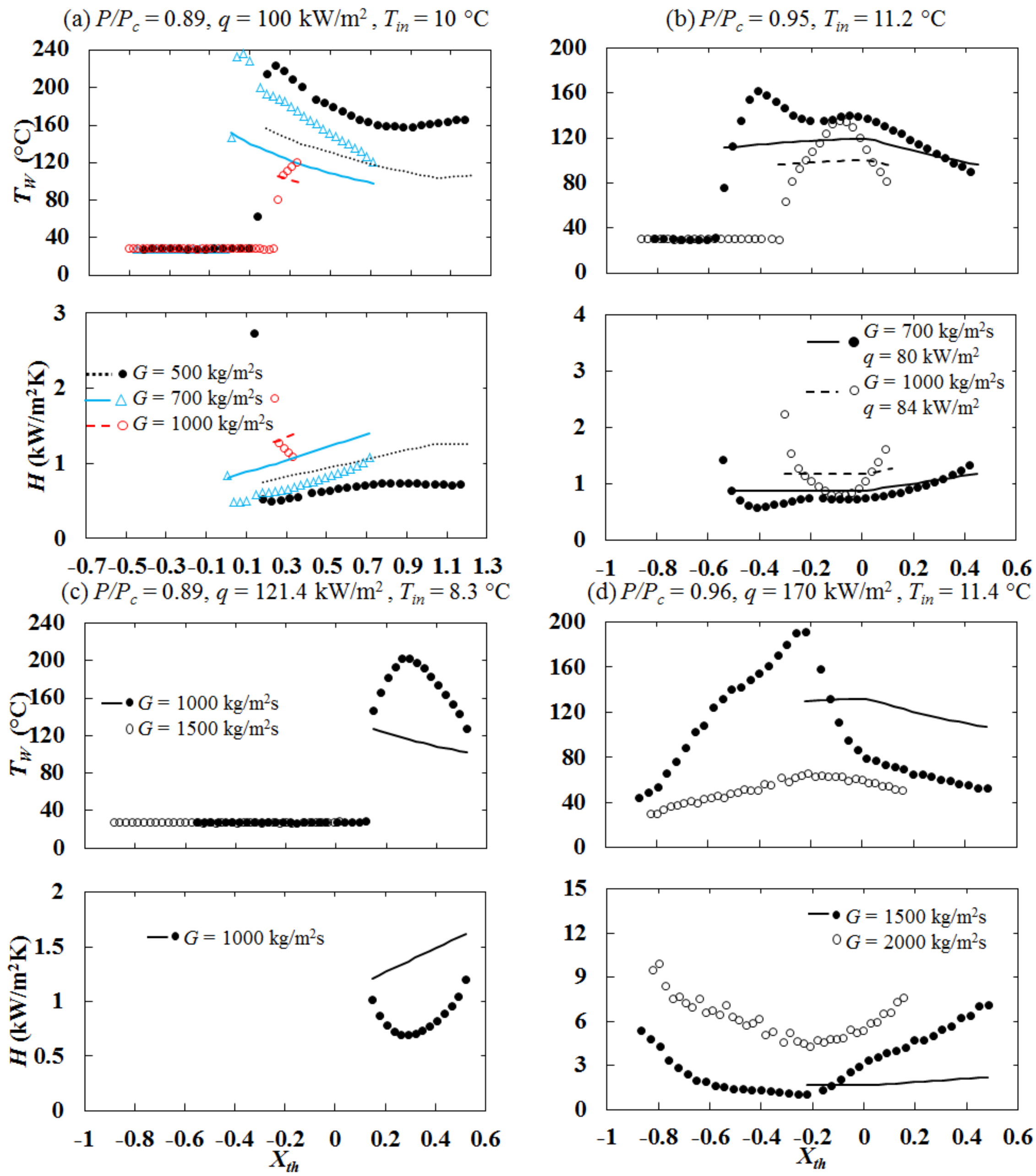

Figure 15: Effect of mass flux on film boiling heat transfer; solid and dashed lines mark predictions of the Dougall-Rohsenow correlation.

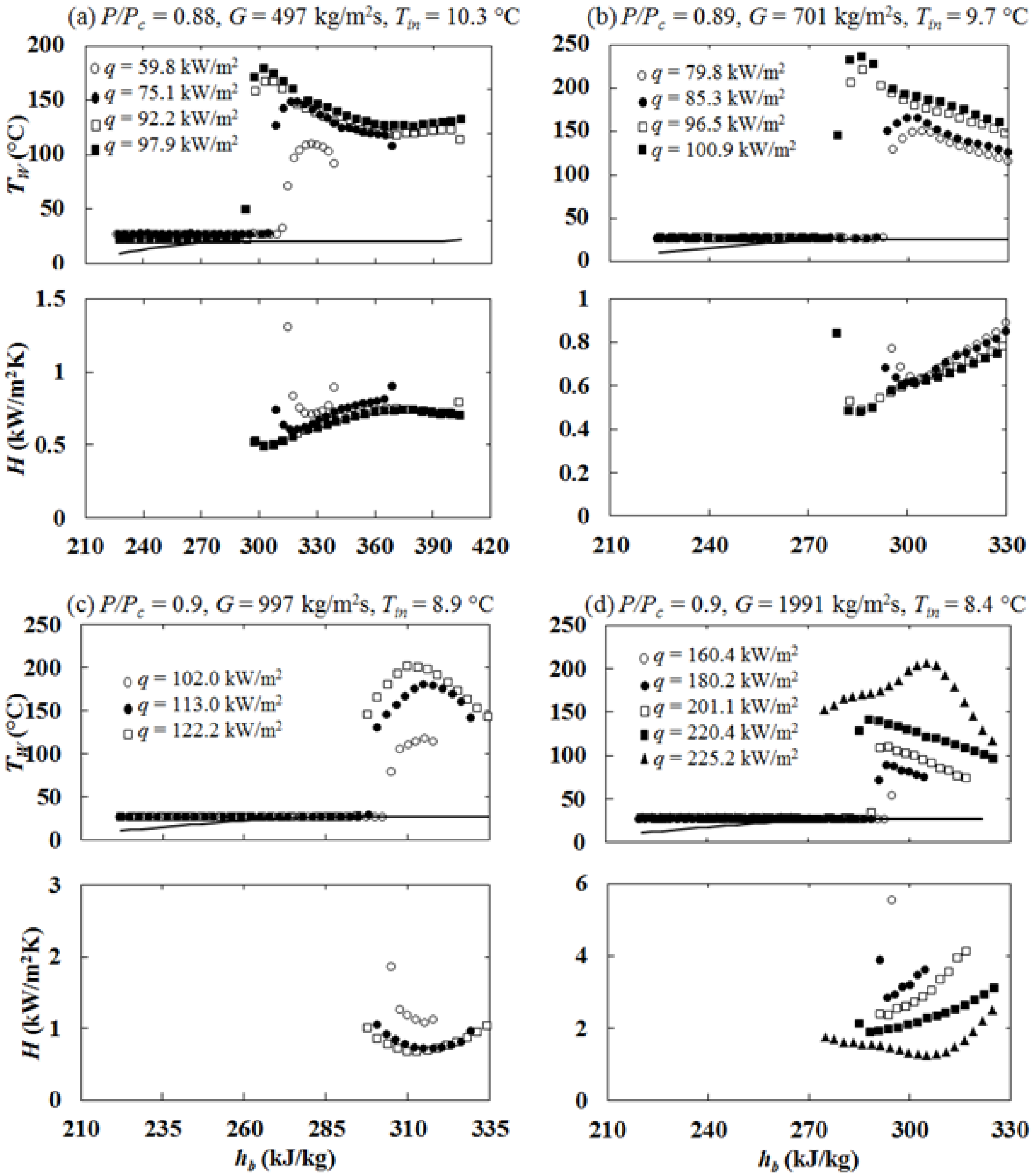

Figure 16: Effect of heat flux on film boiling heat transfer; P/P_c = 0.88-0.90.

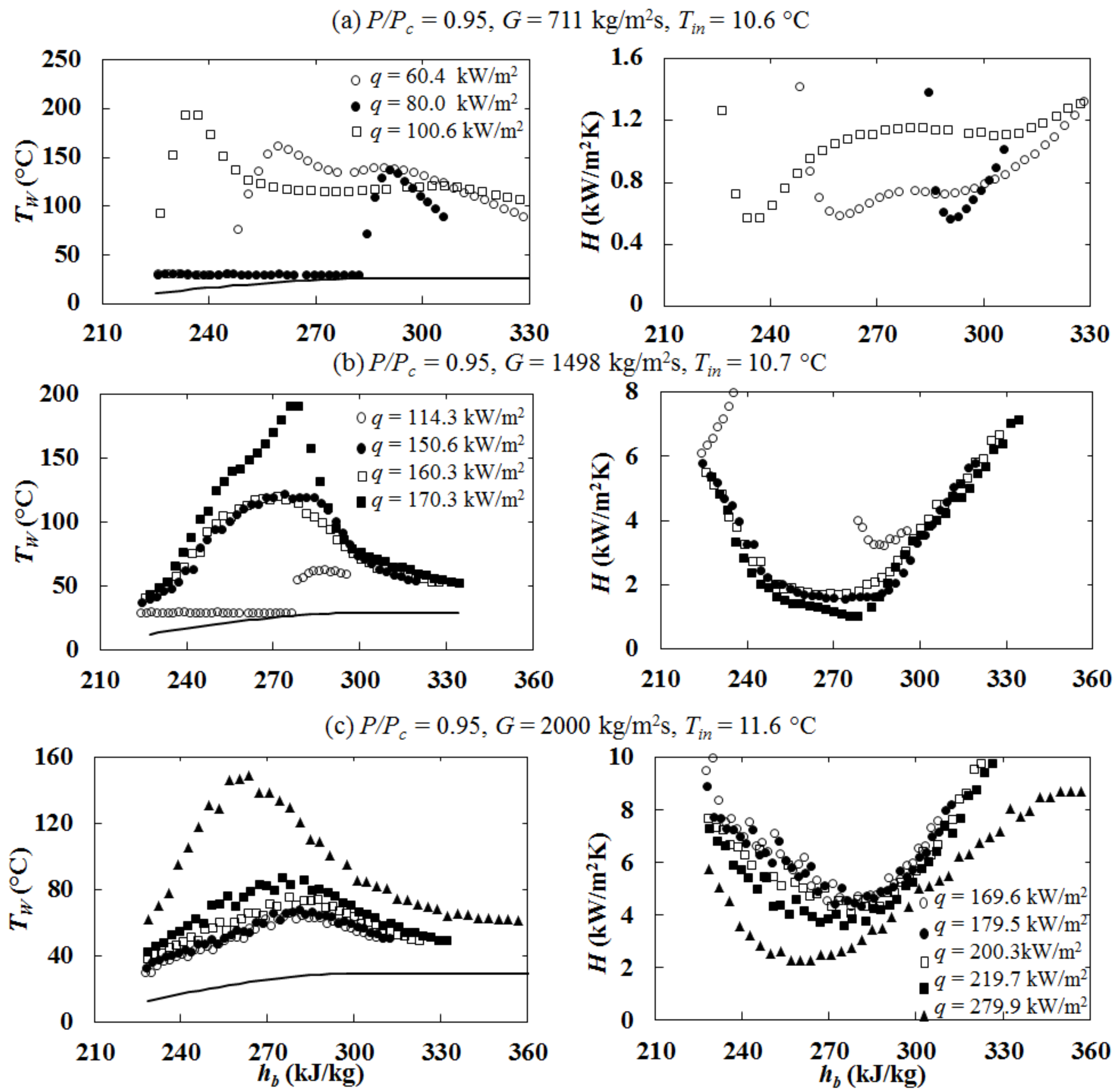

Figure 17: Effect of heat flux on film boiling heat transfer; P/P_c = 0.95.

5. Impact of flow obstacles on subcritical heat transfer and CHF

This section presents the subcritical heat transfer results obtained in a tube equipped with obstacles; the obstacle configurations are listed in Table 1 and the test conditions are specified in Table 2. The experiments were performed by gradually increasing the heat flux, as described in Section 4.1.

5.1 Impact on Pre-CHF Heat Transfer

Figure 18 shows the effect of flow obstruction on heat transfer in liquid for configurations 1 and 2 and mass fluxes in the range between 115 and 1000 kg m^{-2} s^{-1}. In general, the heat transfer coefficient closely downstream of the obstacles was enhanced and the enhancement decreased exponentially with downstream distance towards the corresponding value in the unobstructed tube. As a measure of the size of the zone of influence of the obstacle, we may define the decay length as the distance Δz_d from the obstacle over which the enhancement is higher than 5%. The first obstacle, located near the start of the heated length, had a short decay length of about 15D. This is similar to the decay length for the same configuration at similar conditions at supercritical pressures; see Eter *et al.* (2016b). The second obstacle had a decay length of about 35D with a maximum heat transfer enhancement of 30-40%. This is also similar to the supercritical observations of Eter *et al.* (2016b).

Figure 19 shows the effect of flow obstruction on nucleate boiling heat transfer for mass fluxes in the range from 115 to 1000 kg m^{-2} s^{-1}. These results show that, for highly subcooled conditions (Figures 19a,b), the flow mixing produced by the obstacle suppressed the occurrence of nucleate boiling and enhanced the local heat transfer. For lower subcoolings and for saturated nucleate boiling (Figures 19c-e), however, the nucleate boiling heat transfer coefficient was extremely high even in the bare tube (the wall temperature was within 1K of the saturation temperature) and no discernible effect of the obstacles on wall temperature was observed.

5.2 Impact on CHF

Groeneveld *et al.* (2001), among others, have shown that the obstacle effect on CHF depends strongly on the degree of flow blockage and the distance Δz_{CHF} between the CHF location and the downstream edge of the nearest upstream obstacle. Based on extensive experimental studies, various predictions show generally that the fractional increase in CHF can be predicted by an equation of the form

$$\frac{\mathrm{CHF}_{obs}}{\mathrm{CHF}_{bare}} = 1 + A' e^{-B' \Delta z_{CHF}/D_h}, \tag{10}$$

where A' and B' depend on the obstacle shape and size. CHF increase was also observed by Doerffer and Groeneveld (1999) in obstacle-equipped tubes cooled by a refrigerant or water at low subcritical pressures.

Figures 20 and 21 illustrate the effect of obstacles on suppressing CHF occurrence. From these results one can extract the CHF values CHF_{obs} for tubes equipped with flow obstructions and the distance Δz_{CHF}. Table 4 tabulates these values along with the flow conditions and the bare-tube CHF_{corr} from the CHF correlation in Appendix B (B-1). The enhanced CHF values were plotted along with the bare-tube CHF correlation in Figure 22. This figure shows that in many cases a relatively large increase in CHF was observed when the distance Δz_{CHF} was relatively short. An examination of Table 4 shows a very significant (90 - 150%) increase in CHF by obstacles with a 250 mm pitch. This is much higher than the 0 - 50 % increase observed for the 500 and 1000 mm pitches, with the exception of one anomalous point at a very high pressure.

Table 4: CHF location and its distance from the nearest upstream obstacle

Experimental conditions					Conditions at boiling crisis			CHF_{corr} (kW m^{-2})	$\frac{CHF_{obs}}{CHF_{bare}}$ -1
P/P_c	P (MPa)	G (kg m^{-2} s^{-1})	T_{in} (°C)	q (kW m^{-2})	X_{th}	z_{do} (m)	Δz_{CHF} (m)		
Configuration 1 (pitch 1000 mm)									
0.92	6.84	526	10.55	97.8	0.06	0.70	0.65	62.4	0.57
0.90	6.69	599	19.91	60.4	0.38	1.30	0.30	45.1	0.34
0.89	6.57	699	9.85	84.9	0.28	1.37	0.37	73.7	0.15
0.91	6.73	1002	9.16	102	0.27	1.80	0.80	78.3	0.30
0.90	6.70	1019	9.05	122.3	0.19	1.36	0.36	102.4	0.19
0.95	7.08	710	11.01	80.0	-0.69	0.40	0.35	67.1	0.19
0.95	7.08	710	11.01	80.0	-0.14	1.21	0.17	56.0	0.43
0.95	7.07	736	10.82	100.4	-0.89	0.05	0.00	74.9	0.34
0.93	6.93	979	11.30	84.1	0.09	1.80	0.8	85.9	-0.02
Configuration 2 (pitch 500 mm)									
0.91	6.72	506	10.73	97.8	0.06	0.70	0.20	69.9	0.40
0.90	6.66	581	19.99	60.4	0.27	1.06	0.56	61.9	-0.02
0.89	6.60	701	10.80	84.9	0.19	1.25	0.75	88.8	-0.04
0.90	6.66	1011	9.09	102.0	0.27	1.80	1.30	85.4	0.19
0.90	6.68	1006	9.13	122.3	0.19	1.30	0.80	101.5	0.20
0.95	7.03	714	10.92	80.0	-0.75	0.40	0.35	68.8	0.16
0.95	7.03	714	10.92	80.0	-0.43	0.73	0.20	62.8	0.27
0.94	7.01	714	10.87	100.4	-0.89	0.05	0.00	87.5	0.15
0.94	7.01	714	10.87	100.4	0.40	0.73	0.17	26.1	2.85
0.94	7.00	992	11.16	84.1	-0.09	1.30	0.8	89.0	-0.06
Configuration 3 (pitch 250 mm)									
0.90	6.70	611	20.20	60.4	0.45	1.40	0.1	31.8	0.90
0.89	6.63	695	10.10	84.9	0.46	1.73	0.1	34.0	1.50

*z_{do} and Δz_{CHF} are the CHF location and its distance from the nearest upstream obstacle, respectively.

5.3 Impact on film boiling heat transfer

Figures 20 and 21 show the effect of flow obstruction on film boiling heat transfer for two pressures. Compared to the bare tube results, the obstacles delayed the CHF occurrence by moving the CHF location downstream and also enhanced the film boiling heat transfer, especially just downstream from the CHF location. In all cases the maximum post-dryout temperature was reduced significantly. In some of the cases with an obstacle pitch of 250 mm, the obstacles completely suppressed CHF occurrence. The observed film boiling heat transfer enhancement ranged from 0-80%.

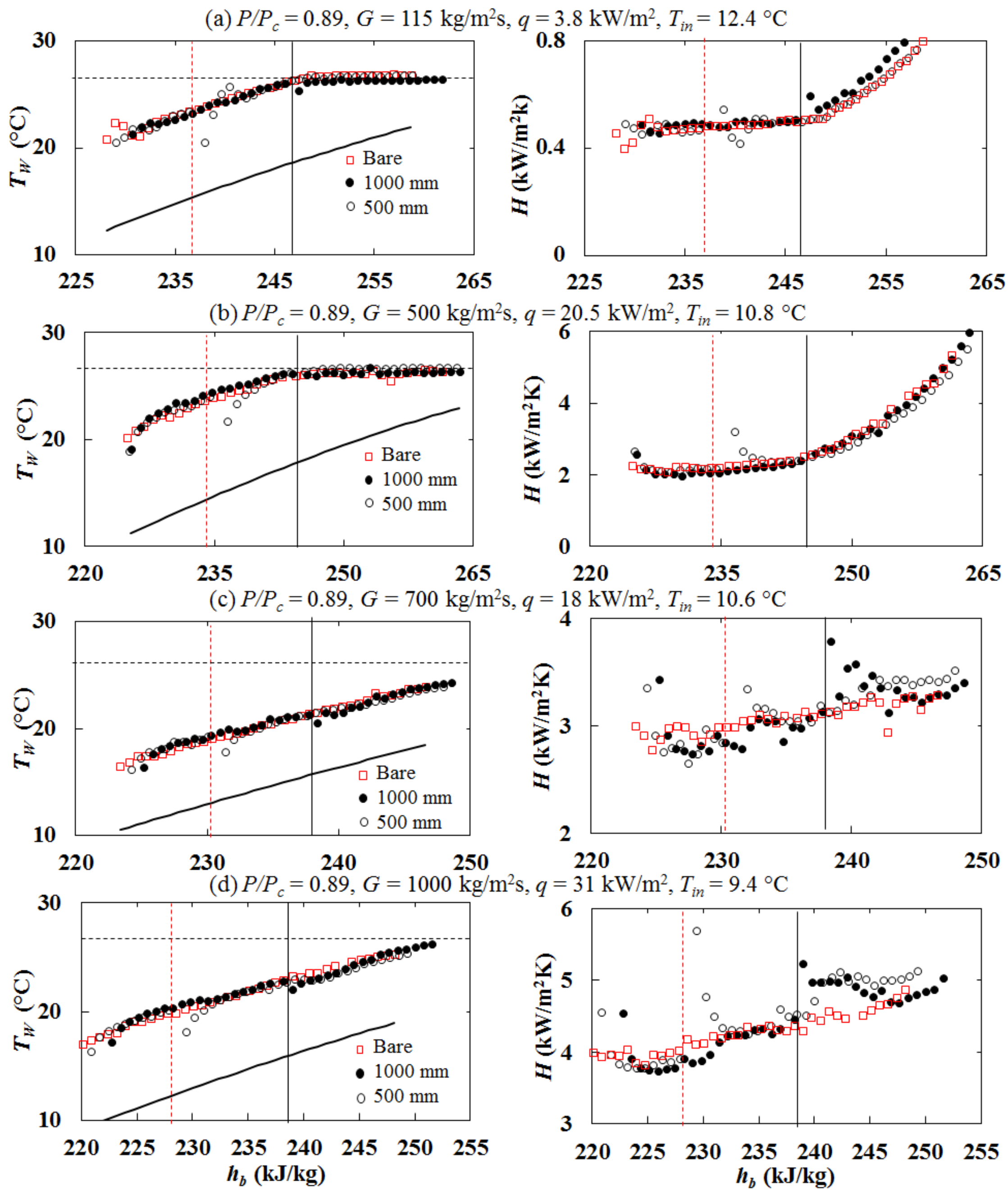

Figure 18: Effect of flow obstruction on single phase heat transfer; the first obstacle was placed at the start of the heated section; vertical dashed red and black solid lines indicate the second obstacle location, either at 500 or 1000 mm, respectively.

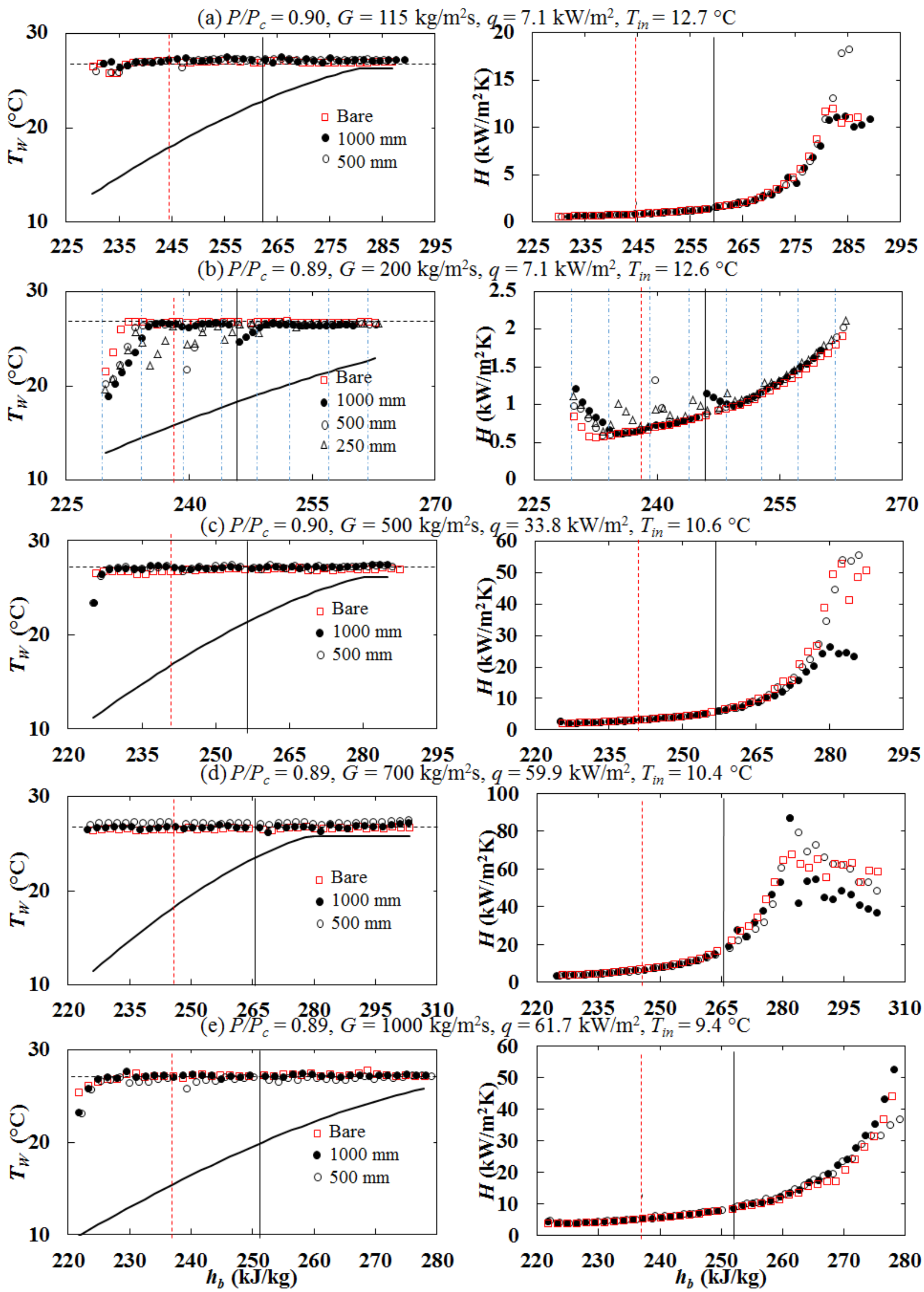

Figure 19: Effect of flow obstruction on nucleate boiling heat transfer; vertical dashed red and black solid lines indicate the second obstacle location, either at 500 or 1000 mm, respectively; blue dashed lines indicate the obstacle locations for a pitch of 250 mm.

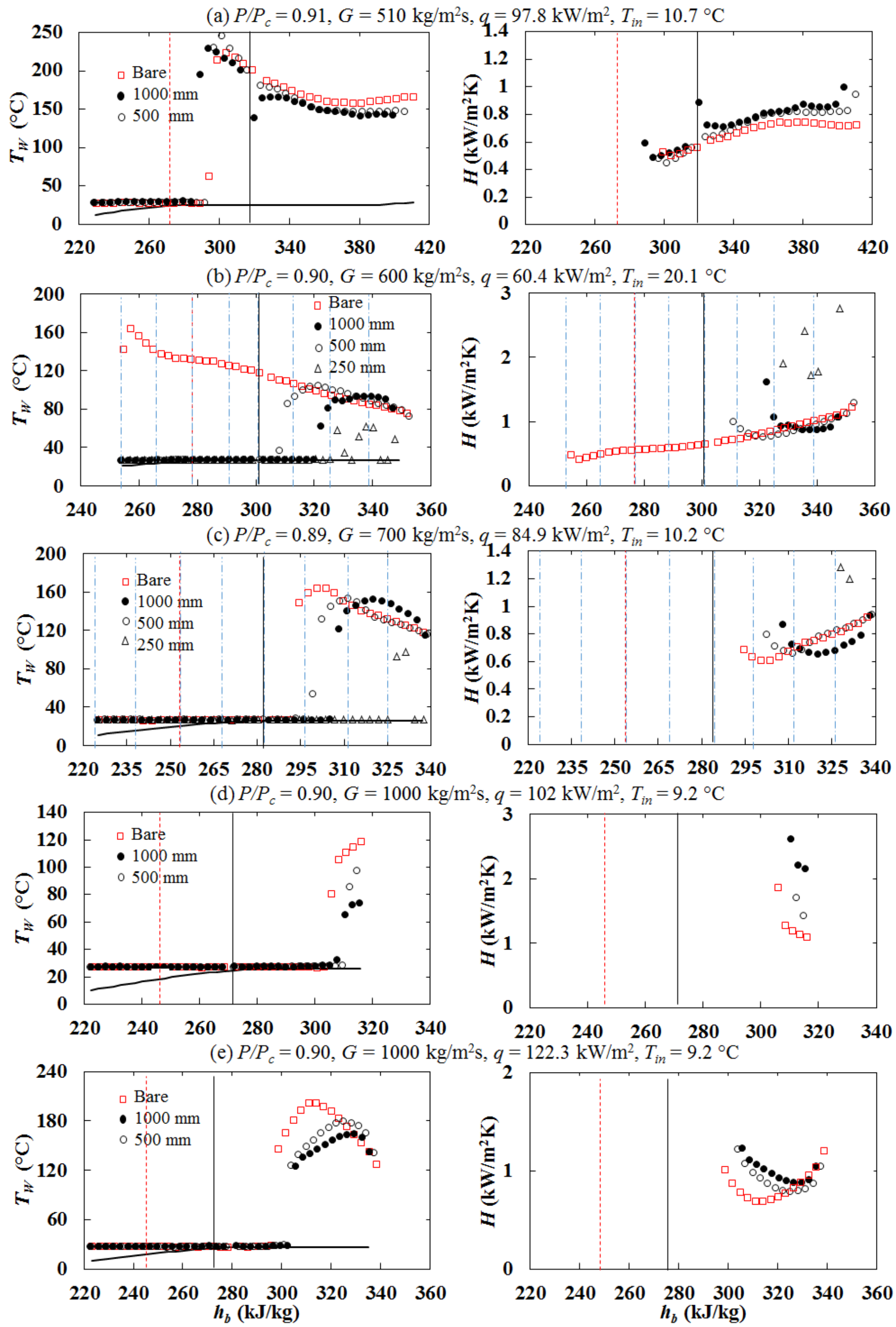

Figure 20: Effect of flow obstruction on CHF location and on film boiling heat transfer ($P/P_c \approx 0.90$); the first obstacle was placed at the start of the heated section; vertical dashed red and black solid lines indicate the second obstacle location, either at 500 or 1000 mm, respectively; blue dashed lines indicate the obstacle location for a pitch of 250 mm.

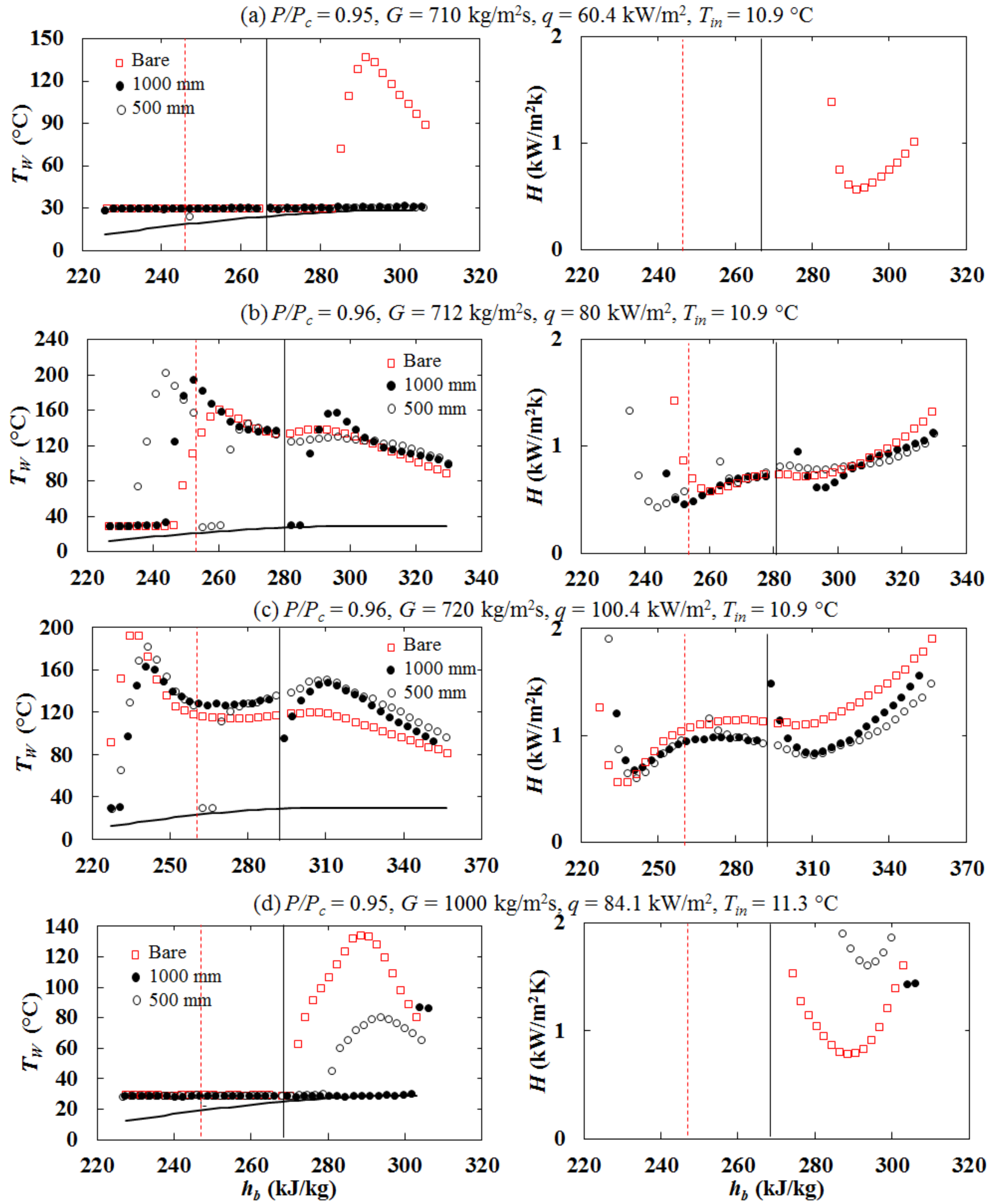

Figure 21: Effect of flow obstruction on CHF location and on film boiling heat transfer ($P/P_c \approx 0.95$); the first obstacle was placed at the start of the heated section; vertical dashed red and solid black lines indicate the second obstacle location at 500 and 1000 mm, respectively.

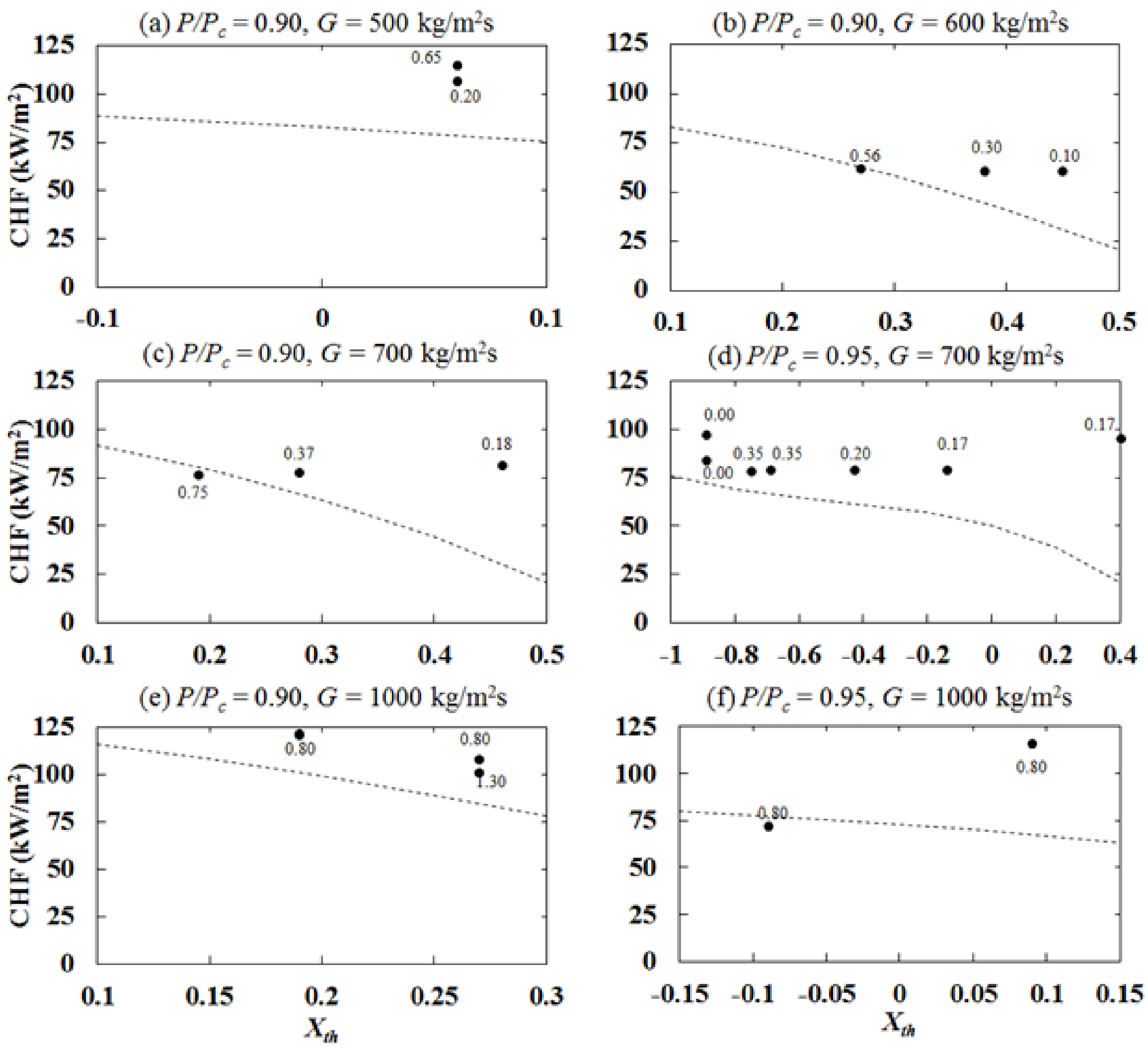

Figure 22: Effect of flow obstacle on CHF at high subcritical pressures; dashed lines correspond to the CHF correlation of Appendix B; numbers next to the symbols indicate the distance, in meters, between the CHF location and the nearest upstream obstacle.

6. Quantification of obstacle-induced heat transfer enhancement

6.1 Heat transfer enhancement in liquid flows

Correlations that describe the effect of single obstacles on the heat transfer coefficient in single-phase flows have been proposed, among others, by Yao *et al.* (1982), Mori *et al.* (2012), Miller *et al.* (2013) and Tanase and Groeneveld (2015). These correlations were generally of the form

$$\frac{\mathrm{Nu}_{obs}}{\mathrm{Nu}_{bare}} = 1 + A\varepsilon^{2}\mathrm{e}^{-B\,\Delta z_d/D_h} \qquad (11)$$

where Nu_{obs} and Nu_{bare} are, respectively, the Nusselt numbers in the obstructed and the bare tubes under the same conditions; A and B are positive empirical constants; ε is the blockage ratio; Δz_d is the axial distance downstream of the downstream edge of the obstacle; and D_h is the hydraulic diameter of the heated channel. This type of correlations predicts a sudden increase of Nusselt number at the downstream edge of the obstacle and subsequent exponential decay of this parameter with distance from this edge. The coefficient A is a measure of the maximum enhancement, whereas the coefficient B is a measure of the extent of the enhancement zone. For comparative purposes, we will define the enhancement decay length as the distance over which the Nusselt number ratio drops to 1.05; this decay length is approximately equal to $3D_h/B$. As a reference, both the Yao *et al.* and Mori *et al.* correlations had A = 5.55, however, the former had a decay length of $23D_h$ (B = 0.13), whereas the latter had a decay length of $60D_h$ (B = 0.05).

Figure 23 shows the experimental ratio $\mathrm{Nu}_{obs}/\mathrm{Nu}_{bare}$, plotted *vs.* $\Delta z_d/D$ for a few cases with different obstacle pitches, two flow blockage ratios, different mass fluxes in the range 115 - 1000 kg m^{-2} s^{-1} and different pressures. Only cases with normal heat transfer in liquid flows in either the bare or the obstructed tube have been considered. It is apparent that the heat transfer enhancement downstream of obstacles placed near the entrance of the heated section was much milder and had a much shorter duration than that downstream of obstacles placed far away from the inlet, as shown in section 5.1. The enhancement characteristics near the inlet, where the thermal boundary layer is in a developing state, would not be truly representative of the obstacle-induced heat transfer enhancement. The same figure shows that predictions by correlations of Yao *et al*. and Mori *et al*. fell between the two sets of liquid data. For comparative purposes, we have fitted different values of the coefficients *A* and *B* to each of the two sets of data; these values are shown in the legend of figure 23. The corresponding decay lengths were approximately 15*D* for the near-entrance obstacle, and 35*D* for the downstream obstacle in the liquid region. In view of the relatively small number of measurements used for these fits and the possible dependence of obstacle-induced enhancement on the local Reynolds number and other parameters, the values mentioned previously should be treated as tentative.

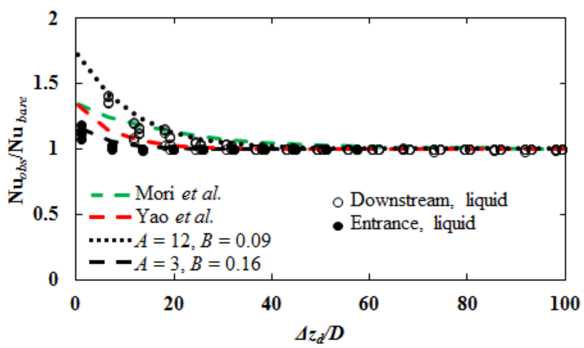

Figure 23: Measured heat transfer enhancement in liquid flows downstream of obstacles and comparison with predictions of previous correlations and present fits.

6.2 CHF increase

Figure 24 is a plot of the small number of available values of the ratio $\mathrm{CHF}_{obs}/\mathrm{CHF}_{bare}$ *vs.* the dimensionless distance $\Delta z_{CHF}/D$ for the $P/P_c \approx 0.90$ cases. A fitted equation of the type of Eq. (10) could roughly describe these data; the corresponding empirical coefficient values were $A' = 3.0$ and $B' = 0.048$. This relationship seems to fit our data better than the correlation of Groeneveld *et al.* (2001), which underestimated most values.

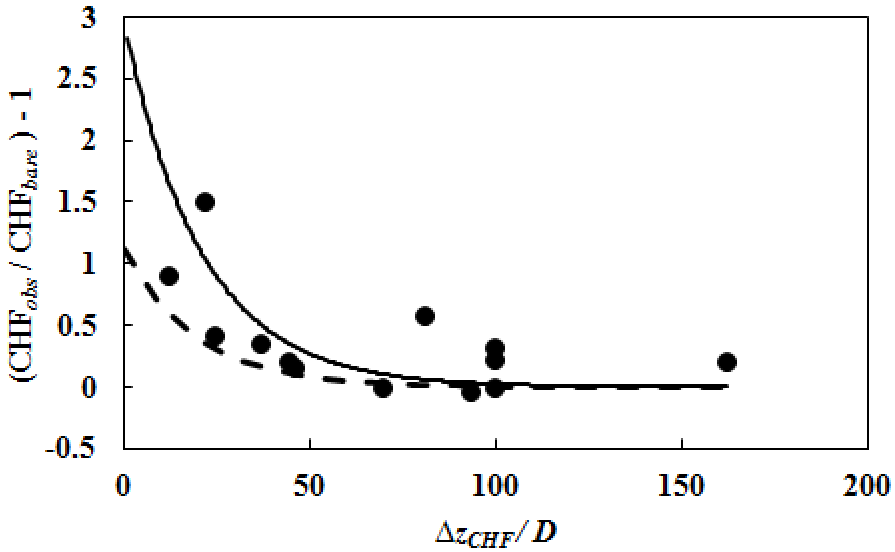

Figure 24: CHF increase downstream of obstacles *vs.* the normalized distance of the CHF location from the nearest upstream obstacle: the solid line denotes the presently fitted exponential relationship, whereas the dashed line denotes the Groeneveld *et al.* (2001) correlation; $P/P_c \approx 0.90$.

7. Conclusions

This article presents and discusses heat transfer measurements obtained in CO_2 flowing vertically upwards in a tube having an ID of 8 mm with and without flow obstructions at high subcritical pressures. In the bare tube, we observed a decrease in the HTC for low mass and heat fluxes; this phenomenon was similar to heat transfer deterioration at supercritical pressures. Obstacles produced an increase in the HTC, which decayed exponentially with distance from the obstacle. For single phase heat transfer in the liquid region, the decay length was short (typically 15D) when the obstacle was placed near the heated test section inlet and increased (to about 35D) when the obstacle was placed downstream. Obstacles suppressed the CHF occurrence locally and shifted the CHF location to a downstream location. The increase in CHF ranged from 0 to 285% and was correlated with the distance of the CHF location from the nearest upstream obstacle. The Dougall-Rohsenow correlation for film boiling at near-critical pressures significantly underpredicted the bare-tube wall temperatures. Increasing the pressure from 0.90P_c to 0.95P_c reduced the maximum film boiling temperature; a further increase in pressure to supercritical conditions (for the same inlet temperature, heat flux and mass flux) resulted in a significant decrease in the maximum wall temperature. In general, the obstacles reduced the maximum wall temperature at all pressures.

ACKNOWLEDGMENTS

This study is part of the Canadian Gen-IV National Program. Funding for this program was provided by Natural Resources Canada through the Office of Energy Research and Development, Atomic Energy of Canada Limited, and Natural Sciences and Engineering Research Council of Canada. The use of bare tube data by Zahlan *et al.* (2015) to supplement our database is gratefully acknowledged.

APPENDIX A. Conversion of water CHF look-up table values into CO_2 equivalents

The conversion followed the fluid-to-fluid modelling procedure at CHF conditions, as presented by Groeneveld et al. (1997). The equivalent water pressure was determined from a given CO_2 pressure using the scaling law

$$\left(\frac{\rho_l}{\rho_g}\right)_{\mathrm{H_2O}} = \left(\frac{\rho_l}{\rho_g}\right)_{\mathrm{CO_2}} \quad \text{(A-1)}$$

The equivalent water mass flux was determined from a given CO_2 mass flux from the scaling law

$$\left(\frac{GD^{0.5}}{(\sigma\rho_l)^{0.5}}\right)_{\mathrm{H_2O}} = \left(\frac{GD^{0.5}}{(\sigma\rho_l)^{0.5}}\right)_{\mathrm{CO_2}} \quad \text{(A-2)}$$

In accordance with the CHF fluid-to-fluid modelling requirement, the thermodynamic qualities at CHF were taken as equal, *i.e.*

$$(X_{th})_{\mathrm{H_2O}} = (X_{th})_{\mathrm{CO_2}} \quad \text{(A-3)}$$

From these values, one can find the equivalent water CHF value from the lookup table and then scale it to CO_2 using the scaling law

$$\left(\frac{\mathrm{CHF}}{h_{fg}G}\right)_{\mathrm{CO_2}} = \left(\frac{\mathrm{CHF}}{h_{fg}G}\right)_{\mathrm{H_2O}} \quad \text{(A-4)}$$

APPENDIX B. Correlation fitted to the CHF data and normalization of CHF predictions

The bare-tube CHF data presented in Table 3 were fitted, within a maximum error of 20%, by the following correlation

$$\mathrm{CHF}_{corr} = (AX_{th} + B)CD \quad \text{(B-1)}$$

where $A = (1.3185\,P/P_c - 1.3336)G + 982.896\,P/P_c - 972.98$

$B = (-0.0969\,P/P_c + 0.1564)G - 1051.4\,P/P_c + 1008.1$

$C = 0.4128X_{th}^{2} + 0.8464X_{th} + 0.9617$

$D = -0.0000001632G^2 + 0.00051914G + 0.6737$

In the analysis presented in this article, we wished to examine the effects of specific parameters on the CHF, while keeping all other parameters constant. Because, however, the various test conditions could not be matched precisely from one run to another, comparisons were made for various sets of nominal flow conditions (nfc) P_0/P_c and G_0. These were cases with combinations of values P_0/P_c = 0.90 or 0.95 and G_o = 500, 700, 1000, 1500 or 2000 kg m^{-2} s^{-1}. The CHF data were normalized to the corresponding nominal flow conditions using the following equation

$$\mathrm{CHF}_{nfc} = \mathrm{CHF}_{exp} + \left.\frac{\partial \mathrm{CHF}_{corr}}{\partial (P/P_c)}\right]_{P=P_{exp}} \left(P_0 - P_{exp}\right)/P_c + \left.\frac{\partial \mathrm{CHF}_{corr}}{\partial (G)}\right]_{G=G_{exp}} \left(G_0 - G_{exp}\right) \quad \text{(B-2)}$$

NOMENCLATURE

CHF	critical heat flux, kW m^{-2}
CHF$_{bare}$	critical heat flux in the bare tube geometry, kW m^{-2}
CHF$_{corr}$	predicted CHF using CHF correlation of Appendix B, kW m^{-2}
CHF$_{nfc}$	normalized predicted CHF using CHF correlation of Appendix B at nominal values of P_o/P_c and G_o, kW m^{-2}
CHF$_{obs}$	critical heat flux in the obstructed tube geometry, kW m^{-2}
D	inside diameter of the tube, mm
f	friction factor
G	mass flux, kg m^{-2} s^{-1}
H	heat transfer coefficient, kW m^{-2} K^{-1}
h_b	specific bulk enthalpy, kJ kg^{-1}
h_{fg}	Latent heat, kJ kg^{-1}
h_{in}	specific enthalpy at inlet, kJ kg^{-1}
h_{out}	specific outlet enthalpy, kJ kg^{-1}
k	thermal conductivity, kW m^{-1} K^{-1}
L_h	heated length, mm
$\dot{m}$	mass flow rate, kg s^{-1}
Nu	Nusselt number
Nu$_b$	bulk Nusselt number
Nu$_{bare}$	Nusselt number in a bare tube
Nu$_{obs}$	Nusselt number in an obstructed tube
P	system pressure, MPa
P_c	critical pressure, MPa
Pr$_b$	bulk Prandtl number
Q_e	nominal electrical power supplied to the test section, kW
q	heat flux, kW m^{-2}
q_{loss}	heat flux to surroundings (heat losses), kW m^{-2}
q^v	volumetric heat generation, kW m^{-3}
Re$_b$	bulk Reynolds number

r_i	test section inner radius, mm
r_o	test section outer radius, mm
T_b	bulk temperature, °C
T_{in}	test section inlet temperature, °C
T_{Pc}	pseudo critical temperature at supercritical pressures, °C
T_s	saturated temperature, °C
T_w	corrected wall temperature, °C
$T_{w,o}$	tube outer wall temperature (measured by thermocouple), °C
U_g	streamwise gas velocity, m s^{-1}
X	vapour quality
X_{th}	thermodynamic quality
z	axial distance from the unheated test section inlet, mm
z_{do}	boiling crisis (CHF conditions) location, mm
z_h	axial distance from the heated test section inlet, mm

Greek symbols

ΔQ_e	power imbalance, W
Δz_{CHF}	axial distance between the CHF location and the downstream edge of the nearest upstream obstacle, mm
Δz_d	axial distance from the downstream end of an obstacle, mm
ε	blockage ratio, %
μ_b	bulk dynamic viscosity, Pa s
μ_g	gas dynamic viscosity, Pa s
ρ_b	fluid density at bulk temperature, kg m^{-3}
ρ_g	gas density at saturation temperature, kg m^{-3}
ρ_l	liquid density at saturation temperature, kg m^{-3}
σ	surface tension, N m^{-1}

Acronyms

DPT	differential pressure transducer
HTC	heat transfer coefficient
ID	tube inner diameter

LHS	left hand side
OD	tube outer diameter
PS	power supply
PT	pressure transducer
RHS	right hand side
SCUOL	University of Ottawa supercritical CO_2 loop
SCWR	super-critical water reactor

REFERENCES

Ackerman, J.W., 1970. Pseudoboiling heat transfer to supercritical pressure water in smooth and ribbed tubes. J. Heat Transfer. 92, 490–498.

Bishop, A.A., Sandberg, R.O., Tong, L.S., 1965. Forced convection heat transfer at high pressure after the critical heat flux. ASME publication, Rept. No. 65-HT-31, USA.

Chen, Y., Bi, K., Zhao, M., Yang, C., Du, K., 2015. Critical heat flux with subcooled flowing water in tubes for pressures from atmosphere to near critical point. Proc. 16th Intern. Topical Meeting on Nuclear Reactor Thermal Hydraulics (NURETH-16), Chicago, USA.

Chun, S., Hong, S., Kikura, H., Aritomi, M., 2007. Critical heat flux in a heater rod bundle cooled by R-134a fluid near the critical pressure. Nucl. Sci. Techn. 44, 1189–1198.

Dittus, F.W., Boelter, L.M.K., 1930. University of California, Berkeley, Publications on Engineering. 2, 443–461.

Doerffer, S., Groeneveld, D.C., 1999. Fluid-to-fluid modelling of critical heat flux enhancement in a tube. Proc. 9th Intern. Topical Meeting on Nuclear Reactor Thermal Hydraulics (NURETH-9), San Francisco, California, USA.

Dougall, R. S., Rohsenow, W. M., 1963. Film boiling on the inside of vertical tubes with upward flow of the fluid at low qualities. MTT Rept. No. 9019-26.

Eter, A., Groeneveld, D., Tavoularis, S., 2016a. An Experimental investigation of supercritical heat transfer in a three-rod bundle equipped with wire-wrap and grid spacers and cooled by carbon dioxide. Nucl. Eng. Des. 303, 173-191.

Eter, A., Groeneveld, D., Tavoularis, S., 2016b. Convective heat transfer to CO_2 -cooled tubes with and without flow obstacles at supercritical pressures. Submitted to Nucl. Eng. Des.

Gnielinski, V., 1976. New equation for heat and mass transfer in turbulent pipe and channel flow, Intern. Chem. Eng. 16, 359–366.

Groeneveld, D.C., Doerffer, S.D., Tain, R.M., Hammouda, N., Cheng, S.C., 1997. Fluid-to-fluid modelling of the Critical Heat Flux and Post-Dryout Heat Transfer. Proc. 4th World Congress on Experimental Heat Transfer, Fluid Mechanics and Thermodynamics, Brussels, June 2-6, 1997. 2, 859-867.

Groeneveld, D.C., Pioro, I.L. Guo, Y., Cheng, S.C., Antoshko, Yu. V., Doerffer, A.Z., 2001. A study of the effect of flow obstacles on the critical heat flux. Report, AECL-12104, FFC-FCT-333.

Groeneveld, D.C., Shan, J.Q., Vasic, A.Z., Leung, L.K.H., Durmayaz, A., Yang, J., Cheng, S.C., Tanase, A., 2006. The 2006 look-up table. Nucl. Eng. Des. 237, 1909-1922.

Hammouda, N., Groeneveld, D.C., Cheng, S.C., 1996. An experimental study of subcooled film boiling of refrigerants in vertical up-flow. Int. J. Heat Mass Transfer. 39, 3799–3812.

Herkenrath, H., Mork-Morkenstein, P., Jung, U., Wecketmann, F.J., 1967. Warmeubergang an Wasser bei Erzwungener Stromung in Druckbereich von 140 bis 250 bar. ECR-3658d, (in German).

Hong, S., Chun, S., Kim, S., Baek, W., 2004. Heat transfer characteristics of an internally heated annulus cooled with R-134a near the critical pressure. J. Korean Nucl. Soci. 36, 403-414.

Incropera, F.P., DeWitt, D.P., Bergman, T.L., Lavine, A.S., 2007. Fundamentals of Heat and Mass Transfer. 6th ed., John Wiley and Sons, Hoboken, USA.

Jiang, K., 2015. An experimental facility for studying heat transfer in supercritical fluids. M.A.Sc. Thesis, Department of Mechanical Engineering, University of Ottawa, Ottawa, Canada.

Katto Y., Ohno H., 1984. An improved version of the generalized correlation of critical heat flux for the forced convective boiling in uniformly heated vertical tubes. Int. J. Heat Mass Transfer. 27, 1641-1648.

Lemmon, E.W., M'cLinden, M.O., Friend, D.G., 2002. Thermophysical properties of fluid systems. NIST Standard Reference Database Number 69, REFPROP: Version 7.0.

Miller, D.J., Cheung, F.B., Bajorek, S.M., 2013. On the development of a grid-enhanced single-phase convective heat transfer correlation. Nucl. Eng. Des. 264, 56-60.

Miropol'Skiy, Z.L., 1962. Heat transfer in film boiling of a steam water mixture in steam generating tubes. Teploenevgetika. 10, 49-53.

Mishima, K., 1984. Boiling burnout at low flow rate and low pressure conditions. Ph.D. Dissertation, Research Reactor Institute, Kyoto University, Japan.

Mori, H., Kaida, T., Ohno, M., Yoshida, S., Hamamoto, Y., 2012. Heat transfer to a supercritical pressure fluid flowing in sub-bundle channels. Nucl. Sci. Technol. 49, 373–383.

Schmidt, K.R., 1960. Thermodynamic investigations of highly-loaded boiler heating surfaces. Source: Mitleillungen der Vereinigung der Grosskesselbesitzer 63, 391, translated from German.

Sudo, Y., Miyata, K., Ikawa, H., Kaminaga, M., Ohkawara, M., 1985. Experimental study of differences in DNB heat flux between upflow and downflow in vertical rectangular channel. Nucl. Sci. Technol. 22, 604–618.

Swenson, H.S., Carver, J.R., Szoeke, G., 1962. The effects of nucleate boiling versus film boiling on heat transfer in power boiler tubes. J. Eng. Power 84, 365-371.

Tanase, A., Groeneveld, D., 2015. An experimental investigation on the effects of flow obstacles on single phase heat transfer. Nucl. Eng. Des. 288, 195-207.

Vijayarangan, B.R., Jayanti, S., Balakrishnan, A.R., 2005. Studies on critical heat flux in flow boiling at near critical pressures. Int. J. Heat Mass Transfer 49, 259–268.

Yao, S.C., Hochreiter, W.J., Leech, W.J., 1982. Heat transfer augmentation in rod bundles near grid spacers. J. Heat Transfer 104, 76-81.

Zahlan, H., Groeneveld, D., Tavoularis, S., Mokry, S., Pioro, I., 2011. Assessment of supercritical heat transfer prediction methods. Proc. 5th Intern. Symp. On Supercritical Water-Cooled Reactors, ISSCWR-5, March 13-16, 2011, Vancouver, British Columbia, Canada, paper ISSCRR5-P008.

Zahlan, H., Groeneveld, D., Tavoularis, S., 2015. Measurements of convective heat transfer to vertical upward flows of CO_2 in circular geometry at near-critical and supercritical pressures. Nucl. Eng. Des. 289, 92-107.

Chapter 7

Further Discussion

The objectives of this chapter are (i) to assess the most promising SCHT correlations and models for normal and deteriorated heat transfer against our experimental data (section 7.1) and (ii) to perform further analysis of the obstacle adverse effect on SCHT (section 7.2).

7.1 Assessment of available correlations for supercritical heat transfer

This section is divided into two sub-sections, normal heat transfer and deteriorated heat transfer. The most promising correlations in the literature are compared with the UO bare tube database to determine the best correlation that can represent SCHT at normal heat transfer conditions. Subsequently the experimental runs showing some evidence of HTD are compared to the prediction methods recommended for these conditions.

7.1.1 Normal heat transfer

The most promising CO_2 correlations of Table 2.1, *i.e.*, Petukhov *et al.* (1961), Krasnoshchekov *et al.* (1967), Jackson (2002) and Bae and Kim (2009), along with the most promising water correlations, namely, Mokry *et al.* (2009) and Churkin *et al.* (2015), were compared with the University of Ottawa 8 mm ID bare tube data for normal heat transfer conditions. The mass flux varied from 200 - 1000 kg m^{-2} s^{-1}, the heat flux range was 3 - 200 kW m^{-2} and the nominal reduced pressures were 1.04 and 1.14.

Table 7.1 shows the error assessment of the tested correlations at the three supercritical subregions (liquid-like, near-critical, and gas-like). The near-critical region is defined as the region for $\left|h_{pc} - h_b\right| \leq 30$ kJ kg^{-1}. The correlations of Mokry *et al.* (2009) and Bae and Kim (2009) provided the best prediction accuracy as shown in Table 7.1. Figure 7.1 shows representative plots of the predicted heat transfer using these two correlations at liquid-like (Figure 7.1a,b), near-critical (Figure 7.1c,d), and gas-like subregions (Figure 7.1e,f).

The overall average error (e_A) and the root mean square error (e_S) were calculated for the tested correlations of the bare tube flows. The average and root mean square errors are defined as

$$error = \left(\frac{H_{pre}}{H_{\exp}}\right)_{un-obstructed} - 1$$

$$e_A = avg_{error} = \frac{\sum_{i=1}^{l} error_i}{l} \times 100 \tag{7.1}$$

$$e_S = rms_{error} = \sqrt{\frac{\sum_{i=1}^{l} error_i^{\,2}}{l}} \times 100$$

Table 7.1: Overall average and rms errors in different supercritical subregions

Correlation	Liquid like region $h_{pc} - h_b < 30$ kJ kg^{-1} (2193 data points)		Near critical region $h_{pc} - h_b| \leq 30$ kJ kg^{-1} (657 data points)		Gas-like region $h_b - h_{pc} \geq 30$ kJ kg^{-1} (406 data points)	
	e_A, %	**e_S, %**	**e_A, %**	**e_S, %**	**e_A, %**	**e_S, %**
Petukhov et al. (1961)	68.2	91.5	114.0	124.0	73.0	79.0
Krasnoshchekov et al. (1967)	42.4	64.1	85.6	99.0	46.3	55.5
Jackson (2002)	46.1	67.6	109.7	127.7	51.5	59.5
Mokry *et al.* (2009)	11.5	56.5	-11.7	30.0	-17.0	23.0
Churkin *et al.* (2015)	129.1	169.7	97.0	108.0	65.0	69.0
Bae and Kim (2009)	-27.2	35.5	-6.2	35.7	-4.2	30.0

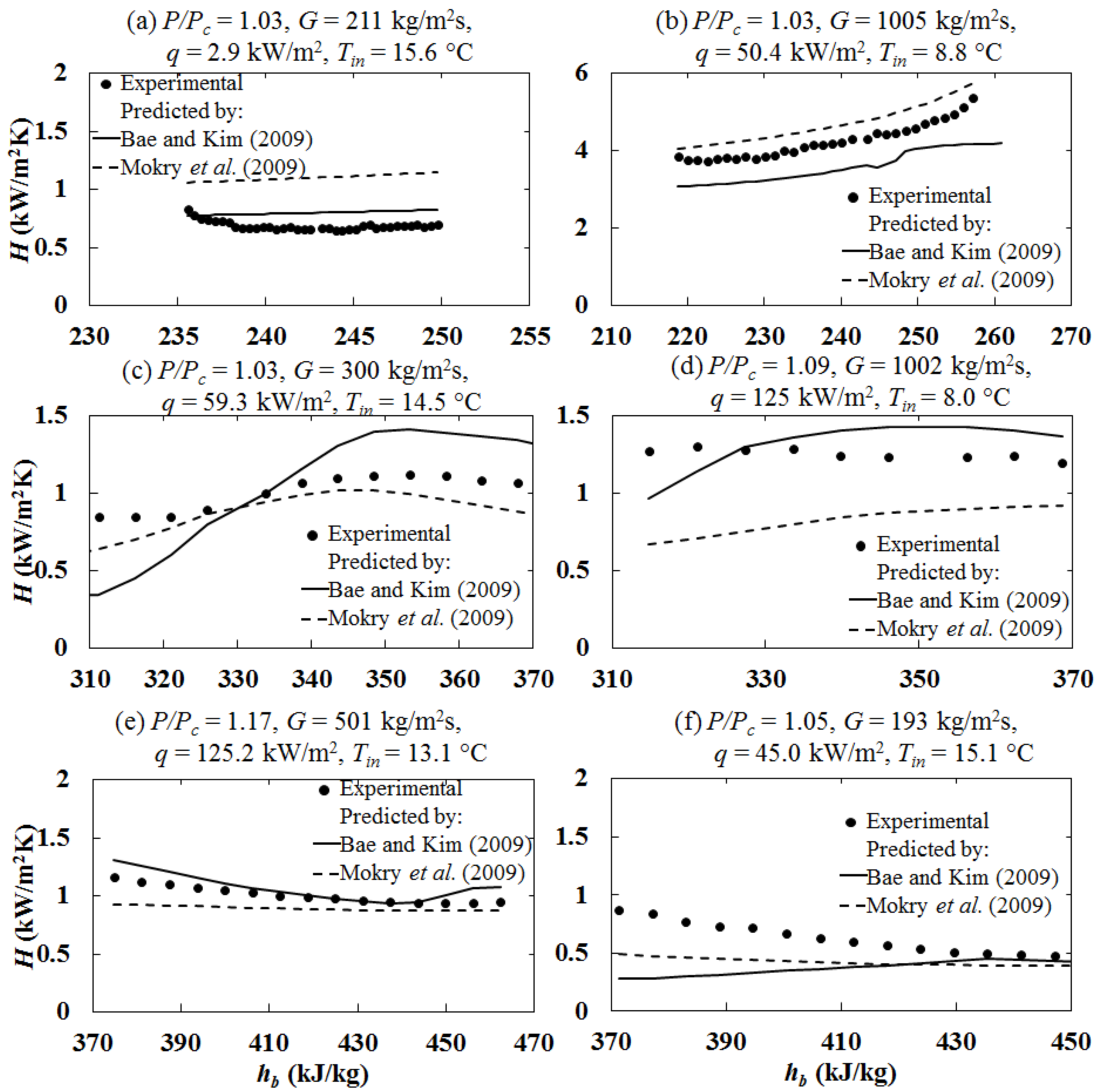

Figure 7.1: Experimental heat transfer coefficient and corresponding predicted values using the correlation of Mokry *et al.* (2009) and Bae and Kim (2009), (Fig. 7.1a, b): liquid-like, (Fig. 7.1c, d): near critical, (Fig. 7.1 e, f): gas-like.

7.1.2 Deteriorated heat transfer

We have assessed prediction methods that can account for HTD (buoyancy effect on heat transfer) including those of Jackson (2010), Jackson *et al.* (2011), Bae and Kim (2009), Cheng *et al.* (2009), and Bae *et al.* (2011). Figure 7.2 shows a comparison of the predicted values along with the CO_2 experimental data of KAERI, obtained in a tube having an ID of 4.57 mm. The LHS plots represent our evaluations of the HTD models at the operating conditions of KAERI experimental data given by Bae *et al.* (2011). The RHS plots represent already published evaluation by Bae *et al.* (2011) of the previous HTD models except the model of Jackson *et al.* (2011) at the same operating conditions of the LHS plots. Note that the prediction methods of Bae and Kim (2009), Bae *et.al* (2011) and Jackson (2011) appear to provide the best agreement with the KAERI data, but none of the models was able to predict all cases of HTD.

The same prediction methods were also tested against the 8 mm ID bare tube data obtained at the University of Ottawa; Table 7.2 shows the error assessment of the tested models for cases presented in Figure 7.3. Table 7.2 and Figure 7.3 show that the Bae and Kim (2009) correlation provided best prediction accuracy for the uOttawa CO_2 data at HTD conditions.

Table 7.2: Overall average and rms errors for HTD conditions

Correlation	Error based on Uof O CO_2 data.	
	e_A, %	e_S, %
Bae and Kim (2009)	-3.4	31.6
Cheng *et al.* (2009)	9.6	61.3
Jackson (2010)	137.0	191.4
Jackson *et al.* (2011)	44.0	65.1
Bae *et al.* (2011)	-28.9	42.6

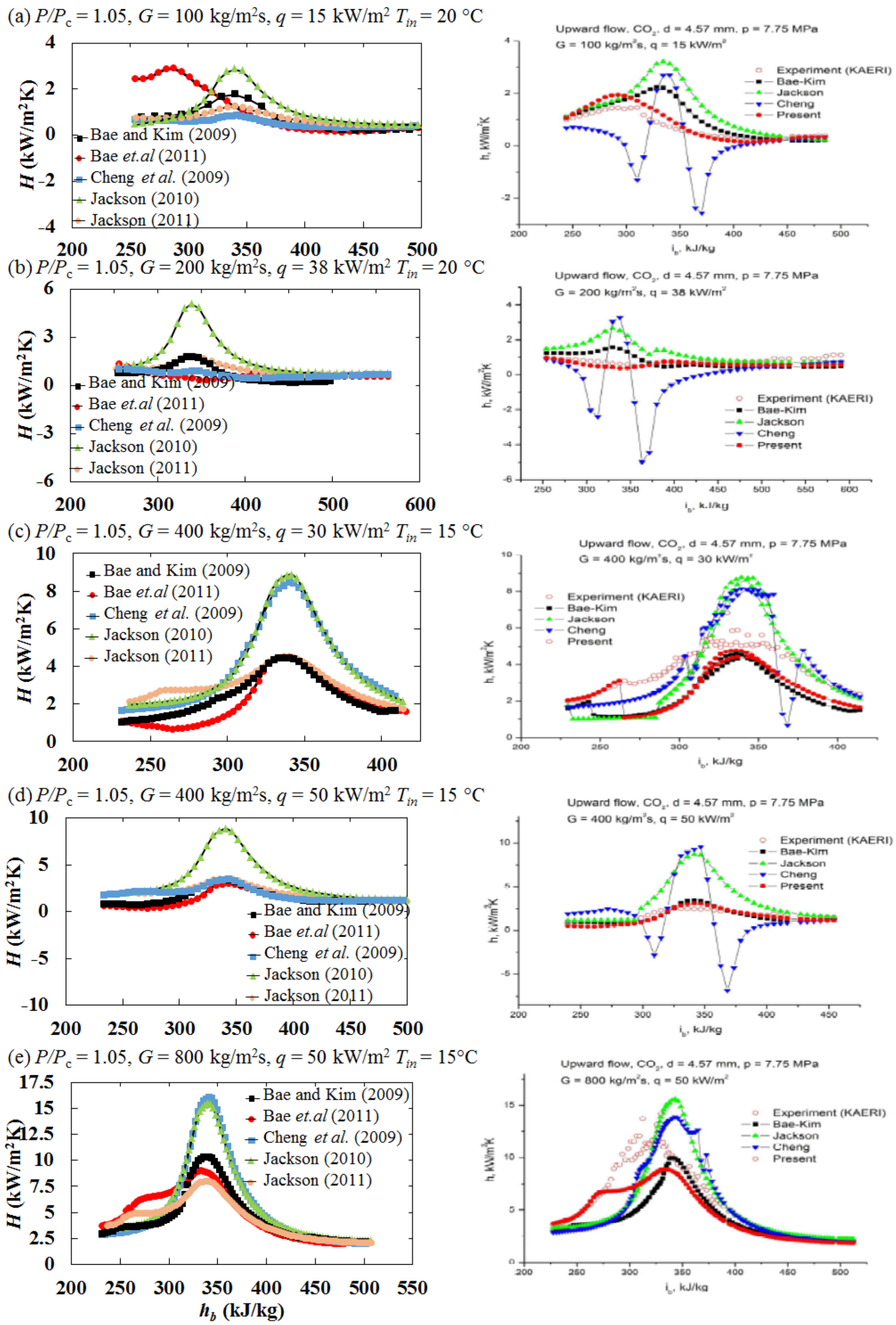

Figure 7.2: LHS: our evaluations of the HTD models at the operating conditions of KAERI experimental data given by Bae *et al.* (2011). RHS: published evaluation by Bae *et al.* (2011) at the same operating conditions of the LHS plots for CO_2 flows in a tube having ID of 4.75 mm, in the RHS, Jackson refers to Jackson (2010) model and 'present' refers to Bae *et al.* (2011d).

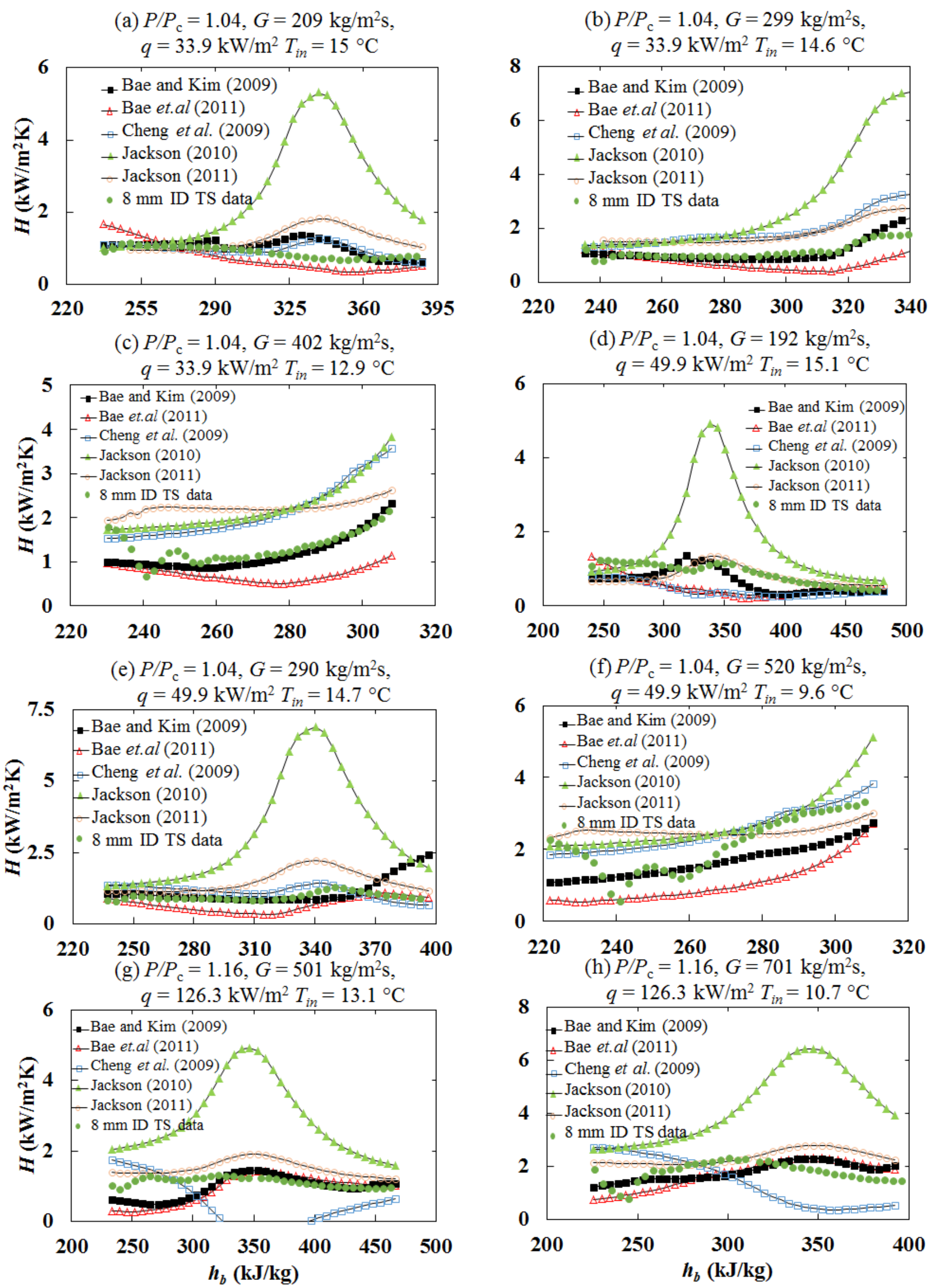

Figure 7.3: Heat transfer coefficient of selected HTD models against the heat transfer coefficient of the CO_2 data obtained in a 8 mm ID bare tube (University of Ottawa database).

7.2 Observed adverse effect of obstacles in the present tests

We have observed that at certain SC flow conditions, the obstacle-induced enhancement downstream from the obstacle was followed by an adverse impact where the HTC showed a dip and fell below the bare tube value as shown in chapter 5 and Figure 7.12 and 7.13. This is followed by a recovery where the HTC can again exceed the bare tube value. Table 7.3 summarizes the specific conditions where the adverse effect of flow obstacles on SCHT was observed while Appendix I specify the experimental flow conditions where this phenomenon was observed along with the corresponding bare-tube data.

7.3 Parameters affecting the adverse effect of obstacles

This adverse effect is obviously important as it can have repercussions in the thermal and safety analysis of SCWR fuel as ignoring this effect could underestimate the sheath temperature. Therefore an examination was made of the conditions or parameter values for which the adverse effect was observed. Figures 7.4 – 7.12 show plots of the ratio R_{SCHT} = HTC_{obs}/HTC_{bare} evaluated at the same flow conditions, as a function of various parameters that could affect HTD. Also indicated on the plots are the boundaries between adverse effect/no adverse effect. Because of experimental uncertainties in evaluating R_{SCHT} an uncertainty margin of 10% is assumed, i.e. an adverse effect is assumed to be present only if $R_{SCHT} < 0.9$. The following parameters were found to control the adverse obstacle effect:

- <u>*Buoyancy*</u>: Section 2.1.2 reviews various papers supporting the assertion that the buoyancy plays a major role in creating HTD conditions. Since the adverse effect is a HTD phenomenon, buoyancy is believed to be important in controlling the obstacle adverse effect. Thus, the buoyancy parameter (Eqn. 7.2) as given by Bae and Kim (2009) and others (section 2.1.2),

$$\mathrm{Bu} = \frac{\mathrm{Gr}}{\mathrm{Re}_b^{2.7}\,\mathrm{Pr}_b^{0.5}} \text{ and } \mathrm{Gr} = \frac{\rho_b\left(\rho_b - \bar{\rho}\right) g D^3}{\mu_b^2} \tag{7.2}$$

  was calculated for the obstructed tube. Figure 7.4 shows that an adverse obstacle effect appears to occur only when $\mathrm{Bu} > 4*10^{-7}$. The presence of a Bu limit is also supported by all HTD models presented in section 2.1.2 although the magnitude may differ. Mechanistically, Jackson (2011) hypothesized that due to Bu; the near-wall layer accelerated and laminarized the flow turbulence. Figure 7.4 suggests that knowledge of the Bu value is not enough to predict whether a certain case might have HTD or not due to the presence of the obstacles.

- *Bulk Temperature*: Figure 7.5 shows that an adverse obstacle effect appears to occur only when $T_b<T_{pc}$. When $T_b>T_{pc}$ the HTD is less likely to occur since the near wall layer and the core flow are both gas-like already, and therefore gradients in properties across flow are small. Because of this and laminarization of near wall layer probably does not occur.
- *Reynolds Number*: Figure 7.6 show that an adverse obstacle effect is less likely to occur at high flows (Re > 84000), where the flow is expected to have high turbulence levels.
- *Distance from upstream blockage*: Figure 7.7 shows that the highest probability of getting an adverse effect is at a distance downstream from the obstacles 6.7 < *L/D* < 50. Our data show that for *L/D* <6.7 enhancement effects suppress any potential adverse effect.
- *q/G parameter* : Figure 7.8 shows that the adverse obstacle effect appears to occur with data corresponding to all *q/G*.
- *Acceleration parameter:* the acceleration effect on the obstacle adverse effect was examined. The acceleration parameter (Eqn. 7.3) is given by Jackson *et al.* (2011) (section 2.1.2). Figures 7.9 and 7.10 show that an adverse obstacle effect appears to occur only when $Ac_b > 3*10^{-7}$ or $Q_b^* < 1800$.

$$Ac_b^* = \frac{Q_b^*}{\mathrm{Re}_b^{1.625}\,\mathrm{Pr}_b} \quad , \; Q_b^* = \frac{\beta_b q D}{k_b} \qquad (7.3)$$

- *Obstacle Pitch:* Figure 7.11 shows that the adverse obstacle effect appears to occur with data corresponding to all obstacle pitches. However, its impact on the SCHT appears to become less severe as the obstacle pitch becomes shorter. Related to Figure 7.7, if the pitch is less than 6.7 *L/D*, no adverse effect will occur.
- *Flow Blockage*: Figure 7.12 shows that the adverse obstacle effect on SCHT can occur at both flow blockage ratios of 13% and 25% ─ for the 13% flow obstruction only the 250 mm obstacle pitch was investigated. The results show that the adverse

effect for the 13% flow blockage is somewhat worse than for the 25% blockage. This could be because the heat transfer enhancement just downstream of the flow blockage was significantly lower for the 13% vs. 25% flow blockage; thus a subsequent drop in HTC brought the 13% data below the bare tube HTC while the 25% blockage required a much greater drop in HTC before they would drop below the corresponding bare tube data.

As a corollary to the above, and from an examination of our data it appears that the following factors either suppress or reduce the severity of the adverse effect:

- high flows or Re (Re > 84000),
- short spacer pitch
- low values of the buoyancy parameter (Bu < $4*10^{-7}$)
- high bulk enthalpy ($h_b > h_{pc}$)
- distance less than 6.7 *L/D* from the nearest upstream obstacle.
- low values of the acceleration parameter ($Ac_b < 3*10^{-7}$).
- high thermal loading values ($Q_b^* > 1800$)

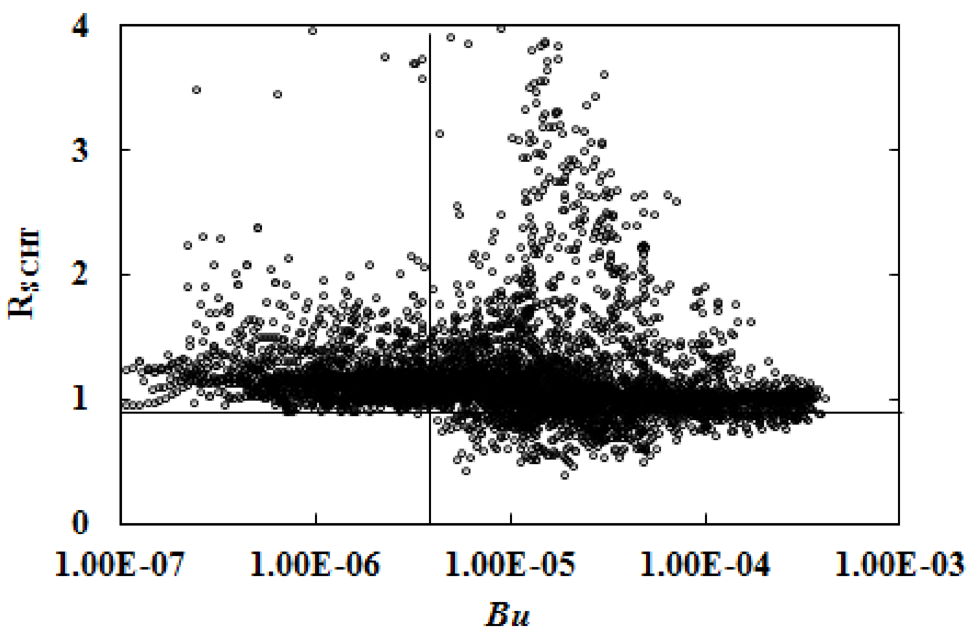

Figure 7.4: Effect of buoyancy (*Bu*) on the ratio of SCHT of obstructed to bare tube (R_{SCHT}) at pressure ratio of 1.04 and 1.13 and G = 200 – 1000 kg m^{-2} s^{-1}, vertical and horizontal lines mark the threshold of Bu and R_{SCHT} <0.9, respectively.

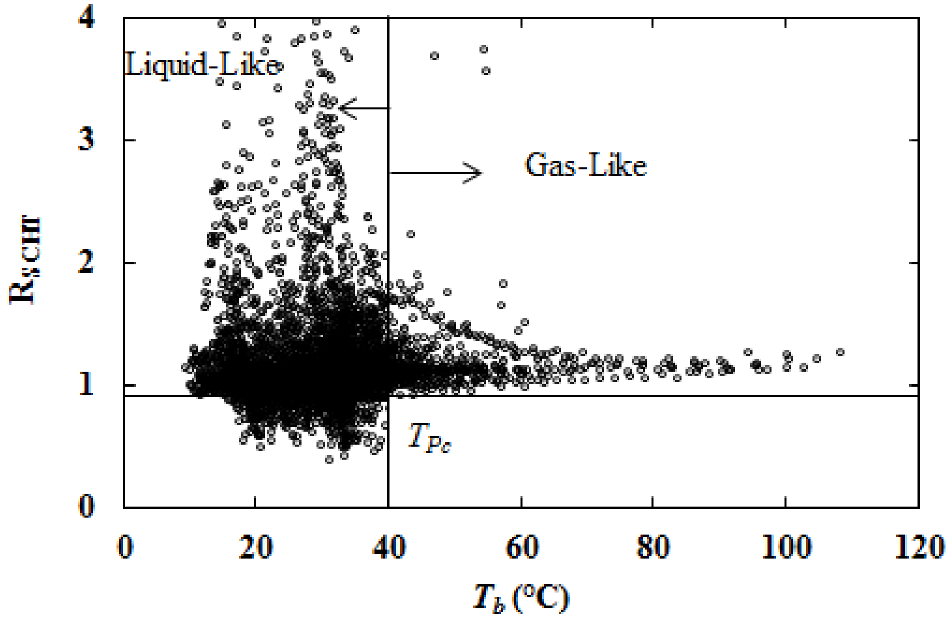

Figure 7.5: Effect of bulk temperature (T_b) on the ratio of SCHT of obstructed to bare tube (R_{SCHT}), at pressure ratio of 1.04 and 1.13 and G = 200 – 1000 kg m^{-2} s^{-1}, vertical line marks the threshold of T_b.

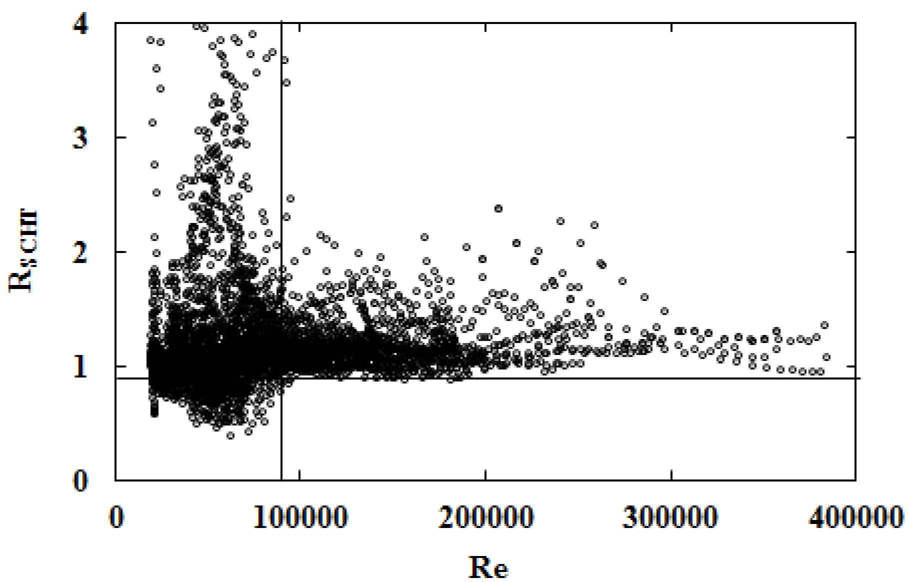

Figure 7.6: Effect of Reynolds number (Re) on the ratio of SCHT of obstructed to bare tube (R_{SCHT}), at pressure ratio of 1.04 and 1.13 and G = 200 – 1000 kg m^{-2} s^{-1}, vertical line marks the threshold of Re.

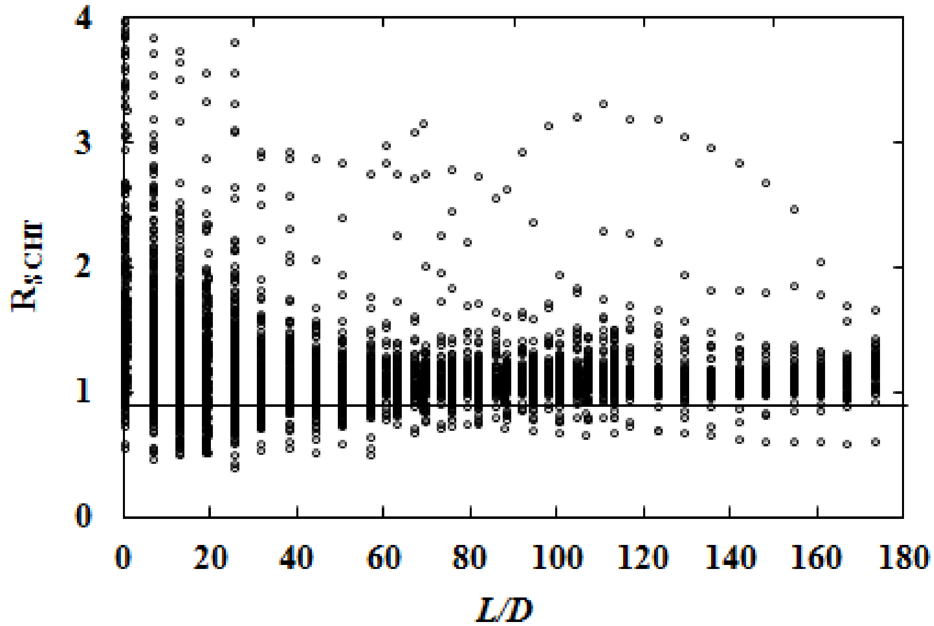

Figure 7.7: Effect of distance downstream from an obstacle (*L/D*) on the ratio of SCHT of obstructed to bare tube (R_{SCHT}), at pressure ratio of 1.04 and 1.13 and G = 200 – 1000 kg m^{-2} s^{-1}.

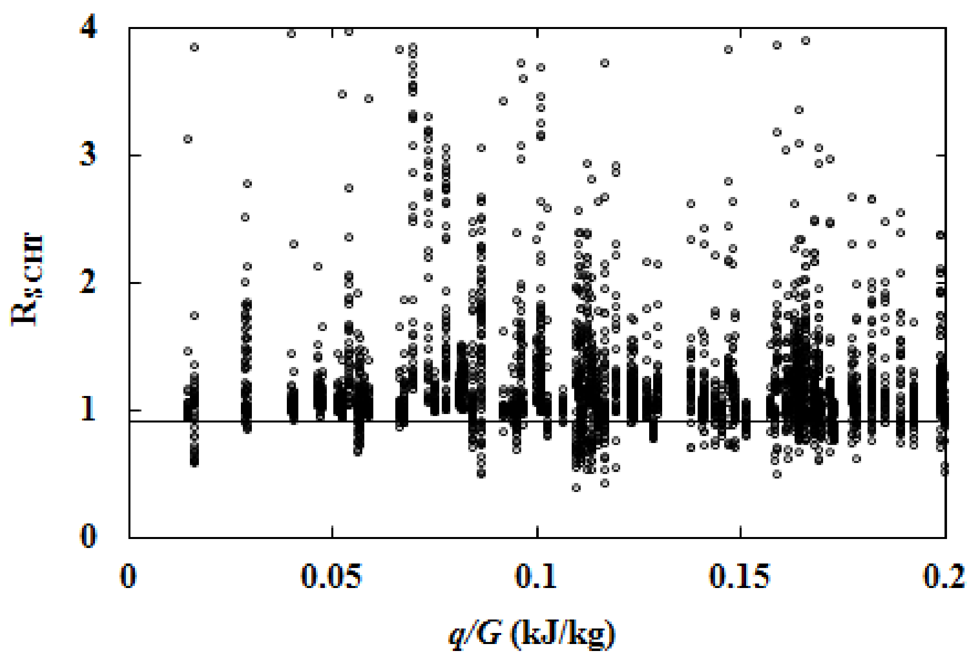

Figure 7.8: Effect of (*q/G*) on the ratio of SCHT of obstructed to bare tube (R_{SCHT}), at pressure ratio of 1.04 and 1.13 and G = 200 – 1000 kg m^{-2} s^{-1}.

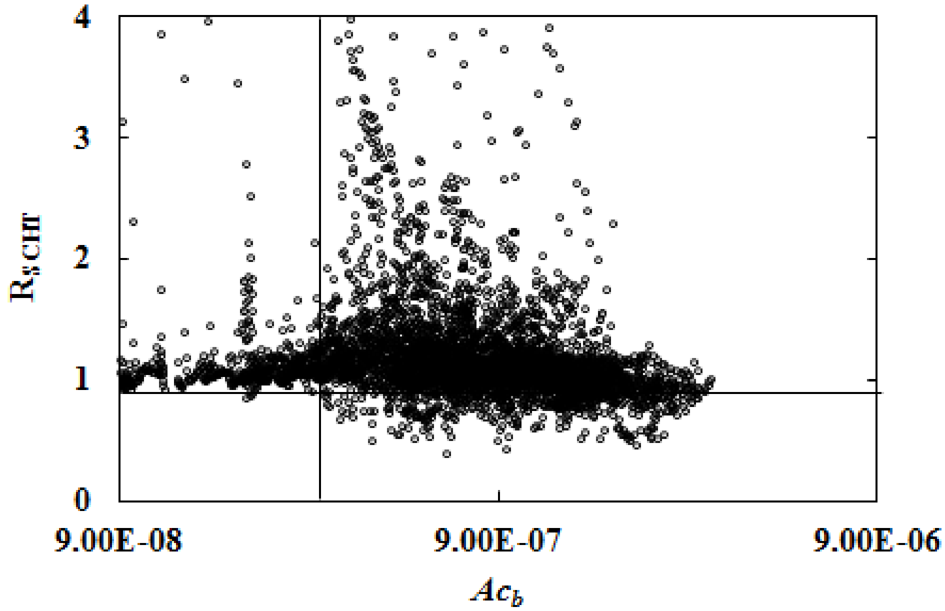

Figure 7.9: Effect of acceleration (Ac_b) on the ratio of SCHT of obstructed to bare tube (R_{SCHT}), at pressure ratio of 1.04 and 1.13 and G = 200 – 1000 kg m^{-2} s^{-1}, vertical line marks the threshold of Ac_b.

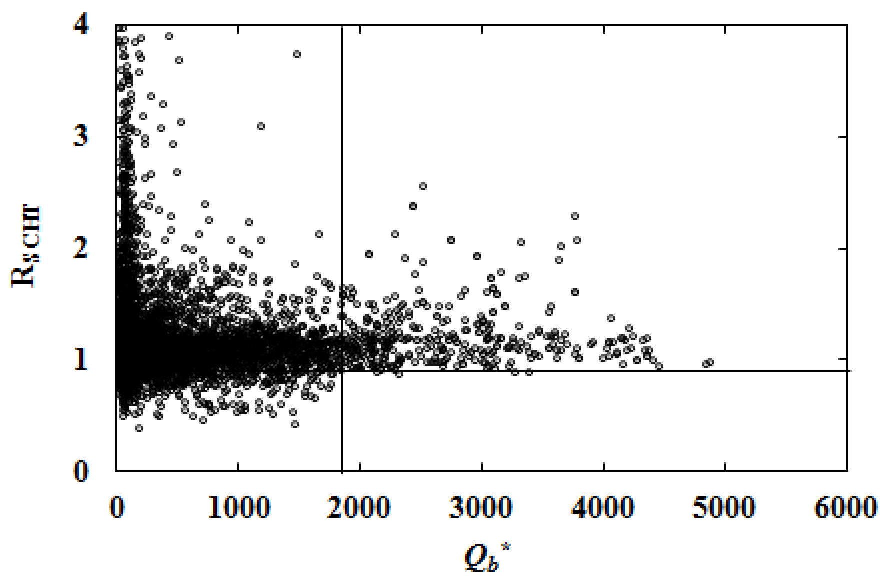

Figure 7.10: Effect of thermal loading parameter (Q_b^*) on the ratio of SCHT of obstructed to bare tube (R_{SCHT}), at pressure ratio of 1.04 and 1.13 and G = 200 – 1000 kg m^{-2} s^{-1}, vertical line marks the threshold of Q_b^*.

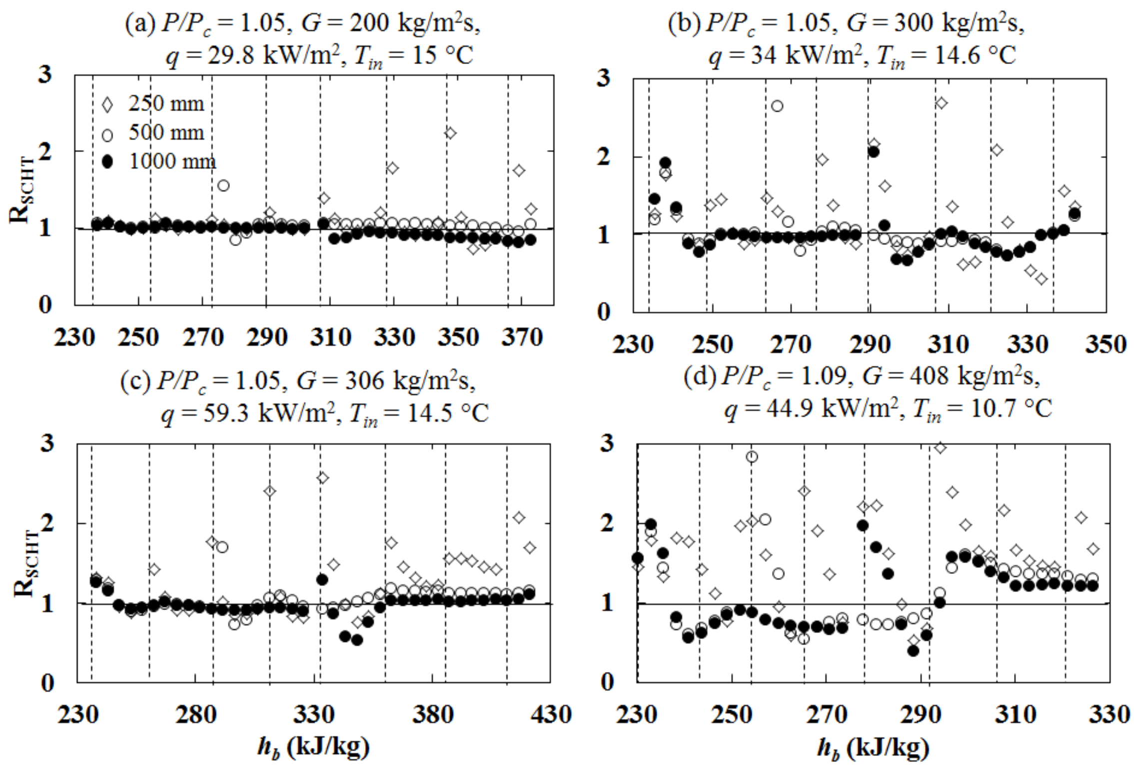

Figure 7.11: Effect of obstacle pitch on R_{SCHT}, dashed lines mark the obstacle locations.

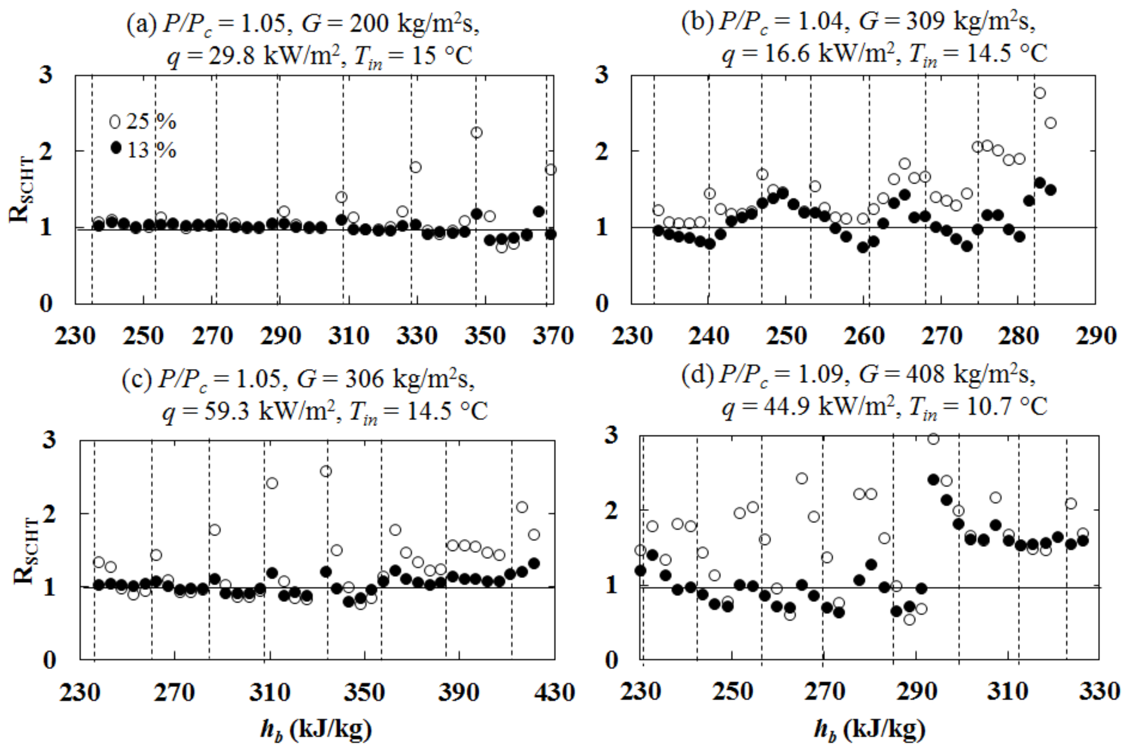

Figure 7.12: Effect of obstacle blockage ratio on R_{SCHT}, dashed lines mark the obstacle locations.

7.4 Discussion

An up-to-date review of the available SCHT correlations was presented in section 2.1. This review showed the different correction factors that were used by several researchers. Based on the correlation assessments performed by others, the correlation of Mokry *et al.* (2009) provided the best prediction for normal heat transfer to SC water. The correlation of Mokry *et al.* (2009) accounts for the variation in density across the tube diameter and calculates Pr based on the integrated specific heat across the tube diameter.

Bazargan (2001) discussed studies that investigated the onset of HTD by considering the ratio of Gr to Re. As concluded by Bazargan (2001), the analytical studies have been limited to finding a criterion for the onset of buoyancy effect. Finally, the applicability of Jackson's solution at supercritical pressures was not successful. The semi-empirical solution was valid only for air flows at certain conditions. In fact, Jackson's 1st published work discussing the HTD issue was in 1979 and since then no other better solutions came up, leaves this phenomenon not well understood. To account for HTD, most correlations and semi-empirical models used a buoyancy parameter.

An assessment of the more promising SCHT correlations against the uOttawa supercritical CO_2 database for normal and HTD conditions was performed. The assessment showed that the correlation of Mokry *et al.* (2009) and Bae and Kim (2009) provided the best predictions in the liquid-like, gas–like, and near critical region for normal heat transfer. During HTD conditions, the correlation of Bae and Kim (2009) provided the best prediction.

It was initially thought that knowledge of the Bu value could be sufficient to predict whether HTD would occur due to the presence of the obstacles. However, Figure 7.4 showed that knowledge of the Bu by itself is not sufficient to predict this effect because at Bu > 4×10^{-7}, R_{SCHT} can either be higher or lower than unity. Section 7.3 has shown that other parameters were also found to play a role in determining whether an adverse effect of obstacles on SCHT is present or not.

After examining Figures 7.4 - 7.12, we can state with some confidence that, based on our data base, the adverse obstacle effect (i.e. $R_{SCHT} < 1$) was observed when the following conditions are satisfied (allowing for experimental uncertainties we used the lower bound $R_{SCHT} < 0.9$):

$$T_b < T_{pc},\ \mathrm{Re} < 84000,\ \mathrm{Bu} > 4*10^{-7},\ L/D > 6.7,\ Ac_b > 3*10^{-7},\ Q_b^* < 1800 \qquad (7.4)$$

The uOttawa data base contains 5472 data points for which R_{SCHT} was calculated. Of this data base 2465 points of the total database satisfied criteria (7.4). However, 1367 data points from the total database were found to have $R_{SCHT} < 1$ and of this total 987 data points satisfied criteria (7.4), and were found to have $R_{SCHT} < 1$.

We also identified the number of data points where an adverse effect was clearly observed after accounting for experimental uncertainties: 535 data points of the total data were found to have $R_{SCHT} < 0.9$, and of this total 446 data points satisfied criterion (7.4).

Figure 7.14 shows a histogram of the obstructed data for several R_{SCHT} intervals. R_{SCHT} appears to have a normal distribution having the highest data population in the range of 1.0 to 1.1. In conclusion, as a rough estimate, criterion 7.4 will identify most of the adverse effect data.

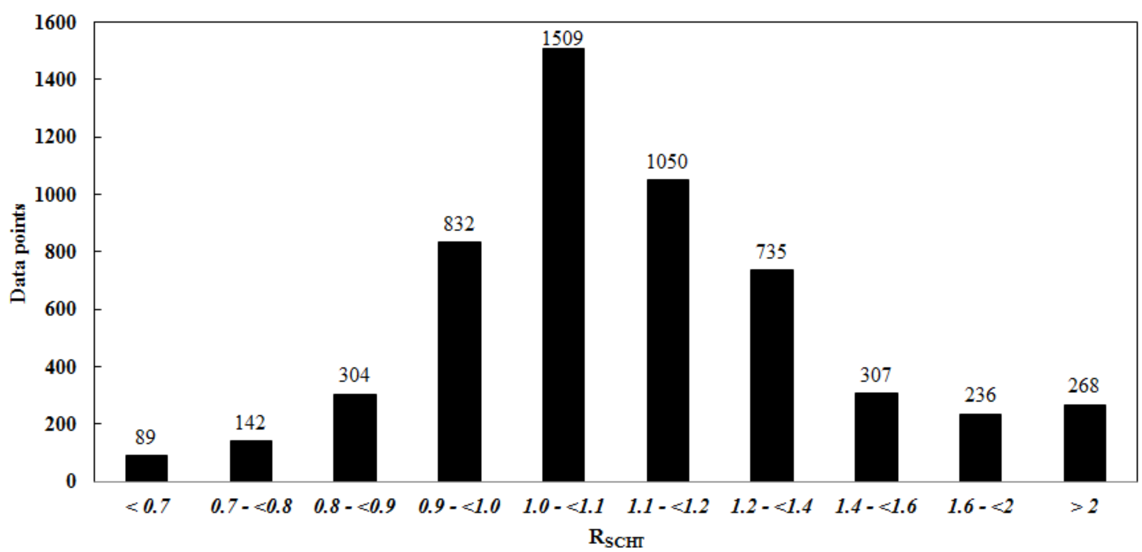

Figure 7.13: Histogram of R_{SCHT} (uOttawa data points)

Table 7.3: Obstructed and bare tube operating conditions of the observed obstacle negative impact (blunt obstacles).

Obstructed tube				Bare tube				Obstacle information		
P/P_c	G (kg m^{-2} s^{-1})	q (kW m^{-2})	T_{in} (°C)	P/P_c	G (kg m^{-2} s^{-1})	q (kW m^{-2})	T_{in} (°C)	Obstacle pitch (mm)	Δz (mm)	ε (%)
1.052	331.2	55.91	11.6	1.046	339.7	56.14	11.1	100	104-154	25
1.039	313.3	29.72	14.1	1.039	293.5	29.66	14.6	100	104-254	25
1.041	307.6	34.10	14.8	1.050	299.4	33.99	14.6	100	104-704	25
1.051	297.0	59.32	14.5	1.039	304.0	59.30	14.8	100	54-254	25
1.081	409.5	44.74	10.8	1.097	414.0	44.79	10.8	100	154-254	25
1.046	196.4	29.68	14.8	1.050	206.3	29.79	15.0	100	4 -904	25
1.034	289.1	29.6	14.4	1.039	293.5	29.7	14.6	50	153-203	25
1.042	295.1	33.9	14.5	1.050	299.4	34.0	14.6	50	153-203	25
1.044	298.0	49.2	14.5	1.051	289.7	49.1	14.7	50	103-203	25
1.039	308.8	59.2	14.4	1.039	304.0	59.3	14.8	50	103-203	25
1.089	398.1	45.0	10.6	1.097	414.0	44.79	10.8	50	203-734	25
1.048	212.1	29.82	14.8	1.050	206.3	29.79	15.0	50	103- 153	25
1.056	207.8	29.82	14.7	1.050	206.3	29.79	15.0	25	103-203	25
1.480	309.6	16.57	14.4	1.440	309.2	16.64	14.5	25	NA	25
1.046	204.7	29.65	15.0	1.050	206.3	29.79	15.0	25	3-203	13
1.014	294.1	16.63	14.8	1.440	309.2	16.64	14.5	25	3-203	13
1.055	307.9	59.19	14.8	1.039	304.0	59.30	14.8	25	53-203	13
1.096	406.3	44.84	10.8	1.097	414.0	44.79	10.8	25	53-203	13

Chapter 8

Conclusion

8.1 Summary

Although there are some studies in the literature that investigated the effects of wire wraps in tubes and annular channels and grid spacers in rod bundles (Table 2.10), these studies had relatively narrow ranges of geometrical and dynamic conditions. In general, very few experimental studies are available for SC flows in rod bundles. These bundles were equipped with grid spacers and none of them was equipped with wire wraps. Also, available wall temperature measurements lack spatial resolution and had large uncertainty, because the outer wall temperature calculation neglected circumferential and axial conduction. Literature is also scarce on systematic investigations of obstacle impact on heat transfer at high subcritical and supercritical pressures. Available information focused on heat transfer enhancement and did not consider separately the liquid-like and gas-like regimes.

In this thesis, the flow obstruction effects on heat transfer at supercritical and high subcritical pressures were investigated in two test sections. First, in a three-rod bundle equipped with wire wraps or grid spacers; detailed surface temperature measurements along and around the three heated rods were collected using internally traversed thermocouples. Second, in a 8 mm ID tube with and without flow obstacles; fixed thermocouples were used to measure the wall temperature. In all experiments, inlet and outlet temperatures, mass flow rate, test section power, and inlet and outlet pressures were measured; these properties were used to calculate the heat transfer coefficient and bulk enthalpy.

The detailed measurements of the three rod bundle allowed us to quantify the uncertainty of the 1-D heat conduction procedure, which is used in most of the analysis of the available literature. We evaluated the uncertainty in heat transfer coefficient calculations caused by the circumferential heat conduction. We developed an approximate method to evaluate the circumferential heat transfer coefficient, which has a maximum error of 5 % compared to 40 % when the 1-D heat conduction procedure is used.

Heat transfer deterioration appears to have occurred for mass fluxes in the approximate range between 200 and 700 kg m^{-2} s^{-1} near the start of the heated section of the rod bundle equipped with either type of spacers as well as in a circular tube under the same flow and heating conditions. The onset of deterioration occurred at a higher heat flux for the wire-wrapped bundle than for the one with grid spacers, and at the lowest heat flux for the tube. For rough purposes, normal heat transfer in either of the rod bundles behaved similarly to the one in the tube and was also compatible with the predictions of the correlation of Jackson. Overall, hear transfer was somewhat more efficient in the wire-wrapped bundle than in the one with grid spacers. For low mass fluxes (roughly 200 and 400 kg m^{-2} s^{-1}), normal heat transfer in the rod bundles was stronger than in the tube; for an intermediate mass flux (700 kg m^{-2} s^{-1}), heat transfer in all three cases had comparable strengths; rather surprisingly, at higher mass fluxes (100 and 1200 kg m^{-2} s^{-1}), heat transfer in the tube appeared to be more efficient than in the rod bundles. The minimum supercritical heat transfer coefficient decreased somewhat with increasing heat flux and decreased strongly at a low mass flux while the effects of pressure and inlet temperature were weak.

The parametric study of flow obstacle effects on the SCHT allowed us to quantify the maximum enhancement of the heat transfer coefficient. The most efficient obstacle geometry was found to be a blunt obstacle having a blockage ratio of 25 % and obstacle pitch of 250 mm.

HTD-like phenomena were observed near the start of the heated length at low mass fluxes for both the bare tube and the obstacle-equipped tube. An examination of the parametric trends has shown that the SC heat transfer coefficient variation with bulk enthalpy is fairly insensitive to inlet temperature and pressure changes, while it is strongly affected by changes in mass and heat fluxes. An important finding of the bare tube experiments is that the dependence of SCHT on mass flux appears to be suppressed at HTD conditions. This may be explained by a conjecture that at HTD conditions the buoyancy effect is sufficiently strong to suppress the dependence of heat transfer on convection effects, which would normally increase with increasing mass flux. Keeping the obstacle pitch short was found to be the most effective method of suppressing HTD. Depending on the flow conditions and the obstacle location, obstacles suppressed HTD or shifted its occurrence to downstream locations. The HTC enhancement decayed exponentially with distance from the obstacle. The decay length was short (typically 15*D* – 35 *D*) for normal heat transfer and liquid-like heat transfer, but increased to up to 60*D* in the gas-like region. For most conditions, the flow obstacles reduced the maximum wall temperatures or had a neutral effect. However, for certain conditions (low flows and enthalpies in the vicinity of the pseudo-critical enthalpy or lower than that), flow obstacles resulted in higher wall temperatures than those in the bare tube reference case, and triggered heat transfer deterioration.

At high subcritical pressures, the bare-tube single phase (liquid) results are in good agreement with Gnielinski's correlation. The obstacle effect decays rapidly at single phase conditions ─ Gnielinski's correlation with Yao's correction may be used for predicting the decaying flow obstruction effect. The bare-tube CHF data at P/P_c = 0.90, after conversion into water-equivalent conditions, are found to be under predicted with the CHF look-up table. Increasing the pressure from P/P_c = 0.9 to 0.95 reduced the maximum film boiling temperature; a further increase in pressure to supercritical conditions (for the same inlet temperature, heat flux and mass flux) resulted in a significant decrease in the maximum wall temperature. The obstacles reduced the maximum wall temperature noticeably at all pressures. Obstacles suppressed the CHF occurrence locally and shifted the CHF location to a downstream location. The increase in CHF depends strongly on the distance from the nearest upstream obstacle and ranged from 0 - 300 %. Available correlations for the effect of flow obstructions on CHF could not provide a satisfactory prediction.

A new finding of this study is an adverse impact of flow obstacles on the SCHT; this adverse impact of flow obstacles on the SCHT is discussed and a criterion to predict the onset of this adverse effect is developed.

8.2 Main contributions

The present study presents a unique set of SCHT measurements obtained in two spacer-equipped test sections: a three-rod bundle equipped with grid spacers and wire wraps and an 8 mm ID tube with and without obstacles at conditions equivalent to that of the SCWR.

The present study is the first systematic investigation of the flow obstacles effect on heat transfer to tube flows at supercritical and high subcritical pressures.

The detailed measurements of the bare 8 mm ID tube at HTD conditions revealed that heat transfer coefficient is independent of the mass flux and it was due to buoyancy forces. This provides a support to the HTD mechanisms caused by buoyancy forces.

New correlations accounts for the obstacle effect on the SCHT in liquid-like and gas-like heat transfer were derived based on the data of the obstructed 8 mm ID tube.

A criterion predicting the onset of the obstacle adverse effect on the SCHT was developed.

8.3 Recommendations for future work

An extension of this work that could be conducted in the same facility is to investigate heat transfer characteristics of upward supercritical refrigerant 134a flows in a 3-rod bundle equipped with wire wraps or grid spacers at conditions similar to the CO_2 conditions that were investigated in this thesis. The purpose of this study is to check the scaling laws of fluid-to-fluid modeling and enhance their accuracy.

The CO_2 databases of the 3-rod bundle and the 8 mm ID tube can be used to validate CFD simulations.

Further research to enhance our understanding of the new finding of this thesis, particularly the adverse impact of flow obstructions on the SCHT, is highly recommended.

References

Ackerman, J.W., 1970. Pseudoboiling heat transfer to supercritical pressure water in smooth and ribbed tubes. J. Heat Transfer. 92, 490–498.

Alekseev,G.V., Silin,V.A., Smirnov, A.M., Subbotin,V.I., 1976. Study of the thermal conditions on the wall of a pipe during the removal of heat by water at a supercritical pressure. J. High Temp. 14(4), 683-687.

Ambrosini, W., Forgione, N., Badiali, S, Jackson, J.D., Sharabi, M., 2013. Capabilities of two low-Reynolds number turbulence models in predicting heat transfer to fluids at supercritical pressure. Proc. 15th Intern. Meeting on Nuclear Reactor Thermalhydraulics, NURETH15. Paper No. 134, Pisa, Italy.

Anglart, H., Persson, P., Hedberg, S., 2005. Experimental investigation of stationary and transient post-dryout heat-transfer in 22.1×10 mm annulus with spacers. Proc. 11th Intern. Meeting on Nuclear Reactor Thermal-Hydraulics (NURETH-11), Avignon, France, October 2−6.

Anklam, T.M., Miller, R.J., White, M.D., 1982. Experimental investigations of uncovered-bundle heat transfer and two-phase mixture-level swell under high-pressure low heat-flux conditions. Oak Ridge National Laboratory (ORNL-5848).

Ankudinov, V.B. and Kurganov, V.A., 1981. Intensification of deteriorated heat transfer in heated tubes at supercritical pressures. J. High Temperatures. 19, 870-874.

Bastron, A., Hofmeister, J., Mayer, L., Schulenberg, T., 2005. Enhancement of heat transfer in HPLWR fuel assemblies. Proc. Intern. Conf. Nuclear Energy Systems for Future Generation and Global Sustainability (GLOBAL-2005), Tsukuba, Japan, Paper No. 36, October 9-13.

Becker, S., Lienhart, H. Durst, F., 2002. Flow around three-dimensional obstacles in boundary layers. J. Wind Engineering and Industrial Aerodynamics. 90, 265–279.

Bae, Y.Y. and Kim, H.Y., 2009. Convective heat transfer to CO_2 at a supercritical pressure flowing vertically upward in tubes and an annular channel. Exp. Therm. Fluid Sci. 33, 329-339.

Bae, Y.Y., Visser, D.C, Chandra., L, Lycklama à Nijeholt J.A., 2010. CFD analysis on the influence of wire wrap spacers on the heat transfer to supercritical CO_2. Proc. Intern. Cong. On Advances in Nuclear Power Plants (ICAPP 2010), San Diego, CA, USA, June 13-17.

Bae, Y.Y., Kim, H.Y., Yoo, T.H., 2011. Effect of a helical wire on mixed convection heat transfer to carbon dioxide in a vertical circular tube at supercritical pressures. Intern. J. Heat and Fluid Flow. 32, 340–351.

Bae, Y.Y., Kim, H.Y., Yoo, T.H., 2011. Assessment of mixed convestion heat transfer at supercritical pressures. Proc. 5th Int. Sym. SCWR (ISSCWR-5), Vancouver, British Columbia, Canada.

Bazaragan, M., 2001. Forced convection heat transfer to turbulent flow of supercritical water in a round horizontal tube. Ph.D Thesis, University of British Columbia.

Bishop, A.A., Sandberg, R.O., Tong, L.S., 1965. Forced convection heat transfer to water at near-critical temperatures and supercritical pressures. A.I.Ch.E.-I.Chem.E Symposium Series No. 2, 77−85.

Bringer, R.P., Smith, J.M., 1957. Heat Transfer in the Critical Region, AIChE Journal. 3, 49–55.

Chandra, L., Lycklama Nijeholt, J.A, Dirk C.V., Roelofs F., 2009. CFD analysis on the influence of wire wrap spacers on heat transfer at supercritical conditions. Proc. 4th Intern. Symp. On Supercritical Water-Cooled Reactors, Heidelberg, Germany, Paper No. 30, March 8-11.

Chen T., 2004. Two-phase flow and heat transfer study. (In Chinese), Xi'an Jiaotong University Press, China, ISBN 7-5605-1892-3. As reported by Pioro and Duffey (2007).

Chen, W., Fang, X., 2014. A new heat transfer correlation for supercritical water flowing in vertical tubes. Int. J. Heat Mass Transfer. 78, 156–160.

Cheng, X., Yang, Y.H., Huang, S.F., 2009. A simplified method for heat transfer prediction of supercritical fluids in circular tubes. Ann. Nucl. Energy. 36, 1120–1128.

Cheng, X., Liu, X.J., Gu, H.Y., 2011. Fluid-to-fluid scaling of heat transfer in circular tubes cooled with supercritical fluids. Nucl. Eng. Des. 241, 498–508.

Churkin, A.N., Deev, V.I., Kharitonov, V.S., 2015. A new correlation of a heat transfer coefficient in supercritical water. Proc. 7th Inter. Symp. On Supercritical Water-Cooled ReactorsISSCWR-7. 15-18 March , Helsinki, Finland.

CIuss, E. M., Jr., 1987. Post critical heat flux heat transfer in a vertical tube including spacer grid effects. M.A.Sc. thesis, Department of Mechanical Engineering, Massachusetts Institute of Technology.

Dittus, F.W., Boelter, L.M.K., 1930. University of California, Berkeley, Publications on Engineering. 2, 443–461.

Doerffer, S., Groeneveld D.C., Schenk J.R., 1996. Experimental study of the effects of flow inserts on heat transfer and critical heat flux. Proc. 4th Int. Conf. On Nuclear Engineering, New Orleans, Louisiana, USA. 41-49, March 10-14.

Dyadyakin, B.V., Popov, A.S., 1977. Heat transfer and thermal resistance of tight seven-rod bundle, cooled with water flow at supercritical pressures. (In Russian), Trans. VTI. 11, 244-253. As reported by Pioro and Duffey (2007).

Era, A., Gaspasi, G. P., Hassid, A., Milani, A., Zavattarelli, R., 1966. Heat transfer data in the liquid deficient region for steam-water mixtures at 70 kg cm^{-3} flowing in tubular and annulai conduits. Topical Report No. 11, CISE-R-184. As reported by Yoder (1985).

Eter, A., Groeneveld, D., Tavoularis, S., 2016. An experimental investigation of supercritical heat transfer in a three-rod bundle equipped with wire-wrap and grid spacers and cooled by carbon dioxide. Nucl. Eng. Des. 303, 173-191.

Farah, A., King, K., Gupta, S., Mokry, S., Pioro, I., 2010. Comparison of selected heat-transfer correlations for supercritical water flowing in vertical bare tubes. Proc. 2nd Canada-China Joint Workshop on Supercritical Water-Cooled Reactors (CCSC-2010) Toronto, Ontario, Canada, April 25-28.

Fedorov, E.P., Yanovskiy, L.S, Krasnyuk, V.I., Dreitser, G.A., 1986. Intensification of heat transfer in heated channels at flow of hydrocarbons of supercritical pressure. (in Russian), in book: Modern Problems of Hydrodynamics and Heat. As reported by Pioro and Duffey (2007).

Fewster, J., Jackson, J.D., 2004. Experiments on supercritical pressure convective heattransfer having relevance to SPWR. Proc. ICAPP'04, Paper 4342, Pittsburgh, PA, USA, June 13−17.

Gabaraev, B.A., Kuznetsov, Yu.N., Pioro, I.L., Duffey, R.B., 2007. Experimental study on heat transfer to supercritical water flowing in 6-m long vertical tubes. Proc. 15th Inter. Conf. On Nuclear Engineering (ICONE-15), April 22-26, Nagoya, Japan, Paper #10692, 8 pages.

Ghajar, A., Asadi, A., 1986. Improved forced convective heat-transfer correlations for liquids in the near-critical region. AIAA Journal 24, 2030-2037.

Gnielinski, V., 1976. New equation for heat and mass transfer in turbulent pipe and channel flow. Intern. Chem. Eng., 16, 359–366.

Goldman, K., 1961. Heat transfer to supercritical water at 5000 psi flowing at high mass flow rates through round tubes. Proc. 1961-62 Heat Transfer conference on International Development in Heat Transfer, August 28 – September 1, 1961. University of Colorado, USA.

Gonin, A.I., Sergeev, V.V., Dispersed flow film boiling heat-transfer in channels with spacer elements. Source and year of publication are unknown.

Griem, H., 1996. A new procedure for the at near-and supercritical prediction pressure of forced convection heat transfer. J. Heat Mass Trans. 3, 301–305.

Griffith, G.D. and R.H. Sabbersky, 1960. Convection in a fluid at supercritical pressures. ARS Journal. 30, 289-291.

Groeneveld, D. C., Yousef, W. W., 1980. Spacing devices for nuclear fuel bundles: A survey of their effect on CHF, post-dryout heat transfer and pressure drop. Proc. ANS / ASME / NRC Intern. Topical Meeting on Nuclear Reactor Thermal Hydraulics, Saratoga Springs, New York pp. 1111-1125.

Gupta, S., Mokry, S., Farah, A., King, K., Peiman, W., Pioro, I., 2010. Developing a heat-transfer correlation for supercritical-water flow in bare vertical tubes and its application. UOIT unpublished report.

Gupta, S., Saltanov, E., Mokry, S.J., Pioro, I., Trevani, L., 2013. Developing empirical heat-transfer correlations for supercritical CO_2 flowing in vertical bare tubes. Nuc. Eng. Des., Vol. 261, pp. 116-131.

Hadaller, G., Banerjee, S., 1969. Heat transfer to superheated steam in round tubes. AECL Report.

Hassan, M. A., Rehme, K., 1981. Heat transfer near spacer grids in gas-cooled rod bundles. Nucl. Tech. 52, 401-414.

Herkenrath, H., Mork-Morkenstein, P., Jung, U., Wecketmann, F.J., 1967. Warmeubergang an Wasser bei Erzwungener Stromung in Druckbereich von 140 bis 250 bar. ECR-3658d, (in German).

Hoffman, H. W. et al., 1970. Experimental studies of the heat transfer and fluid dynamic characteristics of rod-cluster-type nuclear reactor fuel elements. Oak Ridge National Laboratory (ORNL-4356). As reported by Yoder (1985).

Holloway, M.V., McClusky, H.L., Beasley, D.E., Conner, M.E., 2004. The effect of support grid features on local, single-phase heat transfer measurements in rod bundles. J. Heat Transfer. 126, 43-53.

Hong, Jong, Y., Hsieh, Shing, S., 1991. An experimental investigation of heat transfer characteristics for turbulent flow over staggered ribs in a square duct. J. Exp. Thermal and Fluid Science. 4, 714-722.

Hong-bo, L., Meng, Z., Han-yang, G., Dong-hua, L., Fei, W., Jian-min, Z., Yong, Z.,Jue, Y., 2013. Heat transfer research on supercritical water flow in 2×2 bundles. Proc. 6th Inter. Symp. On Supercritical Water-Cooled Reactors ISSCWR-6. Shenzhen, Guangdong, China.

Hongzhi, L., Wang, H., Luo, Y., Hongfang, G., Shi, X., Chen, T., Laurien, E., Zhu,Y., 2009. Experimental investigation on heat transfer from a heated rod with a helically wrapped wire inside a square vertical channel to water at supercritical pressures. Nucl. Eng. Des. 239, 2004–2012.

Hsu, Y.Y, Smith, J.M., 1961. The effect of density variation on heat transfer in the critical region. Trans. ASME Heat Transfer. 176-182.

Jackson, J.D., Hall, W.B., 1979. Influences of buoyancy on heat transfer to fluids flowing in vertical tubes under turbulent conditions, in turbulent forced convection in channels and bundles. S. Kakaç and D.B. Spalding (editors), Hemisphere Publishing Corp., Washington, USA. 2, 613−641.

Jackson, J.D., Fewster, J., 1975. Forced convection data for supercritical pressure fluids. HTFS 21540.

Jackson, J. D., 2002. Consideration of the heat transfer properties of supercritical pressure water in connection with the cooling of advanced nuclear reactors. Proc. 13th Pacific Basin Nuclear Conference Shenzhen City, China.

Jackson, J. D., 2008. A semi-empirical model of turbulent convective heat transfer to fluids at supercritical pressure. Proc. 16th Intern. Conf. On Nuclear Engineering, Orlando, USA,

Jackson, J. D., 2009. Validation of an extended heat transfer equation for fluids at supercritical pressure. Proc. 4th Intern. Symp. Supercritical Water-Cooled Reactors (ISSCWR-4), Heidelberg, Germany, March 8-11, Paper 24.

Jackson, J. D., 2010. An extended model of variable property developing mixed convection heat transfer in vertical tubes. Proc. 1st Meeting of International Specialists on Supercritical Pressure Heat Transfer and Fluid Dynamics, University of Pisa, Pisa, Italy, July 5-8.

Jackson, J. D., Jiang, P.X., Liu, B. and Zhao, C.R., 2011. Interpreting and categorizing experimental data on forced and mixed convection heat transfer supercritical pressure fluids using physically-based models. Proc. 5th Int. Sym. SCWR (ISSCWR-5) P103 Vancouver, British Columbia, Canada, March 13-16.

Jiang, K., 2015. An experimental facility for studying heat transfer in supercritical fluids. M.A.Sc. Thesis, Department of Mechanical Engineering, University of Ottawa. Canada.

Jaromin, M., Anglart, H., 2013. A numerical study of the turbulence Prandtl number impact on heat transfer to supercritical water flowing upward under deteriorated conditions. Proc. 15th Intern. Topical Meeting on Nuclear Reactor Thermalhydraulics, NURETH15, 134, Pisa, Italy.

Kalinin, E.K., Dreitser, G.A., Kopp, I.Z., Myakohin, A.S., 1998. Effective heat transfer surfaces. (In Russian), Energoatomizdat Publishing House, Moscow, Russia, 408 Pages. As reported by Pioro and Duffey (2007).

Kamenetsky, B., Shitsman, M., 1970. Experimental investigation of turbulent heat transfer to supercritical water in a tube with circumferentially varying heat flux. Proc. 4th Intern. Heat Transfer Conference, Paris-Versailles, France, Elsevier Publishing Company. 4, Paper No. B 8.10. As reported by Pioro and Duffey (2007).

Kamenetskii, B.Ya., 1980. The effectiveness of turbulence promoters in tubes with nonuniformity heated perimeters under conditions of impaired heat transfer. J. Thermal Engineering. 27, 222–223. As reported by Pioro and Duffey (2007).

Karoutas, Z., Gu, C.Y., Scholin, B., 1995. 3-D Flow analyses for design of nuclear fuel spacer. Proc. 7th Intern. Meeting on Nuclear Reactor Thermal-Hydraulics (NURETH-7). 3153–3174, 10-15 September.

Kim, I.G., Korol'kov, B.P., 1991. Enhancement of steady-state post-dryout heat transfer in an annulus with spacers. Heat-transfer Soviet Research. 23, 649–657.

Kirillov PL, Yur'ev Yu S, Bobkov VP., 1990. Handbook of thermal-hydraulics calculations (In Russian). Energoatomizdat Publishing House, Moscow.

Kirillov, P., Pometko, R., Smirnov, A., 2005. Experimental study on heat transfer to supercritical water flowing in 1- and 4-m-Long Vertical Tubes. Proc: GLOBAL 05, Tsukuba, Japan. October 9−13.

Kondrat'ev, N.S., 1971. Trans. IVth all-union conference on heat transfer and hydraulics at movement of two-phase flow inside elements of power engineering machines and apparatuses, Leningrad, Russia. About regimes of the deteriorated heat transfer at flow of supercritical pressure water in tubes, 71–74 (in Russian).

Kraan, M., M.M.W. Peeters, M.V. Fernandez Cid, G.F. Woerlee, W.J.T. Veugelers G.J. Witkamp, 2005. The influence of variable physical properties and buoyancy on heat exchanger design for near- and supercritical conditions. J. Supercritical Fluids. 34, 99–105.

Krasnoshchekov, E.A., Protopopov, V.S., Feng, W., Kuraeva, I.V, 1967. Experimental study of the heat transfer in the supercritical region of carbon dioxide. Convective heat exchange in a homogenous medium, translated from Russian. J. Heat Mass Transfer. Vol. 1.

Krasnoshchekov, E. A. and Protopopov, V.S., 1967. Experimental study of heat exchange in carbon dioxide in the supercritical range at high temperature drops. Teplofizika Vysokikh Tempraturi (High Temp.). 4.

Krett, V., Majer, J., 1971. Temperature field measurement in the region of spacing elements. ZJE-114, Skoda Works, Pilsen, Czechoslovakia. As reported by Yoder (1985).

Kuang, B., Zhang, Y.Q., Cheng, X., 2008. A new, wide-ranged heat transfer correlation of water at supercritical pressures in vertical upward ducts. Proc. 7th Inern. Topical Meeting on Nuclear Reactor Thermal Hydraulics, Operation and Safety (NUTHOS-7), Seoul, Korea, October 5-9, Paper 189.

Kurganov, V.A., Zeigarnik, Yu.A., Maslakova, I.V., 2013. Heat transfer and hydraulic resistance of supercritical pressure coolants. Part III: Generalized description of SCP fluids normal heat transfer, empirical calculating correlations, integral method of theoretical calculations. Int. Journal Heat Mass Transfer 67, 535-547.

Lee, R.A., Haller, K.H., 1974. Supercritical water heat transfer developments and applications. Proc. 5th Intern. Heat Transfer Conf. 4, 335–339. Tokyo, Japan, September 3 – 7. As reported by Pioro and Duffey (2007).

Lee, S. L., Cho, S. K., Sheen, H. J., 1982. Reentrainment of droplets from grid spacer in mist flow portion of LOCA reflood of PWR. Joint NRC/ANS Meeting on Basic Thermal Hydraulic Mechanisms in LWR Analysis, Bethesda, MD, 477-92.

Leung, L.K.H., Groeneveld, D.C., Zhang, J., 2005. Prediction of the obstacle effect on film-boiling heat-transfer. Nucl. Eng. Des. 235, 687-700.

Liu, X., Kuang, B., Ni, C., Cheng, X., 2011. Look-up table establishment of supercritical water heat transfer in vertical upward flow and tube size effect investigation. Proc. 5th Int. Sym. SCWR (ISSCWR-5) .Vancouver, British Columbia, Canada, March 13-16.

Loewenberg, F., Laurien, E., Class, A., Schulenberg, T., 2008. Supercritical water heat transfer in vertical tubes: A look-up table. Nucl. Energy 50, 532-538.

Marek, J., Rehme, K., 1979. Heat-transfer in smooth and roughened rod bundles near spacer grids. Presented at the American Society of Mechanical Engineers (ASME) Winter Annual Meeting, 163–170, Dec. 2–7. As reported by Yoder (1985).

Mikielewicz, D. P., Shehata, A. M., Jackson, J. D., McEligot, D. M., 2002. Temperature, velocity and mean turbulence structure in strongly heated internal gas flows, comparison of numerical predictions with data. Int. J. Heat Mass Transfer 45, 4333–4352.

Miller, D.J., Cheung, F.B., Bajorek, S.M., 2013. On the development of a grid-enhanced single-phase convective heat transfer correlation. Nucl. Eng. Des. 264, 56-60.

Miropolski, Z.L., Shitsman, M.E., 1957. Heat transfer to water and steam at variable specific heat (in near critical region), Soviet Physics. Technical Physics. 27, 2359-2372. English translation 2196-2208.

Mokry, S., Gospodinov, Ye., Pioro, I., and Kirillov, P., 2009. Supercritical water heat-transfer correlation for vertical bare tubes. Proc. 17th Intern. Conf. On Nuclear Engineering ICONE-17, Brussels, Belgium, July 12-16.

Mori, H., Kaida, T., Ohno, M., Yoshida, S., Hamamoto, Y., 2012. Heat transfer to a supercritical pressure fluid flowing in sub-bundle channels. Nucl. Sci. Technol. 49, 373–383.

Morris, D. G., Mullins, C. B., Yoder, G. L., 1982. An analysis of transient film boiling of high pressure water in a rod bundle. Oak Ridge National Laboratory (ORNL-5848). As reported by Yoder (1985).

Niceno, B., Sharabi, M., 2013. Large eddy simulation of turbulent heat transfer at supercritical pressures. Nucl. Eng. Des. 261, 44– 55.

Ornatsky,A.P., Glushchenko, L.F., Simoin, E.T., Kalatchev, S.I., 1970. The research of temperature conditions of small diameter parallel tubes cooled by water under SCPs, HT conf. 4, 1-10.

Peng, S.W., Revellin, R., Groeneveld, D.C., Vasic, A.Z., Shang, D., Cheng, S.C., 2003. Effects of flow obstacles on film boiling heat-transfer. Nucl. Eng. Des. 222, 89−95.

Petukhov, B.S., Kirillov, V.V., 1958. On the question of heat transfer to a turbulent flow of fluids in pipes. Thermal Engineering. 4, 63-68.

Petukhov, B.S., Kransnoschekov, E.A., Protopopov, V.S., 1961. An investigation of heat transfer to fluids flowing in pipes under supercritical conditions. Proc. 1961-62 Heat Transfer Conf. On Inter. Development in Heat Transfer, August 28 – September 1. University Colorado, Boulder, Colorado, USA.

Petukhov, B.S., Medvetskaya, N.V., 1979. Turbulent flow and heat transfer in heated tubes foe single phase heat carriers with near critical parameters, Teplofizika Vysokikh Temperature (High Temperature). 17, 343-350.

Pioro, I. L., Duffey, R.B., 2007. Heat transfer and hydraulic resistance at supercritical pressures in power-engineering applications. ASME Press, New York.

Pioro, I.L., Khartabil, H.F., 2005. Experimental study on heat transfer to supercritical carbon dioxide flowing upward in a vertical tube. Proc. 13th Int. Conf. On Nuclear Engineering (ICONE-13), Beijing, China, May 16-20.

Podila, K., Rao, Y.F., 2015. CFD simulation of supercritical flow and heat transfer in a three rod wire wrapped bundle. Proc. Proc. 16th Intern. Meeting on Nuclear Reactor Thermal-Hydraulics (NURETH-16). Chicago, IL, August 30-September 4.

Protopopov, V.S., Silin, V.A., 1973. Approximate method of calculating the start of local deterioration of heat transfer at supercritical pressure. High Temp. 11 (2), 399–401.

Rehme, K., Trippe, G., 1979. Pressure drop and velocity distribution in rod bundles with spacer grids. Nucl. Eng. Des. 62, 349−359.

Richards, G., Harvel, G.D., Pioro, I.L., Shelegov, A.S., Kirillov, P.L., 2013. Heat transfer profiles of a vertical, bare, 7-element bundle cooled with supercritical Freon R-12. Nucl. Eng. Des. 264, 246-256.

Seider, N. M., Tate, G. E., 1963. Heat transfer and pressure drop of liquids in tubes. Ind. Eng. Chem. 28 (12), 1429–1435.

Sergeev, V.V., 2005. One-dimensional model of post-dryout heat-transfer. Proc. 11th Intern. Meeting on Nuclear Reactor Thermal-Hydraulics (NURETH-11), Avignon, France, October 2−6.

Sergeev, V.V., Gonin, A.I., Remizov, O.V., 1990. Supercritical heat exchange in channels with spacer elements. Atomnaya Energiya (Soviet Res.). 68, 445−447.

Shan, J., Chen, X., 2010. Subchannel analysis of wire wrapped SCWR assembly. Proc. 18th Intern. Conf. On Nuclear Engineering ICONE18, Xi'an, China, May 17-21.

Shin, B.S., Soo, B., Chang., S.H., 2003. An experimental work on the relation between flow structure and CHF by various spacer grids in 2*2 rod bundle with R-134a. Proc. 10th Intern. Topical Meeting on Nuclear Reactor Thermal Hydraulics (NURETH-10) Seoul, Korea, October 5-9.

Shiralkar, B.S., Griffith, P., 1970. The effect of swirl, inlet conditions, flow direction, and tube diameter on the heat transfer to fluids at supercritical pressure. J. Heat Transfer. 92, 465–474.

Shitsman, M.E., 1967. Temperature conditions of evaporative surfaces at supercritical pressures. Electrical Stations, 27-30. As reported by Pioro and Duffey (2007).

Silin, V.A., Voznesensky, V.A., Afrov, A.M., 1993. The light water integral reactor with natural circulation of coolant at supercritical pressure B=500 SKDI. Nucl. Eng. Des. 144, 327-336.

Soussa, J.M.M., 2002. Turbulent flow around a surface-mounted obstacle using 2D-3C DPIV. J. Experiments in Fluids. 33, 854–862.

Stosic, Z., 1995. The rod bundle spacer effects on post-dryout heat-transfer augmentation analyzed by the model HECHAN 2.1. Trans. ASME/JSME Thermal Engineering Conf. 2.

Swenson, H.S., Carver, J.R., Kakarala, C.R., 1965. Heat transfer to supercritical water in smooth-bare tubes. J. Heat Transfer. 4, 477–484.

Tanase, A., Groeneveld, D., 2015. An experimental investigation on the effects of flow obstacles on single phase heat transfer. Nucl. Eng. Des. 288, 195-207.

Terekhov, V.I., Yarygina, N.I., Zhdanov, R.F. 2002. Some features of a turbulent separated flow and heat transfer behind a step and a rib. J. Applied Mechanics and technical Physics. 43, 888-894.

Uchida, H., Kono, N., 1999. An experimental investigation of grid spacer effect on post DNB heat-transfer. Proc. 7th Inter. Conf. On Nuclear Engineering, Tokyo, Japan, April 19−23.

Vikhrev, Yu. V., Barulin, Yu. D., Kon'kov, A. S., 1967. A study of heat transfer in vertical tubes at supercritical pressures. Heat Transfer in Tubes, UDC 536.24.001.5.

Vlcek, J., Weber, P., 1970. The experimental investigation of a local (spot) heat transfer coefficient in the fuel spacers area. Australian Atomic Energy Commission Research Establishment LIB/TRANS 250. As reported by Yoder (1985).

Vágó, T., Kiss, A., Tóth, S., Aszódi, A., 2013. Numerical investigation on the inlet and outlet effect of heated test section of SCWR fuel qualification test design. Proc. 15th Intern. Topical Meeting On Nuclear Reactor Thermalhydraulics, NURETH15. 134, Pisa, Italy.

Wang, H, Qincheng, Bi*, Yang, Z, Gang, W, Richa, H., 2011. Experimental investigation on heat transfer of supercritical pressure water in annular flow geometry. Proc. 5th Intern. Symp. On Super-Critical Water Reactor (ISSCWR-5) Vancouver, British Columbia, Canada.

Wang, H, Qincheng, Bi*, Yang, Z, Gang, W, Richa, H., 2012. Experimental and numerical study on the enhanced effect of spiral spacer to heat transfer of supercritical pressure water in vertical annular channels. J. Applied Thermal Engineering. 48, 436-445.

Wang, H., Qincheng B., Linchuan W., Haicai L., Laurence K.H., 2014. Experimental investigation of heat transfer from a 2 × 2 rod bundle to supercritical pressure water. Nucl. Eng. Des. 275, 205–218.

Watts, M. J., and Chou, C-T., 1982. Mixed convection heat transfer to supercritical pressure water. Proc. 7th, IHTC, Munich, Germany. 495–500.

Wang, S., Yuan, L.Q., Leung, L.K.H., 2010. Assessment of supercritical heat- transfer correlations against AECL database for tubes. Proc. 2nd Canada-China Joint Workshop on Supercritical Water-Cooled Reactors (CCSC-2010) Toronto, Ontario, Canada, April 25-28.

Wang, C., Li, H., 2014. Evaluation of the heat transfer correlations for supercritical pressure water in vertical tubes. Heat Transfer Engineering, 35, 685–692.

Wong, S., Hochreiter, L.E., 1981. Analysis of the FLECT SEASET unblocked bundle steam cooling and boil off tests. NUREG/CR-1533.

Yamagata, K., Nishikawa, K., Hasegawa, S., Fujii, T., Yoshida, S., 1972. Forced convective heat transfer to supercritical water flowing in tubes. Int. J. Heat Mass Transfer. 15 (12), 2575–2593.

Yang, S.K. and Khartabil, H.F., 2005. Normal and deteriorated heat transfer correlations for Supercritical Fluids. Trans. American Nuclear Society. Washington, D.C., USA. 93, 635–637.

Yang, S.-K, 2013. Heat transfer modes in supercritical fluids. Proc. 15th Intern. Topical Meeting on Nuclear Reactor Thermal-hydraulics, (NURETH- 15), Pisa, Italy, May 12-17, Paper NURETH15-547.

Yao, M., Nakatani, M., Suzuki, K., 1995. Flow visualization and heat transfer experiments in a turbulent channel flow obstructed with an inserted square rod. Intern. Heat and Fluid Flow. 16, 389-397.

Yao, S.C., Hochreiter, W.J., Leech, W.J., 1982. Heat transfer augmentation in rod bundles near grid spacers. J. Heat Transfer. 104, 76-81.

Yoder, G. L., 1985. Heat transfer near spacer grids in rod bundles. National Heat Transfer Conference, Denver, Colorado.

Yoder, G. L., Morris, D. G., Mullins, C. B., Ott, L. J., 1982. Dispersed flow film boiling in rod bundle geometry-steady state heat transfer data and correlation comparisons. Oak Ridae National Laboratory (ORNL/5822). As reported by Yoder (1985).

Yoder, G. L., Morris, D. G., Mullins, C. B., Ott, L. J., 1983. Dispersed-flow film boiling heat transfer data near spacer grids in a rod bundle. Nucl. Techn. 60, 304-313.

Yongliang, Li., Huang, Y., Xiao, Y., Donghua, Lu., Xiao. Z., 2010. Progress of thermal-hydraulic research on SCWR in NPIC. Proc. 2nd Canada-China Joint Workshop on Supercritical Water-Cooled Reactors (CCSC) P059 Toronto, Ontario, Canada.

Zahlan, H., 2008. Flow obstacle effect on film boiling heat transfer with uniform and non-uniform axial heat flux. M.A.Sc. Thesis, Mechanical Engineering Department, University of Ottawa. Canada.

Zahlan, H., Jiang, K., Tavoularis, S., Groeneveld, D., 2013. Measurements of heat transfer coefficient, CHF and heat transfer deterioration in flows of CO_2 at near-critical and supercritical pressures. Proc. 6th Intern. Symp. On Supercritical Water-Cooled Reactors (ISSCWR-6), Shenzhen, Guangdong, China.

Zahlan, H., Groeneveld, D., Tavoularis, S., 2014. Fluid-to-fluid scaling for convective heat transfer in tubes at supercritical and high subcritical pressures. Int. J. Heat Mass Transfer 73, 274–283.

Zahlan, H., Groeneveld, D., Tavoularis, S., 2015. Measurements of convective heat transfer to vertical upward flows of CO_2 in circular geometry at near-critical and supercritical pressures. Nucl. Eng. Des. 289, 92-107.

Zahlan, H., Tavoularis, S., Groeneveld, D.C., 2015. A look-up table for trans-critical heat transfer in water-cooled tubes. Nucl. Eng. Des. 285, 109–125.

Zhao, M., Gu, H.Y., Cheng, X., 2013. Experimental study on heat transfer of supercritical water flowing downward in circular tubes. Ann. Nucl. Energy. 63, 339–349.

Zhu, X.J., Bi, Q.C., Yang, D., Chen, T.K, 2009. An investigation on heat transfer characteristics of different pressure steam–water in vertical upward tube. Nucl. Eng. and Des. 239, 381–388

Zwolinski, S., Anderson, M., Corradini, M., Licht, J., 2011. Evaluation of fluid-to-fluid scaling method for water and carbon dioxide at supercritical pressure. Proc. 5th Intern. Symp. On Supercritical Water-Cooled Reactors (SCWR5), Vancouver, Canada.

Appendix I: Heat Transfer Coefficient of the Obstructed and Bare Tube Showing The Obstacles Negative Impact On The SCHT

Obstructed tube					Bare tube								
P/P_c	G (kg m^{-2} s^{-1})	q (kW m^{-2})	T_{in} (°C)	H (kW m^{-2}K^{-1})	P/P_c	G (kg m^{-2} s^{-1})	q (kW m^{-2})	T_{in} (°C)	H (kW m^{-2}K^{-1})	Obstacle pitch (mm)	Δz (mm)	ε (%)	R_{SCHT}
1.052	331.2	55.91	11.6		1.046	339.7	56.14	11.1		100		25	
				1.29					0.98		3		1.32
				1.03					0.71		53		1.45
				0.84					0.76		103		1.11
				0.82					0.85		153		0.96
				0.83					0.91		203		0.91
				0.84					0.92		253		0.91
				0.86					0.87		303		0.99
				0.84					0.84		353		1.00
				0.84					0.83		403		1.01
				0.84					0.82		453		1.02
				0.84					0.81		503		1.04
				0.84					0.81		553		1.04
				0.84					0.81		603		1.04
				0.86					0.81		653		1.06
				0.86					0.81		703		1.06
				0.87					0.81		753		1.07
				0.88					0.81		803		1.09
				0.87					0.81		853		1.07
				0.90					0.82		903		1.10
				1.53					0.83		4		1.84
				0.86					0.85		54		1.01
				0.59					0.85		104		0.69
				0.71					0.89		154		0.80
				1.03					0.92		204		1.12
				1.44					1.00		254		1.44

				1.74					1.10		304		1.58
				1.73					1.18		354		1.47
				1.64					1.27		404		1.29
				1.51					1.30		454		1.16
				1.48					1.35		504		1.10
				1.38					1.34		554		1.03
				1.31					1.30		604		1.01
				1.27					1.28		654		0.99
				1.22					1.25		704		0.98
				1.20					1.24		754		0.97
				1.15					1.20		804		0.96
				1.13					1.19		854		0.95
				1.28					1.25		904		1.02
1.039	313.3	29.72	14.1		1.039	293.5	29.66	14.6		100		25	
				1.80					1.26		3		1.43
				1.58					0.84		53		1.88
				1.32					0.78		103		1.69
				0.98					0.92		153		1.07
				0.76					1.02		203		0.75
				0.81					1.06		253		0.76
				0.93					1.01		303		0.92
				1.00					0.98		353		1.02
				1.02					0.97		403		1.05
				1.00					0.98		453		1.02
				0.96					0.98		503		0.98
				0.95					0.97		553		0.98
				0.94					0.98		603		0.96
				0.95					0.98		653		0.97
				0.95					0.98		703		0.97
				0.95					0.98		753		0.97
				0.96					0.98		803		0.98
				0.95					0.98		853		0.97
				0.98					0.99		903		0.99
				2.40					1.00		4		2.40
				1.60					1.00		54		1.60
				0.86					0.99		104		0.87

				0.69					0.99		154		0.70
				0.82					0.99		204		0.83
				0.97					0.99		254		0.98
				1.11					1.00		304		1.11
				1.14					0.99		354		1.15
				1.07					0.99		404		1.08
				0.99					0.98		454		1.01
				1.02					1.04		504		0.98
				1.01					1.11		554		0.91
				1.01					1.15		604		0.88
				1.06					1.22		654		0.87
				1.10					1.34		704		0.82
				1.22					1.39		754		0.88
				1.32					1.48		804		0.89
				1.52					1.59		854		0.96
				2.07					1.79		904		1.16
1.041	307.6	34.10	14.8		1.050	299.4	33.99	14.6		100		25	
				1.76					1.21		3		1.45
				1.49					0.77		53		1.94
				1.08					0.80		103		1.35
				0.83					0.95		153		0.87
				0.81					1.03		203		0.79
				0.89					1.03		253		0.86
				0.98					0.99		303		0.99
				0.99					0.98		353		1.01
				0.96					0.97		403		0.99
				0.94					0.96		453		0.98
				0.92					0.96		503		0.96
				0.92					0.96		553		0.96
				0.92					0.95		603		0.97
				0.93					0.96		653		0.97
				0.92					0.95		703		0.97
				0.92					0.94		753		0.98
				0.93					0.94		803		0.99
				0.92					0.94		853		0.98
				0.94					0.95		903		0.99

				2.00					0.97		4		2.06
				1.14					1.01		54		1.13
				0.71					1.03		104		0.69
				0.70					1.06		154		0.66
				0.83					1.06		204		0.78
				0.97					1.10		254		0.88
				1.13					1.13		304		1.00
				1.16					1.13		354		1.03
				1.09					1.11		404		0.98
				1.00					1.13		454		0.88
				1.06					1.27		504		0.83
				1.14					1.47		554		0.78
				1.17					1.60		604		0.73
				1.31					1.69		654		0.78
				1.48					1.75		704		0.85
				1.71					1.73		754		0.99
				1.77					1.74		804		1.02
				1.87					1.78		854		1.05
				2.16					1.71		904		1.26
1.051	297.0	59.32	14.5		1.039	304.0	59.30	14.8		100		25	
				0.95					0.75		3		1.27
				0.89					0.77		53		1.16
				0.84					0.87		103		0.97
				0.87					0.95		153		0.92
				0.86					0.91		203		0.95
				0.85					0.88		253		0.97
				0.88					0.86		303		1.02
				0.84					0.85		353		0.99
				0.83					0.86		403		0.97
				0.83					0.88		453		0.94
				0.82					0.89		503		0.92
				0.82					0.89		553		0.92
				0.81					0.89		603		0.91
				0.82					0.89		653		0.92
				0.80					0.87		703		0.92
				0.80					0.85		753		0.94

				0.80					0.85		803		0.94
				0.78					0.85		853		0.92
				0.81					0.90		903		0.90
				1.29					1.00		4		1.29
				0.93					1.07		54		0.87
				0.63					1.10		104		0.57
				0.59					1.12		154		0.53
				0.86					1.13		204		0.76
				1.06					1.12		254		0.95
				1.12					1.08		304		1.04
				1.10					1.07		354		1.03
				1.05					1.02		404		1.03
				0.99					0.96		454		1.03
				0.96					0.92		504		1.04
				0.90					0.89		554		1.01
				0.87					0.85		604		1.02
				0.84					0.81		654		1.04
				0.81					0.79		704		1.03
				0.80					0.77		754		1.04
				0.78					0.75		804		1.04
				0.77					0.74		854		1.04
				0.91					0.82		904		1.11
1.081	409.5	44.74	10.8		1.097	414.0	44.79	10.8		100		25	
				2.23					1.77		3		1.26
				1.90					1.52		53		1.25
				1.74					1.12		103		1.55
				1.56					0.79		153		1.97
				1.25					0.77		203		1.62
				0.81					0.98		253		0.83
				0.65					1.16		303		0.56
				0.78					1.24		353		0.63
				0.89					1.20		403		0.74
				0.98					1.15		453		0.85
				1.00					1.10		503		0.91
				0.96					1.10		553		0.87
				0.89					1.12		603		0.79

				0.87					1.16		653		0.75
				0.85					1.19		703		0.71
				0.86					1.22		753		0.70
				0.88					1.27		803		0.69
				0.86					1.30		853		0.66
				0.90					1.32		903		0.68
				2.66					1.36		4		1.96
				2.33					1.38		54		1.69
				1.82					1.34		104		1.36
				0.98					1.34		154		0.73
				0.54					1.34		204		0.40
				0.83					1.39		254		0.60
				1.43					1.43		304		1.00
				2.29					1.46		354		1.57
				2.39					1.51		404		1.58
				2.37					1.57		454		1.51
				2.36					1.69		504		1.40
				2.29					1.74		554		1.32
				2.18					1.79		604		1.22
				2.23					1.86		654		1.20
				2.28					1.86		704		1.23
				2.36					1.91		754		1.24
				2.33					1.91		804		1.22
				2.43					2.01		854		1.21
				2.68					2.21		904		1.21
1.046	196.4	29.68	14.8		1.05	206.3	29.79	15.0		100		25	
				0.92					0.90		3		1.02
				1.02					0.96		53		1.06
				1.10					1.08		103		1.02
				1.12					1.13		153		0.99
				1.10					1.09		203		1.01
				1.09					1.08		253		1.01
				1.13					1.07		303		1.06
				1.09					1.06		353		1.03
				1.08					1.06		403		1.02
				1.08					1.07		453		1.01

				1.08					1.07		503		1.01
				1.07					1.07		553		1.00
				1.06					1.05		603		1.01
				1.06					1.05		653		1.01
				1.05					1.04		703		1.01
				1.03					1.03		753		1.00
				1.02					1.02		803		1.00
				0.99					1.00		853		0.99
				0.99					0.98		903		1.01
				0.97					0.93		4		1.04
				0.78					0.91		54		0.86
				0.77					0.87		104		0.89
				0.79					0.84		154		0.94
				0.77					0.81		204		0.95
				0.74					0.79		254		0.94
				0.71					0.76		304		0.93
				0.67					0.74		354		0.91
				0.65					0.71		404		0.92
				0.63					0.69		454		0.91
				0.62					0.68		504		0.91
				0.60					0.68		554		0.88
				0.58					0.66		604		0.88
				0.57					0.66		654		0.86
				0.57					0.67		704		0.85
				0.59					0.69		754		0.86
				0.59					0.72		804		0.82
				0.63					0.77		854		0.82
				0.80					0.94		904		0.85
1.034	289.1	29.6	14.4		1.039	293.5	29.7	14.6		50		25	
				1.42					1.26		3		1.13
				1.45					0.84		53		1.73
				1.15					0.78		103		1.47
				0.91					0.92		153		0.99
				0.89					1.02		203		0.87
				0.95					1.06		253		0.90
				1.01					1.01		303		1.00

				1.04					0.98		353		1.06
				1.02					0.97		403		1.05
				1.01					0.98		453		1.03
				5.47					0.98		3		5.58
				2.52					0.97		53		2.60
				1.32					0.98		103		1.35
				0.78					0.98		153		0.80
				0.88					0.98		203		0.90
				1.02					0.98		253		1.04
				1.09					0.98		303		1.11
				1.09					0.98		353		1.11
				1.05					0.99		403		1.06
				1.01					1.00		484		1.01
				1.01					1.00		534		1.01
				0.99					0.99		584		1.00
				0.99					0.99		634		1.00
				0.99					0.99		684		1.00
				1.01					0.99		734		1.02
				1.03					1.00		784		1.03
				1.02					0.99		834		1.03
				1.03					0.99		884		1.04
				1.00					0.98		934		1.02
				1.03					1.04		984		0.99
				1.03					1.11		1034		0.93
				1.01					1.15		1084		0.88
				1.06					1.22		1134		0.87
				1.09					1.34		1184		0.81
				1.19					1.39		1234		0.86
				1.26					1.48		1284		0.85
				1.42					1.59		1334		0.89
				1.87					1.79		1384		1.04
1.042	295.1	33.9	14.5		1.050	299.4	34.0	14.6		50		25	
				1.44					1.21		3		1.19
				1.39					0.77		53		1.81
				1.05					0.80		103		1.31
				0.89					0.95		153		0.94

				0.91					1.03		203		0.88
				0.96					1.03		253		0.93
				0.99					0.99		303		1.00
				0.99					0.98		353		1.01
				0.98					0.97		403		1.01
				0.97					0.96		453		1.01
				5.83					0.96		3		6.07
				2.54					0.96		53		2.65
				1.11					0.95		103		1.17
				0.75					0.96		153		0.78
				0.88					0.95		203		0.93
				0.99					0.94		253		1.05
				1.04					0.94		303		1.11
				1.02					0.94		353		1.09
				0.99					0.95		403		1.04
				0.96					0.97		484		0.99
				0.95					1.01		534		0.94
				0.93					1.03		584		0.90
				0.94					1.06		634		0.89
				0.94					1.06		684		0.89
				0.96					1.10		734		0.87
				1.02					1.13		784		0.90
				1.03					1.13		834		0.91
				1.06					1.11		884		0.95
				1.06					1.13		934		0.94
				1.14					1.27		984		0.90
				1.19					1.47		1034		0.81
				1.18					1.60		1084		0.74
				1.30					1.69		1134		0.77
				1.46					1.75		1184		0.83
				1.71					1.73		1234		0.99
				1.78					1.74		1284		1.02
				1.89					1.78		1334		1.06
				2.11					1.71		1384		1.23
1.044	298.0	49.2	14.5		1.051	289.7	49.1	14.7		50		25	
				1.09					0.81		3		1.35

				0.99					0.78		53		1.27
				0.90					0.89		103		1.01
				0.91					0.98		153		0.93
				0.90					0.96		203		0.94
				0.90					0.92		253		0.98
				0.89					0.90		303		0.99
				0.89					0.89		353		1.00
				0.88					0.88		403		1.00
				0.89					0.88		453		1.01
				7.57					0.88		3		8.60
				1.80					0.88		53		2.05
				0.72					0.88		103		0.82
				0.74					0.88		153		0.84
				0.86					0.87		203		0.99
				0.92					0.86		253		1.07
				0.94					0.85		303		1.11
				0.88					0.83		353		1.06
				0.85					0.84		403		1.01
				0.86					0.86		484		1.00
				0.88					0.90		534		0.98
				0.89					0.92		584		0.97
				0.94					0.98		634		0.96
				1.03					1.06		684		0.97
				1.19					1.17		734		1.02
				1.47					1.23		784		1.20
				1.51					1.28		834		1.18
				1.47					1.24		884		1.19
				1.38					1.19		934		1.16
				1.37					1.15		984		1.19
				1.29					1.10		1034		1.17
				1.22					1.05		1084		1.16
				1.19					1.01		1134		1.18
				1.15					0.97		1184		1.19
				1.13					0.95		1234		1.19
				1.08					0.92		1284		1.17
				1.06					0.90		1334		1.18

				1.18					0.96		1384		1.23
1.039	308.8	59.2	14.4		1.039	304.0	59.3	14.8		50		25	
				0.96					0.75		3		1.28
				0.91					0.77		53		1.18
				0.85					0.87		103		0.98
				0.85					0.95		153		0.89
				0.84					0.91		203		0.92
				0.84					0.88		253		0.95
				0.84					0.86		303		0.98
				0.84					0.85		353		0.99
				0.84					0.86		403		0.98
				0.84					0.88		453		0.95
				8.42					0.89		3		9.46
				1.52					0.89		53		1.71
				0.65					0.89		103		0.73
				0.70					0.89		153		0.79
				0.84					0.87		203		0.97
				0.91					0.85		253		1.07
				0.94					0.85		303		1.11
				0.87					0.85		353		1.02
				0.86					0.90		403		0.96
				0.93					1.00		484		0.93
				1.00					1.07		534		0.93
				1.06					1.10		584		0.96
				1.14					1.12		634		1.02
				1.19					1.13		684		1.05
				1.24					1.12		734		1.11
				1.28					1.08		784		1.19
				1.24					1.07		834		1.16
				1.17					1.02		884		1.15
				1.09					0.96		934		1.14
				1.06					0.92		984		1.15
				0.99					0.89		1034		1.11
				0.95					0.85		1084		1.12
				0.91					0.81		1134		1.12
				0.88					0.79		1184		1.11

				0.87					0.77		1234		1.13
				0.84					0.75		1284		1.12
				0.83					0.74		1334		1.12
				0.94					0.82		1384		1.15
1.089	398.1	45.0	10.6		1.097	414.0	44.79	10.8		50		25	
				2.20					1.77		3		1.24
				1.91					1.52		53		1.26
				1.74					1.12		103		1.55
				1.50					0.79		153		1.90
				1.11					0.77		203		1.44
				0.71					0.98		253		0.72
				0.71					1.16		303		0.61
				0.84					1.24		353		0.68
				0.93					1.20		403		0.78
				1.01					1.15		453		0.88
				7.17					1.10		3		6.52
				3.10					1.10		53		2.82
				2.30					1.12		103		2.05
				1.58					1.16		153		1.36
				0.74					1.19		203		0.62
				0.66					1.22		253		0.54
				0.89					1.27		303		0.70
				0.99					1.30		353		0.76
				1.06					1.32		403		0.80
				1.07					1.36		484		0.79
				0.99					1.38		534		0.72
				0.96					1.34		584		0.72
				1.01					1.34		634		0.75
				1.07					1.34		684		0.80
				1.19					1.39		734		0.86
				1.59					1.43		784		1.11
				2.09					1.46		834		1.43
				2.43					1.51		884		1.61
				2.39					1.57		934		1.52
				2.53					1.69		984		1.50
				2.46					1.74		1034		1.41

				2.49					1.79		1084		1.39
				2.52					1.86		1134		1.35
				2.52					1.86		1184		1.35
				2.59					1.91		1234		1.36
				2.54					1.91		1284		1.33
				2.58					2.01		1334		1.28
				2.88					2.21		1384		1.30
1.048	212.1	29.82	14.8		1.05	206.3	29.79	15.0		50		25	
				0.96					0.90		3		1.07
				1.03					0.96		53		1.07
				1.09					1.08		103		1.01
				1.14					1.13		153		1.01
				1.10					1.09		203		1.01
				1.09					1.08		253		1.01
				1.09					1.07		303		1.02
				1.09					1.06		353		1.03
				1.09					1.06		403		1.03
				1.09					1.07		453		1.02
				4.98					1.07		3		4.65
				1.65					1.07		53		1.54
				0.89					1.05		103		0.85
				0.98					1.05		153		0.93
				1.09					1.04		203		1.05
				1.11					1.03		253		1.08
				1.07					1.02		303		1.05
				1.03					1.00		353		1.03
				1.01					0.98		403		1.03
				0.98					0.93		484		1.05
				0.95					0.91		534		1.04
				0.91					0.87		584		1.05
				0.89					0.84		634		1.06
				0.86					0.81		684		1.06
				0.83					0.79		734		1.05
				0.81					0.76		784		1.07
				0.78					0.74		834		1.05
				0.76					0.71		884		1.07

				0.73					0.69		934		1.06
				0.72					0.68		984		1.06
				0.70					0.68		1034		1.03
				0.68					0.66		1084		1.03
				0.68					0.66		1134		1.03
				0.67					0.67		1184		1.00
				0.69					0.69		1234		1.00
				0.70					0.72		1284		0.97
				0.74					0.77		1334		0.96
				0.98					0.94		1384		1.04
1.056	207.8	29.82	14.7		1.050	206.3	29.79	15.0		25		25	
				0.95					0.90		3		1.06
				1.05					0.96		53		1.09
				1.11					1.08		103		1.03
				1.12					1.13		153		0.99
				1.10					1.09		203		1.01
				1.22					1.08		3		1.13
				1.10					1.07		53		1.03
				1.06					1.06		103		1.00
				1.08					1.06		153		1.02
				1.10					1.07		203		1.03
				1.19					1.07		3		1.11
				1.13					1.07		53		1.06
				1.04					1.05		103		0.99
				1.04					1.05		153		0.99
				1.07					1.04		203		1.03
				1.25					1.03		3		1.21
				1.06					1.02		53		1.04
				0.98					1.00		103		0.98
				0.97					0.98		153		0.99
				1.29					0.93		203		1.39
				1.02					0.91		3		1.12
				0.85					0.87		53		0.98
				0.82					0.84		103		0.98
				0.81					0.81		153		1.00
				0.95					0.79		203		1.20

				1.36					0.76		3		1.79
				0.71					0.74		53		0.96
				0.65					0.71		103		0.92
				0.67					0.69		153		0.97
				0.74					0.68		203		1.09
				1.52					0.68		3		2.24
				0.76					0.66		53		1.15
				0.49					0.66		103		0.74
				0.52					0.67		153		0.78
				0.61					0.69		203		0.88
				3.67					0.72		3		5.10
				1.36					0.77		53		1.77
				1.17					0.94		103		1.24
1.48	309.6	16.57	14.4		1.44	309.2	16.64	14.5		25		25	
				1.72					1.41		3		1.22
				1.43					1.34		53		1.07
				1.35					1.29		103		1.05
				1.33					1.27		153		1.05
				1.34					1.26		203		1.06
				1.76					1.22		3		1.44
				1.50					1.21		53		1.24
				1.40					1.20		103		1.17
				1.37					1.17		153		1.17
				1.40					1.16		203		1.21
				1.89					1.12		3		1.69
				1.64					1.10		53		1.49
				1.52					1.04		103		1.46
				1.49					1.14		153		1.31
				1.50					1.25		203		1.20
				1.99					1.29		3		1.54
				1.72					1.38		53		1.25
				1.67					1.49		103		1.12
				1.68					1.51		153		1.11
				1.72					1.56		203		1.10
				1.91					1.55		3		1.23
				1.89					1.36		53		1.39

				1.85					1.13		103		1.64
				1.84					1.00		153		1.84
				1.92					1.16		203		1.66
				2.28					1.37		3		1.66
				2.18					1.57		53		1.39
				2.23					1.67		103		1.34
				2.13					1.66		153		1.28
				2.19					1.51		203		1.45
				2.74					1.34		3		2.04
				2.48					1.20		53		2.07
				2.43					1.21		103		2.01
				2.42					1.29		153		1.88
				2.47					1.30		203		1.90
				5.10					1.28		3		3.98
				3.50					1.27		53		2.76
				3.24					1.37		103		2.36
1.046	204.7	29.65	15.0		1.050	206.3	29.79	15.0		25		13	
				0.91					0.90		3		1.01
				1.02					0.96		53		1.06
				1.13					1.08		103		1.05
				1.13					1.13		153		1.00
				1.12					1.09		203		1.03
				1.11					1.08		3		1.03
				1.12					1.07		53		1.05
				1.08					1.06		103		1.02
				1.10					1.06		153		1.04
				1.10					1.07		203		1.03
				1.11					1.07		3		1.04
				1.07					1.07		53		1.00
				1.06					1.05		103		1.01
				1.06					1.05		153		1.01
				1.09					1.04		203		1.05
				1.08					1.03		3		1.05
				1.02					1.02		53		1.00
				1.00					1.00		103		1.00
				0.98					0.98		153		1.00

				1.02					0.93		203		1.10
				0.88					0.91		3		0.97
				0.85					0.87		53		0.98
				0.81					0.84		103		0.96
				0.78					0.81		153		0.96
				0.81					0.79		203		1.03
				0.78					0.76		3		1.03
				0.67					0.74		53		0.91
				0.67					0.71		103		0.94
				0.64					0.69		153		0.93
				0.65					0.68		203		0.96
				0.79					0.68		3		1.16
				0.55					0.66		53		0.83
				0.55					0.66		103		0.83
				0.58					0.67		153		0.87
				0.62					0.69		203		0.90
				0.87					0.72		3		1.21
				0.71					0.77		53		0.92
				0.76					0.94		103		0.81
1.014	294.1	16.63	14.8		1.440	309.2	16.64	14.5		25		13	
				1.34					1.41		3		0.95
				1.21					1.34		53		0.90
				1.13					1.29		103		0.88
				1.09					1.27		153		0.86
				1.02					1.26		203		0.81
				0.96					1.22		3		0.79
				1.09					1.21		53		0.90
				1.29					1.20		103		1.08
				1.33					1.17		153		1.14
				1.36					1.16		203		1.17
				1.47					1.12		3		1.31
				1.52					1.10		53		1.38
				1.49					1.04		103		1.43
				1.48					1.14		153		1.30
				1.49					1.25		203		1.19
				1.55					1.29		3		1.20

				1.57					1.38		53		1.14
				1.47					1.49		103		0.99
				1.31					1.51		153		0.87
				1.14					1.56		203		0.73
				1.26					1.55		3		0.81
				1.42					1.36		53		1.04
				1.49					1.13		103		1.32
				1.43					1.00		153		1.43
				1.31					1.16		203		1.13
				1.56					1.37		3		1.14
				1.58					1.57		53		1.01
				1.60					1.67		103		0.96
				1.41					1.66		153		0.85
				1.14					1.51		203		0.75
				1.29					1.34		3		0.96
				1.39					1.20		53		1.16
				1.40					1.21		103		1.16
				1.25					1.29		153		0.97
				1.15					1.30		203		0.88
				1.72					1.28		3		1.34
				2.01					1.27		53		1.58
				2.03					1.37		103		1.48
1.055	307.9	59.19	14.8		1.039	304.0	59.30	14.8		25		13	
				0.76					0.75		3		1.01
				0.80					0.77		53		1.04
				0.89					0.87		103		1.02
				0.95					0.95		153		1.00
				0.94					0.91		203		1.03
				0.93					0.88		3		1.06
				0.86					0.86		53		1.00
				0.82					0.85		103		0.96
				0.84					0.86		153		0.98
				0.85					0.88		203		0.97
				0.98					0.89		3		1.10
				0.81					0.89		53		0.91
				0.80					0.89		103		0.90

				0.80					0.89		153		0.90
				0.84					0.87		203		0.97
				1.00					0.85		3		1.18
				0.74					0.85		53		0.87
				0.77					0.85		103		0.91
				0.79					0.90		153		0.88
				1.19					1.00		203		1.19
				1.04					1.07		3		0.97
				0.86					1.10		53		0.78
				0.93					1.12		103		0.83
				1.07					1.13		153		0.95
				1.19					1.12		203		1.06
				1.31					1.08		3		1.21
				1.18					1.07		53		1.10
				1.07					1.02		103		1.05
				0.98					0.96		153		1.02
				0.96					0.92		203		1.04
				1.01					0.89		3		1.13
				0.93					0.85		53		1.09
				0.88					0.81		103		1.09
				0.84					0.79		153		1.06
				0.82					0.77		203		1.06
				0.87					0.75		3		1.16
				0.89					0.74		53		1.20
				1.07					0.82		103		1.30
1.096	406.3	44.84	10.8		1.097	414.0	44.79	10.8		25		13	
				1.80					1.77		3		1.02
				1.58					1.52		53		1.04
				1.33					1.12		103		1.19
				1.10					0.79		153		1.39
				0.87					0.77		203		1.13
				0.92					0.98		3		0.94
				1.11					1.16		53		0.96
				1.07					1.24		103		0.86
				0.90					1.20		153		0.75
				0.82					1.15		203		0.71

				1.08					1.10		3		0.98
				1.08					1.10		53		0.98
				0.95					1.12		103		0.85
				0.81					1.16		153		0.70
				0.83					1.19		203		0.70
				1.22					1.22		3		1.00
				1.09					1.27		53		0.86
				0.89					1.30		103		0.68
				0.83					1.32		153		0.63
				1.44					1.36		203		1.06
				1.75					1.38		3		1.27
				1.28					1.34		53		0.96
				0.86					1.34		103		0.64
				0.94					1.34		153		0.70
				1.32					1.39		203		0.95
				3.43					1.43		3		2.40
				3.11					1.46		53		2.13
				2.74					1.51		103		1.81
				2.52					1.57		153		1.61
				2.70					1.69		203		1.60
				3.13					1.74		3		1.80
				2.85					1.79		53		1.59
				2.81					1.86		103		1.51
				2.85					1.86		153		1.53
				2.98					1.91		203		1.56
				3.12					1.91		3		1.63
				3.10					2.01		53		1.54
				3.49					2.21		103		1.58